UNIVERSITY OF HULL

Matrix isolation studies of transition metal halides and main group Lewis acid–base complexes

Being a Thesis submitted for the Degree of

Doctor of Philosophy (PhD)

In the University of Hull

By

Ahmed Khairy Ali Mohammed Sakr

BSc. Chemistry, Tanta University, Egypt

MSc. Inorganic Chemistry, Benha University, Egypt

September 2018

Abstract

The main purpose of this work was to synthesise and study the binary fluorides of nickel, cobalt and chromium, and the binary halides of palladium and molybdenum in solid argon matrices. Both UV/vis spectroscopy and FTIR spectroscopy were employed to identify the products formed. Additionally, this work also investigated the reaction between SiF_4 with alkyl phosphines.

In the beginning, the work focused on isolation of atomic nickel, cobalt, molybdenum, and palladium in neat argon matrices. The FTIR data revealed the interaction of nickel and fluorine atoms in solid argon matrix and the formation of nickel fluoride molecules NiF, NiF_2, and NiF_4 and also provided evidence for the formation of NiF_3 molecules. Moreover, cobalt atoms trapped in a matrix of argon doped with fluorine yielded the formation of CoF, CoF_2, CoF_3, CoF_4, and Co_2F_2 molecules. Furthermore, molybdenum fluoride species in an argon matrix have been obtained, which is the first observation of the vibrational modes for MoF and MoF_2 in matrices. The geometry of MoF_2 species was assigned to be bent with a bond angle of $132°$. In addition, FTIR data indicated the formation of matrix isolated chromium fluorides in solid argon matrix. The study succeeded in the characterisation of CrF and CrF_6 molecules, as well as the previously identified CrF_2, CrF_3, CrF_4 and CrF_5. The IR band related to CrF_6 is observed at 757 cm^{-1}. A computational study suggested that $PdCl_2$ is linear.

The reaction between SiF_4 and PMe_3 at cryogenic temperatures led to the formation of a SiF_4-PMe_3 complex and indicated the formation of two different species. The reaction between SiF_4 and PEt_3 revealed the formation of a 1:1 adduct of trigonal bipyramid structure with axial PEt_3 of $SiF_4.PEt_3$ and a 1:2 complex of *trans*–$[SiF_4.(PEt_3)_2]$ structure. The results were supported by computational data.

Acknowledgements

List of Publication and Presentations

Publications

1. Harris, N.; Sakr, A. K.; Snelling, H. V.; Young, N. A., X–ray absorption study of platinum and palladium atoms in argon matrices: evidence for platinum in a substitutional site and a short Pd–Ar interaction, *J. Mol. Struct.,* **2018**, *1172*, 80–88.

Presentations

1. XXXIV European Congress on Molecular Spectroscopy–EUCOMS 2018, 19th–24th August 2018, Coimbra, Portugal. (Poster)
2. PG colloquium, 22nd January 2018, Department of Chemistry, University of Hull. (Oral presentations)
3. RSC Dalton Division North Regional Meeting 2017, University of Sheffield, UK. (Poster)

Contents

Chapter 1

Chapter 4

Chapter 5

Chapter 6

Appendices

List of Figures

List of Tables

List of Abbreviations

DFT	Density Functional Theory
ESR	Electron Spin Resonance
FTIR	Fourier Transform Infrared
K	Kelvin
NIR	Near infrared
PEt_3	Triethyl phosphine
PMe_3	Trimethyl phosphine
IR	Infrared
UV	Ultraviolet
XRD	X–ray diffraction

Chapter 1

Introduction

1.1 Matrix isolation

1.1.1 Introduction

Matrix isolation consists of a series of experimental techniques where guest atoms or molecules are trapped into host materials.[1] These trapped species cannot react chemically with the host materials and cannot diffuse or interact with any other materials. There are different kinds of host material; it can be a crystalline solid, a polymer, or a glass formed by freezing liquid or gas. Accordingly, the term matrix isolation is generally used to describe a technique of trapping atoms or molecules into solidified inert gases at a low temperatures, typically around 10 K.

1.1.2 History of matrix isolation

Researchers discovered very simple ways for liquefying gases to perform experiments at low temperature in the second half of nineteenth century. The liquefication of nitrogen below 77 K was one of the most important early breakthroughs. In a short time, the different behaviour of many organic substances at low temperature had been observed by chemists; they had no phosphorescence at room temperature but emitted light when cooled to the boiling point of liquid nitrogen. A simple experiment involves submerging a material of interest into coolant liquid nitrogen or liquid air, with visible emission being activated by irradiation with UV light or X–rays. George Pimentel and his group played a vital role in developing matrix isolation techniques. In 1954, Pimentel at al. developed a new technique to trap reactive species by using noble gases under vacuum at low temperature.[2] As the noble gases are chemically inert and completely transparent throughout a wide spectral range, they are ideally suited to be solid hosts in matrix isolation experiments.

1.1.3 Matrix isolation today

The progress in technology has had a significant effect on the development of the matrix isolation technique. The closed cycle helium variants of cryostats became more advanced and became available to be used easily, and are now available down to 4 K, which allow the routine use of neon where the interaction between the host and guest is

minimised. New analysis techniques have been used such as UV/vis spectroscopy, vibrational spectroscopic techniques, and mass spectrometry which can only be used during deposition, by removing part of the matrix by bombardment, or during evaporation of the matrix. Moreover, advanced processes for interacting materials were being developed for instance photolysis and pyrolysis. As a result, the formation and characterisation of reactive species in matrices became more achievable.[3] The application of matrix isolation succeeded in generating different reactive species,[4-14] and transition metals halides compounds,[15] and continues up to date.

1.1.4 The Structure of the Matrix

Researchers were interested to identify the precise fine structure of the solid matrices. There is an expected degree of epitaxy because the matrices are formed on a single crystal of either alkali halide or sapphire. A study was performed by Young et al.[16] using X–ray absorption fine structure and another study performed by Langel et al.[17] using neutron and X–ray diffraction for pure krypton deposited were firmly able to identify the fine structure of the matrix. It is noteworthy that when considering cage effects, the close packed structure should be considered as well. All inert gases take shape of a face–centred cubic (fcc) structure,[18] except helium which crystallises with a hexagonal close–packed structure (hcp). In addition, argon tends to form (hcp) in case of the matrix contains impurities.

1.2 3d–transition metals fluorides

1.2.1 Scandium

ScF_2 isolated in different rare gases matrices has been achieved.[19, 20] The antisymmetric stretching mode was reported at 685 cm^{-1} and at 699 cm^{-1} in solid Ar and Ne matrices, respectively. Also, bond angle was reported at 135º.[19, 20] Moreover, the isolation of ScF_2 in both argon and xenon matrices was investigated by electron spin resonance (ESR) spectroscopy.[21] The study identified the ground state of Sc^{2+} as ^2D, and the excited levels were detected at 25500 cm^{-1} being ^2S and for ^2P at 62000 cm^{-1}.

ScF_3 matrix isolated in Ne, Ar, and N matrices has also been detected. The vibrational spectrum of ScF_3 revealed that its structure is planar.[22] IR spectroscopy was used to study ScF_3 isolated in solid rare-gas and N_2 matrices.[23] This study proposed that the geometry of ScF_3 could be D_{3h} (trigonal planar) or nearly planar C_{3v} (trigonal)

geometry. Computational studies using both the Hartree–Fock–Roothaan method and CISD + Q method were used to study the vibrational spectrum and the molecular structure of matrix isolated ScF_3. The calculations defined the geometry of ScF_3 as a planar (D_{3h} symmetry).[24] The influence of free CO molecules interacting with ScF_3 and different lanthanides fluorides isolated in solid argon matrix was also studied. It was observed that the vibrational frequencies of ScF_3 shifted to high frequencies; these shifts were in reverse to the radius of each metal.[25, 26]

1.2.2 Titanium

In 1969, the infrared absorption spectrum of TiF_2 matrix isolated in solid argon and neon matrices were recorded and displayed peaks at 740 cm^{-1} and 752 cm^{-1}, respectively. Moreover, the bond angle calculated was 130º suggesting a bent geometry of TiF_2.[19, 20, 27] Additionally, the ESR spectrum recorded by De Vore *et al.* manifested that TiF_2 is a bent molecule.[28] Eventually, these results were found unreliable; a study conducted at the University of Hull to investigate the molecular geometry of TiF_2 isolated in an argon matrix provided different results.[29] The interpretation of matrix IR spectra indicated that bands at 740 cm^{-1} are in fact due to TiF_3, and those at 677.73 cm^{-1} and 673.81 cm^{-1} are attributed to TiF_2, whilst theoretical calculation provided a bond angle of 166º. As a consequence, the geometry of TiF_2 is close to linearity.[29, 30]

A study carried out by Hastie *et al.* demonstrated that the shape of TiF_3 species isolated in rare gas matrices has a degree of nonplanarity.[27] Further studies determined that TiF_3 is a trigonal planar structure (D_{3h}).[28, 31] The geometry of TiF_4 molecule was investigated using gaseous electron diffraction and ultraviolet photoelectron spectroscopy; the investigations revealed that the structure of TiF_4 is tetrahedral symmetry (T_d).[31-33]

1.2.3 Vanadium

The early investigation to study the IR absorptions of vanadium fluorides in a matrix and its geometry was conducted by Hastie *et al.*[19] The V–F asymmetric stretching mode of VF_2 was observed at 740.1 cm^{-1} in a matrix of Ar and at 752.8 cm^{-1} a matrix of Ne. The geometry of VF_2 was found to be bent with a bond angle of 130º. Similarly, a study conducted by Hargittai *et al.* using the electron diffraction technique determined that the molecular structure of VCl_2 was bent with a bond angle of 115º.[34] Following this study, experiments were carried out by DeVore *et al.* using electron spin resonance (ESR)

3

technique to study the first row metal fluorides molecules.[35] Further study was conducted to isolate VF_2 and VF_3 molecules in noble gas matrixes, the IR absorptions spectra of $\nu_3(VF_2)$ band was recorded at 600 cm^{-1}.[36] The recorded frequency of VF_2 molecules in this study was different to the early value investigated by Hastie *et al.*[19] In addition, the band of VF_3 molecules was located at 660 cm^{-1}.

The reinterpretation of the VF_3 absorptions was obtained in another experimental work. VF_3 molecules were isolated in both solid Ar and Ne matrices.[37] The peak located at 649 cm^{-1} in the Raman spectrum was assigned to VF_3 isolated in Ar matrix, while the IR absorption spectra showed two bands at 733.2 and 731.8 cm^{-1} for VF_3 in a matrix of Ar and bands recorded between 737 and 742 cm^{-1} were attributed to VF_3 in solid Ne matrix. Furthermore, the theoretical calculations based on the IR spectrum revealed that VF_3 has D_{3h} symmetry (trigonal planar) with bond angles of 119º. Solomonik, *et al.* carried out a study to identify theoretically the molecular structure of VF_3 isolated in Ar and Ne matrices based on previous data collected by matrix isolation IR and Raman spectroscopy. The study indicated the D_{3h} configuration of VF_3 and suggested the splitting of IR absorptions bands because of a Jahn–Teller distortion.[38]

Vanadium pentafluorides have been comprehensively studied using matrix isolation IR spectroscopy. The IR assignments of VF_5 isolated in a nitrogen matrix were observed at 806 and 769 cm^{-1}, while the vibrational frequencies of isolated VF_5 molecules in solid Ar matrix were obtained at 802 and 771 cm^{-1}.[39] The study demonstrated that VF_5 has D_{3h} symmetry; this result was found in agreement with former study done for VF_5 molecules isolated in a matrix of argon.[40] Besides, the mechanism of photolysis process indicated that VF_5 molecules isolated in noble gas matrices decompose into VF_4 and VF_3 species followed by a secondary process involves decomposition of VF_3 to produce VF_2 molecules.[39]

1.2.4 Chromium

The fluorides of chromium have been widely explored and talked about and reported in the literature. Molecular CrF in the solid state has been reported,[41, 42] only a few theortical studies investigated the electronic state of CrF.[41-44] Several studies were conducted to investigate CrF_2, CrF_3, and CrF_4 species in rare gas matrices.[19, 20, 45-52] Few studies were carried out in investigate the formation of CrF_5 is rare gas matrices indicating the molecular structure as distorted trigonal bipyramid C_{2v}.[44, 53-55] The formation of matrix

isolated CrF_6 molecules is still contentious.[53-58] As a study of chromium fluorides is presented in Chapter 6, the detailed literature survey is presented there.

1.2.5 Manganese

Few studies have been undertaken to characterise the binary fluorides of manganese. IR spectroscopy detected the absorption band of matrix isolated MnF_2 molecules at 700.1 cm^{-1} in a matrix of Ar and at 722.1 cm^{-1} in a matrix of Ne.[19, 20] A study was carried out by Van Leirsburg reported the same observation a few years later.[51] The geometry of MnF_2 was found as linear. Additionally, the ESR technique was used to study MnF_2 as well as MnF molecules isolated in rare gas matrices, and provided evidence for the linearity of MnF_2 species.[59]

MnF_3 was studied most extensively amongst all the manganese fluorides. A spectroscopic study was carried out by Bukhmarina, *et al*. to investigate the configuration of MnF_3 molecules trapped in inert gas matrices. The study suggested the molecular geometry of MnF_3 is D_{3h} symmetry.[60] One year later, Solomonik *et al*. found that the geometry of MnF_3 is almost T–shaped symmetry (C_{2v}) after taking into account Jahn–Teller effect.[61, 62] The calculated data assumed that the length of one of Mn–F bonds is shorter than the others. Further study investigated the effect of Jahn–Teller effect on the geometry of MnF_3 suggesting its molecular structure as planar with bond angles of 106.4, 106.4, and 143.3°.[63] Moreover, the study confirmed that one of the Mn–F bonds is shorter than the others.

Research was carried out between Moscow State University and University of Rome to characterise the molecular shape of MnF_4 in the vapour phase though reaction of MnF_3 with TbF_4.[64] The FTIR absorption spectrum of MnF_3 had two peaks at 758.5 and 711.2 cm^{-1} attributed to the stretching modes of Mn–F bonds, while new absorptions at 794.5 and 176.6/172.9 cm^{-1} were revealed for the vapours of MnF_3 and TbF_4 mixture. These bands were considered as evidence for MnF_4 molecules. The molecular geometry of MnF_4 was suggested as (T_d) tetrahedral symmetry. Recently, research by Brosi *et al*. failed to detect MnF_4 and MnF_5 molecules through ablation of manganese atoms in the presence of fluorine gas diluted in different rare gas matrices.[65] The study raised a doubt on former results about preparation of high–valent manganese fluorides.[64]

1.2.6 Iron

Molecular FeF in a matrix has not been studied, however some theoretical studies were carried out to investigate the bending energy and excitation state. Koukounas and Mavridis in their study suggested the bond length as 1.783 Å and the binding energy for the ground state as 456 kJ mol^{-1} using variational multireference (MRCI) and coupled-cluster RCCSD(T) methods.[66]

A few molecular iron fluorides were reported, including FeF_2, FeF_3, and also FeF_4. A cooperative study was carried out at Moscow State University and the University of Southampton by Osin, Davliatshin, and Ogden who disclosed the ambiguity of the molecular shape of FeF_2 and FeF_3.[49] Iron fluoride molecules were produced by passing fluorine gas over heated iron metal and trapping iron atoms in a Ar gas matrix. The geometry of FeF_2 was described as linear; it was compatible with previous reports of iron difluoride species.[19, 20, 67, 68] In addition, the molecular arrangement of FeF_3 was not definitely determined, although it was suggested that a D_{3h} geometry fits the data marginally better than a C_{3v} pyramidal symmetry. In 2002, molecular FeF_3 was produced by laser evaporation method, where Fe atoms were evaporated in presence of SF_6/Ar gas matrix. From the gathered data it was proposed that the geometry of FeF_3 as a D_{3h} symmetry (planar).[69]

Rau *et al*. used FTIR spectroscopy to characterise FeF_4 species isolated in a solid argon matrix. The absorption band of FeF_4 molecules was located at 758.5 cm^{-1}, whilst a weak peak at 763.3 cm^{-1} corresponded to the iron isotope pattern of $^{54}FeF_4$.[70] Additionally, the geometrical arrangement of FeF_4 molecules was assumed by a T_d or D_{4h} symmetry. Schlöder *et al*. carried out experimental work to reinvestigate the formation FeF_4 molecules in a matrix.[71] The IR absorption bands were compatible with the literature.[70] Nonetheless, the computational calculations suggested the configuration of the molecule of FeF_4 as a D_{2d} distortioned tetrahedral geometry.[71]

1.2.7 Cobalt

Some studies have been completed to identify the electronic ground state and excited states of CoF and also confirmed the vibrational frequency of CoF previously detected at 662.6 cm^{-1}.[72-76] Several studies using IR as well as Raman spectroscopy have detected CoF_2 molecules isolated in noble gas matrices.[19, 20, 47, 77] The molecular structure of CoF_2 was found to be linear with F–Co–F bond angle of 180°.[19] CoF_3 molecules have

also been studied, and the IR absorptions bands of CoF_3 isolated in solid Ar matrix were reported.[37, 78] The geometry of CoF_3 was identified as trigonal planar (D_{3h}).[78]

CoF_4 was prepared by reaction of TbF_4 with CoF_3 at high temperature, Mass spectrometry and FTIR spectroscopy were employed to detect CoF_4 species isolated in solid argon matrix.[79] The literature data will be covered in more detail in Chapter 4.

1.2.8 Nickel

No spectroscopic data were reported for molecular matrix isolated NiF or NiF_3, while some theoretical and experimental study were undertaken to investigate the electronic configuration of NiF as well as NiF_3 molecules.[62, 66, 80-84] Nickel trifluoride molecules were suggested as trigonal planar molecules and a mixture of valence Ni(II)/Ni(IV) compounds, while solid state NiF_4 is very reactive. NiF_2 molecules have been studied widely since 1965. The IR spectrum of matrix isolated NiF_2 in solid Ar and Ne matrices has been recorded.[19, 20, 47, 51, 77, 85, 86]

1.2.9 Copper

Ahmed at al. carried out cooperative research between Physical Chemistry Laboratory at Oxford University and Université des Science et Techniques de Lille to analyse the rotational structure of the CuF molecule.[87] The ground state for CuF was resolved to be $^1\Sigma^+$. Following this investigation, three of Ahmed's co–authors conducted a theoretical work. The study concluded that the obtained vibrational frequencies of CuF were assigned to transition structure between excited state $Cu^+(3d^94s)F^-(2p^6)$ and $Cu^+(3d^{10})F^-(2p^6)$ X $^1\Sigma^+$ ground state.[88] The IR bands at 615.9 and 613.7 cm^{-1} were attributed to stretching mode of ^{63}Cu–F and ^{65}Cu–F bonds, respectively.[89] Furthermore, the electronic spectra of Cu atoms isolated in rare gas matrices were obtained using synchrotron radiation by Hormes *et al.*[90] Koukounas and Mavridis carried out a theoretical investigation of 3d transition metals fluorides using two basis sets variational multireference (MRCI) as well as coupled-cluster RCCSD(T) methods and suggested the bond length for CuF as 1.748 Å and the binding energy for the ground state as 410 kJ.mol^{-1}.[66]

The ESR technique was used to investigate the molecular structure of CuF_2 trapped in Ar and Ne matrices by Kasai *et al.*[91] The collected data indicated that CuF_2 is linear. The electronic structure of copper diflourides was detected by photoelectron

spectroscopy. The authors suggested that the valence of metal was derived from 3d orbitals.[92] Hastie *et al*. employed vibrational spectroscopy to identify matrix isolated CuF_2 molecules in Ar and Ne matrices; the peaks observed at 743.9 cm^{-1} and 766.5 cm^{-1} were assigned to CuF_2 isolated in Ar and Ne matrices, respectively.[19, 20, 77, 93] These data were in agreement with spectroscopic study completed by Van Leirsburg *et al*.[51] In 2003, research conducted at Moscow State University using laser ablation to evaporate Cu atoms in presence of F_2/Ar gas matrix yielding matrix isolated CuF_2 molecules in solid argon matrix.[94] The obtained IR spectrum demonstrated the formation of CuF_2 molecules, the peaks between 742.8 and 738.9 cm^{-1} were assigned to CuF_2.

Solomonik *et al*. conducted a computational study focusing on the ground state as well as the excited state of CuF_3 molecules. The study revealed that the structure of $^1A_1$ ground state was C_{3v} T–shaped symmetry. On the other side, the geometry of $^3A´_2$ triplet excited state was found as D_{3h} trigonal planar structure.[95] The IR absorption band was proposed at 786 cm^{-1}.[96] Experimental evidence for CuF_3 was provided from a matrix isolation/laser ablation study. The vibational frequencies observed at 762.3 and 757.9 cm^{-1} were due to the asymmetric stretching mode of $^{63}CuF_3$ and $^{65}CuF_3$ in solid Ar matrix.[96]

1.3 References

1. S. Craddock and J. A. Hinchcliffe, *Matrix isolation: A technique for the study of reactive inorganic species, Cambridge University Press, Cambridge*, 1975.
2. E. Whittle, D. A. Dows and G. C. Pimentel, *J. Chem. Phys.*, 1954, **22**, 1943.
3. G. E. Ewing, W. E. Thompson and G. C. Pimentel, *J. Chem. Phys.*, 1960, **32**, 927-932.
4. H. E. Hallam, *Vibrational Specroscopy of Trapped Species, Wiley, London*, 1973.
5. M. Moskovits and G. A. Ozin, *Cryochemistry, Wiley-Interscience, New York*, 1976.
6. R. N. Perutz, *Annu. Rep. Prog. Chem., Sect. C: Phys. Chem.*, 1985, **82**, 157-191.
7. M. J. Almond and A. J. Downs, *Spectroscopy of Matrix Isolated Species, Wiley, Chichester*, 1989.
8. L. Andrews and M. Moskovits, *Chemistry and Physics of Matrix-Isolated Species, North-Holland, Amsterdam*, 1989.
9. M. J. Almond, *Short-Lived Molecules, Ellis Horwood, Chichester*, 1990.
10. M. J. Almond and R. H. Orrin, *Annu. Rep. Prog. Chem., Sect. C: Phys. Chem.*, 1991, **88**, 3-44.
11. M. J. Almond, *Annu. Rep. Prog. Chem., Sect. C: Phys. Chem.*, 1997, **93**, 3-56.
12. I. R. Dunkin, *Matrix isolation techniques: a practical approach, Oxford University Press, New York*, 1998.
13. M. J. Almond and K. S. Wiltshire, *Annu. Rep. Prog. Chem., Sect. C: Phys. Chem.*, 2001, **97**, 3-60.
14. M. J. Almond and N. N. Goldberg, *Annu. Rep. Prog. Chem., Sect. C: Phys. Chem.*, 2007, **103**, 79-133.
15. M. J. Linevsky, *J. Chem. Phys.*, 1961, **34**, 587-590.
16. I. R. Beattie, N. Binsted, W. Levason, J. S. Ogden, M. D. Spicer and N. A. Young, *High Temp. Sci.*, 1990, **26**, 71-86.
17. W. Langel, W. Schuller, E. Knözinger, H. W. Fleger and H. J. Lauter, *J. Chem. Phys.*, 1988, **89**, 1741-1742.
18. E. R. Dobbs and G. O. Jones, *Theory and properties of solid argon*, 1957, **20**, 516-564.
19. J. W. Hastie, R. H. Hauge and J. L. Margrave, *J. Chem. Soc. D*, 1969, 1452-1453.
20. J. L. Margrave, J. W. Hastie and R. H. Hauge, *Amer. Chem. Soc., Div. Petrol. Chem., Prepr.*, 1969, **14**, E11-E13.
21. L. B. Knight and M. B. Wise, *J. Chem. Phys.*, 1979, **71**, 1578-1581.
22. R. H. Hauge, J. W. Hastie and J. L. Margrave, *J. Less-Common Metals*, 1971, **23**, 359-365.
23. J. W. Hastie, R. H. Hauge and J. L. Margrave, *J. Less-Common Met.*, 1975, **39**, 309-334.
24. V. G. Solomonik and O. Y. Marochko, *J. Struct. Chem.*, 2001, **41**, 725-732.
25. R. H. Hauge, S. G. Gransden and J. L. Margrave, *Proc. - Electrochem. Soc.*, 1978, **78-1**, 310-319.
26. R. H. Hauge, S. E. Gransden and J. L. Margrave, *J. Chem. Soc., Dalton Trans.*, 1979, 745-748.
27. J. W. Hastie, R. H. Hauge and J. L. Margrave, *J. Chem. Phys.*, 1969, **51**, 2648-2656.
28. T. C. De Vore and W. Weltner, Jr., *J. Am. Chem. Soc.*, 1977, **99**, 4700-4703.
29. I. R. IBeattie, P. J. Jones and N. A. Young, *Angew. Chem. Int. Ed. Engl.*, 1989, **28**, 313-315.
30. A. V. Wilson, A. J. Roberts and N. A. Young, *Angew. Chem., Int. Ed.*, 2008, **47**, 1774-1776.

31. I. R. Beattie, P. J. Jones and N. A. Young, *Angew. Chem.*, 1989, **101**, 322-324.
32. G. V. Girichev, V. M. Petrov, N. I. Giricheva and K. S. Krasnov, *J Struct Chem.*, 1982, **23**, 45-49.
33. R. S. Ram, J. R. D. Peers, Y. Teng, A. G. Adam, A. Muntianu, P. F. Bernath and S. P. Davis, *J. Mol. Spectrosc.*, 1997, **184**, 186-201.
34. M. M. Hargittai, O. V. Dorofeeva and J. Tremmel, *Inorg. Chem.*, 1985, **24**, 3963-3965.
35. T. C. DeVore, R. J. Van Zee and W. Weltner, Jr., *Proc. - Electrochem. Soc.*, 1978, **78-1**, 187-198.
36. O. V. Blinova, Y. B. Predtechenskii and L. D. Schcherba, *Khim. Fiz.*, 1982, 1562-1564.
37. V. N. Bukhmarina, A. Y. Gerasimov and Y. B. Predtechenskii, *Vib. Spectrosc.*, 1992, **4**, 91-94.
38. V. G. Solomonik, J. E. Boggs and J. F. Stanton, *J. Phys. Chem. A*, 1999, **103**, 838-840.
39. E. G. Hope, *J. Chem. Soc., Dalton Trans.*, 1990, 723-725.
40. O. V. Blinova, D. D. Moldavskii, Y. B. Predtechenskii and L. D. Shcherba, *Khim. Fiz.*, 1983, 1363-1369.
41. P. Koivisto, S. Wallin and O. Launila, *J. Mol. Spectrosc.*, 1995, **172**, 464-468.
42. O. Launila, *J. Mol. Spectrosc.*, 1995, **169**, 373-395.
43. A. Hamdan and M. Korek, *Can. J. Chem.*, 2011, **89**, 1304-1311.
44. J. Jacobs, H. S. P. Mueller, H. Willner, E. Jacob and H. Buerger, *Inorg. Chem.*, 1992, **31**, 5357-5363.
45. R. Wei, Q. Li, Y. Gong, L. Andrews, Z. Fang, K. S. Thanthiriwatte, M. Vasiliu and D. A. Dixon, *J. Phys. Chem. A*, 2017, **121**, 7603-7612.
46. L. Cui-Lian, Z. Ka-Qiou and Z. Yi-Yang, *Physica B (Amsterdam)*, 1995, **205**, 335-340.
47. V. N. Bukhmarina, A. Y. Gerasimov, Y. B. Predtechenskii and V. G. Shklyarik, *Opt. Spektrosk.*, 1988, **65**, 876-881.
48. O. V. Blinova, V. G. Shklyarik and L. D. Shcherba, *Zh. Fiz. Khim.*, 1988, **62**, 1640-1642.
49. S. B. Osin, D. I. Davliatshin and J. S. Ogden, *J. Fluorine Chem.*, 1996, **76**, 187-192.
50. N. B. Balabanov, V. G. Solomonik and V. V. Sliznev, *Zh. Neorg. Khim.*, 1997, **42**, 1173-1179.
51. D. A. Van Leirsburg and C. W. DeKock, *J. Phys. Chem.*, 1974, **78**, 134-142.
52. L. Hedberg, K. Hedberg, G. L. Gard and J. O. Udeaja, *Acta Chem. Scand.*, 1988, **42A**, 318-323.
53. E. G. Hope, P. J. Jones, W. Levason, J. S. Ogden, M. Tajik and J. W. Turff, *J. Chem. Soc., Dalton Trans.*, 1985, 1443-1449.
54. F. Brosi, T. Vent-Schmidt, S. Kieninger, T. Schloeder, H. Beckers and S. Riedel, *Chem. - Eur. J.*, 2015, **21**, 16455-16462.
55. T. Schlöder, F. Brosi, B. J. Freyh, T. Vent-Schmidt and S. Riedel, *Inorg. Chem.*, 2014, **53**, 5820-5829.
56. E. G. Hope, P. J. Jones, W. Levason, J. S. Ogden and M. Tajik, *J. Chem. Soc., Chem. Commun.*, 1984, 1355-1356.
57. E. Jacob and H. Willner, *Chem. Ber.*, 1990, **123**, 1319-1321.
58. E. G. Hope, W. Levason and J. S. Ogden, *Inorg. Chem.*, 1991, **30**, 4873-4874.
59. T. C. DeVore, R. J. Van Zee and W. Weltner, Jr., *J. Chem. Phys.*, 1978, **68**, 3522-3527.
60. V. N. Bukhmarina and Y. B. Predtechenskii, *Opt. Spektrosk.*, 1996, **80**, 762-765.

61. V. G. Solomonik, V. V. Sliznev and N. B. Balabanov, *Z. Phys. Chem. (Munich)*, 1997, **200**, 77-82.
62. P. Mondal and W. Domcke, *J. Phys. Chem. A*, 2014, **118**, 3726-3734.
63. M. M. Hargittai, B. Réffy, M. Kolonits, C. J. Marsden and J. L. Heully, *J. Am. Chem. Soc.*, 1997, **119**, 9042-9048.
64. S. Nunziante Cesaro, J. V. Rau, N. S. Chilingarov, G. Balducci and L. N. Sidorov, *Inorg. Chem.*, 2001, **40**, 179-181.
65. F. Brosi, T. Schloeder, A. Schmidt, H. Beckers and S. Riedel, *Dalton Trans.*, 2016, **45**, 5038-5044.
66. C. Koukounas and A. Mavridis, *J. Phys. Chem. A*, 2008, **112**, 11235–11250.
67. M. J. Linevsky, *Spectroscopic studies of the vaporization of high temperature materials*, Gen. Elec. Co., 1968.
68. J. W. Stout, M. I. Steinfeld and M. Yuzuri, *J. Appl. Phys.*, 1968, **39**, 1141-1142.
69. Y. Yamada, *Hyperfine Interact.*, 2002, **139/140**, 77-85.
70. J. V. Rau, N. S. Cesaro, N. S. Chilingarov, M. S. Leskiv, G. Balducci and L. N. Sidorov, *Inorg. Chem. Commun.*, 2003, **6**, 643–645.
71. T. Schloeder, T. Vent-Schmidt and S. Riedel, *Angew. Chem., Int. Ed.*, 2012, **51**, 12063-12067.
72. T. Okabayashi and M. Tanimoto, *J. Mol. Spectrosc.*, 2003, **221**, 149-155.
73. X. Zhang, J. Guo, T. Wang, L. Pei, Y. Chen and C. Chen, *J. Mol. Spectrosc.*, 2003, **220**, 209-213.
74. T. C. Steimle, T. Ma, A. G. Adam, W. D. Hamilton and A. J. Merer, *J. Chem. Phys.*, 2006, **125**, 064302.
75. A. G. Adam and W. D. Hamilton, *J. Mol. Spectrosc.*, 2001, **206**, 139-142.
76. Z. Zhang, J. Guo, X. Yu, J. Zheng and Y. Chen, *J. Mol. Spectrosc.*, 2007, **244**, 117-121.
77. J. W. Hastie, R. H. Hauge and J. L. Margrave, *High Temp. Sci.*, 1969, **1**, 76-85.
78. G. V. Girichev, N. I. Giricheva, O. G. Krasnova, A. V. Krasnov, S. A. Shlykov, E. G. Rakov and S. V. Khaustov, *J. Struct. Chem.*, 1992, **33**, 838-843.
79. J. V. Rau, S. N. Cesaro, N. S. Chilingarov and G. Balducci, *Inorg. Chem.*, 1999, **38**, 5695-5697.
80. C. Focsa, C. Dufour and B. Pinchemel, *J. Mol. Spectrosc.*, 1997, **182**, 65–71.
81. Y. Chen, J. Jin, C. Hu, X. Yang, X. Ma and C. Chen, *J. Mol. Spectrosc.*, 2000, **203**, 37–40.
82. J. Jin, Y. Chen, X. Yang, Q. Ran and C. Chen, *J. Mol. Spectrosc.*, 2001, **208**, 18–24.
83. Y. Krouti, T. Hirao, C. Dufour, A. Boulezhar, B. Pinchemel and P. F. Bernath, *J. Mol. Spectrosc.*, 2002, **214**, 152–174
84. B. Pinchemel, T. Hirao and P. F. Bernath, *J. Mol. Spectrosc.*, 2002, **215**, 262–268.
85. D. E. Milligan, M. E. Jacox and J. D. McKinley, *J. Chem. Phys.*, 1965, **42**, 902-905.
86. S. Besnainou and J. L. Whitten, *J. Am. Chem. Soc.*, 1978, **100**, 3692-3698.
87. F. Ahmed, R. F. Barrow, H. A. Chojnicki, C. Dufour and J. Schamps, *J. Phys. B: At. Mol. Opt. Phys.*, 1982, **15**, 3801-3818.
88. C. Dufour, J. Schamps and R. F. Barrow, *J. Phys. B: At. Mol. Opt. Phys.*, 1982, **15**, 3819-3828.
89. Y. Gong and L. Andrews, *J. Inorg. Chem.*, 2012, **51**, 667-673.
90. J. Hormes, R. Grinter, B. Breithaupt and D. M. Kolb, *J. Chem. Phys.*, 1983, **78**, 158-166.
91. P. H. Kasai, E. B. Whipple and W. Weltner, Jr., *J. Chem. Phys.*, 1966, **44**, 2581-2591.

92.   J. M. Dyke, N. K. Fayad, J. G. D. and A. Morris, *J. Chem. Soc., Faraday Trans. 2*, 1980, **76**, 1672-1682.
93.   W. Weltner, *Advan. High Temp. Chem.*, 1969, **2**, 85-105.
94.   A. S. Vnukov, D. I. Davliatshin and S. B. Osin, *Vestn. Mosk. Univ., Ser. 2: Khim.*, 2003, **44**, 172-174.
95.   V. G. Solomonik, J. E. Boggs and J. F. Stanton, *J. Mol. Struct. (THEOCHEM)*, 2000, **496**, 213-216.
96.   X. Wang, L. Andrews, F. Brosi and S. Riedel, *Chem. - Eur. J.*, 2013, **19**, 1397-1409.

Chapter 2

Experimental

2.1 Risk assessment

In the beginning, COSHH forms were prepared and completed before carrying out any experimental work as demonstrated in Table 2.1 below.

Table 2.1 COSHH forms prepared.

COSHH forms	Reference
Preparation of fluorine (gas) / argon (gas) mixture	Reference: I/NAY/AKS/01 Reference: I/NAY/AKS/06 Reference: I/NAY/AKS/09
Characterisation of nickel fluorides	Reference: I/NAY/AKS/02 Reference: I/NAY/AKS/05
Characterisation of cobalt fluorides	Reference: I/NAY/AKS/03
Characterisation of palladium chlorides/ bromides/ fluorides/ iodides	Reference: I/NAY/AKS/04
Characterisation of molybdenum fluorides/ chlorides	Reference: I/NAY/AKS/07
Characterisation of complexes formed between SiF_4 and PMe_3, PEt_3 using FTIR Spectroscopy	Reference: I/NAY/AKS/08
Characterisation of chromium fluorides	Reference: I/NAY/AKS/10

2.2 Materials

The nickel, cobalt, chromium, palladium, molybdenum, tantalum, and different prepared matrix gases were all standard laboratory chemicals as listed in Table 2.2 below.

Table 2.2 Materials used in experimental work.

Materials	Supplier	Purity (metal)/Dilution (gas)
Nickel	Aldrich	99.9%
Cobalt	Goodfellow	99.99%
Molybdenum	Unknown	Unknown
Chromium	Goodfellow	99.7%
Palladium	Aldrich	99.9%
Tantalum	Goodfellow	99.9%
Argon	Energas	99.99%
Fluorine	Air Liquide supplied as 10%F_2/Ar	0.2%, 0.5% , 1%, 2%, 5%, 10% F_2/Ar
Chlorine	Energas 99.5%	1%, 2%, 2.5%, 5%, 10% Cl_2/Ar
Bromine	BDH	1%, 2% Br_2/Ar
Iodine	BDH	0.6%, 1% I_2/Ar

2.3 Decanting of Gases

During the experiments different gas mixtures have been used with different concentrations. Argon, which is considered an inert gas, was the first gas used. In addition, different reactive halogen gases were diluted in argon. In case of F_2/Ar, the process was conducted using a metal vacuum line in the roof lab. The stock supply of 10% F_2/Ar gas mixture was diluted with argon in well passivated stainless steel containers to give the desired concentration of F_2/Ar (0.2% F_2/Ar, 0.5% F_2/Ar, 1% F_2/Ar, 2%, and 5% F_2/Ar.) The other halogens (Cl_2, Br_2, and I_2) were handled in a glass vacuum line. Cl_2/Ar and Br_2/Ar mixtures ranging from 1% to 10% were made using standard manometric procedures with a glass vacuum line. The Cl_2 had been previously decanted from a stainless steel cylinder into a 1 L glass bulb. The Br_2 was freeze–thaw degassed three times in a small (10 mL) tap ampoule before use. The vapour pressure of I_2 is relatively low (*ca*. 0.25 torr at room temperature), so in this case elemental iodine was placed into a 2 L glass bulb, and argon added to achieve dilutions of 0.6% I_2/Ar and

1% I_2/Ar. The I_2 was purified by vacuum sublimation in the 2 L flask prior to the addition of argon.

2.4 Thermal Evaporation – Metal Deposition

A furnace was used to evaporate metals. As seen in Figure 2.1, it consists of two pieces of Pyrex; the forward water cooled part can be adjusted to different length and the position of the furnace within the vacuum chamber. The rear part of the furnace contains two electrodes made of copper, they were held in place by Araldite. The metal filament was connected to these electrodes with screws. Moreover, water was used to cool the electrodes and glassware to protect it from cracking. The furnace was mounted onto the front port of the vacuum chamber, as displayed in Figure 2.1. The 6 mm Cu disc was positioned into front port, it acts as a radiation or heat shield to stop the high temperature furnace warming the deposition window. It collimates the beam of atoms which stops the outer windows getting dirty after every experiment. Furthermore, it concentrates the trapped species into the deposition surface. The power supply transformer was used to provide electrical current, up to 40 A, able to produce vapour species from the filament. The voltmeter connected to the copper electrodes was used to measure the voltage and current was measured through a gauge on the interface of the power supply transformer. An initial current was employed to outgas the filament in order to remove any unfavourable impurities specifically traces of H_2O and CO_2 on the surface of filament. Prior to turning the cryostat, incremental increases of current/voltage were used to achieve the optimum conditions required for metal evaporation, by identifying the conditions when there was a permanent vapour pressure.
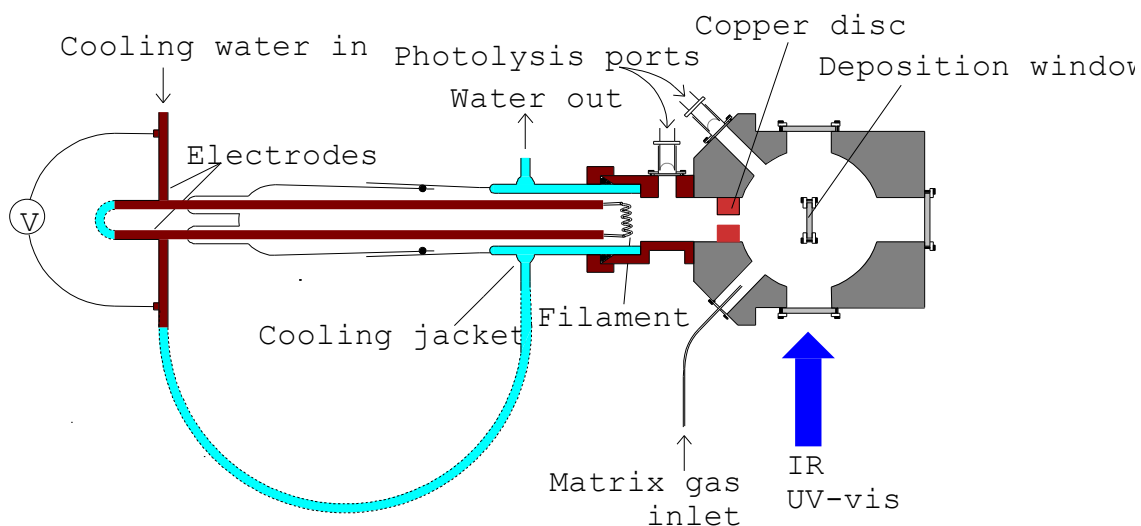
Figure 2.1: *The left hand side of the diagram shows the construction of the furnace used to evaporate the copper wire. Whereas the right hand side shows the arrangement of the vacuum chamber when being used for UV–Vis/IR spectroscopy. Note the inner window is angled towards the spectrometer beam and away from the gas inlet. The electrodes in this diagram are connected to a cell containing the species to be evaporated, a different set-up to the filament used in this experiment.* [1]

The structure of the filament depends on the cost of metal used and the temperature required to obtain sufficient vapour pressure. For nickel and molybdenum experiments it was possible to use a filament constructed only of the metal of interest, but for Co, Cr and Pd it was necessary to use a tantalum filament as a support, and mount the metal of interest within in it. Tantalum was selected because of its high melting point (3020 °C) and low vapour pressure at the temperatures required (*ca.* 9.97×10^{-12} torr). Tantalum was chosen over tungsten because it is much more ductile. The nickel filament consisted of five strands of nickel wire of 0.5 mm diameter and 7 cm length wound together, as shown in Figure 2.2. This design has been used to carry out all nickel evaporation experiments.

Figure 2.2: *Nickel filament consisting of five strands of Ni metal*

In case of cobalt filament, some modifications have been implemented because of the high cost of cobalt metal. As seen in Figure 2.3, the filament was made up of five strands of tantalum wire having a diameter of 0.5 mm and 7 cm length wound together to form the same shape of nickel filament, and then the tantalum wires were wound around a cobalt rod of 1.5 mm diameter and 0.5 cm length.

Figure 2.3: *Cobalt filament consisting of five strands of Ta metal wound around a Co rod.*

The palladium filament consisted of two strands of palladium wire of 0.25 mm diameter and 7 cm length and three strands of tantalum wire having a diameter of 0.5 mm and 7 cm length wound together to form the shape of the filament, and then a small amount of palladium wire was looped on the coil part of the filament. The evaporation of molybdenum atoms was very challenging because of the high melting point of molybdenum and the temperatures required to evaporate atoms 2890 °C. In this case the filament was made solely of molybdenum, and the filament was made of seven strands of molybdenum wires of 0.25 mm diameter and 7 cm length wound together, as shown in Figure 2.4. This design has been used to carry out all molybdenum evaporation experiments.

Figure 2.4: *The shape of molybdenum filament consisting of seven strands of Mo metal.*

Chromium metal is hard to form wires, so the chromium filament was made up of two strands of tantalum wire with a diameter of 0.5 mm and 7 cm length wrapped together to form a coil shape, and then the tantalum wires were looped around a chromium bar of

1 cm length and 2 mm × 2 mm side length, as displayed in Figure 2.5 below. The photograph in Fig 2.5 shows the filament after an experiment, where the surface has turned green, at the start of the experiment the Cr had a metallic appearance.

Figure 2.5: *The shape of chromium filament and a tantalum support consisting of two strands of Ta metal wound around a Cr bar.*

2.5 Matrix Isolation UV/Vis Spectroscopy

The matrix isolation UV/vis experiments were conducted to define and optimize the generation of atomic species of nickel, cobalt, palladium, and molybdenum. Moreover, they were used to record the spectra of nickel fluoride, cobalt fluoride, palladium chloride, palladium bromide, palladium iodide, and molybdenum chloride species. The equipment consists of a vacuum chamber mounted in the path of the beam of the Cary 5E UV–vis–NIR spectrometer, as presented in Figure 2.6.[1] The data were collected and saved on a computer attached to the UV–vis–NIR spectrometer by using the Varian Cary 5 software package. The UV/vis spectra were run in the range of 4000–55000 cm^{-1}. The time required for recording UV–visible spectra is longer than the time required for gathering FTIR spectra.
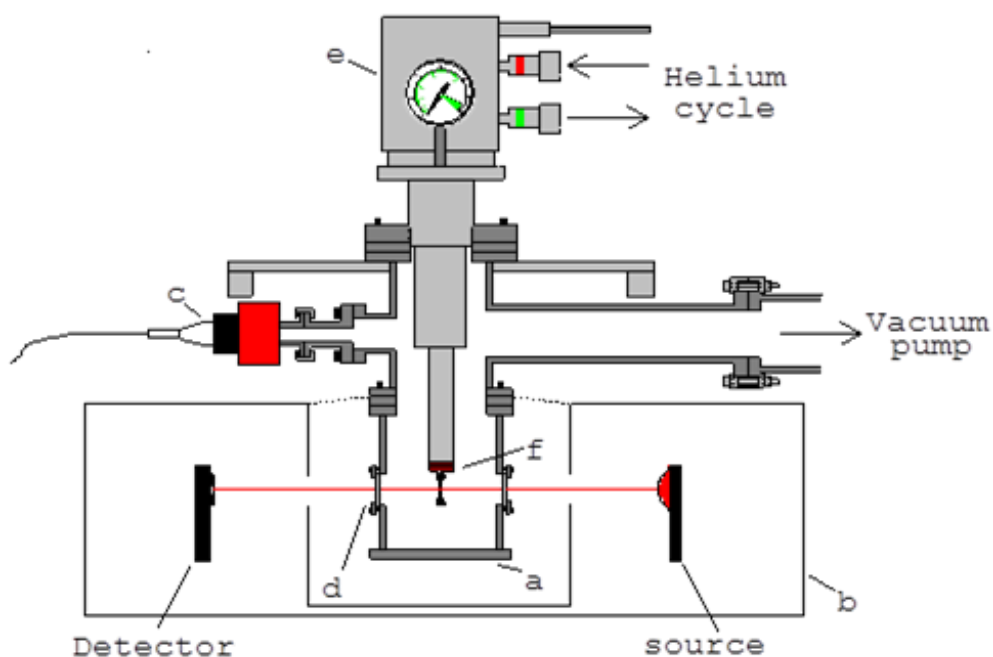
Figure 2.6: *Diagram of a vacuum chamber mounted in the path of the beam of the spectrometer (a) vacuum chamber, (b) spectrometer, (c) vacuum gauge (Penning), (d) Outer window, (e) Closed cycle He cryostat, (f) Deposition window in window holder screwed onto cold station of cryostat with indium seals/gasket.* [1]

The two parallel ports (outer windows) of the vacuum chamber contain CaF_2 windows, where the transmission range of CaF_2 is $850-77000$ cm^{-1}. The front port of the vacuum chamber was allocated to the evaporation furnace. The metal canister or the glass bulb containing the matrix gas was attached to one of the ports beside the furnace through a stainless steel tube, whilst the CaF_2 window on the other side was used for photolysis. The vacuum chamber was linked to two different sorts of pumps; the first pump was an Edwards rotary pump, it was used to attain a vacuum of about 1×10^{-2} mbar. The other pump was an Edwards Diffstak 100 vapour diffusion pump, which was fitted with a liquid nitrogen trap to condense any impurities, Figure 2.7 shows the diffusion pump and liquid nitrogen trap. The diffusion pump works to set the vacuum pressure lower 1×10^{-6} mbar before conducting experiments. The vacuum pressure was recorded by Edwards Penning pressure gauge connected to the diffusion pump.

Figure 2.7*: An Edwards Diffstak 100 vapour diffusion pump and liquid nitrogen trap.*

The original matrix experiments used liquid hydrogen cryostat with a base temperature of 20 K, and all the attendant dangers. Then liquid helium for 4 K and closed cycle helium systems for about 10–14 K became much more popular, and now closed cycle systems can deliver 4 K performance. Figure 2.8 shows the diagram of the cryostat. A closed cycle helium cryostat was able to cool the spectroscopic window to 9.2 K in about one hour.[2-4]
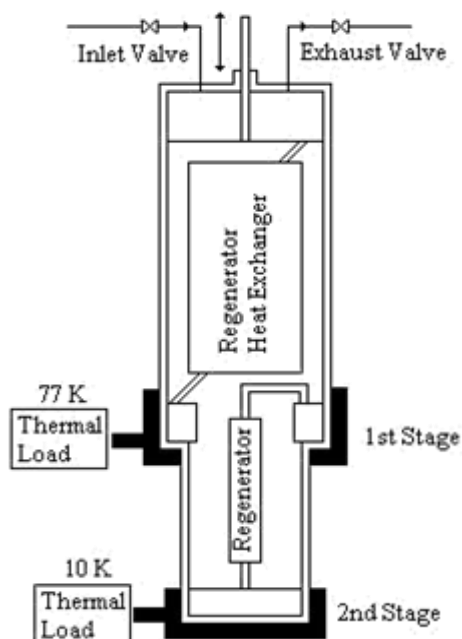
Figure 2.8 *Schematic of the internal workings of the expander in a two stage closed cycle helium cryostat.* [2]

As illustrated in Figure 2.9, the cryostat was situated in the vacuum chamber and the CaF_2 window at the tip of the cryostat was used as a deposition surface. The spectroscopic window could be rotated by 90º so as to expose the formed matrix to the path of the radiation during recording of the spectra. The temperature was monitored with either hydrogen bulb temperature gauge or a silicon diode detector.
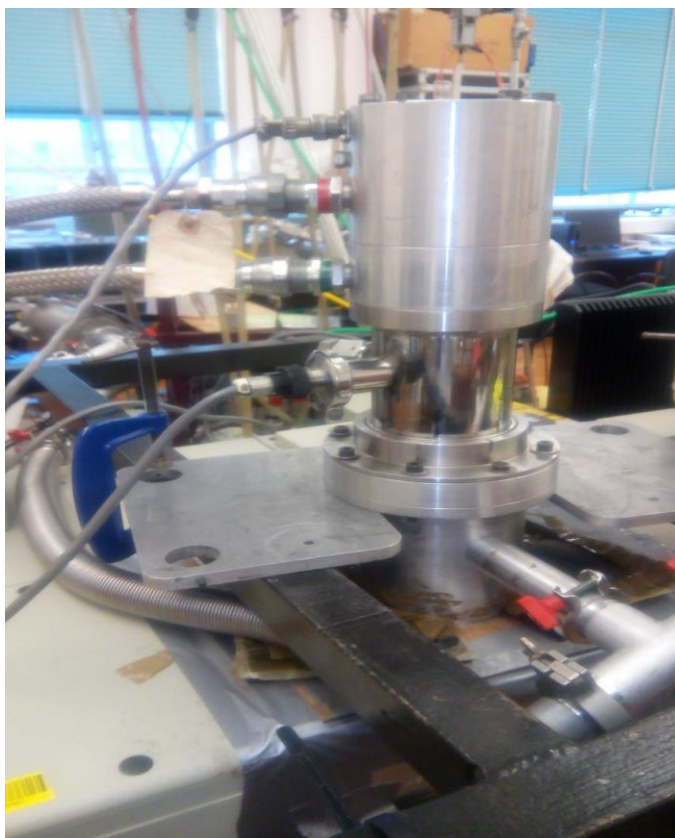
Figure 2.9*: Vacuum chamber and the cryostat mounted onto it.*

In the beginning of the experiments, the filament was heated up to a level slightly higher than the evaporation of atomic species before turning the cryostat on. The spectroscopic window was set in the position of recording a UV/vis spectrum during this process. The baseline was recorded at temperature at 9.8 K. Before starting the deposition process, a thin layer of gas mixture was laid down onto the cooled surface of the cryostat; the purpose of 5–6 minutes of the matrix gas is to try to keep the window as clean as possible for subsequent experiments. By applying argon on its own, the metal atoms and compounds are not in direct contact with the CaF_2 or CsI windows and so hopefully when the argon warms up it will take all the other compounds with it. This is not 100% successful each time, so after a few experiments the window does need cleaning. Sequential scans were run during the deposition. After the deposition of the solid matrix, photolysis was carried out for 10 minutes using visible light (800–400 nm), 200–410 nm, and broadband photolysis by 40–200 W Research QTH Sources, ORIEL Instruments. Moreover, the matrix was annealed at different temperatures 15–40 K for 5 minutes using digital temperature controller model SI9600–1 Scientific Instruments. A spectrum was run after each process. After the deposition of the solid matrix, photolysis was carried out for 10 minutes using visible light (700–400 nm), 200–410 nm, and broadband photolysis using a 40–200 W Hg–Xe ORIEL Instruments. In addition, the matrix was annealed at

different temperatures of 15–40 K for 5 minutes using a Scientific Instruments SI9600–1 digital temperature controller. A spectrum was run after each process.

2.6 Matrix Isolation Fourier Transform Infrared (FTIR) Spectroscopy

The aim of the matrix isolation FTIR experiments was to detect the vibrational modes of different molecular species of nickel fluorides, cobalt fluorides, palladium chlorides, and molybdenum chlorides and fluorides isolated in solid argon. The equipment was similar to matrix isolation UV/vis spectroscopy, yet it had some modifications. The apparatus consists of a Bruker Equinox55 Fourier transform infrared spectrometer controlled by Bruker Opus 3.0 Software installed onto the attached computer. A vacuum chamber fixed *in situ* in the sample compartment of the spectrometer, as shown in Figure 2.6. The deposition window was CsI as this withstands the temperature cycling much better than KBr. In case of using the far IR range, the outer parallel windows made of CsI have been used, as it transmits IR light down to 200 cm^{-1}.

The furnace used for the evaporation of elements was positioned, behind a copper disc, into the front port of the vacuum chamber. In addition, the matrix gas inlet was mounted onto one of the ports to the side of the furnace, while the other port was covered with a CaF_2 window (UV transparent) and used for photolysis. The vacuum chamber was connected to a pumping system comprising an Edwards rotary pump and an Edwards E04 vapour diffusion pump fitted with a liquid nitrogen trap; this pumping system experiments to be carried out at pressures lower than 1×10^{-6} mbar. Two Edwards Penning gauges were used to monitor the vacuum pressure. When the matrix gas was laid down, the pressure of the system was 2×10^{-5} mbar.

The cryostat was situated in the vacuum chamber and was able to be rotated by 90º so that the spectroscopic window could be in either the sample deposition position, or spectral recording position. The deposition surface was composed of CsI, as it absorbs IR light down to 200 cm^{-1}. A Scientific Instruments model SI9600–1 digital temperature controller was used to monitor and control the temperature of inner window through diodes.

FTIR spectra were collected based on the chemical properties of gas mixtures either in the mid-infrared (MIR) range, $400–4000 \text{ cm}^{-1}$, using a beam splitter made of KBr and a CsI or KBr windowed DTGS detector, or in the far–infrared (FIR) range from 200 to 600 cm^{-1}, using a Mylar beam splitter and a PE windowed DTGS detector. In the

beginning, the background spectra were run before collecting FTIR spectra for samples. The spectra were recorded at different resolution of 0.5 cm^{-1}, 1 cm^{-1}, and 2 cm^{-1}. The 2 cm^{-1} resolution spectra were run to examine the progress of the matrix during deposition process, while the spectra of a 0.5 cm^{-1} and 1 cm^{-1} resolution were recorded in order to observe any isotopic structure on the IR bands. Each spectrum has been computed as an average of 250 successive scans in order to improve the signal to noise ratio. The deposition window was put in the position of recording a spectrum during this process. As soon as the formation of the solid matrix was revealed, the same experimental procedures of photolysis and annealing processes were applied.

2.7 Computational Calculations

DFT calculations using the G09W programme were carried out to identify the geometric and electronic ground state for each MF$_n$ molecule as well as Lewis acid–base. Vibrational frequencies were calculated to confirm that a ground state had been identified as negative frequencies indicate a transition state. The calculated vibrational frequencies were also used to help with the assignment of the features in the IR spectra. A B3LYP functional was used for all calculations, both the 6–311G (+d) and the def2tzvpp basis set were used for nickel fluorides and cobalt fluorides, while the def2tzvpp basis set was used for the palladium chlorides, molybdenum fluorides, and Lewis acid–base for reaction of silicon tetrafluoride with alkyl phosphines.

2.8 References

1. N. Harris, *PhD thesis, The University of Hull*, 2001.
2. I. R. Dunkin, *Matrix isolation techniques: a practical approach, Oxford University Press, New York*, 1998.
3. M. J. Almond and K. S. Wiltshire, *Annu. Rep. Prog. Chem., Sect. C: Phys. Chem.*, 2001, **97**, 3-60.
4. M. J. Almond and N. N. Goldberg, *Annu. Rep. Prog. Chem., Sect. C: Phys. Chem.*, 2007, **103**, 79-133.

Chapter 3

Nickel fluorides

3.1. Introduction

A number of studies were carried out to investigate NiF molecules, whilst no spectroscopic data were found for molecular matrix isolated NiF. Focsa *et al*. recorded the dispersed excitation spectroscopy of NiF, studying the five electronic transitions, and identified two new electronic states and the five low–lying states of NiF.[1] In 2000, laser–induced fluorescence was employed to study NiF produced by the reaction of SF_6 with nickel atoms generated through discharge–sputtering.[2] The study confirmed the same results previously obtained by Focsa *et al*.[1] The NiF was studied in the range of 435–570 nm by laser–induced fluorescence. The LIF spectrum indicated eight electronic transitions of NiF, the ground state and the low–lying states have been identified.[3] The vibration interval in the upper level state was determined as 687.8 cm^{-1},[3] which is higher than the value previously reported by 17.8 cm^{-1}.[1] The difference in values was due to the repulsion of close–lying states.[3] The LIF spectrum for NiF was recorded in the region 17500−25000 cm^{-1}, where NiF was generated from the reaction of Ni atoms with SF_6.[4] The excitation spectrum illustrated the presence of twelve electronic states of NiF. Pinchemel *et al*. investigated the emission spectrum of NiF in the near infrared region by Fourier transform spectroscopy. Three electronic transition bands were observed in the range 6000−12000 cm^{-1} at 10850, 11100, 11180 cm^{-1} leading to detection of two new electronic states above the ground state.[5, 6] The vibrational frequency of NiF was observed at 644 cm^{-1}.[6] Furthermore, a high resolution spectrum of NiF was also recorded in the 18000–24000 cm^{-1} range. The study identified eight excited states that are above the ground state.[7] A theoretical study was performed by Koukounas and Mavridis using two different basis sets and variational multireference (MRCI) and coupled−cluster RCCSD(T) methods stating that the binding energy for the ground state of NiF was 430.9 kJ.mol^{-1} (103 kcal.mol^{-1}) and the equilibrium bond length was 1.736 Å.[8]

Numerous studies have focused on matrix–isolated NiF_2 molecules. The first investigation to characterise NiF_2 molecules in a solid argon matrix was undertaken by Milligan *et al*. in 1965. The IR spectrum collected showed the peaks near to 780 cm^{-1}, and the weak peaks observed between 715−736 cm^{-1} were assigned to the formation of the dimer form of NiF_2.[9] The symmetry of NiF_2 was suggested at linearity. Four years

later, Hastie *et al.* confirmed the same results through their studies to investigate the molecular geometry of the first row transition metals difluorides.[10-12] These studies reported the NiF_2 bond angle as $156\pm8°$, although it should be noted that these calculations are very sensitive, so a change of 0.1–0.2 cm^{-1} in the measured separation of the $^{58}NiF_2$ and $^{60}NiF_2$ peaks would result in the prediction of a linear geometry.[13] Van Leirsburg *et al.* used matrix isolation infrared spectroscopy to detect the formation of NiF_2 species trapped in a matrix of Ar, alongside the interaction of molecules such as: N_2, CO, NO, and O_2 with matrix isolated NiF_2 in a solid Ar matrix.[14] The vibrational frequencies of NiF_2 molecules were observed at 779.4 cm^{-1}, 774 cm^{-1}, 796 cm^{-1}, and 765.1 cm^{-1}. These absorptions were also related to isotope patterns of nickel difluorides molecules; $^{58}NiF_2$, $^{60}NiF_2$, $^{62}NiF_2$, and $^{64}NiF_2$ respectively, while bands located at 666–670 cm^{-1} were assumed to be due to a dimer form of NiF_2.[14] The same results were reported from a theoretical study by Besnainou *et al.*[15] In 1988, Bukhmarina *et al.* reinvestigated the isolation of NiF_2 species in inert gas matrices through the vibrational spectra.[16] The absorptions of NiF_2 were also observed around 780 cm^{-1}, which was in agreement with previous study.[14]

Theoretical studies undertaken by Popov calculated the bands related to NiF_3 at 295, 433, and 1031 cm^{-1}. The calculation proposed the geometry of NiF_3 as NiF molecule with two fluorine atoms associated with it in non–binding distance 3.25 Å.[17] Recently, the computational calculations were used to detect the configuration of NiF_3 considering the Jahn–Teller effect on the IR absorption spectra.[18] The absorption band of the bending mode was 198 cm^{-1}. The proposed IR spectra in most cases were unresolved. A further theoretical study reinvestigate the Jahn–Teller and spin orbit coupling effects for the $^4E'$ state of NiF_3 revealed that the spin orbit coupling was strong ($\Delta = 234$ cm^{-1}) for bending and stretching modes.[19] No experimental data for molecular NiF_3 and NiF_4 molecules exists. The reason for few experimental data for molecular NiF_3 or NiF_4 is that the solid state "NiF_3" is a mixed valence Ni(II)/Ni(IV) compound,[20, 21] and solid state NiF_4 is very reactive and unstable above –65 °C.[22, 23] Also, the characterisation of Ni_2F_5 indicated it is a mixture of NiF_2 and NiF_3.[24]

Therefore, whilst NiF_2 is well characterised in cryogenic matrices, there is no data available for NiF, NiF_3, or NiF_4. Whilst there is gas phase data available for NiF, there is uncertainty about the vibrational wavenumber in the ground state. The aim of the work described in this chapter is to synthesise the unknown NiF, NiF_3, and NiF_4 in solid Ar matrices, and elucidate their structures by spectroscopic means.

3.2 Results and Discussion

3.2.1 UV/Vis Spectra of Ni in Ar

The process to optimise the production of atomic nickel in argon was very slow, and many trials were carried out to determine the conditions required to evaporate nickel species. Firstly, a filament consisting of nickel wire wrapped on a tantalum former was used as in previous work for palladium,[25] but this was not successful as the nickel melted without producing atomic nickel. After that, a new design of filament was implemented; the filament was made of pure strands of nickel wrapped together. It has been used efficiently and this design was then used in all of the nickel experiments reported below. The melting point of nickel is 1452 °C, while the temperature required to get a vapour pressure of 1×10^{-3} torr is 1380 °C.[26]

The temperature of the deposition window was set at 11.8 K and the pressure in the chamber was 2×10^{-6} mbar. Initially, argon gas was laid down for 5 minutes on the cooled window of the cryostat to try to keep the window as clean as possible for subsequent experiments. The nickel filament was heated with 28 A electrical current using a voltage of 0.819 V for 60 minutes and the UV–visible spectrum was recorded. As seen in Figure 3.1a, two major peaks at 30250 and 31380 cm^{-1} were observed with a weak peak at 32850 cm^{-1}, followed by two strong overlapped peaks at 34850 and 35300 cm^{-1} and a tiny peak at 37500 cm^{-1}. In addition, a broad peak was found at 43230 cm^{-1} followed by a weak peak at 46280 cm^{-1}. These peaks are in good agreement with those for Ni atoms in solid argon matrix reported previously.[27-29] Furthermore, no peaks were observed in the region of 18900–22500 cm^{-1}; this region was shown previously to indicate the formation of isolated Ni_2 and Ni_3 molecules in solid argon.[29-31] This observation indicates that both the energy used to evaporate nickel as well as the nickel to argon ratio were not high enough to deposit Ni_2 and Ni_3 in solid argon. Furthermore, it was observed that the end of the spectrum became slightly noisier at high wavenumbers from 48500 cm^{-1} onwards. It is more likely due to lower light throughput at higher energy because of scattering of the argon matrix rather than true absorption. The solid matrix was photolysed using visible light photolysis (400–700 nm) and the optical spectrum is presented in Figure 3.1b. The spectrum has the same shape, and there was no change in intensity of peaks. The optical spectrum was recorded after exposing the solid matrix to 200–410 nm photolysis. Figure 3.1c illustrates that the intensity of peak at 43230 cm^{-1} increased, while the intensity of other peaks shrunk slightly. The solid matrix was exposed to 10 minutes

of broadband photolysis and the optical spectrum is given in Figure 3.1d. The peak at 43230 cm^{-1} grew again. In return, all of other bands decreased a little.[32] Figure 3.1e demonstrates the solid matrix after further 10 minutes of visible light photolysis, the spectrum has the same shape, and no obvious change in intensity recorded.
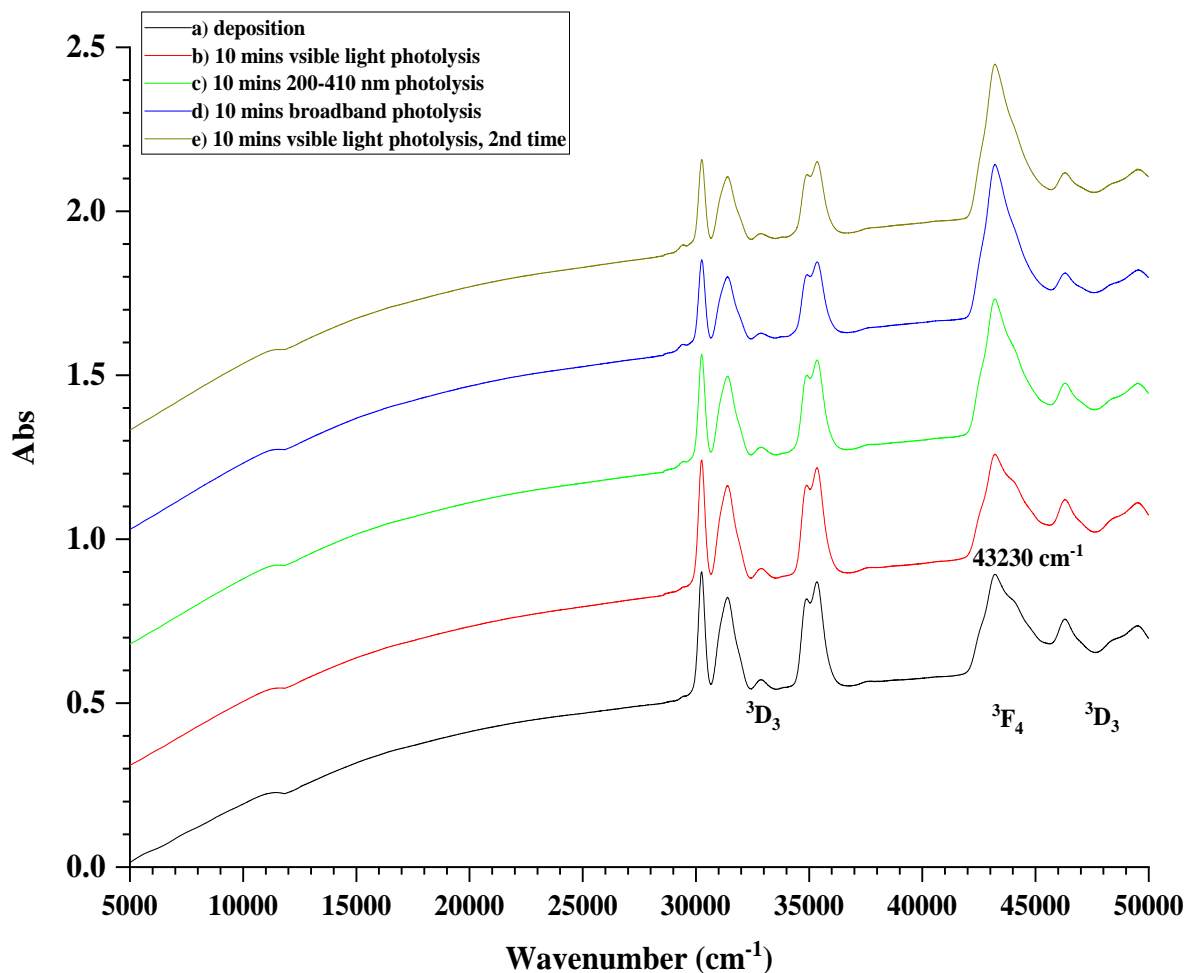
Figure 3.1: *UV/Vis spectra of atomic Ni in an Ar matrix (a) after deposition, (b) after 10 mins visible light photolysis, (c) after 10 mins 200–410 nm photolysis, (d) after 10 mins broadband photolysis, (e) after further 10 mins visible light photolysis.*

Table 3.1: Absorptions (cm^{-1}) observed and previous studies of Ni atoms isolated in Ar matrix.

Experiment	Ref [33]	Ref [30]	Assignments/ Ground state
30250 cm^{-1}	30300 cm^{-1}	30350 cm^{-1}	z^{3}P$_2$←^{3}D$_3$
31380 cm^{-1}	31350 cm^{-1}	31530 cm^{-1}	z^{3}F$_4$←^{3}D$_3$
32850 cm^{-1}	32900 cm^{-1}	33050 cm^{-1}	z^{3}G$_5$←^{3}D$_3$
34850 cm^{-1}	34700 cm^{-1}	34960 cm^{-1}	y^{3}F$_4$←^{3}D$_3$
35300 cm^{-1}	35300 cm^{-1}	35530 cm^{-1}	y^{3}D$_3$←^{3}D$_3$
37500 cm^{-1}	37450 cm^{-1}	–	y^{1}F$_3$←^{3}D$_3$
43230 cm^{-1}	45850 cm^{-1}	43620 cm^{-1}	y^{3}G$_5$←^{3}F$_4$
46280 cm^{-1}	46300 cm^{-1}	46540 cm^{-1}	x^{3}P$_2$←^{3}D$_3$

After the photolysis process was completed, the matrix was warmed up to investigate any changes and the possibility of forming dimer or trimer forms of nickel. Figure 3.2b demonstrates the UV–visible spectrum of Ni atoms in solid argon matrix after 5 minutes of annealing at 15 K. The peak at 43230 cm^{-1} decreased. Upon annealing at 20 K for 5 minutes, the band at 43230 cm^{-1} decreased distinctly as seen in Figure 3.2c. After a further 5 minutes of annealing at 25 K, the UV–visible spectrum was recorded and is shown in Figure 3.2d. The 43230 cm^{-1} peak disappeared. Figure 3.2e illustrates the UV–visible spectrum of the matrix after 5 minutes of annealing at 30 K. The intensity of bands at 30250, 31380, 32850, 35300, 37500 and 46280 cm^{-1} became weaker. It indicates that the deposited solid matrix has started to evaporate. Upon annealing to 35 K for 5 minutes, as demonstrated in Figure 3.2f, the intensity of all peaks diminished again and the noise in the spectrum increased from 43000 cm^{-1} onwards. Eventually, the spectrum was more scattered because the baseline has risen remarkably. The ground state of Ni in gas phase is ^{3}F$_4$ (3d^8 4s^2).[28] While in matrix isolation, Ni atoms can be in both ground state ^{3}F$_4$ (3d^8 4s^2) and ground state ^{3}D$_3$ (3d^9 4s^1) as these are only separated by only 205 cm^{-1} in the gas phase, and the ground state inverts because of greater matrix repulsion of the 4s electrons compared to the 3d electrons.[32-40] The features at 29000–38000 cm^{-1} and 45500–50000 cm^{-1} are associated with the ^{3}D$_3$ state, while the features at 42000–45500 cm^{-1} are due to the ^{3}F$_4$ state as seen in Table 3.1. The assignment of the excited state is really complicated, especially as the excited states appears to be a mixture, so only the ground state is given in Table 3.1.[34] On broadband photolysis the substantial increase in intensity of the peak at 43230 cm^{-1} is due to Ni atoms converting from the ^{3}D$_3$ (3d^9 4s^1) state to the ^{3}F$_4$ (3d^8 4s^2) state, which has been reported previously.[32] Similar behaviour has been detected for

Ni atoms trapped in solid Kr, indicating the presence of features due to $^3F_4$ and $^3D_3$ states and that the photolysis involved z $^3P_2^0 \leftarrow {}^3D_3$ excitation, followed by decay to the $^3F_4$ ground state.[35] On annealing the intensity of the $^3F_4$ feature at 43230 cm^{-1} decreased quickly much more than those of the $^3D_3$ state, as the $^3F_4$ state is thermally unstable.[33, 34] Therefore, the electronic absorption spectra of Ni atoms is complicated even in the absence of F_2.
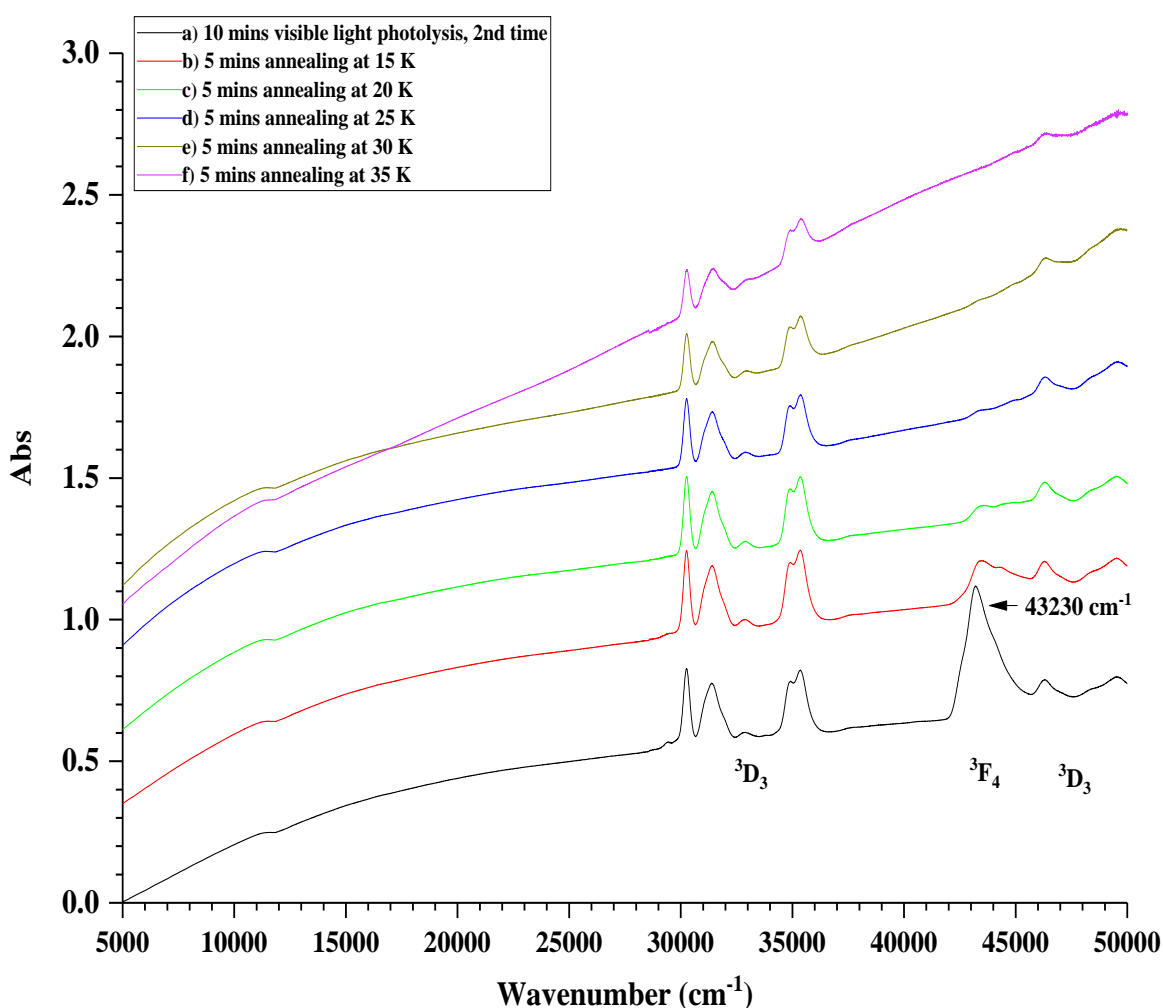
Figure 3.2: *UV/Vis spectra of atomic Ni in an Ar matrix (a) after further 10 mins visible light photolysis, (b) after 5 mins annealing at 15 K, (c) after 5 mins annealing at 20 K, (d) after 5 mins annealing at 25 K, (e) after 5 mins annealing at 30 K,(f) after 5 mins annealing at 35 K.*

3.2.2 UV/Vis Spectra of 1% F_2 in Ar

Figure 3.3a was taken after a layer of the 1% F_2 in Ar gas matrix was laid down for 45 minutes on the deposition surface of the cryostat at 11.9 K. This was to investigate the purity of the gas mixture and to identify any chemical components found before conducting the interaction between transition metals and fluorine in argon gas mixture. A tiny broad band was obtained at 35000 cm^{-1} that is due to F_2 in solid argon matrix.[41] In

addition to this, 10 minutes of photolysis process was carried out using visible light, 200–410 nm, broadband, and further visible light, respectively. Sequential scans were recorded after each process and are presented in Figures 3.3b–3.3e. The UV–visible spectra indicated that no change was found.
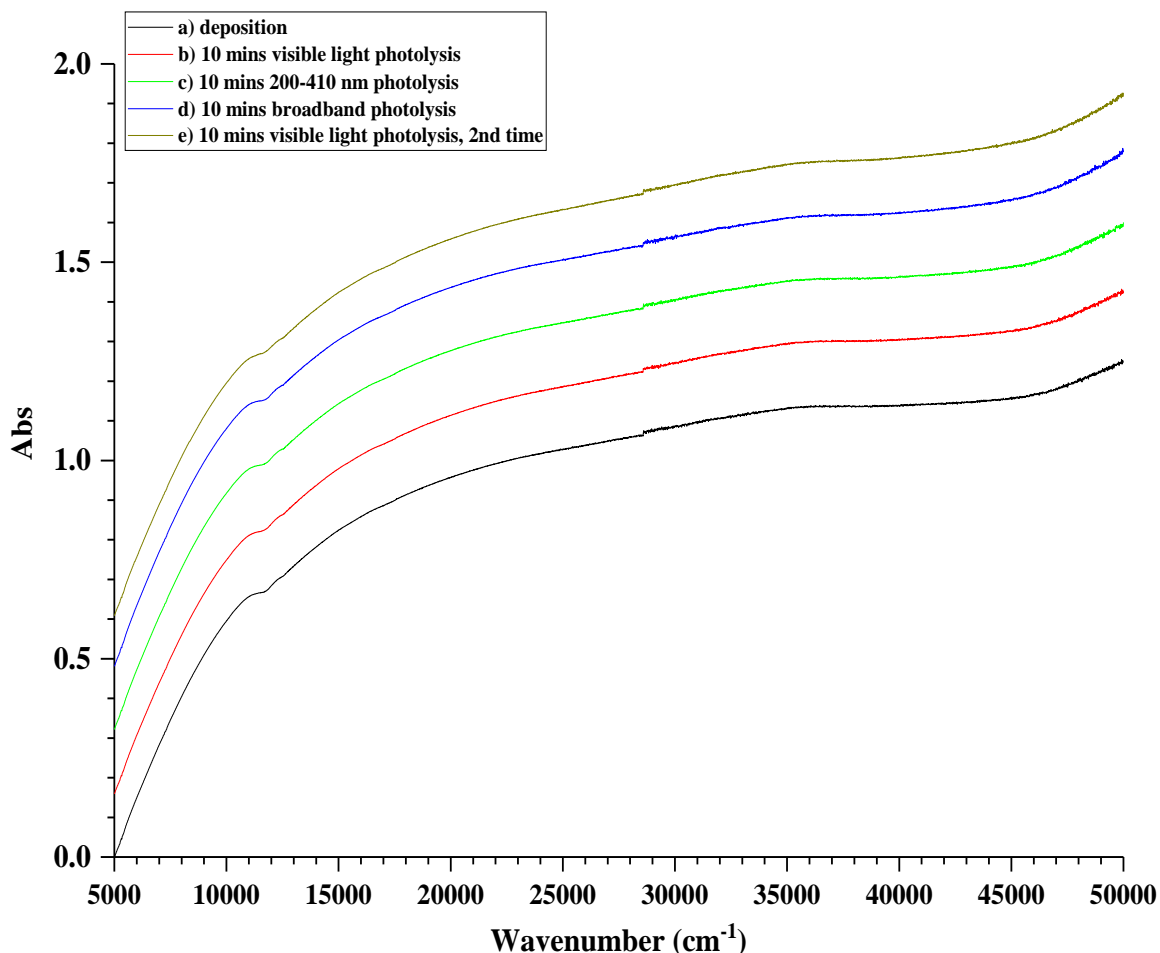
Figure 3.3: *UV/Vis spectra of a 1% F_2/Ar matrix (a) after deposition, (b) after 10 mins visible light photolysis, (c) after 10 mins 200–410 nm photolysis, (d) after 10 mins broadband photolysis, (e) after further 10 mins visible light photolysis.*

Subsequently, the solid matrix was annealed after the photolysis process was performed. Figures (3.4b–3.4e) display no significant change was observed when heating up the matrix for 5 minutes from 14 K to 20, 24, 30 and 35 K, respectively. Moreover, the spectra were increasingly scattered as the baseline has risen with the passing of time and became noisier at high wavenumbers. The same experimental steps were undertaken using 0.5% F_2 in Ar matrix gas and the same results were obtained. As a result, there are no impurities detected in the fluorine in argon gas mixture which might interfere with the assignment of peaks in the spectra containing both F and Ni atoms.
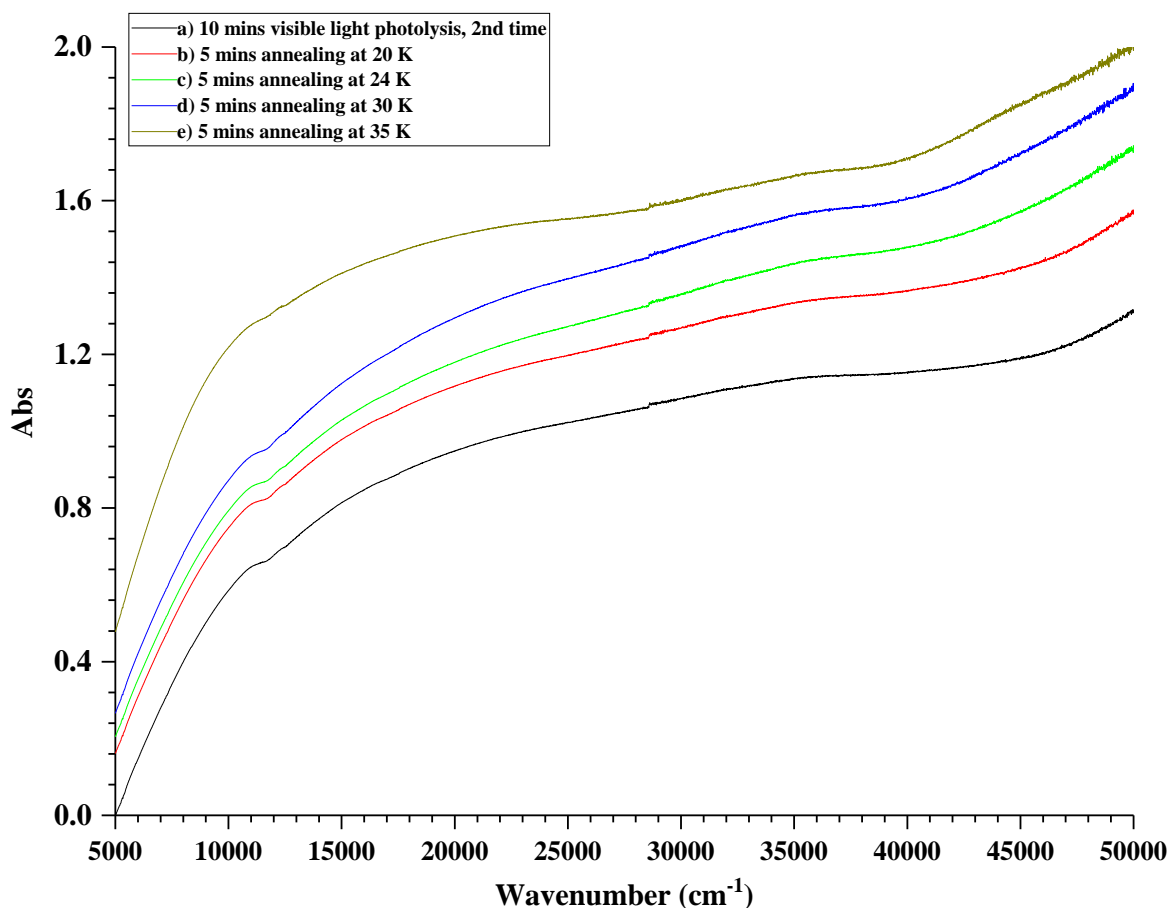
Figure 3.4: *UV/Vis spectra of a 1% F$_2$/Ar matrix (a) after further 10 mins visible light photolysis, (b) after 5 mins annealing at 20 K, (c) after 5 mins annealing at 24 K, (d) after 5 mins annealing at 30 K, (e) after 5 mins annealing at 35 K.*

3.2.3 UV/Vis Spectra of Ni in 1% F$_2$/Ar

The concentration of 1% of fluorine in argon gas matrix has been used in this study to investigate the formation of nickel fluoride molecule in a matrix of solid Ar. The same experimental conditions have been implemented to form nickel fluorides in solid argon matrix; the deposition window was cooled down at 11.5 K and the pressure was 2 × 10^{-6} mbar. The evaporation process was performed using a 32 A electrical current at 0.872 V. The UV–visible spectrum was run after 75 minutes of deposition and is presented in Figure 3.5a. The same peaks previously observed in the spectrum of nickel atoms were found, four strong peaks and two weak peaks were found in the region between 29500 and 38000 cm^{-1} at 30250, 31380, 32850, 34850, 35300, and 37500 cm^{-1}, and one broad asymmetric peak at 43230 cm^{-1} followed by weak peak at 46250 cm^{-1}. Amazingly, no additional peaks were observed. These bands together were considered as evidence of the generation of atomic nickel only, without any noticeable amount of the presence other nickel species. The matrix was exposed to visible light photolysis for 10 minutes and the spectrum is shown in Figure 3.5b. The same shape of peaks was noticed

33

without change in intensity of any peaks. Figure 3.5c demonstrates the spectrum after 10 minutes of 200–410 nm photolysis, the intensity of all peaks decreased slightly except the peak at 43230 cm^{-1} which has the same intensity; nonetheless, no additional peaks were detected. 10 minutes of broadband photolysis was applied and the UV–visible spectrum was recorded and is given in Figure 3.5d. The peaks between 29000–40000 cm^{-1} reduced dramatically, while the shape of peaks in the region 40000–5000 cm^{-1} changed and the original bands at 43230, 46250, 48370 cm^{-1} were replaced with new peaks at 43390, 45640 and 48370 cm^{-1}. The solid matrix was photolysed by using 10 minutes of visible light again; the recorded spectrum indicates no appreciable change as shown in Figure 3.5e. The photolysis process works on producing more excited atomic fluorine.[42, 43] As a consequence, it becomes highly reactive and has the ability to migrate to nickel sites into the solid matrix. Although, no further peaks were observed after the photolysis process, the visible decrease in intensity of the atomic nickel bands is more likely because of consumption of atomic nickel and formation of nickel fluoride species in the solid argon matrix. It is noteworthy that in the UV/vis spectra for Ni/Ar in the absence of F_2 the peaks for Ni atoms converting from the $^3D_3$ ($3d^9 4s^1$) state to the $^3F_4$ ($3d^8 4s^2$) state on photolysis, and when F_2 is present the $^3F_4$ state seems to disappear.
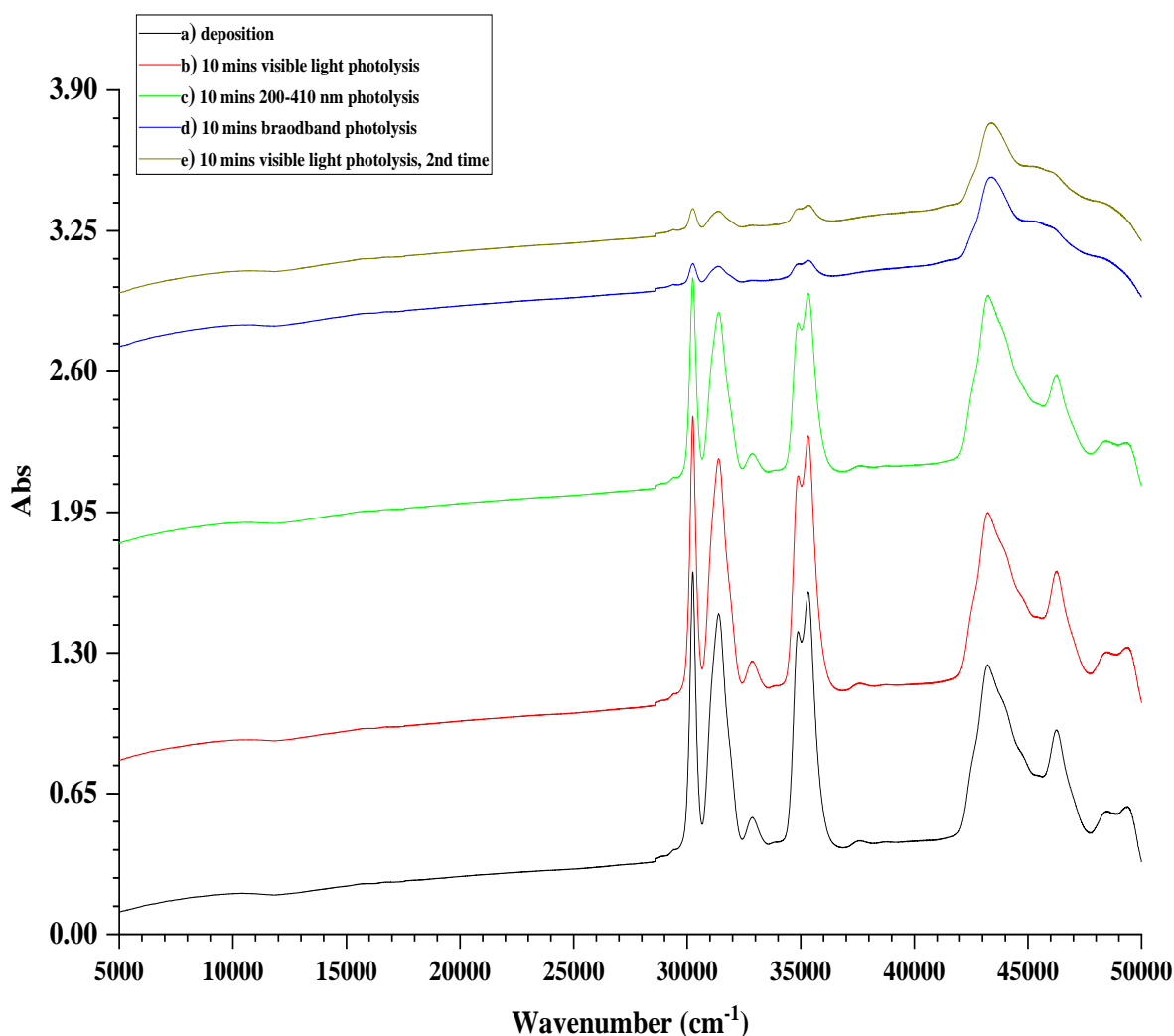
Figure 3.5: *UV/Vis spectra of atomic Ni in a 1% F$_2$/Ar matrix (a) after deposition, (b) after 10 mins visible light photolysis, (c) after 10 mins 200–410 nm photolysis, (d) after 10 mins broadband photolysis, (e) after further 10 mins visible light photolysis.*

After the photolysis process was conducted, the solid matrix was annealed for 5 minutes at 15 K, the UV/vis spectra in Figure 3.6b shows that the two new broad bands at 46000 and 48950 cm^{-1} became more intense, while the peak at 43390 cm^{-1} was reduced in intensity. Figure 3.6c displays the matrix after 5 minutes heating up to 20 K; the broad peaks at 46000 and 48950 cm^{-1} just grow in intensity slightly, with no considerable change in intensity of the other peaks. Additionally, scattering was increased at the higher energy end of the spectrum. The intensities of the peaks at 46000 and 48950 cm^{-1} were reduced after heating the solid matrix to 25 K for 5 minutes as displayed in Figure 3.6d. Sequential scattering was evident in the spectra as well. After 5 minutes of further annealing to 30 K, the optical spectrum in Figure 3.6e shows that all peaks had reduced in intensity. The solid matrix was warmed up to 35 K for 5 minutes, the intensity of all peaks became smaller again. Furthermore, the spectrum was significantly scattered and became noisier from 43000 cm^{-1} onwards as seen in Figure 3.6f. Similar results had been

achieved by using 0.5% of F_2 in Ar gas mixture, but with less intense peaks. The two broad peaks at 46000 and 48950 cm^{-1} barely increased after annealing at 15 and 20 K, followed by a slight diminishment on heating the solid matrix to 25, 30, and 35 K. Nonetheless, the peak at 43390 cm^{-1} shrank on annealing, which indicated that it does not belong to the same species. As seen in Figure 3.7 below, there is a fundamental change at 46000 and 48950 cm^{-1} observed only in UV/vis spectra of Ni atoms isolated in 1% F_2/Ar gas mixture on annealing after the photolysis process and not observed in the optical spectra of Ni atoms isolated in neat Ar gas. Hence, it is considered crucial evidence for the interaction of Ni and fluorine atoms in solid argon matrix.
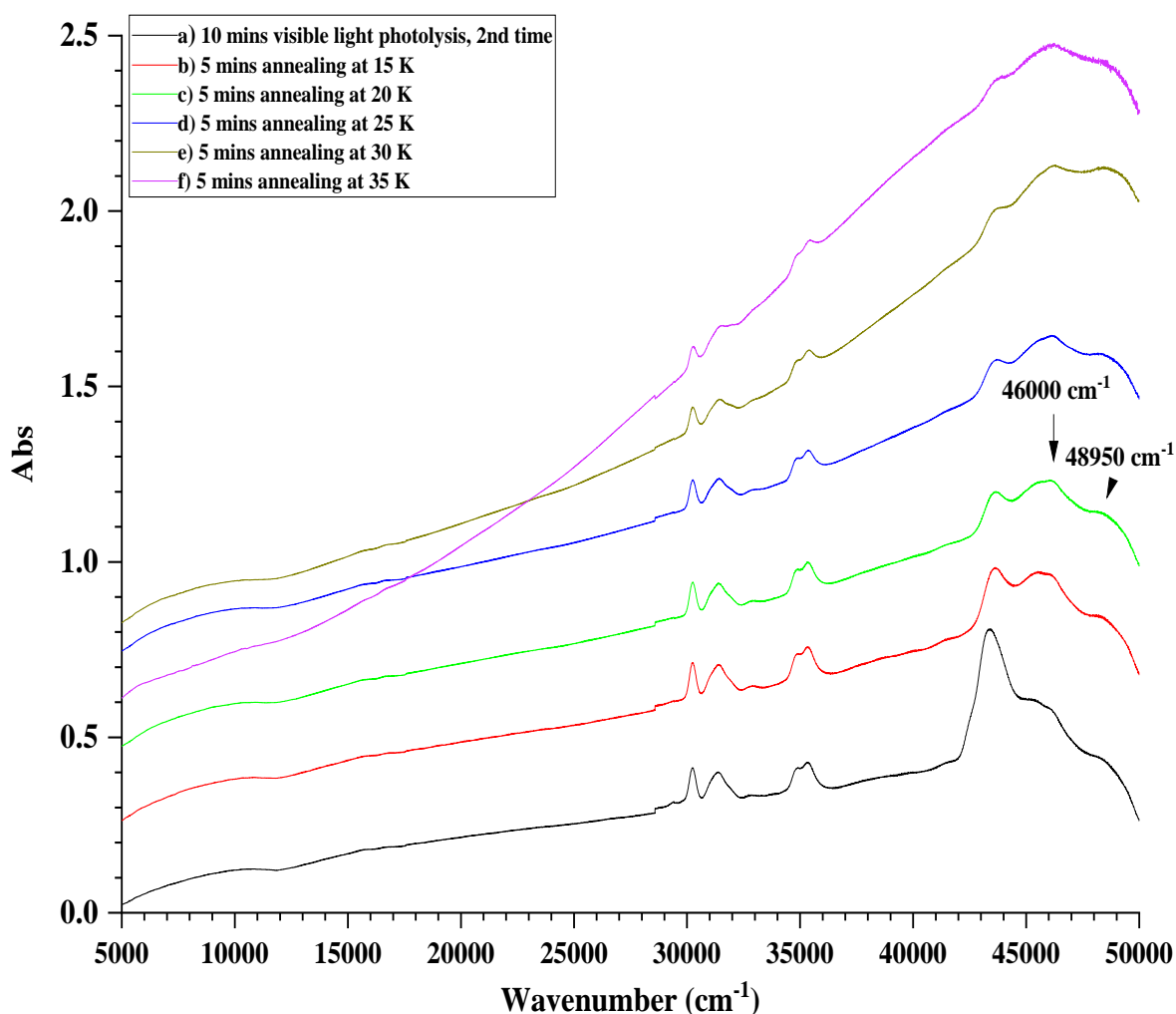
Figure 3.6: *UV/Vis spectra of atomic Ni in a 1% F_2/Ar matrix (a) after further 10 mins visible light photolysis, (b) after 5 mins annealing at 15 K, (c) after 5 mins annealing at 20 K, (d) after 5 mins annealing at 25 K, (e) after 5 mins annealing at 30 K, (f) after 5 mins annealing at 35 K.*

In previous work, no UV absorptions were observed for NiF$_2$, but these experiments were carried out with photographic plates.[9] For NiCl$_2$ in an argon matrix there are intense charge transfer absorptions observed at 28350 cm^{-1}.[44] Using an optical

electronegativity value of 3.0 for χ_{Cl}, allows for an estimate of χ_{Ni} of 2.055 in triatomics such as $NiCl_2$ and NiF_2. The value of χ_{Ni} in combination with a χ_F value of 3.9 predicts charge transfer transitions of *ca.* 55000 cm^{-1} for NiF_2. Regarding to higher oxidation state nickel fluorides, the lowest energy charge transfer transition would be expected at significantly lower energies. Therefore, the bands at 46000 and 48950 cm^{-1} can be assigned to NiF_2 charge transfer transitions.
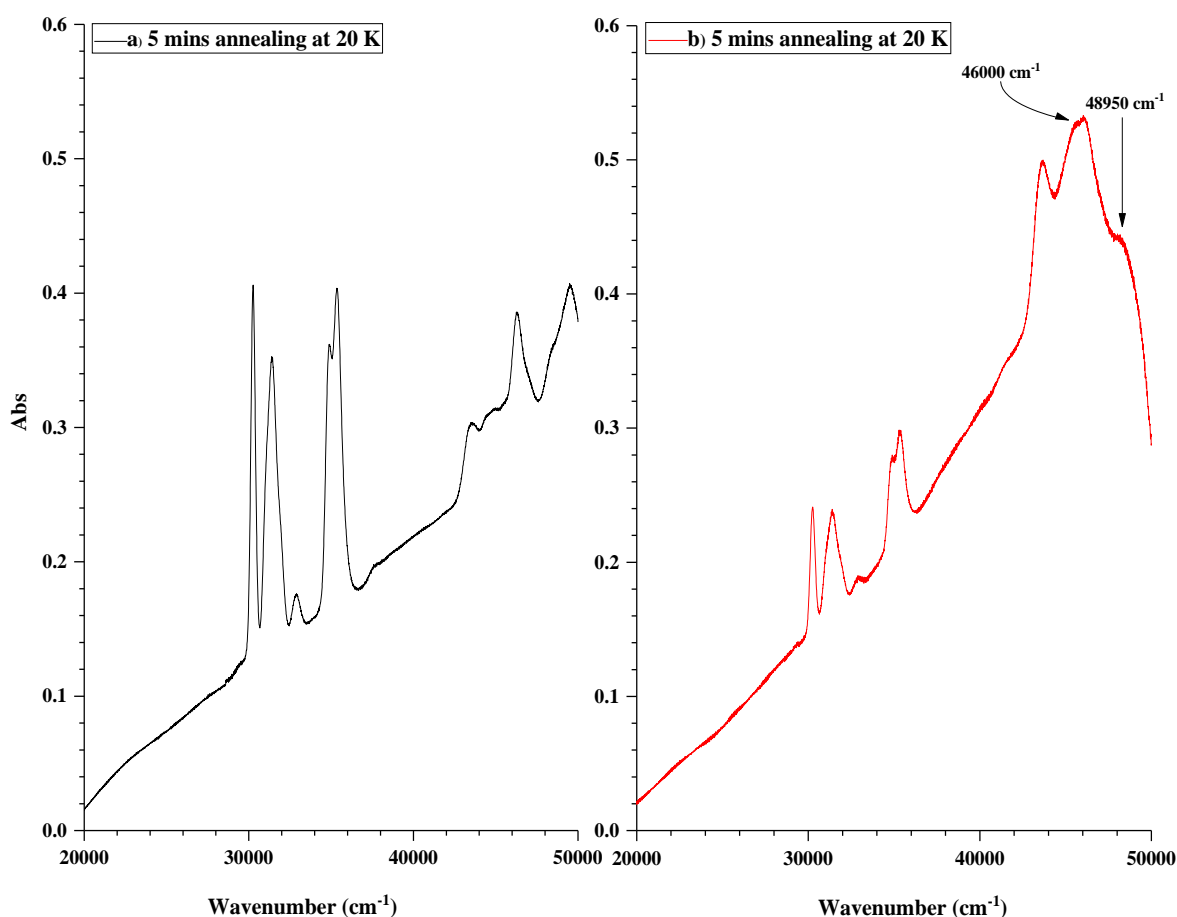
Figure 3.7: *UV/Vis spectra of (a) atomic Ni in an Ar matrix after 5 mins annealing at 20 K, (b) atomic Ni in a 1% F$_2$/Ar matrix after 5 mins annealing at 20 K.*

The data present in UV/vis spectra provide strong evidence for the isolation of nickel fluorides molecules in solid argon matrix. It has been illustrated that the interaction between atomic nickel and fluorine in the matrix is comparatively minor till photolysis is performed.

3.2.4 FTIR Spectra of Ni in a 0.5% F$_2$/Ar matrix

Nickel atoms were trapped in a 0.5% F$_2$/Ar matrix in order to prepare different nickel fluoride molecules. Different concentrations of F$_2$ in argon gas matrix were used

to study the formation of nickel fluorides in solid Ar; 0.5% F_2/Ar was found to be the best concentration to be used and the peaks obtained are sharper. Similar results have been achieved by using both a 1% F_2 in argon matrix and a 2% F_2 in argon matrix. A nickel filament was heated at 1.027 V with 41 A of electrical current. The experiments were carried out at a pressure of 2×10^{-6} mbar and the temperature of the matrix was 10 K. First of all, a thin layer of 0.5% F_2 in Ar matrix gas was laid down onto the cooled surface of the cryostat. An infrared spectrum run after 60 minutes of deposition is shown in Figure 3.8a. Bands observed at 779.4 cm^{-1} and 774.4 cm^{-1} are assigned to asymmetric stretching modes of NiF_2 with its various isotopes; $^{58}NiF_2$ and $^{60}NiF_2$, respectively. These data are completely consistent with data published before.[14] Furthermore, a peak at 625.8 cm^{-1} has been obtained which has not been observed previously; it may probably be related to a new nickel fluoride species. In addition to the features shown in Figure 3.8a, bands were also observed at 1913 cm^{-1} and 1941 cm^{-1} which belong to carbonyl fluoride (OCF_2); these two bands are due to Fermi resonance of v_1 and $2v_2$ which are the symmetric stretching mode of both v_{C-F} and v_{C-O},[45] a peak at 2090 cm^{-1} is due to an interaction of Ni with N_2 to form NiN_2,[46] and a peak at 1273 cm^{-1} is due to the presence of CF_4, which is a common impurity in F_2 gas.[47] Furthermore, bands at 2345 and 662 cm^{-1} are due to matrix isolated CO_2, vibrational fine structure between 2500 and 2200 cm^{-1} and the 667 cm^{-1} band all belong to CO_2 in gas phase, a peak at 2140 cm^{-1} is due the stretching mode of CO, and a complex set of bands located between 1600–1650 cm^{-1} and 3700–3800 cm^{-1} are due to rotational fine structure of H_2O molecules in the argon matrix.[48, 49] The interaction between nickel atoms and the 0.5% F_2/Ar gas mixture on deposition is relatively weak. The solid matrix was then photolysed by using visible light for 10 minutes. The IR spectrum is presented in Figure 3.8b. The peak at 625.8 cm^{-1} barely increased in intensity. This peak is more likely to be NiF molecules; it is in very good agreement with literature data.[6] Moreover, the computational calculations support this assumption, the B3LYP/def2tzvpp calculations for NiF suggested the IR band at 614.36 cm^{-1} and the B3LYP/6–311G(+d) calculations suggested as 606.61 cm^{-1} as seen in Table 3.2. The intensities of peaks between 779.4 cm^{-1} and 769.4 cm^{-1} assigned to NiF_2 in solid argon matrix also increased marginally. The relative intensities of these bands are consistent with various isotopes of Ni in NiF_2. This result corresponds to the B3LYP/def2tzvpp calculations with the value of calculation error equals 20 cm^{-1} as well as the B3LYP/6–311G(+d) calculations with *ca* 11 cm^{-1} calculation error. It is obvious that the Ni isotopic separation in NiF is much lower than in NiF_2, implying much less movement of the nickel in NiF than in NiF_2. Furthermore, very weak peaks are found at

797.1 cm^{-1} and 791.9 cm^{-1}. Unfortunately, the IR spectrum after deposition was collected only at 2 cm^{-1} resolution, whilst other spectra for solid matrix after photolysis and annealing processes were collected at 2 cm^{-1} as well as 1 cm^{-1} resolution. The IR spectrum given in Figure 3.8c for the matrix after 10 minutes of visible light photolysis was collected again at 1 cm^{-1} resolution. The change of resolution effected on peaks, the NiF$_2$ peaks get sharper and slightly more intense, and the CO$_2$ peak splits into two. The splitting of the CO$_2$ bending peaks has been observed before.[50]
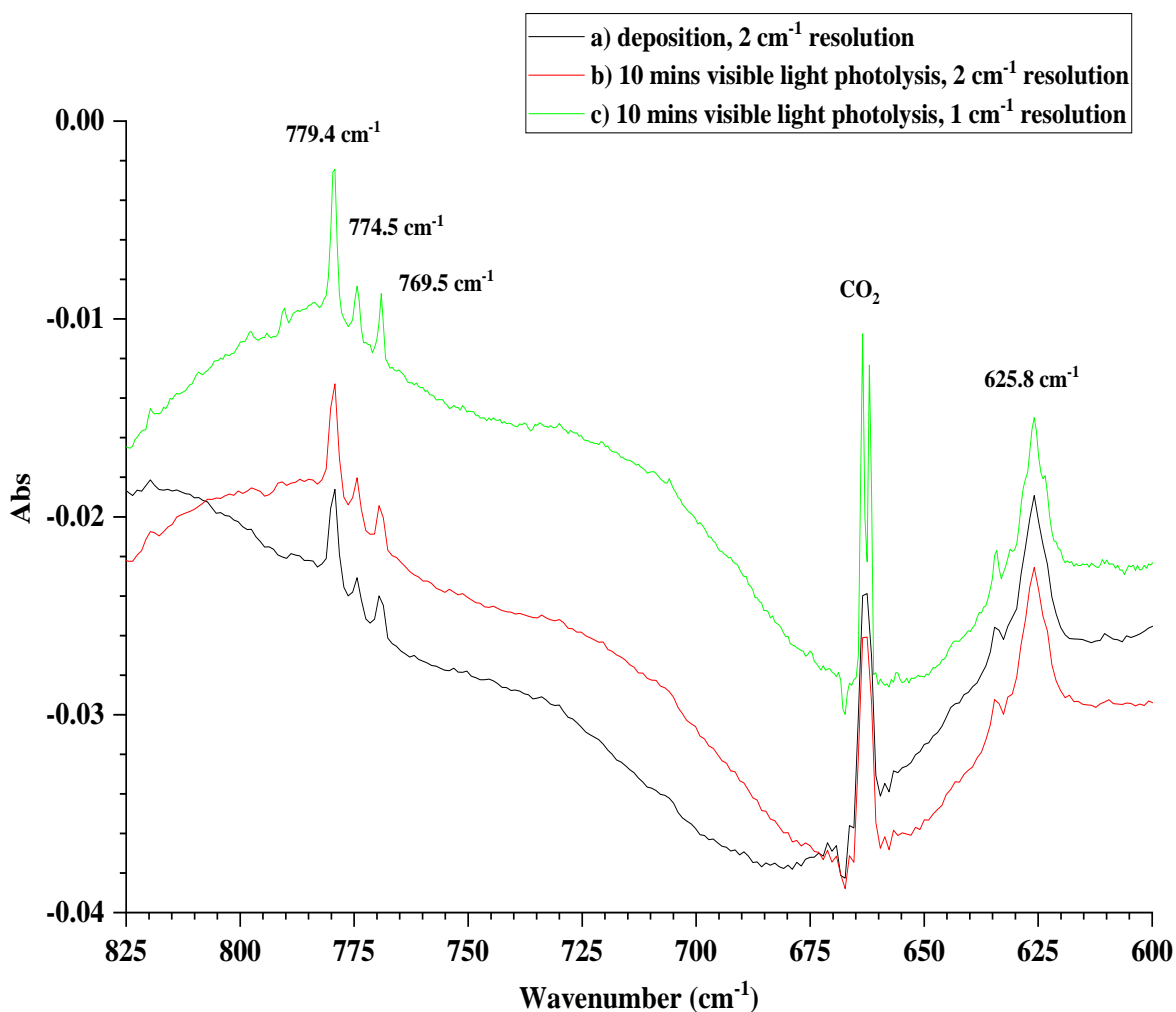
Figure 3.8: *FTIR spectra of atomic Ni in 0.5% F$_2$/Ar matrix (a) after deposition at 2 cm^{-1} resolution, (b) after 10 mins visible light photolysis at 2 cm^{-1} resolution, (c) after 10 mins visible light photolysis at 1 cm^{-1} resolution.*

Table 3.2: Vibrational frequencies (cm^{-1}) observed and calculated of NiF and NiF$_2$ molecules in a matrix of Ar.

Assignments	Observed	Ref [5]	Calculated B3LYP/6–311G(+d)	Calculated B3LYP/def2tzvpp
NiF	625.8 cm^{-1}	–	606.61 cm^{-1}	614.36 cm^{-1}
^{64}NiF$_2$	–	765.1 cm^{-1}	780.31 cm^{-1}	784.66 cm^{-1}
^{62}NiF$_2$	769.4 cm^{-1}	771.9 cm^{-1}	782.74 cm^{-1}	789.37 cm^{-1}
^{60}NiF$_2$	774.4 cm^{-1}	774.2 cm^{-1}	785.24 cm^{-1}	794.35 cm^{-1}
^{58}NiF$_2$	779.4 cm^{-1}	779.3 cm^{-1}	790.47 cm^{-1}	799.64 cm^{-1}
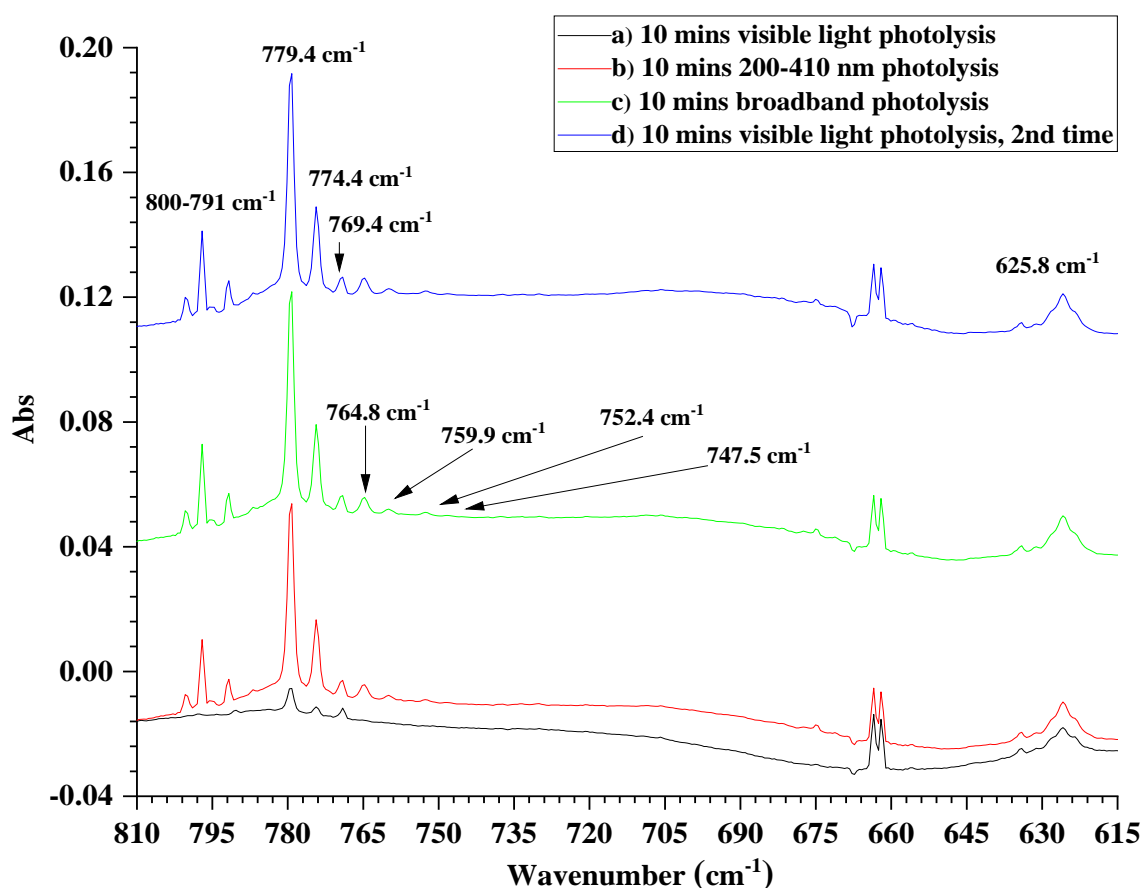
Figure 3.9: *FTIR spectra of atomic Ni in 0.5% F$_2$/Ar matrix (a) after 10 mins visible light photolysis, (b) after 10 mins 200–410 nm photolysis, (c) after 10 mins broadband photolysis, (d) after further 10 mins visible light photolysis.*

Figure 3.9b illustrates the IR spectrum after 10 minutes of 200–410 nm photolysis. As a result, the excited atomic fluorine atoms produced are quite reactive and are able to spread throughout the argon matrix to the sites hosting nickel, where 337 nm (UV) irradiation gives rise to "hot" F atoms which can travel up to 100 Å in solid Ar.[42, 43, 51] The peaks between 779.4 cm^{-1} and 769.4 cm^{-1} grew considerably, and also the band

located at 625.8 cm^{-1} grew indicating the reaction of thermally mobile fluorine atoms with the nickel atoms. Furthermore, new weak peaks observed at 764.8 and 759.9 cm^{-1} could be a second set of Ni isotopes; ^{58}NiF$_2$ and ^{60}NiF$_2$. New tiny peaks observed at 752.4 and 747.5 cm^{-1}, and new peaks were observed at 800.2 and 795.1 cm^{-1}; they were barely visible in the previous spectra. Nonetheless, the intensity of bands at 797.1 cm^{-1} and 791.9 cm^{-1} increased. Bands between 800 cm^{-1} and 791 cm^{-1} are most likely due to high valent nickel fluoride species such as, NiF$_3$ and NiF$_4$. The matrix was exposed to broadband photolysis for 10 minutes. As seen in Figure 3.9c, all the bands increased again slightly. Figure 3.9d displays the matrix after exposure to further 10 minutes of visible light photolysis. The intensity of all absorption bands were the same, no change was recorded. Therefore, UV photolysis results in the formation of mobile fluorine atoms which react with nickel atoms to form NiF, NiF$_2$ and potentially higher nickel fluorides, which are then stable in the presence of visible light.
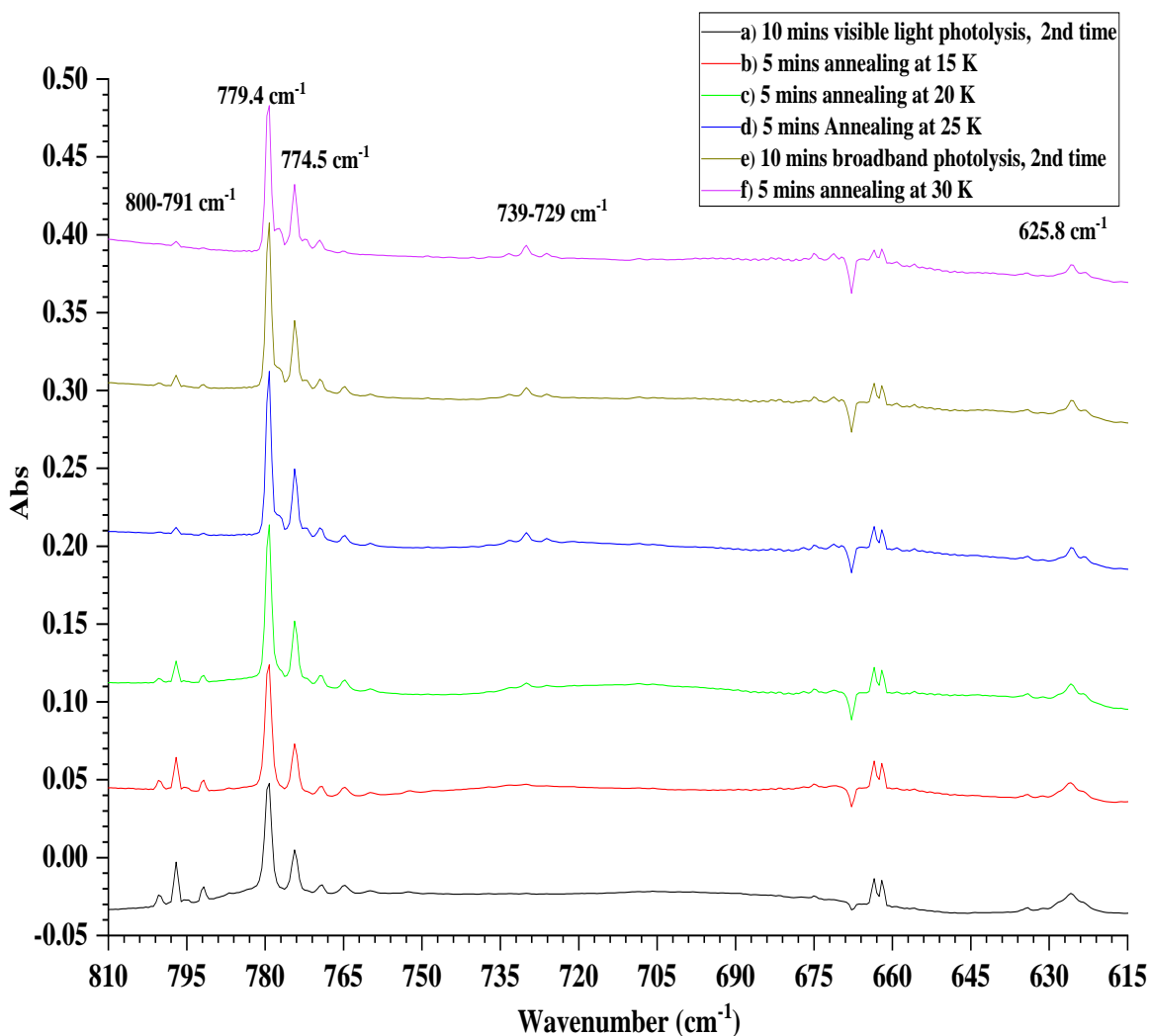
Figure 3.10: *FTIR spectra of atomic Ni in 0.5% F$_2$/Ar matrix (a) after further 10 mins visible light photolysis, (b) after 5 mins annealing at 15 K, (c) after 5 mins annealing at 20 K, (d) after 5 mins annealing at 25 k, (e) after further 10 mins broadband photolysis, (f) after 5 mins annealing at 30 K.*

The annealing process was performed after photolysis; it allows the matrix to become softer. As a consequence, trapped molecules can either reorient to a more stable interaction with the argon host, or migrate through the matrix; it was carried out to study the formation of dimers, and the behaviour of bands between 800 cm^{-1} and 791 cm^{-1}. Figure 3.10b is the spectrum recorded after warming the matrix to 15 K for 5 minutes. The intensity of absorptions bands assigned to NiF$_2$ increased slightly whereas, the peak present at 625.8 cm^{-1} shrank. Also, bands at frequencies between 800 cm^{-1} and 791 cm^{-1} decreased. Figure 3.10c shows the spectrum after 5 minutes of annealing at 20 K. The band at 625.8 cm^{-1} assigned to matrix–isolated NiF molecules became weaker. The peaks between 779.4 cm^{-1} and 769.4 cm^{-1} grew slightly. In contrast, peaks at 800.2 cm^{-1}, 797.1 cm^{-1}, 795.1 cm^{-1}, and 791.9 cm^{-1} decreased, particularly, the peaks at 795.1 cm^{-1} decreased considerably because it was already very weak comparing with the features at

42

800.2, 797.1 and 791.7 cm^{-1}, and so if it reduces to the same extent as the others it almost disappears. The tiny features observed at 752.4 and 747.5 cm^{-1} disappeared. New weak peaks are observed between 729 cm^{-1} and 736 cm^{-1} accompanied by two shoulders at 772.4 and 777.3 cm^{-1}; these peaks can be assigned to the formation of the dimer form of NiF$_2$, which has been reported by Dolphus E. Milligan *et al.*[9] Figure 3.10d shows the IR spectrum of the matrix after annealing again at 25 K for 5 minutes. The peak at 625.8 cm^{-1} decreased in intensity, and peaks between 779.4 and 769.4 cm^{-1} related to NiF$_2$ in solid argon and its various isotopes decreased. The intensity of bands at 800.2 cm^{-1}, 797.1 cm^{-1}, 795.1 cm^{-1}, and 791.9 cm^{-1} also decreased. In particular, the bands at 800.2 and 795.1 cm^{-1} almost disappeared. However, peaks between 729 cm^{-1} and 736 cm^{-1} increased again and also the two shoulders at 772.4 and 777.3 cm^{-1} became more intense. The matrix was exposed to broadband photolysis for 10 minutes as seen in Figure 3.10e. The intensity of the absorption bands between 800 cm^{-1} and 791 cm^{-1} increased slightly, whilst the intensity of other features did not change. Furthermore, no evidence for the two tiny peaks at 752.4 and 747.5 cm^{-1}. Figure 3.10f shows the IR spectrum after 5 minutes of annealing at 30 K, peaks located between 729 cm^{-1} and 736 cm^{-1} and the two shoulders at 772.4 and 777.3 cm^{-1} increased as well. The intensity of other peaks decreased. Figure 3.11 shows the effect of photolysis followed by the annealing process on the features between 800 and 791 cm^{-1}; it shows the consistent behaviour of the two sets of bands at 797.1 and 791.9 cm^{-1}, labelled (1), and bands at 800.2 and 795.1 cm^{-1}, labelled (2), throughout experiments, as they grew by photolysis and decayed by annealing. In addition, it displays the IR absorption bands related to dimer form of NiF$_2$ observed between 736–729 cm^{-1} and the two tiny peaks at 752.4 and 747.5 cm^{-1} more clearly.
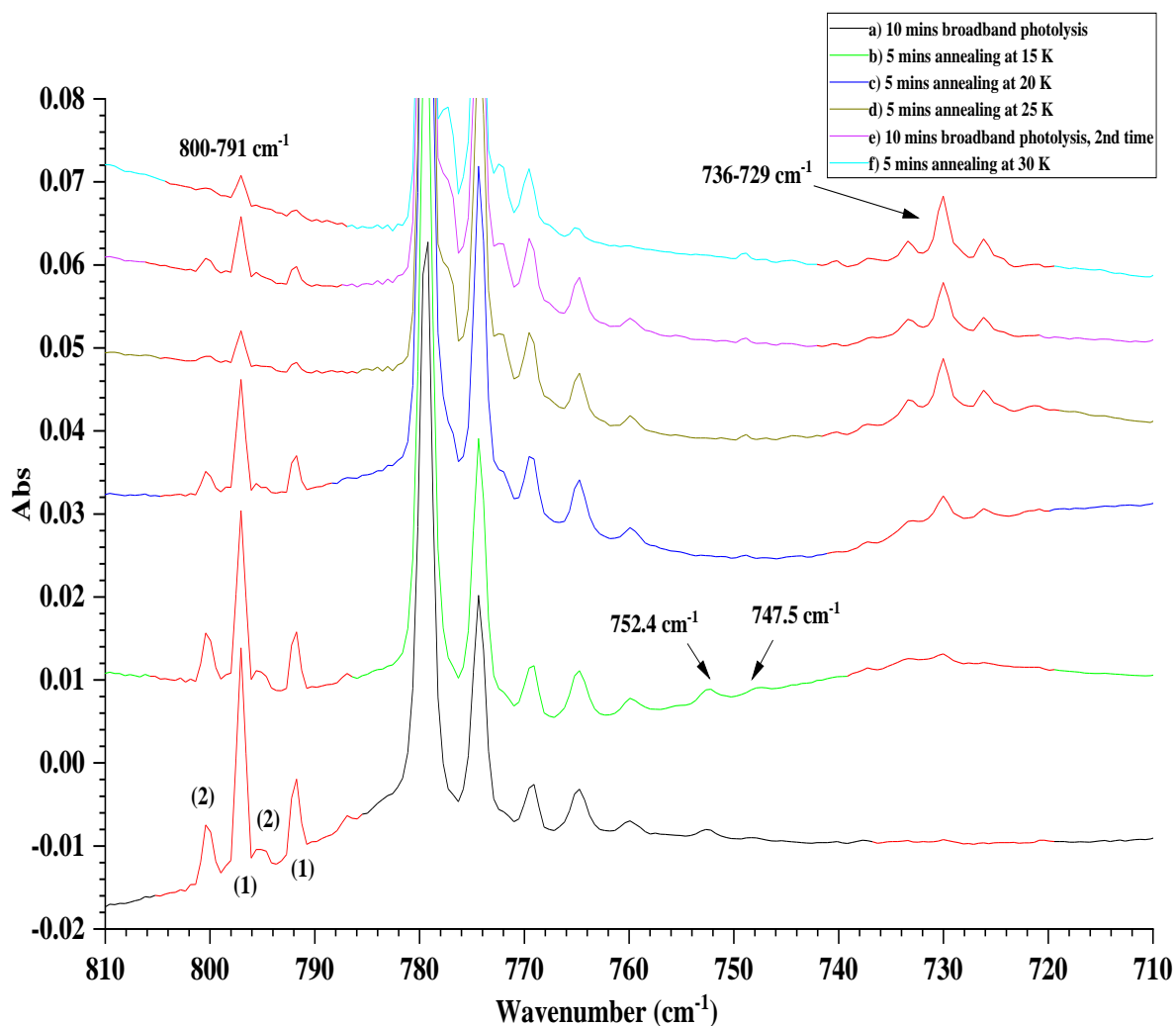
Figure 3.11: *FTIR spectra of atomic Ni in 0.5% F_2/Ar matrix (a) after 10 mins broadband photolysis, (b) after 5 mins annealing at 15 K, (c) after 5 mins annealing at 20 K, (d) after 5 mins annealing at 25 K, (e) after further 10 mins broadband photolysis, (f) after 5 mins annealing at 30 K.*

The same experiment was performed again as seen in Figure 3.12a, but this time the annealing was carried out before photolysis. The same features were observed at 779.4 and 774.4 cm^{-1} due to NiF$_2$ with its characteristic isotope pattern. Additionally, a peak at 625.8 cm^{-1} was obtained as well. The annealing process was conducted directly after deposition instead of visible photolysis, Figures 3.12b–3.12d show the IR spectra run after 5 minutes of annealing to 15, 20, and 25 K, respectively. The intensity of the peak at 625.8 cm^{-1} decreased a little, while the intensity of peaks due to NiF$_2$ grew slightly. Furthermore, peaks were observed between 729 cm^{-1} and 736 cm^{-1} in conjunction with two shoulders at 772.4 and 777.3 cm^{-1} due to the formation of the dimer form of NiF$_2$ molecules.[9] Astonishingly, no peaks were obtained between 800 and 791 cm^{-1} or at 752.4 and 747.5 cm^{-1} as was observed in the previous experiment. The matrix was exposed to 10 minutes visible light photolysis as presented in Figure 3.12e. There is no considerable

change recorded. Figure 3.12f demonstrates the spectrum after 10 minutes of 200–410 nm; the peaks between 800 and 791 cm^{-1} are obtained as well as two tiny features at 752.4 and 747.5 cm^{-1} and grew slightly when the matrix exposed to 10 minutes of broadband photolysis, as presented in Figure 3.12g.
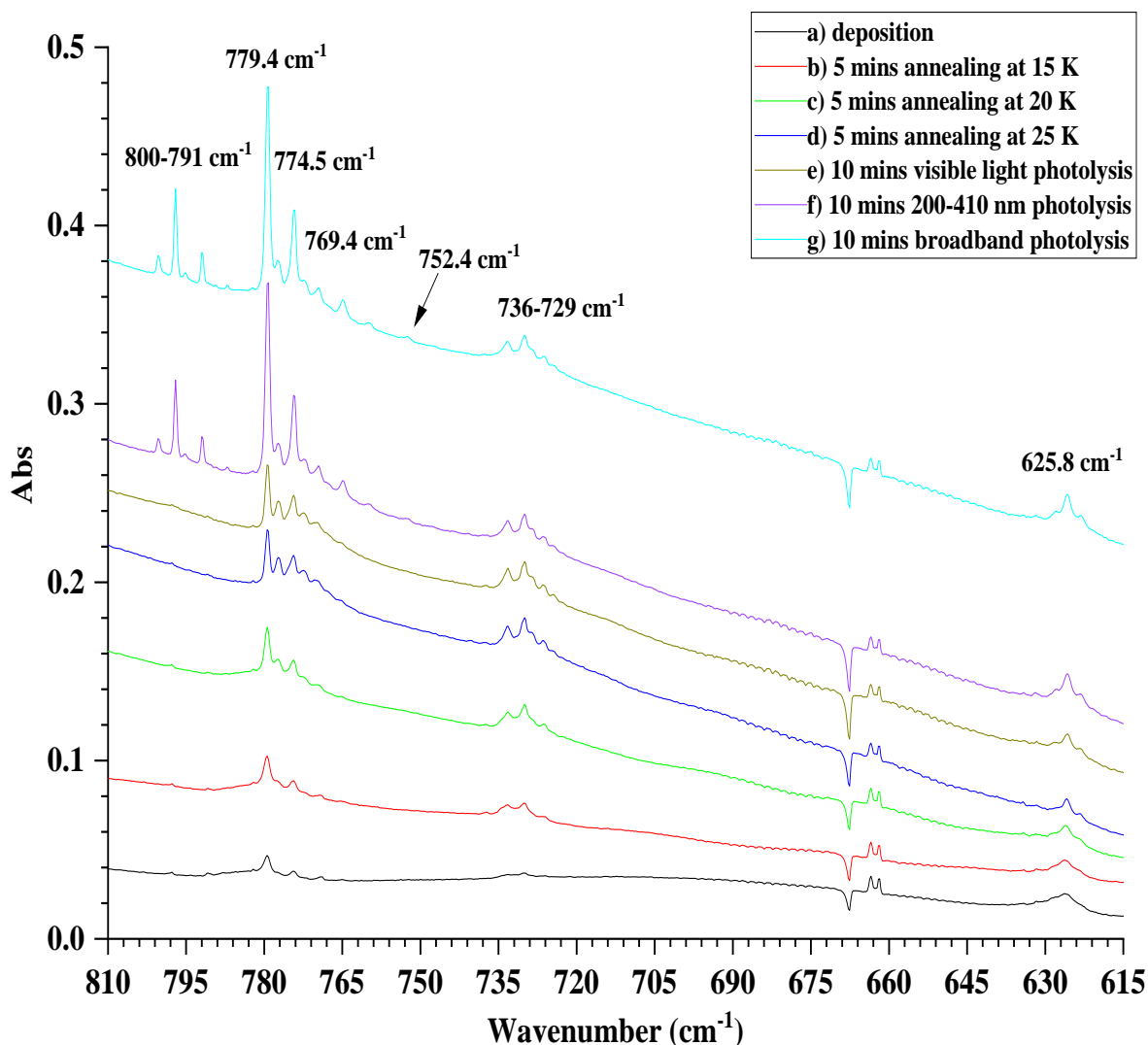
Figure 3.12: *FTIR spectra of atomic Ni in 0.5% F$_2$/Ar matrix (a) after deposition, (b) after 5 mins annealing at 15 K, (c) after 5 mins annealing at 20 K, (d) after 5 mins annealing at 25 k, (e) after 10 mins visible light photolysis, (f) after 10 mins 200–410 nm photolysis, (g) after 10 mins broadband photolysis.*

The formation of features between 800 and 791 cm^{-1} only after UV photolysis in both experiments confirms the suggestion that these absorption bands belong to higher valent nickel fluorides than NiF and NiF$_2$ species, as the excited atomic fluorine produced spreads throughout the argon matrix to react with nickel atoms. Furthermore, the persistent relative behaviour of the features between at 800 and 791 cm^{-1} throughout both different experiments, the annealing after the photolysis process, as they increased by photolysis and decreased by annealing (Figure 3.11), and the annealing followed by the

photolysis process as given in Figure 3.12, gives a crucial indication that peaks between 800 and 791 cm^{-1} attributed to same nickel fluoride species and not two different species. Also, the two tiny peaks at 752.4 and 747.5 cm^{-1} are only formed by UV irradiation and demolished by annealing to 20 K and they behave differently to the 800–791 cm^{-1} bands (Figure 3.11), indicating that these bands could be assigned to different species of high valent nickel fluorides than NiF and NiF$_2$ species.

3.2.4.1 Computational calculations

The computational calculations were performed using both B3LYP/def2tzvpp and B3LYP/6–311G(+d) within G09W in order to assign the peaks of nickel fluoride molecules. The calculated peak position of the nickel fluoride molecules and their characteristic isotope patterns at two different half−width 0.5 and 1.0 is displayed in Figure 3.13 below. In addition, the suggested infrared spectra for all nickel fluoride species at half−width 0.5 cm^{-1} using both B3LYP/def2tzvpp and B3LYP/6–311G(+d) are demonstrated in Figures 3.14 and 3.15, respectively. The calculated electronic ground state, the bond lengths, and the bond angles using B3LYP/def2tzvpp and B3LYP/6–311G(+d) are listed in Tables 3.3 and 3.4, respectively. The calculations of NiF and NiF$_2$ are relatively consistent with the experimental data achieved (Table 3.2). The geometrical shape of NiF$_2$ is suggested to be linear, same result was obtained using the experimental wavenumbers and SVFF bond angle calculator for XY$_2$ molecules assuming no interaction between stretching and bend modes.[26] Also, the formation energy of high– spin is lower than low–spin electronic configuration as previously reported.[52] The theoretical calculations using B3LYP/def2tzvpp for nickel trifluorides suggested two bands at 737.29 and 650.33 cm^{-1}, while the B3LYP/6–311G(+d) calculations proposed two vibrational frequencies at 720.33 and 636.6 cm^{-1}. These calculations indicate that the two very very weak bands obtained at 752.4 and 747.5 cm^{-1}, which disappeared on annealing to 20 K, might be due to NiF$_3$, but there was no sign of the lower wavenumber bands in the spectra. Also, the calculations indicated that high–spin NiF$_3$ is lower in energy than low–spin, and that it is in a Y–shaped configuration. The calculations of NiF$_4$ do not match with the experimental data obtained, the wavenumber values are a long way out of the set of bands observed between at 800 cm^{-1} and 791 cm^{-1}. NiF$_4$ calculated using B3LYP/def2tzvpp revealed two IR active Ni–F stretching modes at 696.37 and 649.86 cm^{-1} for a distorted tetrahedral geometry of NiF$_4$ and high–spin electronic configuration is more favourable than low–spin. Furthermore, starting the calculations with either high– spin tetrahedral or high–spin square planar configuration ends to tetrahedral geometry

with –0.017 kJ.mol^{-1} difference in energy. The theoretical data using B3LYP/6–311G(+d) sets proposed two peaks at 673.03 and 633.03 cm^{-1} and the configuration of NiF$_4$ as a distorted tetrahedral. In addition, the B3LYP/6–311G(+d) calculations indicated that the high–spin NiF$_4$ has lower energy than low–spin as well. The energy level diagram in Figure 3.16 shows the relative energies for different spin states of NiF$_4$ calculated using B3LYP/def2tzvpp as well as B3LYP/6–311G(+d) basis sets. The triplet state using B3LYP/def2tzvpp was distorted seesaw and square plane for B3LYP/6–311G(+d). The singlet states were distorted seesaw for B3LYP/def2tzvpp and B3LYP/6–311G(+d) basis sets. Moreover, the calculations of all suggested geometries for nickel fluoride molecules are inserted in appendix A. It is obvious that the separation between the ^{58}Ni and ^{60}Ni peaks in the "new" peaks is the same as those for NiF$_2$, and that the two sets of bands both are more likely belong to NiF$_4$ species which were in a square planar geometry.

Table 3.3: The calculated geometry of nickel fluoride species using B3LYP/def2tzvpp.

Assignments	Molecular structure	Electronic ground state	F–Ni–F Bond angles	Ni–F Bond lengths (Å)
NiF	—	—	—	1.758
NiF$_2$	Linear	$^3\Sigma_g$	180.0°	(1.715)×2
NiF$_3$	Y–shaped	^{4}A"	112.44°, 123.75°, 123.81°	(1.731)×2, 1.714
NiF$_4$	Tetrahedral	^{5}A	(111.26°)×2, 105.97°, 105.98°, 111.30 °, 111.21°	(1.717)×4

Table 3.4: The calculated geometry of nickel fluoride species using B3LYP/6–311G(+d).

Assignments	Molecular structure	Electronic ground state	F–Ni–F Bond angles	Ni–F Bond lengths (Å)
NiF	—	—	—	1.769
NiF$_2$	Linear	^{3}B$_1$	179.97°	(1.723)×2
NiF$_3$	Y–shaped	—	(123.53°)×2, 112.95°	(1.741)×2, 1.725
NiF$_4$	Tetrahedral	^{5}A	(106.23°)×2, 111.03°, 111.08°, 111.17°, 111.18°,	(1.747)×4
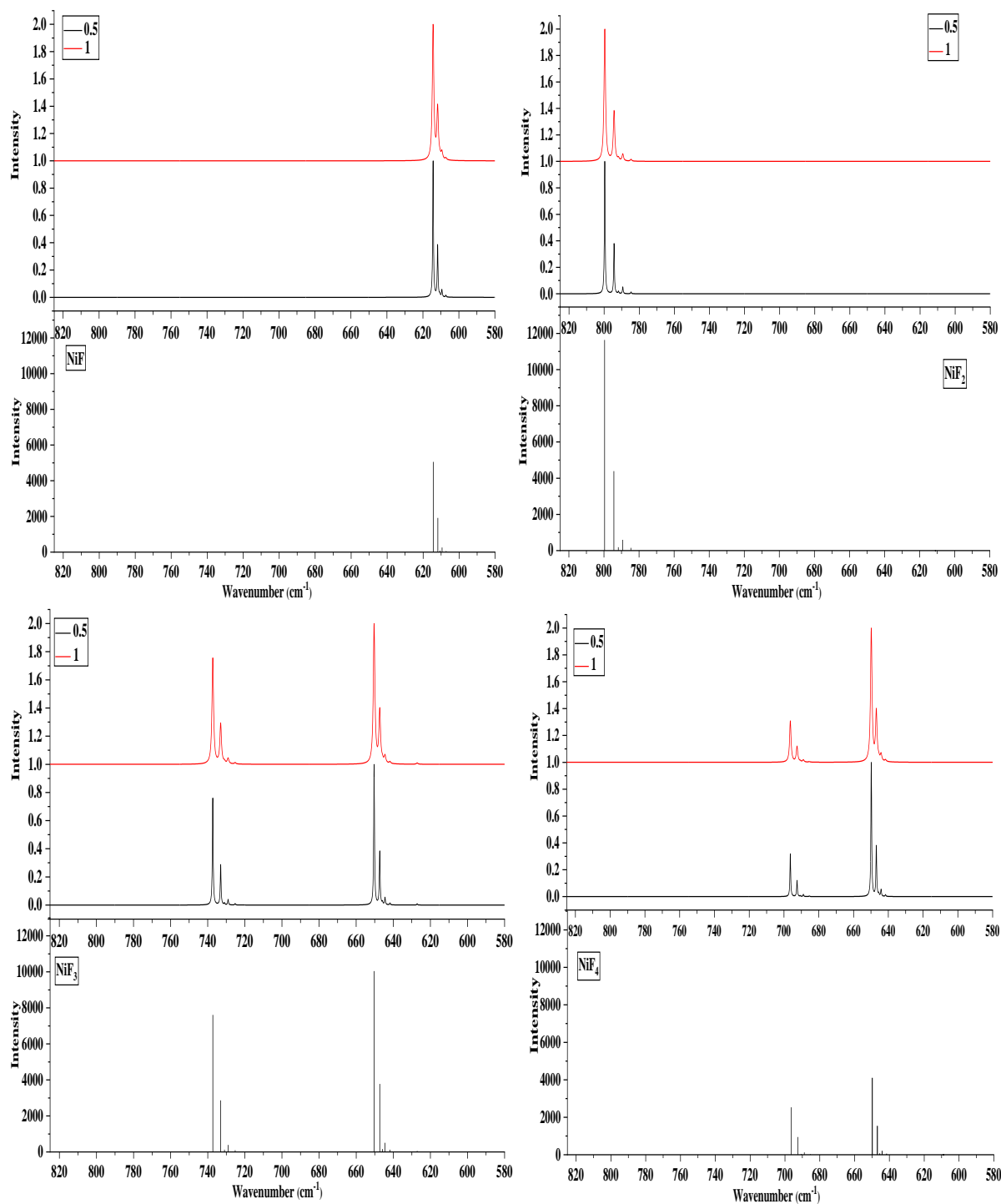
Figure 3.13: *Calculated (B3LYP/def2tzvpp) IR spectra of isotopes of Ni fluoride molecules at two different half−widths 0.5 and 1.0 cm⁻¹.*
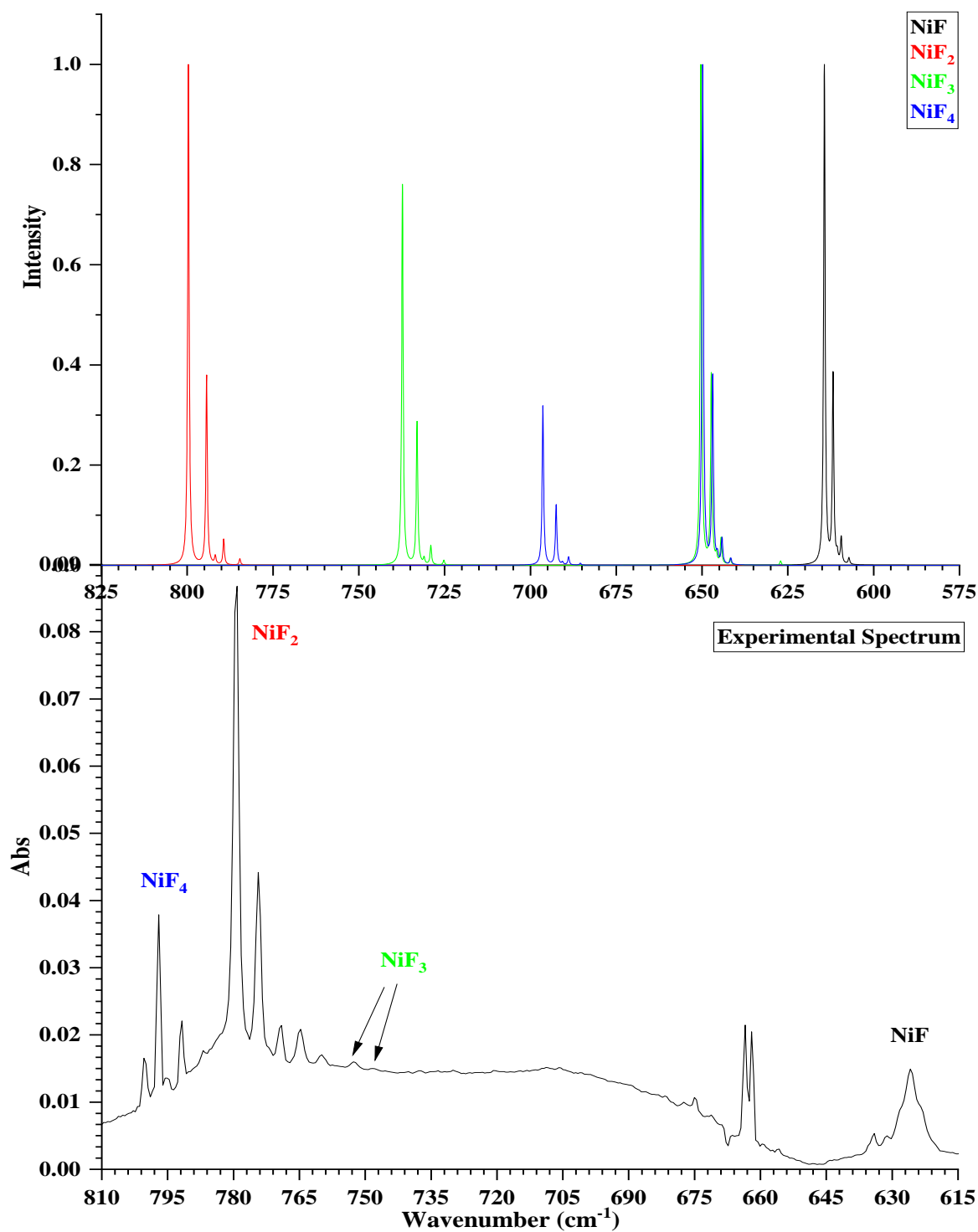
Figure 3.14: *Calculated (B3LYP/def2tzvpp) IR spectrum of all Ni fluoride molecules and their isotope patterns at half−width 0.5 cm⁻¹and experimental FTIR spectrum of atomic Ni in 0.5% F₂/Ar matrix.*
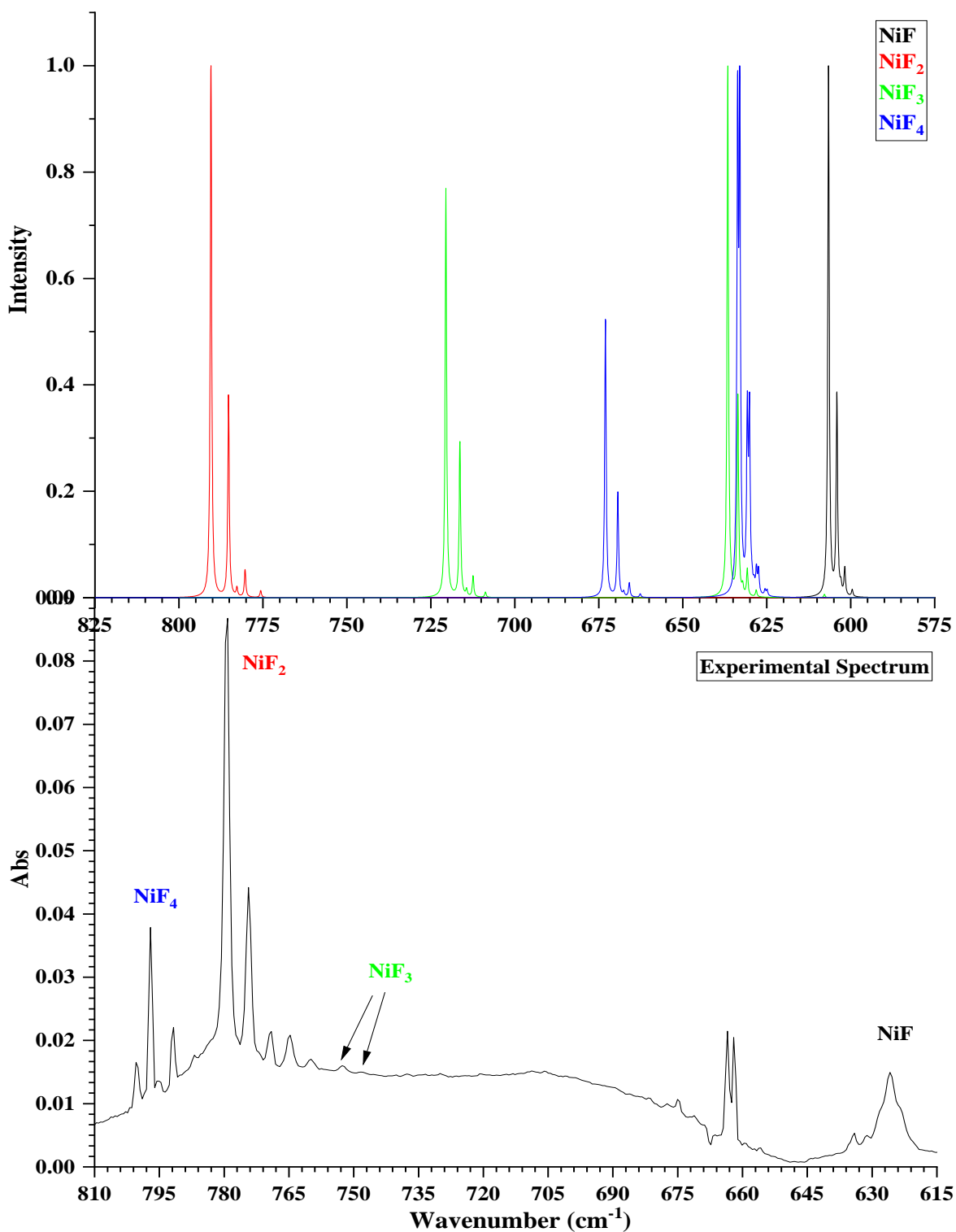
Figure 3.15: *Calculated (B3LYP/6–311G(+d)) IR spectrum of all Ni fluoride molecules and their isotope patterns at half−width 0.5 cm⁻¹ and experimental FTIR of atomic Ni in 0.5% F₂/Ar matrix.*
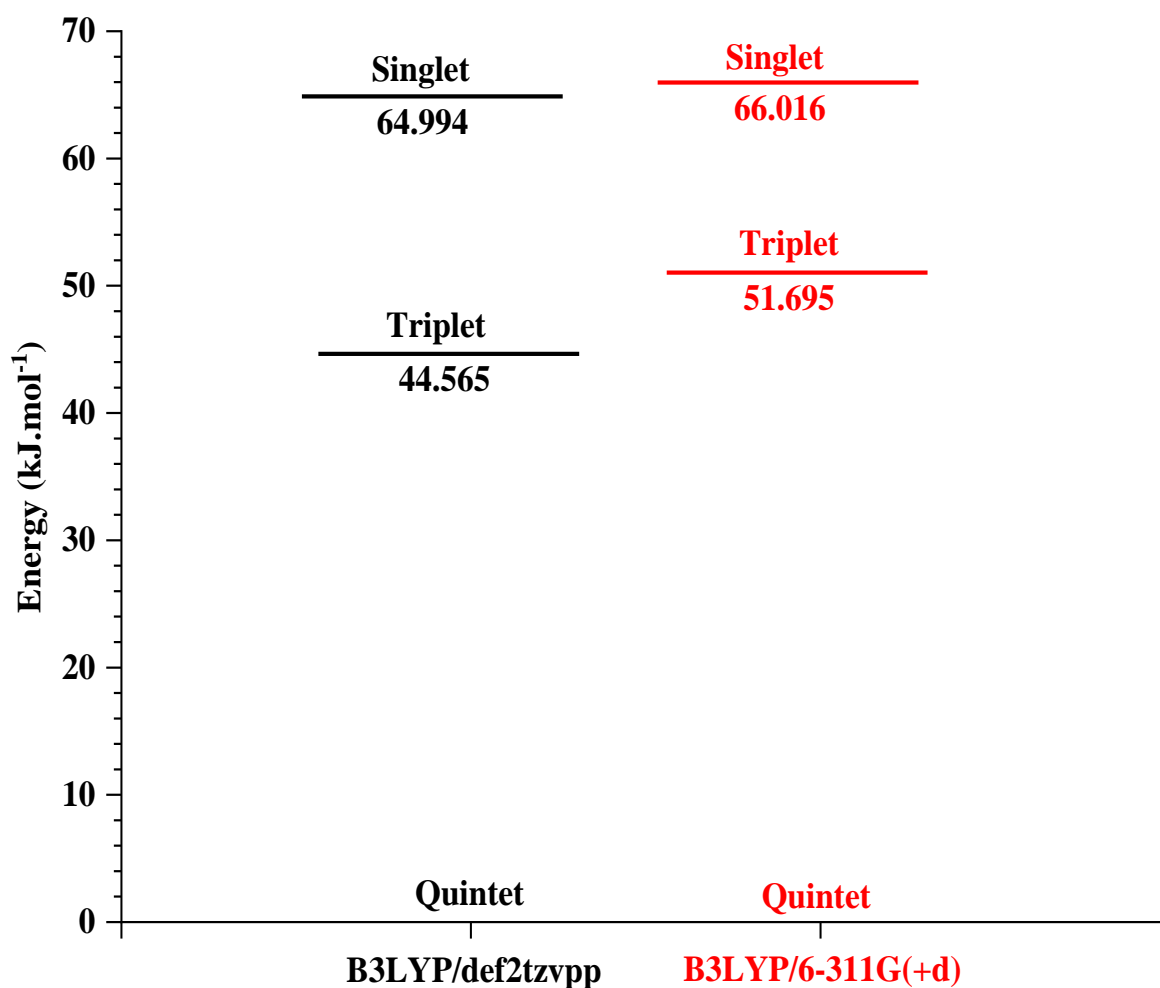
Figure 3.16: *Calculated energy level diagram for NiF₄ using (B3LYP/def2tzvpp) and (B3LYP/6–311G(+d)) sets.*

3.2.4.2 Thermodynamic study

Thermodynamic calculations have also been conducted to study the relative stability of nickel fluoride species. The overall reaction enthalpy data according to reaction between Ni atoms and F_2 molecules are given in Figure 3.17.The data reveal that NiF species have the highest energy, while NiF_4 species have the lowest energy, so it is the most favourable. Principally, more NiF_4 molecules are expected to be formed, if there are enough fluorine atoms. Furthermore, the stepwise reaction enthalpy was calculated as well. As demonstrated in Figure 3.18 below, the energy of NiF_3 lies above a line connecting NiF_2 and NiF_4 giving an indication that NiF_3 is unstable and could disproportionate into NiF_2 and NiF_4. In contrast, NiF_2 lies below a line connecting NiF and NiF_3, it would be expected that NiF and NiF_3 could comproportionate to form NiF_2 which is more stable. Thus, the features at 800.2, 797.1, 795.1, and 791.9 cm^{-1} are strongly suggested to be NiF_4 molecules and their isotope patterns.
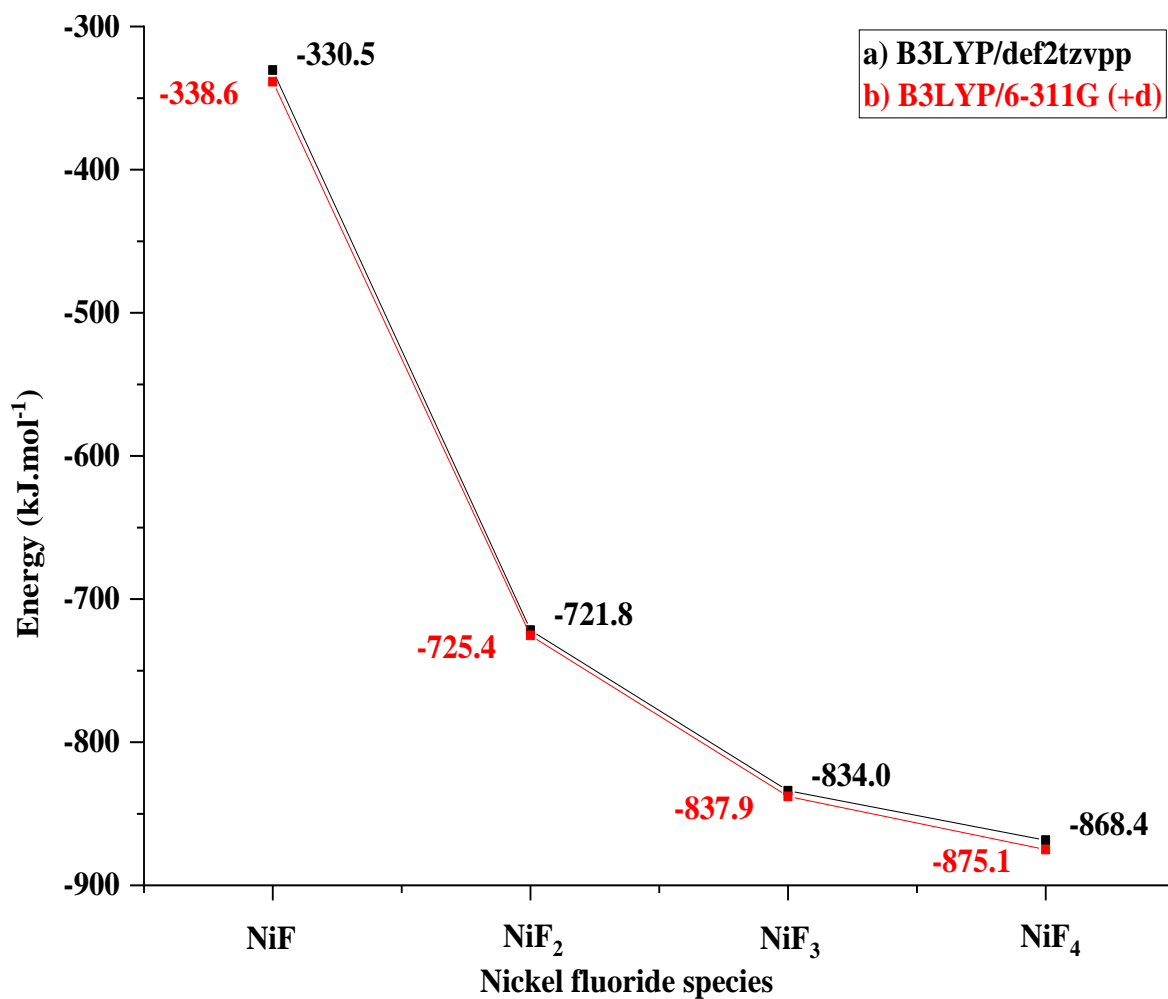
Figure 3.17: *Overall reaction enthalpy of NiF$_n$ species for the reaction of Ni atoms and F$_2$ molecules.*
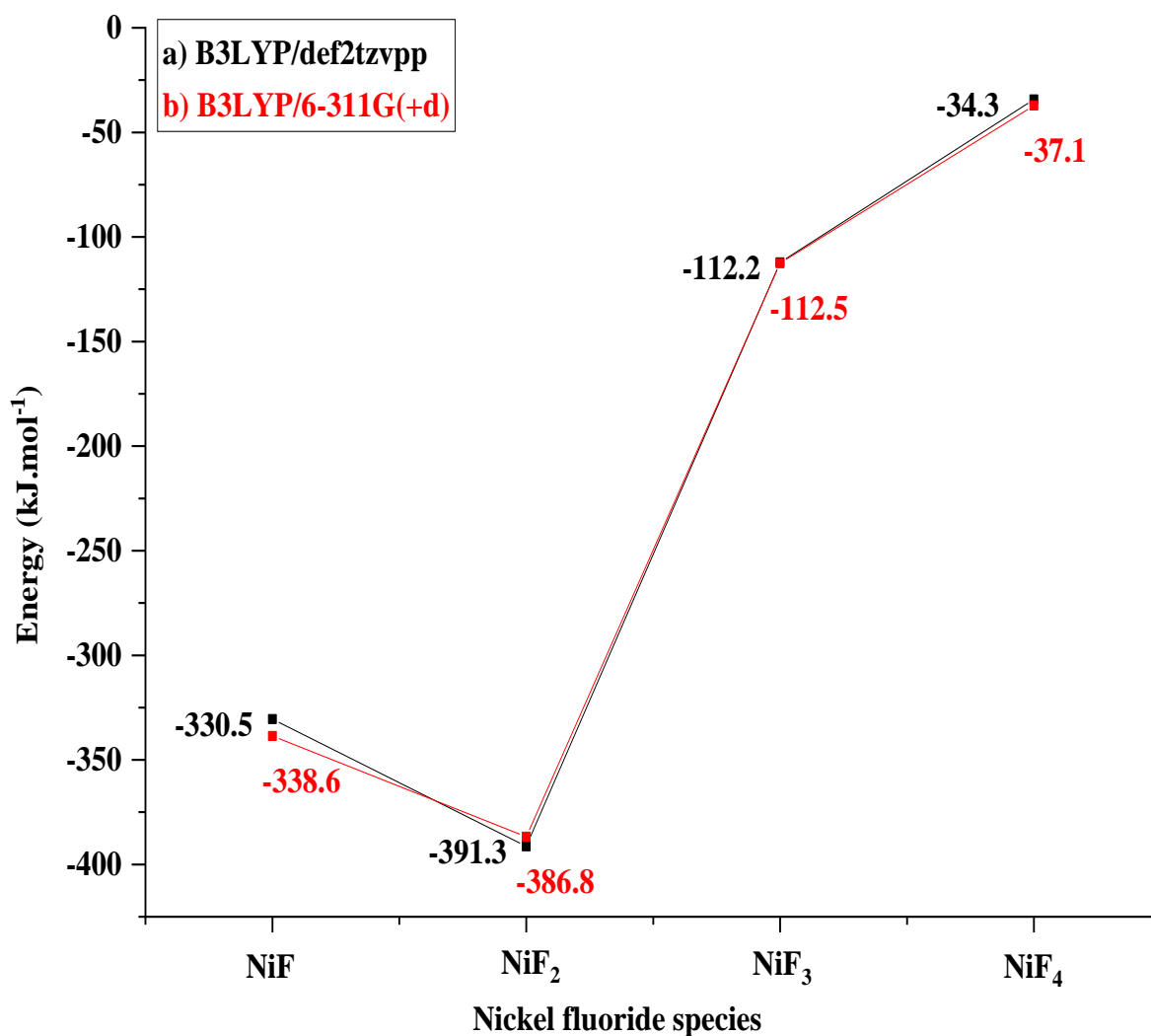
Figure 3.18: *Stepwise reaction enthalpy of NiF$_n$ species for the reaction of Ni atoms and F$_2$ molecules.*

3.3 Conclusion

UV–vis spectroscopy has been used to determine the optimum conditions for producing atomic nickel, and confirming the presence of two ground states that can be interchanged by photolysis and annealing. Matrix isolation infrared spectroscopy was employed to characterise the vibrational frequencies of the nickel fluoride species isolated in argon rare–gas matrix.

The UV/vis spectrum has two major peaks at 30250 and 31380 cm^{-1} and a weak peak at 32850 cm^{-1}, followed by two strong overlapped peaks at 34850 and 35300 cm^{-1} and a tiny peak at 37500 cm^{-1}. In addition, a broad peak was found at 43230 cm^{-1} followed by a weak peak at 46280 cm^{-1}. These peaks are assigned to the isolation of Ni atoms in a solid argon matrix matrix, which has been previously documented.[27-29] No absorptions were found in the region of 18900–22500 cm^{-1}; which was reported earlier to indicate the

isolation of diatomic and triatomic nickel in a solid argon matrix. Photolysis and annealing up to different temperature did not provide evidence for the formation of Ni_2 and Ni_3 species in argon matrix. The optical spectra of nickel isolated in solid argon matrices doped with low concentration of fluorine were recorded. The same peaks formerly observed in the spectrum of nickel were found. The intensity of all peaks decreased dramatically when the broadband photolysis was applied and two broad peaks at 46000 and 48950 cm^{-1} were formed and grew after annealing at 15 and 20 K, followed by a slight diminish on heating the solid matrix to 25, 30, and 35 K. The vital change at 46000 and 48950 cm^{-1} observed only in UV/vis spectra of Ni atoms isolated in 1% F_2/Ar gas mixture on annealing after photolysis process is considered a crucial evidence for the interaction of Ni and fluorine atoms in solid argon matrix and the formation nickel fluoride molecules.

Furthermore, the data provided by FTIR later are substantially considered. Bands observed between 779.4 cm^{-1} and 769.4 cm^{-1} are assigned to asymmetric stretching modes of NiF_2 with its various isotope patterns. These data are completely consistent with data published before. A peak observed at 625.8 cm^{-1} is assigned to matrix isolated NiF supported by the computational calculations, this peak has not been previously reported. Photolysis using different wavelengths of irradiation led to increasing the intensity of absorption bands of nickel fluorides species. The peaks observed between 729 cm^{-1} and 736 cm^{-1} accompanied with two shoulders at 772.4 and 777.3 cm^{-1} after annealing are related to the dimer form of NiF_2. Furthermore, the two tiny bands obtained at 752.4 and 747.5 cm^{-1} after photolysis that disappeared on annealing are also due to high–valent nickel fluorides, the computational calculations attributed these band to NiF_3. Weak peaks obtained at 800 cm^{-1} and 791 cm^{-1} after photolysis and decay by annealing are due to the presence of high–valent nickel fluorides in solid argon matrix as well. The persistent relative behaviour of the features at 800–791 cm^{-1} indicates that they belong to the same nickel fluoride species and not two different species. The calculations data for NiF_4 using two different basis sets do not match with the experimental data obtained, the wavenumber values are a long way out of the set of bands observed between at 800–791 cm^{-1}. It is obvious that the separation of the two sets of peaks recorded between at 800 cm^{-1} and 791 cm^{-1} was consistent with the separation between the ^{58}Ni and ^{60}Ni in a linear NiF_2 unit, and that the two sets of bands both are more likely due to high–spin NiF_4 species which were in a square planar geometry.

3.4 Summary

First observation of NiF in solid Ar matrix; it was identified by band obtained at 625.8 cm^{-1}. First observation of matrix–isolated NiF$_3$ at identified by bands at 752.4 and 747.5 cm^{-1}. Theoretic studies suggested this molecule adopts a distorted trigonal planar geometry. These two tiny bands were obtained after photolysis and diminished by annealing. Moreover, first observation of NiF$_4$ in solid Ar matrix, which was identified by bands between 800–791 cm^{-1}; calculations did not help to resolve the geometry between tetrahedral and square planar cases.

3.5 References

1. C. Focsa, C. Dufour and B. Pinchemel, *J. Mol. Spectrosc.*, 1997, **182**, 65–71.
2. Y. Chen, J. Jin, C. Hu, X. Yang, X. Ma and C. Chen, *J. Mol. Spectrosc.*, 2000, **203**, 37–40.
3. J. Jin, Y. Chen, X. Yang, Q. Ran and C. Chen, *J. Mol. Spectrosc.*, 2001, **208**, 18–24.
4. J. Jin, Q. Ran, X. Yang, Y. Chen and C. Chen, *J. Phys. Chem. A*, 2001, **105**, 11177-11182.
5. B. Pinchemel, T. Hirao and P. F. Bernath, *J. Mol. Spectrosc.*, 2002, **215**, 262–268.
6. M. Benomier, A. Van Groenendael, B. Pinchemel, T. Hirao and P. F. Bernath, *J. Mol. Spectrosc.*, 2005, **233**, 244-255.
7. Y. Krouti, T. Hirao, C. Dufour, A. Boulezhar, B. Pinchemel and P. F. Bernath, *J. Mol. Spectrosc.*, 2002, **214**, 152–174
8. C. Koukounas and A. Mavridis, *J. Phys. Chem. A*, 2008, **112**, 11235–11250.
9. D. E. Milligan, M. E. Jacox and J. D. McKinley, *J. Chem. Phys.*, 1965, **42**, 902-905.
10. J. W. Hastie, R. H. Hauge and J. L. Margrave, *J. Chem. Soc. D*, 1969, 1452-1453.
11. J. L. Margrave, J. W. Hastie and R. H. Hauge, *Amer. Chem. Soc., Div. Petrol. Chem., Prepr.*, 1969, **14**, E11-E13.
12. J. W. Hastie, R. H. Hauge and J. L. Margrave, *High Temp. Sci.*, 1969, **1**, 76-85.
13. O. M. Wilkin, N. Harris, J. F. Rooms, E. L. Dixon, A. J. Bridgeman and N. A. Young, *J. Phys. Chem. A*, 2018, **122**, 1994-2029.
14. D. A. Van Leirsburg and C. W. DeKock, *J. Phys. Chem.*, 1974, **78**, 134-142.
15. S. Besnainou and J. L. Whitten, *J. Am. Chem. Soc.*, 1978, **100**, 3692-3698.
16. V. N. Bukhmarina, A. Y. Gerasimov, Y. B. Predtechenskii and V. G. Shklyarik, *Opt. Spektrosk.*, 1988, **65**, 876-881.
17. A. V. Popov, *Russ. J. Phys. Chem.*, 2005, **79**, 732-735.
18. P. Mondal and W. Domcke, *J. Phys. Chem. A*, 2014, **118**, 3726-3734.
19. P. Mondal, D. Opalka, L. V. Poluyanov and W. Domcke, *J. Chem. Phys.*, 2012, **136**, 084308.
20. C. Shen, L. C. Chacón, N. Rosov, S. H. Elder, J. C. Allman and N. Bartlett, *Comptes Rendus de l'Academie des Sciences - Series IIc: Chemistry*, 1999, **2**, 557-563.
21. A. L. Hector, E. G. Hope, W. Levason and M. T. Weller, *Z. Anorg. Allg. Chem.*, 1998, **624**, 1982-1988.
22. B. Žemva, K. Lutar, L. Chacón, M. Fele-Beuermann, J. Allman, C. Shen and N. Bartlett, *J. Am. Chem. Soc.*, 1995, **117**, 10025-10034.
23. B. Žemva, K. Lutar, A. Jesih, W. J. Casteel and N. Bartlett, *J. Chem. Soc., Chem. Commun.*, 1989, 346-347.
24. M. Tramsek and B. Žemva, *Acta Chim. Slov.*, 2002, **49**, 209-220.
25. A. V. Wilson, A. J. Roberts and N. A. Young, *Angew. Chem., Int. Ed.*, 2008, **47**, 1774-1776.
26. M. Moskovits and G. A. Ozin, *Cryochemistry, Wiley-Interscience, New York*, 1976.
27. D. M. Mann and H. P. Broida, *J. Chem. Phys.*, 1971, **55**, 84-94.
28. W. E. Klotzbücher and G. A. Ozin, *Inorg. Chem.*, 1976, **15**, 292-295.
29. A. B. Anderson, *J. Chem. Phys.*, 1977, **66**, 5108-5111.
30. M. Moskovits and J. E. Hulse, *J. Chem. Phys.*, 1977, **66**, 3988-3994.
31. F. Ahmed and E. R. Nixon, *J. Chem. Phys.*, 1979, **71**, 3547-3549.
32. M. Vala, M. Eyring, J. Pyka, J. C. Rivoal and C. Grisolia, *J. Chem. Phys.*, 1985, **83**, 969-974.

33. R. Grinter and D. R. Stern, *J. Chem. Soc., Faraday Trans. 2*, 1983, **79**, 1011-1020.
34. W. Schroeder, R. Grinter, W. Schrittenlacher, H. H. Rotermund and D. M. Kolb, *J. Chem. Phys.*, 1985, **82**, 1623-1630.
35. C. P. Barrett, R. G. Graham and R. Grinter, *Chem. Phys.*, 1984, **86**, 199-204.
36. T. A. Cellucci and E. R. Nixon, *J. Chem. Phys.*, 1984, **81**, 1174-1177.
37. W. Schrittenlacher, W. Schroeder, H. H. Rotermund and D. M. Kolb, *Chem. Phys. Lett.*, 1984, **109**, 7-12.
38. M. Tomonari, H. Tatewaki and T. Nakamura, *J. Chem. Phys.*, 1986, **85**, 2875-2884.
39. G. H. Jeong and K. J. Klabunde, *J. Chem. Phys., Vol.*, 1989, **91**, 1958-1971.
40. B. Breithaupt, J. E. Hulse, D. M. Kolb, H. H. Rotermund, W. Schroeder and W. Schrittenlacher, *Chem. Phys. Lett.*, 1983, **95**, 513-516.
41. J. F. Rooms, A. V. Wilson, I. Harvey, A. J. Bridgeman and N. A. Young, *Phys. Chem. Chem. Phys.*, 2008, **10**, 4594-4605.
42. J. Feld, H. Kunttu and V. A. Apkarian, *J. Chem. Phys.*, 1990, **93**, 1009-1020.
43. E. Y. Misochko, A. V. Akimov and C. A. Wight, *Chem. Phys. Lett.*, 1997, **274**, 23-28.
44. O. M. Wilkin, N. Harris, J. F. Rooms, E. L. Dixon, A. J. Bridgeman and N. A. Young, *J. Phys. Chem. A*, 2018, **122**, 1994-2029.
45. P. D. Mallinson, D. C. Mckvan, J. H. Holloway and I. A. Oxto, *Spectrochim. Acta, Part A*, 1975, **31A**, 143-159.
46. L. Manceron, M. E. Alikhani and H. A. Joly, *Chem. Phys.*, 1998, **228**, 73–80.
47. A. V. Cherevatova, T. D. Kolomiistova, D. N. Shchepkin, K. G. Tokhadze, Z. Mielke, S. Coussan and P. Roubin, *J. Mol. Spec.*, 2006, **238**, 64-71.
48. R. L. Redington and D. E. Milligan, *J. Chem. Phys.*, 1962, **37**, 2162-2166.
49. R. L. Redington and D. E. Milligan, *J. Chem. Phys.*, 1963, **39**, 1276-1284.
50. S. B. Osin, D. I. Davlyashin and J. S. Ogden, *Russ. J. Phys. Chem.*, 2001, **75**, 294-302.
51. E. Y. Misochko, V. A. Benderskii, A. U. Goldschleger, A. V. Akimov and A. F. Shestakov, *J. Am. Chem. Soc.*, 1995, **117**, 11997-11998.
52. S. G. Wang and W. H. E. Schwarz, *J. Chem. Phys.*, 1988, **109**, 7252-7262.

Chapter 4

Cobalt fluorides

4.1 Introduction

A number of studies were carried out to investigate CoF molecules. DeVore *et al.* used electron spin resonance (ESR) technique to study the first row metal fluorides molecules at cryogenic temperature, however they could not succeed to investigate CoF molecules.[1] Adam *et al.* used laser induced fluorescence technique to investigate CoF in gas phase; vibrational frequency observed at 662.6 cm^{-1} was assigned to CoF.[2] One year later, CoF was prepared by heating CF_4 and Co metal at 2300 °C; the FTIR spectrum was collected on the range 9000$-$12500 cm^{-1}. Three bands were recorded at 10161, 10289, and 10340 cm^{-1} related to the highest transition states.[3] Some studies have been undertaken to identify the electronic ground state and excited states of CoF and also confirmed the vibrational frequency of CoF previously detected at 662.6 cm^{-1}.[4-8] Moreover, a theoretical study conducted by Popov calculated the vibrational frequency of CoF at 689 cm^{-1}, which corresponded to experimental data reported previously.[2] In 2008, a computational study performed by Koukounas and Mavridis using two different basis sets and vibrational multireference (MRCI) and coupled$-$cluster RCCSD(T) methods suggested that the binding energy for the ground state of CoF is 385$-$410 kJ.mol^{-1} (92$-$98 kcal mol^{-1}) and the equilibrium bond length was 1.736 Å.[9] Furthermore, no published studies were found for molecular matrix isolated CoF.

Hastie *et al.* employed matrix isolation IR spectroscopy to study CoF_2 molecules. The stretching mode of CoF_2 molecules in solid argon matrix was located at 723.1 cm^{-1}, while the absorption feature at 745.7 cm^{-1} was assigned to CoF_2 species trapped in a neon matrix.[10-12] In 1988, Bukhmarina *et al.* reinvestigated the CoF_2 molecules isolated in noble gas matrices using IR and Raman spectroscopy. The vibrational band of cobalt difluoride was detected at 722.9 cm^{-1} in an Ar matrix and at 745.6 cm^{-1} in a matrix of Ne.[13] In 2002, XRD was employed to investigate the formation of CoF_2 throughout thermal decomposition of CoF_3 indicating the generation of CoF_2 molecules.[14]

Cobalt trifluoride is considered in many research papers because of its use as a fluorinating agent for many organic components.[15] Girichev *et al.* used the electron diffraction technique to obtain the geometry of CoF_3 molecules. The study claimed that

CoF$_3$ has D$_{3h}$ planar symmetry.[16] This conclusion was consistent with IR and Raman spectroscopic study that defined the geometry of CoF$_3$ as D$_{3h}$ symmetry.[17]

CoF$_4$ was prepared by interaction of TbF$_4$ with CoF$_3$ at high temperature.[18] Mass spectrometry as well as FTIR spectroscopy was employed to detect CoF$_4$ species in the gas phase. An IR absorption band detected at 767.8 cm^{-1}, not associated with CoF$_2$ or CoF$_3$ molecules, and was assigned to CoF$_4$ in an Ar matrix. In spite of evident achievement in the formation of CoF$_4$, the study was not able to identify the molecular arrangement of CoF$_4$ molecules.[19]

The aim of the work in this chapter is to synthesise CoF and CoF$_4$ molecules in a solid Ar matrix, and identify the structure CoF$_4$ molecules.

4.2 Results and Discussion

4.2.1 UV/Vis Spectra of Co in Ar

The melting point of cobalt is 1495 °C, while the temperature required to get a vapour pressure of 1×10^{-3} torr is 1382 °C.[20] Evaporation of cobalt atoms from a filament as described in chapter 2 was performed using 30 A and 1.046 V and the argon gas was introduced at a pressure of 2×10^{-6} mbar and the deposition temperature was 11.5 K. The UV/vis spectrum in Figure 4.1a was gathered after 90 minutes of deposition using the above conditions. Two peaks were found at 29600 cm^{-1} and 30750 cm^{-1} accompanied by three peaks at 34300 cm^{-1}, 35700 cm^{-1}, and 36980 cm^{-1}. In addition, a weak peak at 39850 cm^{-1}, medium peak at 40800 cm^{-1}, weak peak at 41850 cm^{-1}, and a strong broad band at 42875 cm^{-1} followed by weak peak at 45000 cm^{-1} were also observed as listed in Table 4.1. These bands were previously detected in the deposition of atomic cobalt in an Ar matrix.[21, 22] In fact, the previous studies revealed that the deposition solely of atomic cobalt is only possible at temperatures of 6.0–4.2 K, while Co$_2$ as well as Co$_3$ species are observed on conducting deposition at temperature higher than 6.0 K.[22] The peaks in the range of 35714–37037 cm^{-1} are attributed to the formation of Co$_2$ species isolated in solid argon matrix and the bands at 29411–31250 cm^{-1} are due to diatomic and triatomic Co species as revealed previously.[22] It is noteworthy that the cryostat used through these experiments was not able to cool down the deposition window to 4.2 K, where it is limited to 10 K. As a consequence, it is likely that the matrix contains a mixture of Co, Co$_2$, and Co$_3$ isolated in solid Ar matrix. The electronic configuration for Co atoms in the ground state is ^{4}F$_{9/2}$ (3d^{7}4s^2). The matrix was exposed to 10 minutes visible light photolysis. As

seen in Figure 4.1b; the visible light photolysis has no effect on the matrix. The UV–visible absorption data in Figure 4.c was recorded after 10 minutes of 200–410 nm photolysis. It shows that the peaks at 29600, 30750, 35700, and 36980 cm^{-1} were reduced in intensity. The matrix was further photolysed for 10 minutes of broadband photolysis, the spectrum located in Figure 4.1d demonstrates a partial decay in the intensity of peaks at 29600, 30750, 39850, 41850 cm^{-1}. Additionally, peaks located at 35700 and 36980 cm^{-1} disappeared. This behaviour is related to the photodissociation of diatomic cobalt and converting to Co atoms, so the intensity of bands at 29600, 30750, 35700, and 36980 cm^{-1} was diminished; and at the same time photoaggregation of atomic cobalt to form dimeric Co_2 species, thus the bands at 39850, 41850 cm^{-1} were decreased as well. This behaviour is in line with a previous study performed by Ozin and Hanlan.[22] Figure 4.1e illustrates the UV/vis spectrum upon exposure to extra 10 minutes of visible light photolysis. As expected essentially no change was observed.

Table 4.1: Absorptions (cm^{-1}) observed and previous studies of Co atoms isolated in Ar matrix.

Experiment	Ref [22]	Ref [21]	Assignments/ Ground state
29600 cm^{-1}	29498 cm^{-1}	29710 cm^{-1}	Co_2, Co_3
30750 cm^{-1}	30769 cm^{-1}	30290 cm^{-1}	Co_2, Co_3
34300 cm^{-1}	34246 cm^{-1}	34260 cm^{-1}	$y^4F°_{9/2} \leftarrow {}^4F_{9/2}$
35700 cm^{-1}	35087cm^{-1}	35160 cm^{-1}	Co_2
36980 cm^{-1}	—	—	Co_2
39850 cm^{-1}	39682 cm^{-1}	39750 cm^{-1}	$y^4D°_{7/2} \leftarrow {}^4F_{9/2}$
40800 cm^{-1}	40485 cm^{-1}	40840 cm^{-1}	$x^4D°_{7/2} \leftarrow {}^4F_{9/2}$
41850 cm^{-1}	41841 cm^{-1}	41740 cm^{-1}	$x^4F°_{9/2} \leftarrow {}^4F_{9/2}$
42875 cm^{-1}	42735 cm^{-1}	42720 cm^{-1}	$w^4F°_{7/2} \leftarrow {}^4F_{9/2}$
45000 cm^{-1}	45045 cm^{-1}	45030 cm^{-1}	$w^4F°_{9/2} \leftarrow {}^4F_{9/2}$
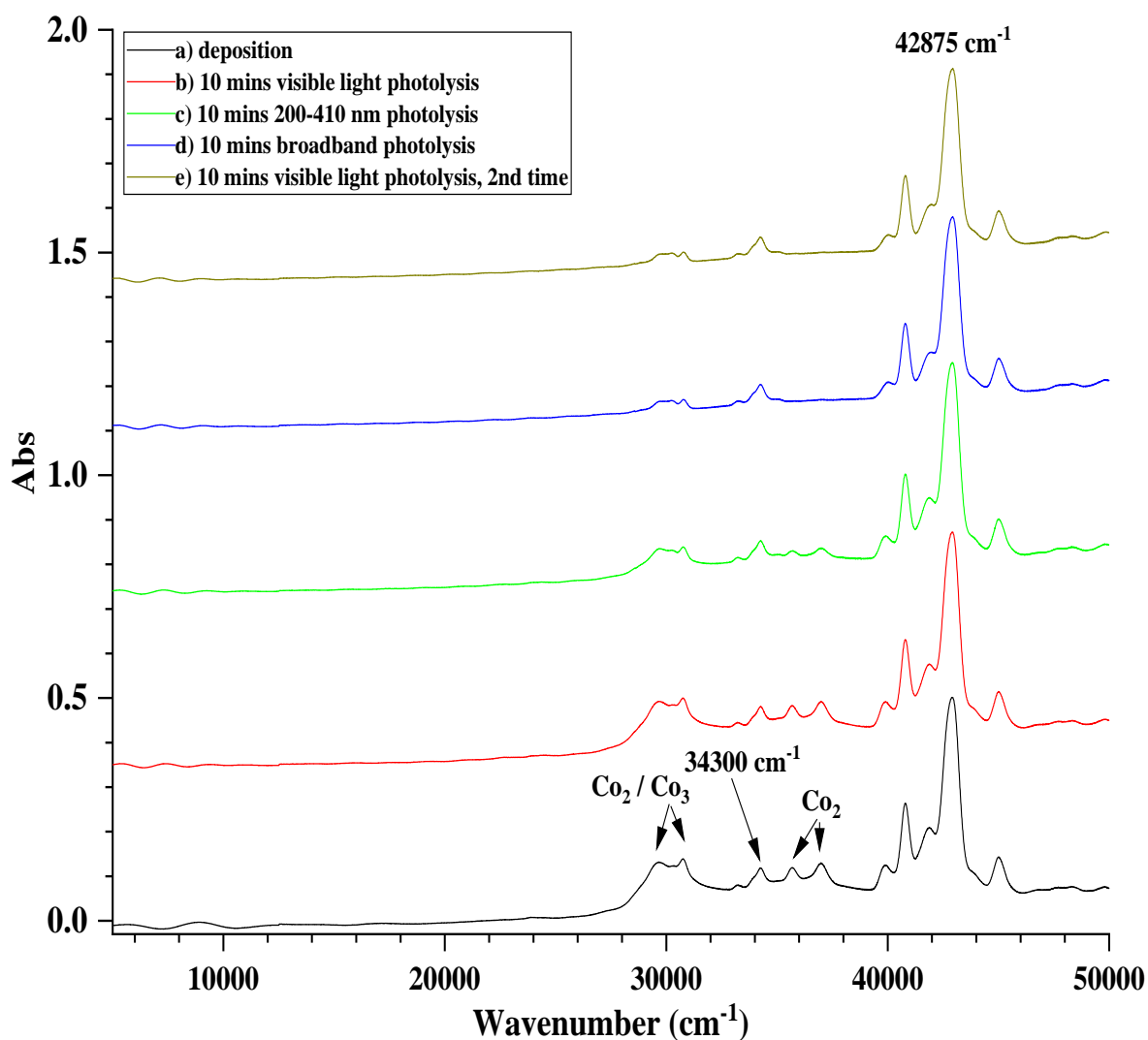
Figure 4.1: *UV/Vis spectra of Co in an Ar matrix (a) after deposition, (b) after 10 mins visible light photolysis, (c) after 10 mins 200–410 nm photolysis, (d) after 10 mins broadband photolysis, (e) after further 10 mins visible light photolysis.*

Figure 4.2b displays the matrix after 5 minutes annealing to 15 K; no changes in peak intensities were observed. The matrix was annealed to 20 K for 5 minutes and the spectrum is given in Figure 4.2c. The intensity of the peaks at 40800 cm^{-1}, 41850 cm^{-1}, and 42875 cm^{-1} decreased. The data in Figure 4.2d were recorded after 5 minutes of warming the matrix up to 25 K; a slight decrease in intensity of all peaks was observed. After 5 minutes of further annealing at 30 K; as is demonstrated in Figure 4.2e, all peaks were diminished and the spectrum showed great scattering. The matrix was warmed up to 35 K for 5 minutes, the absorption bands at 29600, 30750, 34300, 39850, 41850 cm^{-1} disappeared, while peaks located at 40800, 42875, and 45000 cm^{-1} shrank, as observed in Figure 4.2f. This is due to the evaporation of the solid Co/Ar mixture. Moreover, the spectrum became significantly scattered.
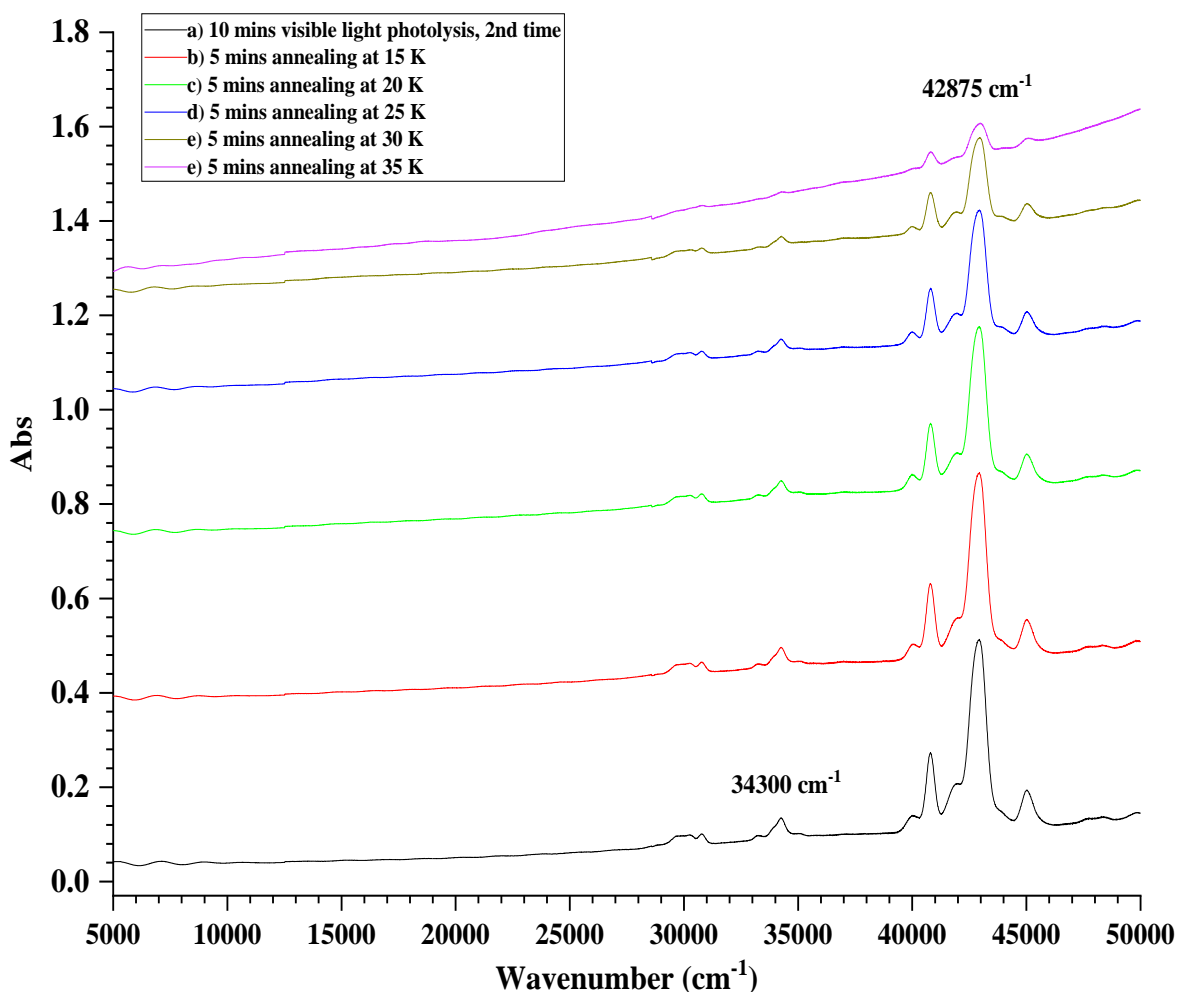
Figure 4.2: *UV/Vis spectra of Co in an Ar matrix (a) after further 10 mins visible light photolysis, (b) after 5 mins annealing at 15 K, (c) after 5 mins annealing at 20 K, (d) after 5 mins annealing at 25 K, (e) after 5 mins annealing at 30 K, (f) after 5 mins annealing at 35 K.*

4.2.2 UV/Vis Spectra of Co in 1% F$_2$/Ar

1% F$_2$ in Ar gas mixture was introduced at a pressure of 2×10^{-6} mbar and the temperature of the deposition surface was 11.5 K. Thermal evaporation of the cobalt filament was achieved using 30.5 A and 1.119 V. This process was carried out for 110 minutes and the spectrum is presented in Figure 4.3a. The same peaks previously observed in the spectrum of Co/Ar were found; two peaks at 29600 and 30750 cm^{-1} followed by three sequential bands at 34300, 35700, and 36980 cm^{-1}, accompanied by a weak peak at 39850 cm^{-1}, medium peak at 40800 cm^{-1}, weak peak at 41850 cm^{-1}, strong broad band at 42875 cm^{-1}, and weak peak at 45000 cm^{-1}. The photolysis process was performed to investigate the reaction between cobalt species and excited fluorine atoms. Figure 4.3b represents the matrix after 10 minutes of visible light photolysis; there is no substantial change in intensity of the absorption bands observed. The UV/vis spectrum after 10 minutes of 200–410 nm photolysis is shown in Figure 4.3c, the peaks at 29600,

30750, 34300, 35700, 36980, and 42875 cm^{-1} decreased. The solid matrix was also exposed to broadband photolysis for 10 minutes as given in Figure 4.3d. All peaks shrank, whereas the peak at 35700 cm^{-1} disappeared. The data in Figure 4.3e indicate that a further 10 minutes of visible light photolysis has no influence on the matrix. It is apparent the different behaviour in presence of F_2/Ar mixture, where all bands were reduced in intensity after photolysis comparing with the decrease in intensity of only peaks belong to Co_2 and Co_3 species in Co/Ar matrix in absence of F_2. It is reasonable that the photolysis process produces mobile fluorine atoms, which spread throughout the argon matrix to the sites hosting cobalt. Therefore, the decrease in intensity of all peaks could be on account of formation of cobalt fluoride molecules in the matrix of solid Ar.
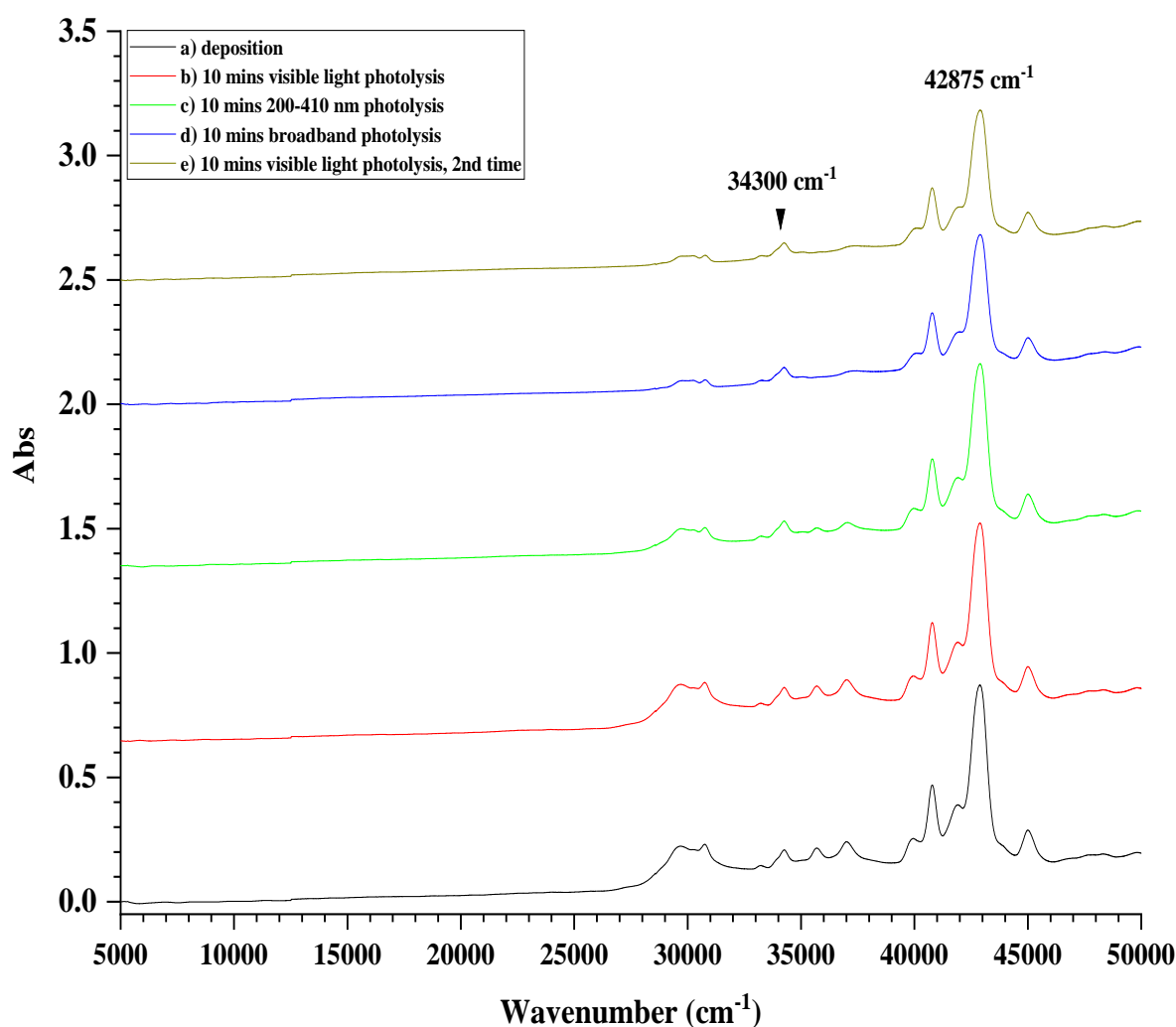
Figure 4.3: *UV/Vis spectra of Co in a 1% F$_2$/Ar matrix (a) after deposition, (b) after 10 mins visible light photolysis, (c) after 10 mins 200–410 nm photolysis, (d) after 10 mins broadband photolysis, (e) after further10 mins visible light photolysis.*

Annealing of the matrix was undertaken directly after the photolysis process so that as the matrix becomes soft, the trapped species can reorient, react with each other or decompose. Annealing the matrix to 15 K for 5 minutes has no effect on the behaviour of

bands as indicated in Figure 4.4b. Upon 5 minutes of heating the matrix to 20 K, the UV/Vis spectrum in Figure 4.4c shows that all peaks became less intense. A further decline in intensity of all peaks was observed in Figure 4.4d after annealing the matrix to 25 K for 5 minutes. Figure 4.4e demonstrates the matrix after 5 minutes of annealing at 30 K, the intensity of all peaks was reduced again, and the peak at 36980 cm^{-1} disappeared. The optical spectrum presented in Figure 4.4f was recorded after warming up the solid matrix to 35 K for minutes, it demonstrates that the intensity of the absorption peaks located at high wavenumbers 40800, 42875, and 45000 cm^{-1} demolished apparently. Meanwhile, peaks at 29600, 30750, 34300, 39850, 41850 cm^{-1} disappeared. Additionally, the amount of scattering in the spectra were gradually increased as the baseline has risen over time. Similar observations have achieved by using 0.5% F_2 in argon gas matrix. Unfortunately, the data gathered from this study do not provide strong evidence for the formation of cobalt fluorides species, even though it was expected that photolysis and annealing processes might lead to an increase/decrease in intensity of peaks and formation of new bands. In previous work, no optical study was performed for investigating CoF_2.[21-23] Using an optical electronegativity value of 3.9 for χ_F, while the estimated optical electronegativity value for χ_{Co} in CoX_2 molecules such as $CoCl_2$ and CoF_2 is 1.6.[23, 24] The expected position of the lowest energy charge transfer absorption band for CoF_2 is *ca.* 69000 cm^{-1}. This value of the predicted absorption band is higher energy than the upper limit of the UV/vis spectrometer. Also, it would be expected that the lowest energy charge transfer bands in CoF_3 or CoF_4 would be lower in energy, but expected to be minor components. Consequently, it is reasonable that no bands obtained in the range of UV/visible data belong to cobalt fluoride species. Instead, the FTIR data described later provide more definitive data.
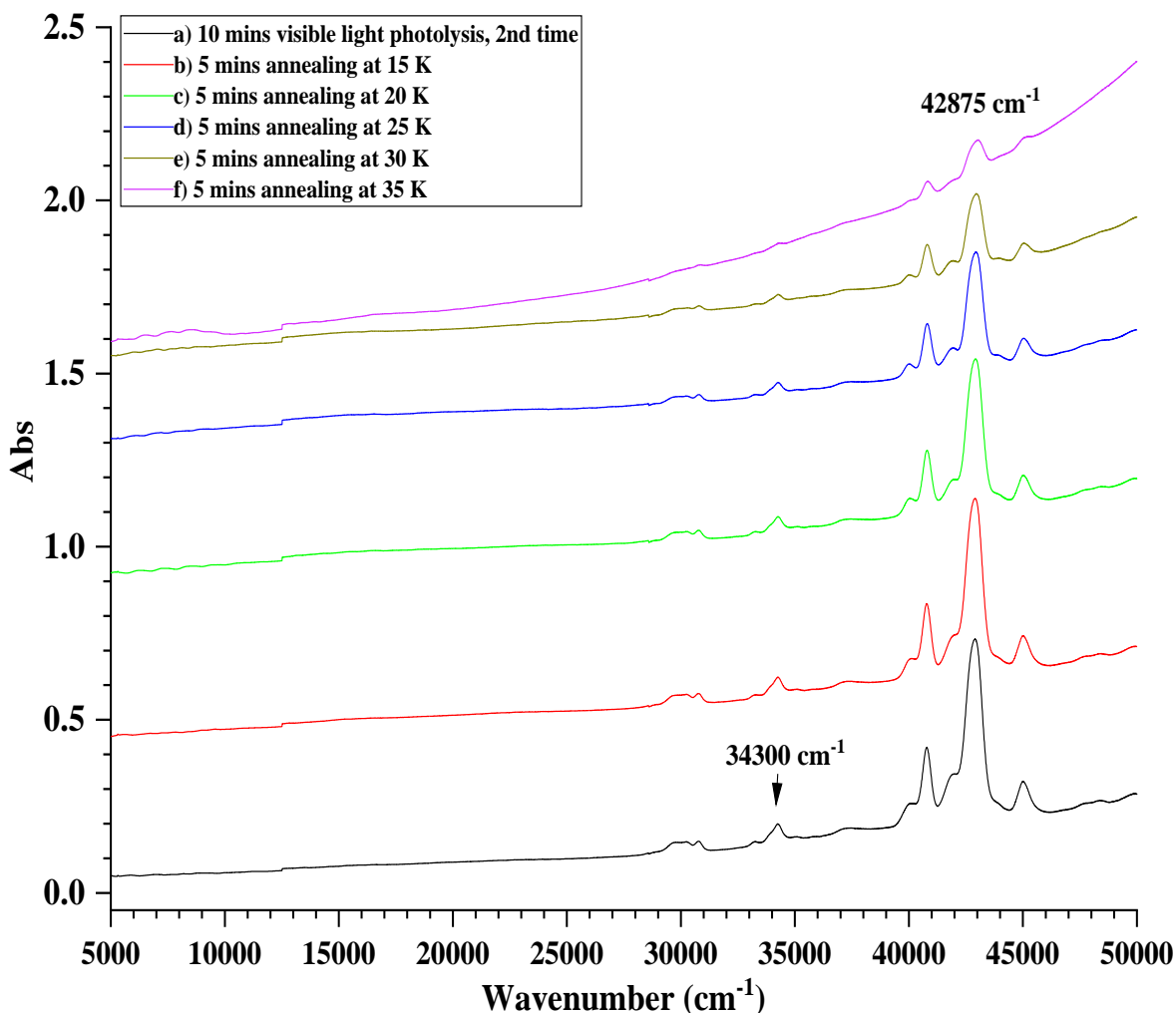
Figure 4.4: *UV/Vis spectra of Co in a 1% F_2/Ar matrix (a) after further 10 mins visible light photolysis, (b) after 5 mins annealing at 15 K, (c) after 5 mins annealing at 20 K, (d) after 5 mins annealing at 25 K, (e) after 5 mins annealing at 30 K, (f) after 5 mins annealing at 35 K.*

4.2.3 FTIR spectra of Co in a 1% F_2/Ar matrix

Infrared spectroscopy has been used to investigate the isolation of cobalt fluorides in an Ar matrix; it aims to characterise CoF, CoF_2, CoF_3, and CoF_4 in solid argon. The experiment was carried out using a 1% F_2 in Ar gas mixture. The use of a 2% F_2/Ar gas caused the peaks of the spectrum to be broader. The optimum conditions for evaporation of cobalt atoms were achieved at 36 A and 1.209 V. A thin layer of 1% F_2 in Ar matrix gas was put down onto the cooled deposition window. The isolation of cobalt in 1% F_2/Ar matrix was run at 10 K and at a pressure of 2×10^{-6} mbar. The IR spectra were recorded after 30, and 60 minutes. Afterwards, photolysis and annealing were also applied to characterise the solid matrix formed. Figure 4.5a shows the IR spectrum of features due to cobalt fluorides species isolated in solid argon at 10 K. The vibrational band observed at 722.8 cm^{-1} with a shoulder at 720.4 cm^{-1} belongs to CoF_2 in solid argon matrix and its

site effects, which is compatible with the literature data.[10, 12, 13, 17, 19] A sharp peak at 637.9 cm^{-1} was observed, which is most likely assigned to the stretching mode of CoF in solid Ar matrix, which is in good agreement with IR band of gas phase CoF detected previously.[2] Also, this assignment was consistent with the theoretical suggestion as seen in table 4.2. There are also some weak peaks at 740–730 cm^{-1}; these are more probably due to dimer form of CoF$_2$ or high–valent cobalt fluoride species. Furthermore, some bands were found which correspond with impurities. The bands at 1913 cm^{-1}, and 1941 cm^{-1} are attributed to carbonyl fluoride (F$_2$CO), these bands have been detected before.[25] It is more likely related to impurities in the can of fluorine, or during the reaction of CO with F$_2$. It probably occurs with the experiment, depending on how much CO is released by the furnace. Other peaks are related to CO, CO$_2$, and H$_2$O vapours.

Table 4.2: Assignments (cm^{-1}) observed and calculated of CoF and CoF$_2$ molecules in solid Ar matrix.

Assignments	Observed	Ref [37]	Calculated B3LYP/6-311G(+d)	Calculated B3LYP/def2tzvpp
CoF	637.9 cm^{-1}	—	609.86 cm^{-1}	618.64 cm^{-1}
CoF$_2$	722.8 cm^{-1}	722.5 cm^{-1}	772.13 cm^{-1}	770.82 cm^{-1}

The matrix was exposed to visible light photolysis for 10 minutes and the IR spectrum is shown in Figure 4.5b. The intensity of the band at 637.9 cm^{-1} assigned to CoF molecules decreased slightly. On the other hand, the peak at 722.8 cm^{-1} assigned to CoF$_2$, along with the peak at 737.1 cm^{-1} increased a little. New weak peaks appeared at 740.5 and 747.1 cm^{-1}. Figure 4.5c shows the IR spectra after exposure to 200–410 nm photolysis for 10 minutes. The intensity of the band at 637.9 cm^{-1} was reduced slightly, whilst the band at 722.8 cm^{-1} increased dramatically. Also, the peaks at 737.1 cm^{-1}, 740.5 cm^{-1}, and 747.1 cm^{-1} became more intense than before. Moreover, two new peaks were formed at 711 and 733.2 cm^{-1} and a tiny band appeared at 728.5 cm^{-1}. Figure 4.5d illustrates the IR spectrum upon 10 minutes of broadband photolysis. The peak at 637.9 cm^{-1} shrank slightly, while the peaks at 722.82, 733.2, 737.1, 740.5, and 747.1 cm^{-1} grew. The absorption at 737.1 cm^{-1} is most likely assigned to isolated CoF$_3$ molecules in solid Ar matrix which has been previously reported.[17, 19] The matrix was exposed to further visible light photolysis for 10 minutes and the IR spectrum is shown in Figure 3.21e. It shows that all peaks have the same shape without any changes in intensity.
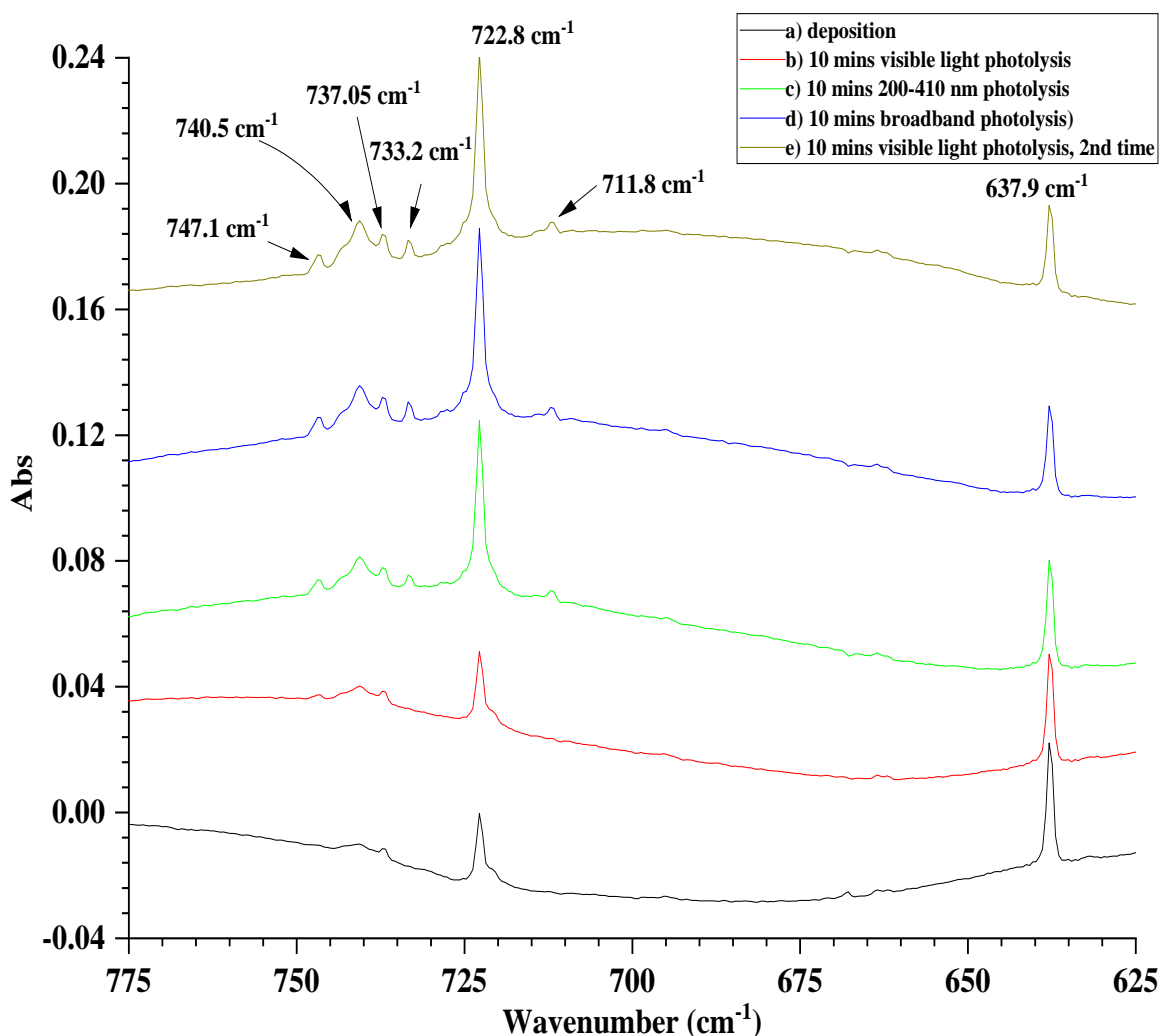
Figure 4.5: *FTIR spectra of atomic Co in a 1% F$_2$/Ar matrix (a) after deposition, (b) after 10 mins visible light photolysis, (c) after 10 mins 200–410 nm photolysis, (d) after 10 mins broadband photolysis, (e) after further 10 mins visible light photolysis.*

Figure 4.6b demonstrates the IR spectrum of isolated cobalt fluorides in solid argon matrix after 5 minutes of annealing at 15 K. The peaks at 733.2 cm^{-1} decreased, while peaks at 728.5 cm^{-1}, 737.1 cm^{-1}, 740.5 cm^{-1}, and 747.1 cm^{-1} increased. All other peaks remained the same intensity. Upon 5 minutes annealing at 20 K, the peak at 733.2 cm^{-1} disappeared and all bands shrank, while the peak at 728.5 cm^{-1} increased slightly; this is shown in Figure 4.6c. After 5 minutes annealing at 25 K, the spectrum in Figure 4.6d was recorded. Peaks at 728.5 and 737.1 cm^{-1} increased, while other bands became less intense than before. Figure 4.6e displays the IR spectrum of the matrix after 5 minutes annealing at 30 K. The peaks at 728.5 and 736 cm^{-1} grew a little, whereas the other observed peaks decreased in intensity. Figures 4.6f and 4.6g show the spectra after 5 minutes annealing at 35 and 40 K, respectively. All the bands became smaller, and also, peaks at 711.8 and 747.1 cm^{-1} disappeared. It is likely that the rigid matrix started to evaporate.
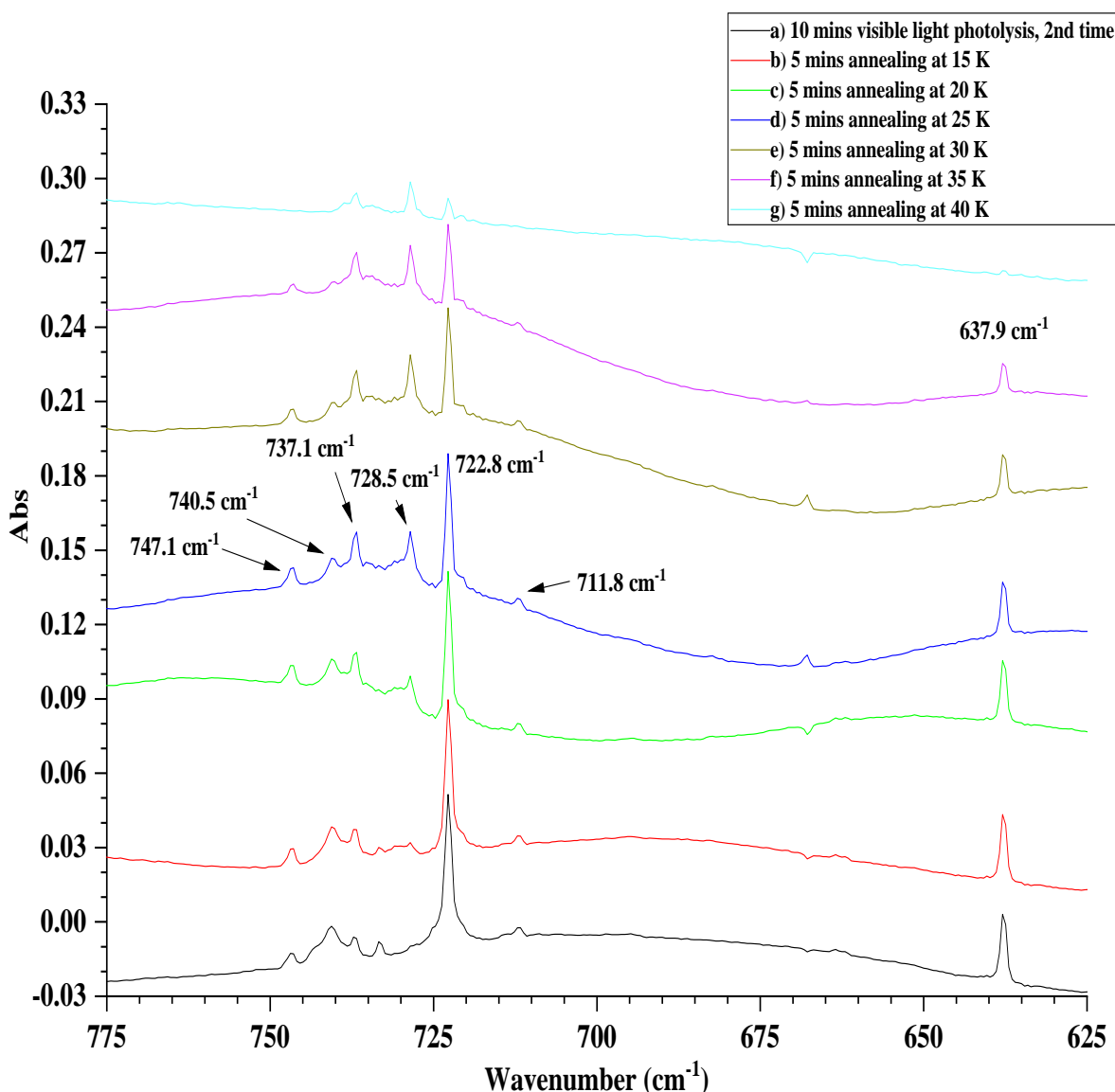
Figure 4.6: *FTIR spectra of atomic Co in a 1% F_2/Ar matrix (a) after further 10 mins visible light photolysis, (b) after 5 mins annealing at 15 K, (c) after 5 mins annealing at 20 K, (d) after 5 mins annealing at 25 K, (e) after 5 mins annealing at 30 K, (f) after 5 mins annealing at 35 K, (g) after 5 mins annealing at 40 K.*

As presented in Figure 4.7, the peak at 711.8 cm^{-1}, which grew on 200–410 nm photolysis and was reasonably constant on annealing, could be attributed to the formation of Co_2F_2 resulting from the reaction of Co_2 species with the mobile fluorine atoms produced by UV photolysis process. The changeable absorption band at 733.2 cm^{-1} which showed unique growth by photolysis and disappeared by annealing at 20 K is most likely assigned to CoF_4 species, even though this assignment is in disagreement with the study performed by Rau *et al*. who assigned the band observed at 737.1 cm^{-1} to CoF_4 which was obtained from the vaporisation of solid CoF_3 and solid TbF_4 at 600 K.[18, 19] It is necessary to note that there is no peak observed at 767 cm^{-1} during this study. The peak at 728.5 cm^{-1} was previously assigned to the formation of dimers of CoF_3 by Rau *et al*.[19]

The persistent behaviour of the features at 740.5 and 747.1 cm^{-1} indicates that they belong to the same species which could be the dimeric form of CoF$_2$.
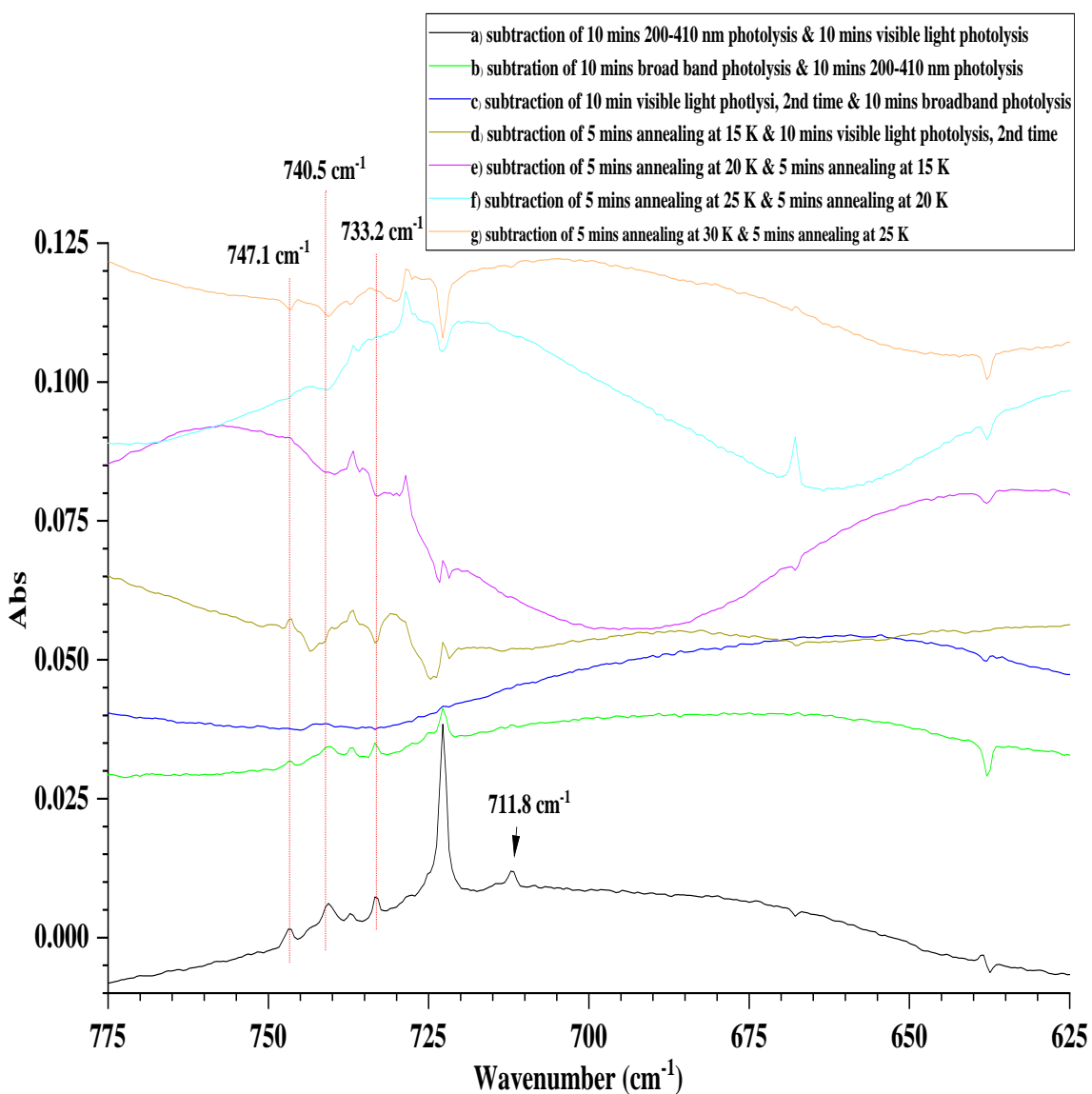
Figure 4.7: *FTIR subtraction spectra of atomic Co on a 1% F$_2$/Ar matrix (a) for 10 mins 200–410 nm photolysis & 10 mins visible light photolysis, (b) for 10 mins broadband photolysis & 10 mins 200–410 nm photolysis, (c) for further 10 mins visible light photolysis & 10 mins broadband photolysis, (d) for 5 mins annealing at 15 K & further 10 mins visible light photolysis, (e) for 5 mins annealing at 20 K & 5 mins annealing at 15 K, (f) for 5 mins annealing at 25 K & 5 mins annealing at 20 K (g) after subtraction of 5 mins annealing at 30 K & 5 mins annealing at 25 K.*

4.2.3.1 Computational calculations

The computational calculations were completed using both B3LYP/def2tzvpp and B3LYP/6−311G(+d) within G09W. Figure 4.8 shows the proposed peak position of cobalt fluoride molecules at two different half−widths 0.5 and 1.0 cm^{-1}. The computed vibrational spectra for all cobalt fluoride species at half−width 0.5 cm^{-1} using

69

B3LYP/def2tzvpp and B3LYP/6−311G(+d) are displayed in Figures 4.9 and 4.10, respectively. The bond lengths, the bond angles, and the electronic ground state were calculated using B3LYP/def2tzvpp as well as B3LYP/6–311G(+d) and are presented in Tables 4.3 and 4.4, respectively. The theoretical calculations of CoF is reliable with the experimental data obtained, the calculations for CoF suggested one band at 618.64 cm^{-1} using B3LYP/def2tzvpp and at 609.86 cm^{-1} for B3LYP/6−311G(+d) calculations confirming that the peak observed at 637.9 cm^{-1} is due to CoF species which has not been reported by matrix isolation IR spectroscopy.[1, 2] The calculated data show that the geometry of CoF_2 is linear, the B3LYP/def2tzvpp calculation suggested the IR absorption band at 770.82 cm^{-1}, while the B3LYP/6−311G(+d) proposed the vibrational frequency at 772.13 cm^{-1} which is about 50 cm^{-1} wavenumbers higher than the CoF_2 band obtained at 722.82 cm^{-1}. Moreover, the computational data revealed that high spin electronic configuration is more favourable than low spin form, which are compatible with previous literature data.[26]

The theoretical data of CoF_3 was inconsistent with the experimental data obtained. The feature assigned to CoF_3 molecules was reported at 737.1 cm^{-1}, while the calculated bands have lower wavenumber values. The calculated data for CoF_3 molecules using B3LYP/def2tzvpp sets proposed two overlapped bands at 727.83 and 723.23 cm^{-1}, while the B3LYP/6−311G(+d) calculation suggested two overlapped bands at 708.53 and 707.40 cm^{-1}. The energy of the high spin form is lower than the low spin and the configuration of CoF_3 is trigonal planar (D_{3h}) symmetry.[19] The B3LYP/def2tzvpp sets suggested the relative energy of CoF_3 between quintet state and singlet state as 258.35 kJ.mol^{-1} and 87.62 kJ.mol^{-1} between quintet and singlet configurations, while the relative energies calculated using B3LYP/6−311G(+d) sets were 266.97 kJ.mol^{-1} between quintet and singlet forms and 90.63 kJ.mol^{-1} between quintet and singlet electronic states.

The B3LYP/def2tzvpp results for CoF_4 calculated the asymmetric stretching mode of $v_{Co–F}$ at 720.45 cm^{-1}, whereas the theoretical B3LYP/6−311G(+d) data suggested one peak at 697.82 cm^{-1}. These data are corresponding with the experimental band obtained at 733.2 cm^{-1}. The molecular arrangement of CoF_4 is suggested as tetrahedral by both calculations. Furthermore, the high spin electronic structure of CoF_4 is more favourable than the low spin. The energy differences were calculated using B3LYP/def2tzvpp between sextet and doublet electronic structures as 106.29 kJ.mol^{-1}, and 81.48 kJ.mol^{-1} between sextet and quartet states. Nonetheless, the B3LYP/6−311G(+d) calculations proposed the relative energies between sextet and

doublet electronic spin states as 160.7 kJ.mol^{-1}, whereas the difference in energy between sextet and quartet electronic forms was 55.02 kJ.mol^{-1}. More details of the calculations are indicated in appendix B of chapter 4.

Table 4.3: The calculated geometry of cobalt fluoride species using B3LYP/def2tzvpp.

Assignments	Molecular structure	Electronic ground state	F–Co–F Bond angles	Co–F Bond lengths (Å)
CoF	—	—	—	1.769
CoF$_2$	Linear	$^4\Sigma_g$	180.0º	(1.722)×2
CoF$_3$	Trigonal planar	$^5A_1$	(119.85º)×2, 120.31º	(1.730)×2, 1.732
CoF$_4$	Tetrahedral	$^6A_1$	(109.47º)×6	(1.730)×4

Table 4.4: The calculated geometry of cobalt fluoride species using B3LYP/6–311G(+d).

Assignments	Molecular structure	Electronic ground state	F–Co–F Bond angles	Co–F Bond lengths (Å)
CoF	—	—	—	1.782
CoF$_2$	Linear	$^4B_1$	179.99º	(1.748)×2
CoF$_3$	Trigonal planar	$^5A_1$	(120.02º)×2, 119.69º	(1.739)×2, 1.740
CoF$_4$	Tetrahedral	$^6A_1$	(109.47º)×6	(1.739)×4
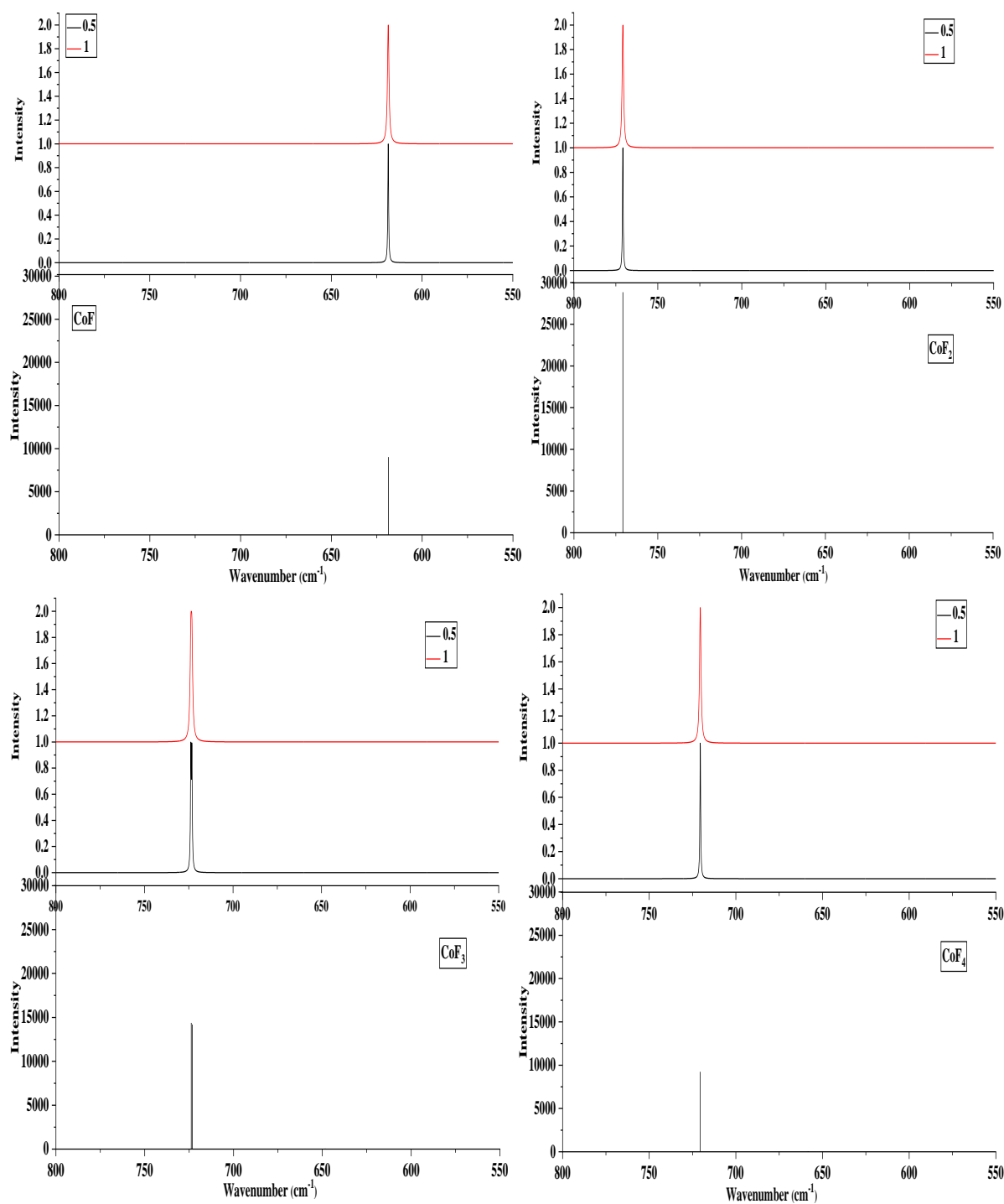
Figure 4.8: *Calculated (B3LYP/def2tzvpp) IR spectra of isotopes of Co fluoride molecules at two different half−widths 0.5 and 1.0 cm^{-1}.*
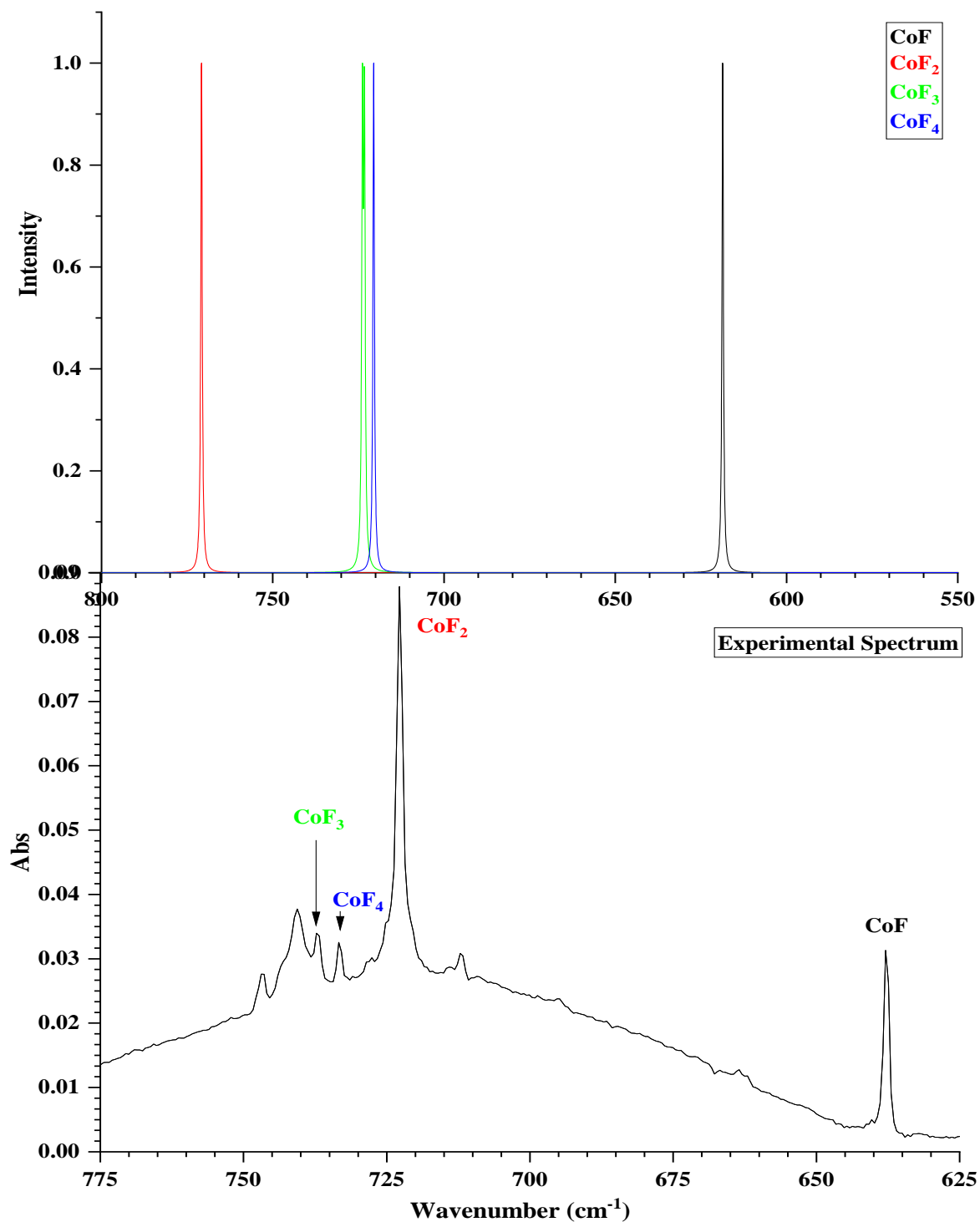
Figure 4.9: *Calculated (B3LYP/def2tzvpp) IR spectrum of all Co fluoride molecules at half−width 0.5 cm⁻¹ and experimental FTIR spectrum for atomic Co in 1% F₂/Ar matrix.*
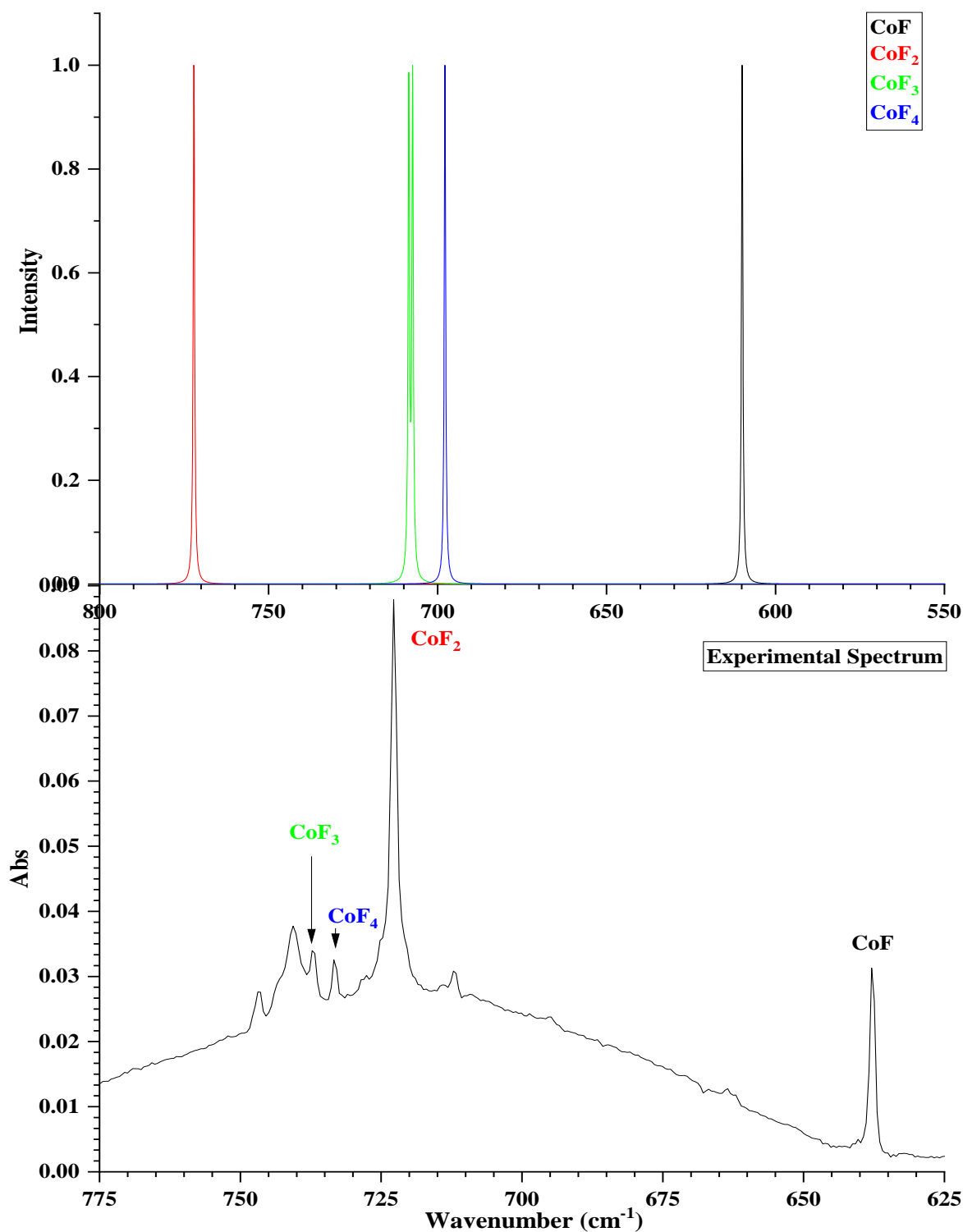
Figure 4.10: *Calculated (B3LYP/6−311G(+d)) IR spectrum of all Co fluoride molecules at half−width 0.5 cm^{-1} and experimental FTIR spectrum for atomic Co in 1% F$_2$/Ar matrix.*

4.2.3.2 Thermodynamic study

The relative stability of cobalt fluoride species has been studied as well. The overall reaction enthalpy for reaction between Co atoms and F$_2$ molecules indicates that CoF$_4$ species have the lowest energy, −1090.4 kJ.mol^{-1}, comparing with other cobalt

fluoride species as present in Figure 4.11. When more fluorine atoms are available, more CoF$_4$ molecules are formed. The stepwise reaction enthalpy was also calculated and is given in Figure 4.12 below, the energy of CoF$_3$ lies above a line connecting CoF$_2$ and CoF$_4$; it points to instability of CoF$_3$ and the possibility of disproportionation into both CoF$_2$ and CoF$_4$. On the other hand, CoF$_2$ is more stable, as it lies below a line linking CoF and CoF$_3$, so CoF and CoF$_3$ molecules are anticipated to comproportionate to form CoF$_2$ species.
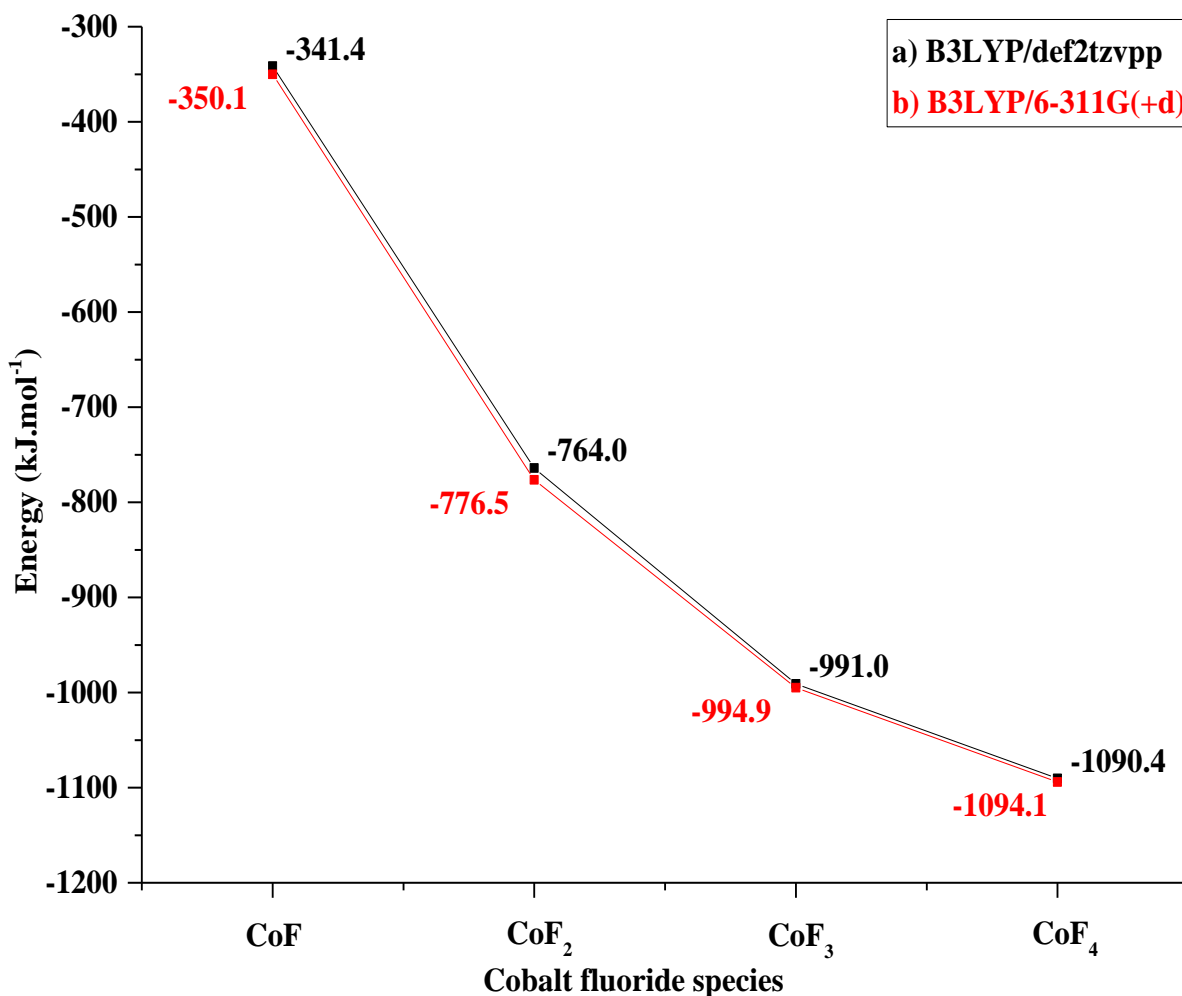
Figure 4.11: *Overall reaction enthalpy of CoF$_n$ species for the reaction of Co atoms and F$_2$ molecules.*
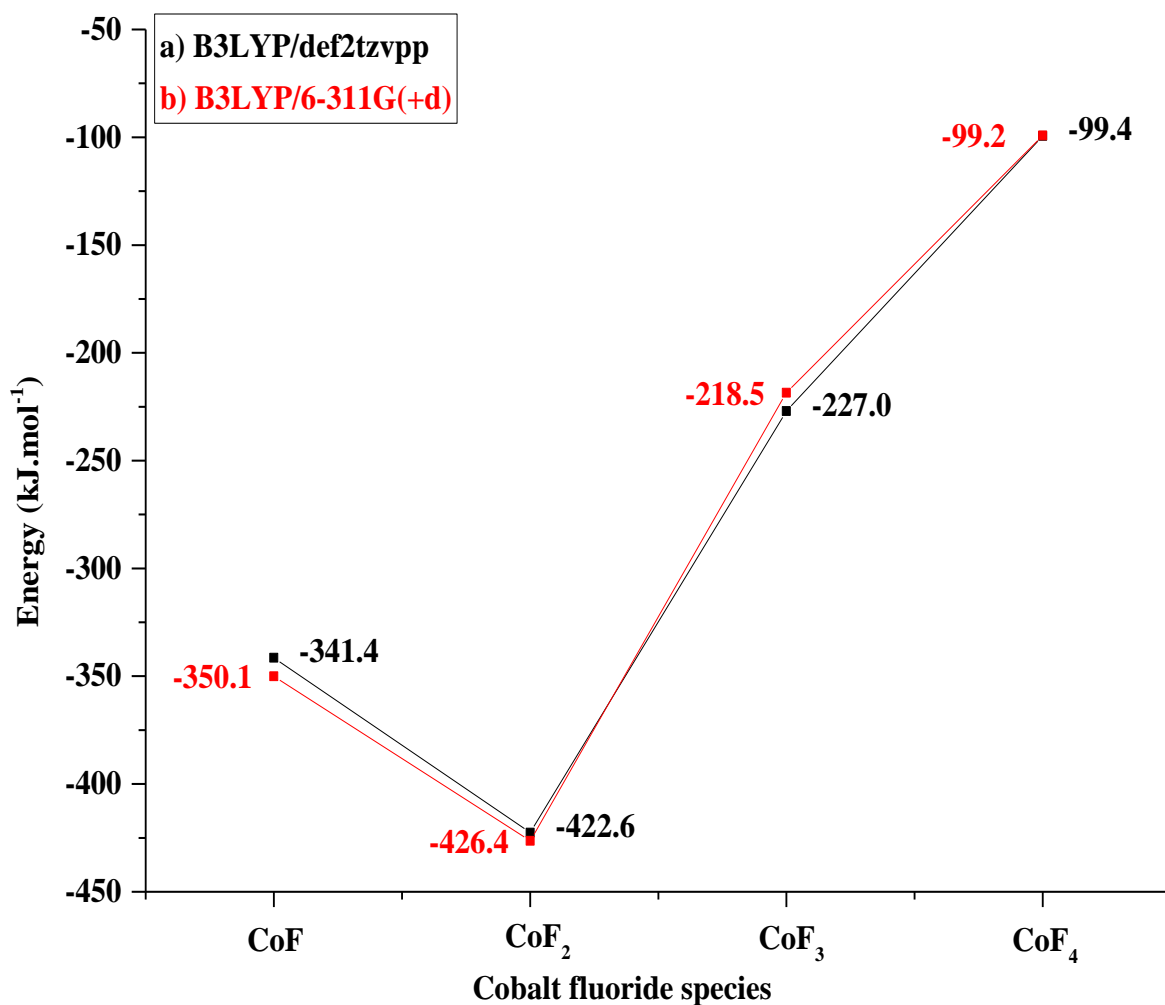
Figure 4.12: *Stepwise reaction enthalpy of CoF_n species for the reaction of Co atoms and F_2 molecules.*

4.3 Conclusion

The optical spectra of cobalt hosted in argon matrix at 11.5 K showed peaks associated with deposition of atomic cobalt in Ar matrix as previously reported.[21, 22] It is noteworthy that the cryostat used through experiments was unable to cool down the deposition window below 10 K, so bands related to of Co_2 and of Co_3 species were also detected.[22] On the other hand, the UV–vis spectra of cobalt trapped in a matrix of argon doped with 1% fluorine yielded the same peaks previously observed in the spectrum of Co/Ar matrix. The application of photolysis and annealing process led to decreases in intensity of all peaks and no new peaks were observed. The simultaneous decay in intensity of all peaks after photolysis is more likely because of reaction with excited fluorine atoms with cobalt atoms in the matrix and formation of cobalt fluoride molecules. The optical electronegativity predicts the position of the lowest energy charge transfer absorption band for CoF_2 at *ca.* 69000 cm^{-1}, which is higher in energy than the UV/vis

range. Instead, FTIR data were more reasonable, as they provided definite data for cobalt fluoride species.

The vibrational spectrum recorded shows a sharp band at 637.9 cm^{-1} assigned to the stretching mode of CoF in solid Ar matrix and a vibrational band 722.8 cm^{-1} arising from the asymmetric stretching mode of CoF_2. A weak intensity peak at 737.1 cm^{-1} is assigned to the matrix isolation of CoF_3 in solid argon. The intensity of bands related to CoF_2 and CoF_3 increased after exposure to photolysis processes, while the CoF peak shrank. The formation of new weak peaks at 711.8, 728.5, 733.2, 740.5, and 747.1 cm^{-1} responding to the application of photolysis and annealing. The peak at 711.8 cm^{-1} which grew by photolysis and was reasonably constant on annealing, could be attributed to the formation of Co_2F_2, while the unstable absorption band at 733.2 cm^{-1} which showed unique growth by photolysis and disappeared by annealing at 20 K is most likely assigned to CoF_4 species. The peak at 728.5 cm^{-1} is assigned to the formation of dimers of CoF_3. Furthermore, the persistent behavior of the absorption features at 740.5 and 747.1 cm^{-1} indicates that they belong to the same species which could be the dimeric form of CoF_2. The theoretical data suggested the geometry of CoF_3 as a quintet trigonal planar symmetry and the geometry of CoF_4 as tetrahedral in a sextet electronic state.

4.4 Summary

First observation of CoF in solid Ar matrix; the FTIR band was recorded at 637.9 cm^{-1}. The absorption band at 733.2 cm^{-1} was assigned to CoF_4 species in solid Ar matrix; its intensity grows by photolysis and disappears by annealing at 20 K. The molecular arrangement of CoF_4 is suggested as tetrahedral by calculations.

4.5 References

1. T. C. DeVore, R. J. Van Zee and W. Weltner, *Proc. - Electrochem. Soc.*, 1978, **78-1**, 187-198.
2. A. G. Adam, L. P. Fraser, W. D. Hamilton and M. C. Steeves, *Chem. Phys. Lett.*, 1994, **230**, 82-86.
3. R. S. Ram, P. F. Bernath and S. P. Davis, *J. Mol. Spectrosc.*, 1995, **173**, 158-176.
4. T. Okabayashi and M. Tanimoto, *J. Mol. Spectrosc.*, 2003, **221**, 149-155.
5. X. Zhang, J. Guo, T. Wang, L. Pei, Y. Chen and C. Chen, *J. Mol. Spectrosc.*, 2003, **220**, 209-213.
6. T. C. Steimle, T. Ma, A. G. Adam, W. D. Hamilton and A. J. Merer, *J. Chem. Phys.*, 2006, **125**, 064302.
7. A. G. Adam and W. D. Hamilton, *J. Mol. Spectrosc.*, 2001, **206**, 139-142.
8. Z. Zhang, J. Guo, X. Yu, J. Zheng and Y. Chen, *J. Mol. Spectrosc.*, 2007, **244**, 117-121.
9. C. Koukounas and A. Mavridis, *J. Phys. Chem. A*, 2008, **112**, 11235–11250.
10. J. W. Hastie, R. H. Hauge and J. L. Margrave, *J. Chem. Soc. D*, 1969, 1452-1453.
11. J. L. Margrave, J. W. Hastie and R. H. Hauge, *Amer. Chem. Soc., Div. Petrol. Chem., Prepr.*, 1969, **14**, E11-E13.
12. J. W. Hastie, R. H. Hauge and J. L. Margrave, *High Temp. Sci.*, 1969, **1**, 76-85.
13. V. N. Bukhmarina, A. Y. Gerasimov, Y. B. Predtechenskii and V. G. Shklyarik, *Opt. Spektrosk.*, 1988, **65**, 876-881.
14. J. V. Rau, V. R. Albertini, N. S. Chilingarov, S. Colonna and M. di Michiel, *Chem. Lett.*, 2002, **31**, 664-665.
15. D. D. Moldavskii, G. G. Furin, L. V. Shkul'tetskaya and B. Y. Eifman, *Russ. J. Appl. Chem.*, 2002, **75**, 959-961.
16. G. V. Girichev, N. I. Giricheva, O. G. Krasnova, A. V. Krasnov, S. A. Shlykov, E. G. Rakov and S. V. Khaustov, *J. Struct. Chem.*, 1992, **33**, 838-843.
17. V. N. Bukhmarina, A. Y. Gerasimov and Y. B. Predtechenskii, *Vib. Spectrosc.*, 1992, **4**, 91-94.
18. N. S. Chilingarov, J. V. Rau, L. N. Sidorov, L. Bencze, A. Popovic and V. F. Sukhoverkhov, *J. Fluor. Chem.*, 2000, **104**, 291-295.
19. J. V. Rau, S. N. Cesaro, N. S. Chilingarov and G. Balducci, *Inorg. Chem.*, 1999, **38**, 5695-5697.
20. M. Moskovits and G. A. Ozin, *Cryochemistry, Wiley-Interscience, New York*, 1976.
21. D. M. Mann and H. P. Broida, *J. Chem. Phys.*, 1971, **55**, 84-94.
22. G. A. Ozin and A. J. L. Hanlan, *J. Inorg. Chem.*, 1979, **18**, 1781-1790.
23. O. M. Wilkin, N. Harris, J. F. Rooms, E. L. Dixon, A. J. Bridgeman and N. A. Young, *The Journal of Physical Chemistry A*, 2018, **122**, 1994-2029.
24. S. S. Batsanov, *Russ. J. Inorg. Chem.*, 2011, **56**, 906-912.
25. P. D. Mallinson, D. C. Mckvan, J. H. Holloway and I. A. Oxto, *Spectrochim. Acta, Part A*, 1975, **31A**, 143-159.
26. S. G. Wang and W. H. E. Schwarz, *J. Chem. Phys.*, 1988, **109**, 7252-7262.

Chapter 5

Molybdenum chlorides and fluorides

5.1 Introduction

The molybdenum atoms and molybdenum halides trapped in rare gas matrices have been widely explored and reported using spectroscopic techniques.

5.1.1 Molybdenum atoms

Molybdenum atoms isolated in argon as well as xenon solid matrices were first reported in 1973, with bands recorded around 27000 and 33000 cm^{-1} for Mo in a solid Xe matrix and the bands of Mo in solid Ar matrix were recorded between 28000 and 34000 cm^{-1}.[1] In 1974, Green *et al*. used matrix isolation ultraviolet spectroscopy to record the optical spectra of Mo atoms isolated in rare gas matrices. The UV bands of Mo atoms in a matrix of solid Ar were observed between 28000 and 34710 cm^{-1} which were in agreement with the earlier study; on annealing the matrix to 20 K bands due to Mo_2 were observed at 19230 and 32785 cm^{-1} (520 and 305 nm); while the UV bands of Mo atoms trapped in a solid Kr matrix were observed between 26300 and 34200 cm^{-1}.[2] Hewett *et al*. carried out a study to trap Mo atoms and MoO_2 species in Ne by passing O_2 over hot molybdenum metal and trapping the products in solid Ne. The UV bands of Mo atoms in neon were observed between 27025 and 35460 cm^{-1} (370 and 282 nm), while the IR bands of MoO_2 were observed at 899 and 948 cm^{-1}, and the bands observed at 922 and 976 cm^{-1} were assigned to MoO_3.[3] A study performed by Klotzbücher and Ozin revealed that Mo_2 and Mo_3 species were observed at 19000/19607 cm^{-1} and 18585 cm^{-1} (510/526 and 538 nm), respectively, after irradiation using 295 nm to excite Mo atoms isolated in solid Kr matrix.[4] A further study used matrix isolation ultraviolet spectroscopy to investigate the reaction of Mo atoms with N_2 and O_2 doped in rare gas matrices, the study indicated that the feature centred at 19305 cm^{-1} belongs to Mo_2 species,[5] which was consistent with previous work.[4] One year later, the same result was obtained by Klotzbücher and Ozin, as the band due to Mo_2 species was recorded at 518 nm (19305 cm^{-1}) in Mo/Ar matrix.[6] The reaction of Mo atoms with a N_2/Kr gas mixture in cryogenic temperature was reinvestigated again; the absorption spectra indicated the formation of MoN_2. Moreover, the absorption band of Mo_2 was observed at 517 nm, while the bulk of peaks at 530 nm were assigned to Mo_3 species.[7] Laser fluorescence spectroscopy was employed to detect

monomer and dimer molybdenum species in the matrix; the Mo atoms absorption bands were located between 28570 and 35460 cm^{-1} (350 and 280 nm) and also the absorption feature at 518 nm (19305 cm^{-1}) was assigned to Mo_2 species isolated in Ar matrix, while the absorption features from Mo_2 doped in a krypton matrix were found in the range between 18515–20405 cm^{-1} (540–490 nm).[8] Soon after, several studies were also conducted to study the isolation of Mo atoms in rare gas matrices.[9-14] Magnetic circular dichroism was employed to study molybdenum atoms isolated in rare gas matrices; the excited state spin orbital coupling constants of Mo/Ar, Mo/Kr, and Mo/Xe matrices were 126.0, 84.5, and 57.5 cm^{-1}, respectively. Whereas in gas phase the value for Mo atoms is 101 cm^{-1}.[15] In addition, the laser ablation technique was used to evaporate molybdenum atoms. The photoluminescence spectrum of Mo atoms isolated in Ar matrix demonstrated three fundamental peaks at 20130, 18225, and 16610 cm^{-1} (496.7, 548.1 and 602.0 nm) in emission mode and are assigned to transition states of Mo atoms.[16] Resonance Raman spectroscopy was employed to detect mass–selected Mo atoms and small oligomers isolated in solid Ar matix. A strong band observed at 394.5 cm^{-1} and two weak bands at 445.0 and 473.3 cm^{-1} were due to Mo_2 species, and these three bands were due to observing the spectrum in different states. While the bands of Mo_3 were observed at 224.5, 236.2, 386.8, and 446.9 cm^{-1}; these bands were due to bending, asymmetric stretching, symmetric stretching mode, and overtone of the asymmetric mode, respectively.[17]

5.1.2 Molybdenum halides

Few studies have been undertaken to study the matrix isolation of molybdenum halides and to detect their molecular geometries. The molecular geometry and the vibrational spectrum of $MoCl_5$ matrix isolated in N_2 and Ar matrices has been identified.[18] The molecular structure of $MoCl_5$ isolated in Ar and N_2 matrices was suggested to be either trigonal bipyramidal (D_{3h}) or square pyramidal (C_{4v}) geometry.[19] The recorded IR absorption bands centered at 408 and 473 cm^{-1} were assigned to Mo−Cl stretching modes of $MoCl_5$ isolated in nitrogen matrix, whereas the IR bands of $MoCl_5$ isolated in Ar matrix were detected at 405 and 470 cm^{-1}. The study indicated a C_{4v} configuration of $MoCl_5$ isolated in N_2 and Ar matrices, but failed to detect $MoCl_6$ molecules.[20] Bellingham *et al*. reported in their spectroscopic study of transition metals pentachlorides in Ar and N_2 matrices that the configuration of $MoCl_5$ is a combination of D_{3h} and C_{4v} geometries for monomer molecules, while the dimer species of $MoCl_5$ is D_{4d} geomtry.[21] A study was undertaken by Fægri *et al*. using gas phase electron diffraction to investigate the

configuration of $MoCl_5$ indicating it is distorted trigonal bipyramid (C_{2v}) symmetry. Restricted Hartee–Fock (RHF) calculations proposed that the D_{3h} symmetry is more stable than the C_{4v} structure, and also suggested the lowest energy geometry is distorted trigonal bipyramid with C_{2v} symmetry.[22] The vapour phase $MoCl_6$ molecules are tremendously sensitive to moisture.[23] A theoretical study undertaken by Siegbahn suggested that the molecular structure of $MoCl_2$ is bent with a Cl–Mo–Cl angle of 142.3°, with a Mo–Cl bond length of 2.43 Å.[24] In 2017, a theoretical study conducted by Sliznev and Belova proposed the configuration of $MoCl_3$ as D_{3h} symmetry and T_d symmetry for $MoCl_4$.[25]

Molybdenum hexafluorides molecules have been widely studied,[26-39] matrix isolation IR spectroscopy detected the absorption of MoF_6 molecules at 737 cm^{-1} in a matrix of Ar.[40-42] The molecular shape of MoF_6 was defined by computational calculations as (O_h) octahedral symmetry.[43] Further studies provided contradictory evidence; Quiñones et al. proposed that the molecular structure of MoF_6 is non−rigid.[44] The quantum calculations demonstrated that the molecular arrangement of MoF_6 is octahedral in the ground state and trigonal prismatic in higher energy levels; this distortion may be because of a Jahn–Teller effect.[44, 45] Research was achieved by Brisdon et al. using X–ray absorption spectroscopy to determine the bond distance value d(Mo−F) for matrix isolated MoF_6; the Mo−F bond length was 1.81 Å.[46] The assignment of MoF_5 is not unambiguous. The first study used the heating of solid MoF_5 and cracking of the polymeric vapour before condensation in solid Ar to investigate the IR and Raman spectra and the molecular structure MoF_5 isolated in a matrix of solid Ar. The IR bands located at 713 and 683 cm^{-1} were attributed to monomeric species of MoF_5, and the polymeric species of MoF_5 matrix isolated in argon were observed at 768, 716, and 704 cm^{-1}; while the Raman bands were observed at 704 and 683 cm^{-1}.[47] The IR and Raman data indicated the geometry of MoF_5 as trigonal bipyramidal with D_{3h} symmetry. Nonetheless, a contrary study proposed that the geometric shape of MoF_5 in solid state as a (C_{4v}) square pyramidal symmetry.[48] Another investigation was achieved by matrix isolation IR spectroscopy to study MoF_5 produced from the photolysis of MoF_6 trapped in Ar matrix. The IR spectrum after photolysis displayed two new absorptions bands which grew in at 693.5 and 658.0 cm^{-1}.[42, 49] These vibrational frequencies were assigned to the formation of MoF_5 species.[42, 49] A further study conducted by introducing F_2/Ar mixtures over heated Mo metal pieces by Osin et al. also revealed that the monomeric MoF_5 molecules exhibit frequencies at 694 and 658 cm^{-1}, and the vibrational frequencies of the trimer

form of MoF_5 were located at 768, 715, 705, 692, and 522 cm^{-1}.[40] In addition, two studies have been undertaken by Giricheva *et al*. in 1997 and 2001 using gas phase electron diffraction and mass−spectrometry to study the molecular geometry of MoF_5; the investigations revealed that the structure of MoF_5 is a distorted bipyramid of C_{2v} geometry.[50, 51] The result was well–matched with a quantum chemistry research conducted by Voit *et al*.[52]

The reaction of Mo with introduced F_2 gas in the presence of Ar gas was studied at high temperature. The IR absorption bands of matrix–isolated MoF_4 molecules in an Ar matrix were detected at 675 cm^{-1} based on thermodynamic calculations; where the vapour gas of MoF_4 species dominates in certain temperatures, and this band grew substantially by increasing the temperature from 700 to 1100 °C.[40, 41]

This result was in agreement with previous matrix study conducted by Blinova and Predtechenskii who prepared MoF_5 from the photolysis,[42] but did not match with the published work by Acquista and Abramowitz who heated and cracked MoF_5.[47] The theoretical calculations defined the shape of MoF_4 as a tetrahedral symmetry.[53] A further electron diffraction study was conducted by Girichev *et al*. a year later, and revealed that the configuration of MoF_4 is tetrahedral as well.[51] The geometry of MoF_4 was proposed as tetrahedral structure by Sliznev and Belova as well.[25] MoF_3 matrix isolated in Ar solid matrix has also been detected;[40, 41 54] the recorded IR spectra of MoF_3 molecules generated by introducing F_2/Ar mixtures over hot Mo metal pieces displayed a weak vibrational band at 633 cm^{-1} assigned to a Mo−F stretching mode. This band was observed by increasing the flow rate of F_2 molecules and the temperature of the flow reactor to 1070 °C.[40, 41] A recent computational study by Sliznev and Belova using XMCQDPT2 methods proposed that the IR band of MoF_3 was observed at 694 cm^{-1}.[25] This study is inconsistent with previous experimental work undertaken by Osin *et al*. assigned the observed band at 633 cm^{-1} to matrix isolated MoF_3 species.[40, 41] A computational study was carried out at The Ivanovo State University of Chemistry and Technology to define the configuration of molybdenum trifluorides as well as tungsten trifluorides molecules. The geometry of MoF_3 was reported to be D_{3h} symmetry.[55]

The matrix IR spectra of $MoOF_4$ isolated in solid Ar showed groups of bands at 1045 and 719 cm^{-1} which are due to Mo=O and Mo–F stretching modes.[56] A recent study was conducted by Wei *et al*. using matrix isolation infrared spectroscopy to investigate the reaction of Mo atoms and OF_2 diluted in Ar gas mixture; the Mo atoms were generated

by laser ablation.[57] $OMoF_2$ has two sets of bands; the IR absorption bands observed between 1007.6–1001.9 cm^{-1} are due to Mo–O vibrational frequency and show the expected isotopic patterns of Mo, and the bands at 652.3–646.0 cm^{-1} are related to the asymmetric stretching mode of F–Mo–F and the isotopic patterns of Mo. Whereas, the band at 633.4 cm^{-1} is due to the symmetric stretching mode of F–Mo–F. Furthermore, the vibrational spectrum of MoOF showed a group of bands centred at 989.3–981.6 cm^{-1} due to Mo–O stretching mode and Mo characteristic isotope patterns.[57] Siegbahn calculated the geometry of MoF_2 as bent with a F–Mo–F angle of 140.1°, while the bond length of Mo–F was calculated to be 1.96 Å.[24] There appear to be no studies that have succeeded in detecting the presence of MoF_2 as well as MoF species in vapour or matrix phase.

There have been many studies using laser ablation,[57-59] and a few examples of passing halogen gases over heated metal filaments or sublimation of molybdenum compounds,[3, 40, 41, 60-62] but none involving the interaction of thermally evaporated molybdenum atoms with halogens trapped in cryogenic matrices. Therefore, this study was carried out to try to identify and characterise the missing molecules MoF and MoF_2 and query the recent assignment of MoF_3 carried out by Sliznev and Belova.[25]

5.2 Results and Discussion

5.2.1 UV/Vis Spectra of Mo in Ar

The melting point of molybdenum is 2610 °C, while the temperature required to get a vapour pressure 1×10^{-3} torr is 2305 °C.[63] The evaporation of molybdenum atoms was carried out using a filament of 4 strands of molybdenum wound together, the evaporation process was achieved at 3.37 V using 10 A of electrical current and the argon gas was laid down at 10.4 K. The deposition process was conducted for 120 minutes and the pressure in the vacuum chamber was 2×10^{-6} mbar. In the beginning, the Ar gas was introduced for 7 minutes to protect the CaF_2 window of the cryostat. As presented in Figure 5.1a and Table 5.1, the optical spectrum contains three medium intensity peaks at 28020, 28600 and 29300 cm^{-1} and a strong asymmetric peak at 34710 cm^{-1} for molybdenum atoms isolated in a solid argon matrix,which correspond very well with previous work.[1, 2] In addition, the two weak bands at 19300 and 32800 cm^{-1} are related to Mo dimers; as reported previously.[2, 5, 6] The spectrum is noisier than in other spectra because of coupling of the cryostat vibration with the vacuum chamber and instrument that could not be eliminated. The ground state of atomic Mo is $^7S_3$ ($4d^5 5s^1$).[2] Figure 5.1b

represents the matrix after exposure to 10 minutes of visible light photolysis; there is no change in the intensity observed. The matrix was also exposed to 200–410 nm photolysis for 10 minutes, and as shown in Figure 5.1c, the peak at 32800 cm^{-1} was reduced. The UV–visible spectrum after 10 minutes of broadband photolysis is shown in Figure 5.1d, and the intensity of the absorption peak at 32800 cm^{-1} was reduced slightly. The matrix was exposed to an extra 10 minutes of visible light photolysis; and from Figure 5.1e it can be seen that this had no effect on the UV/vis spectrum. It appears that after photolysis, the amount of dimer is reduced compared to monomer species. The behaviour of Mo$_2$ bands after photolysis is in disagreement with previous experimental work by Ozin and Klotzbücher who suggested the generation of Mo$_2$, Mo$_3$, and clusters species by 366 nm photolysis.[64]

Table 5.1: Absorptions (cm^{-1}) observed and previous studies of Mo atoms isolated in Ar matrix.

Experiment	Ref [1]	Ref [2]	Assignments/ Ground state
19300 cm^{-1}	19342 cm^{-1}	19320 cm^{-1}	Mo$_2$
28020 cm^{-1}	27972 cm^{-1}	28020 cm^{-1}	z^{7}P$_2$←^{7}S$_3$
28600 cm^{-1}	28571 cm^{-1}	28600 cm^{-1}	z^{7}P$_3$←^{7}S$_3$
29300 cm^{-1}	29282 cm^{-1}	39300 cm^{-1}	z^{7}P$_4$←^{7}S$_3$
32800 cm^{-1}	32750 cm^{-1}	32810 cm^{-1}	Mo$_2$
34710 cm^{-1}	34600 cm^{-1}	34710 cm^{-1}	y^{7}P$_4$←^{7}S$_3$
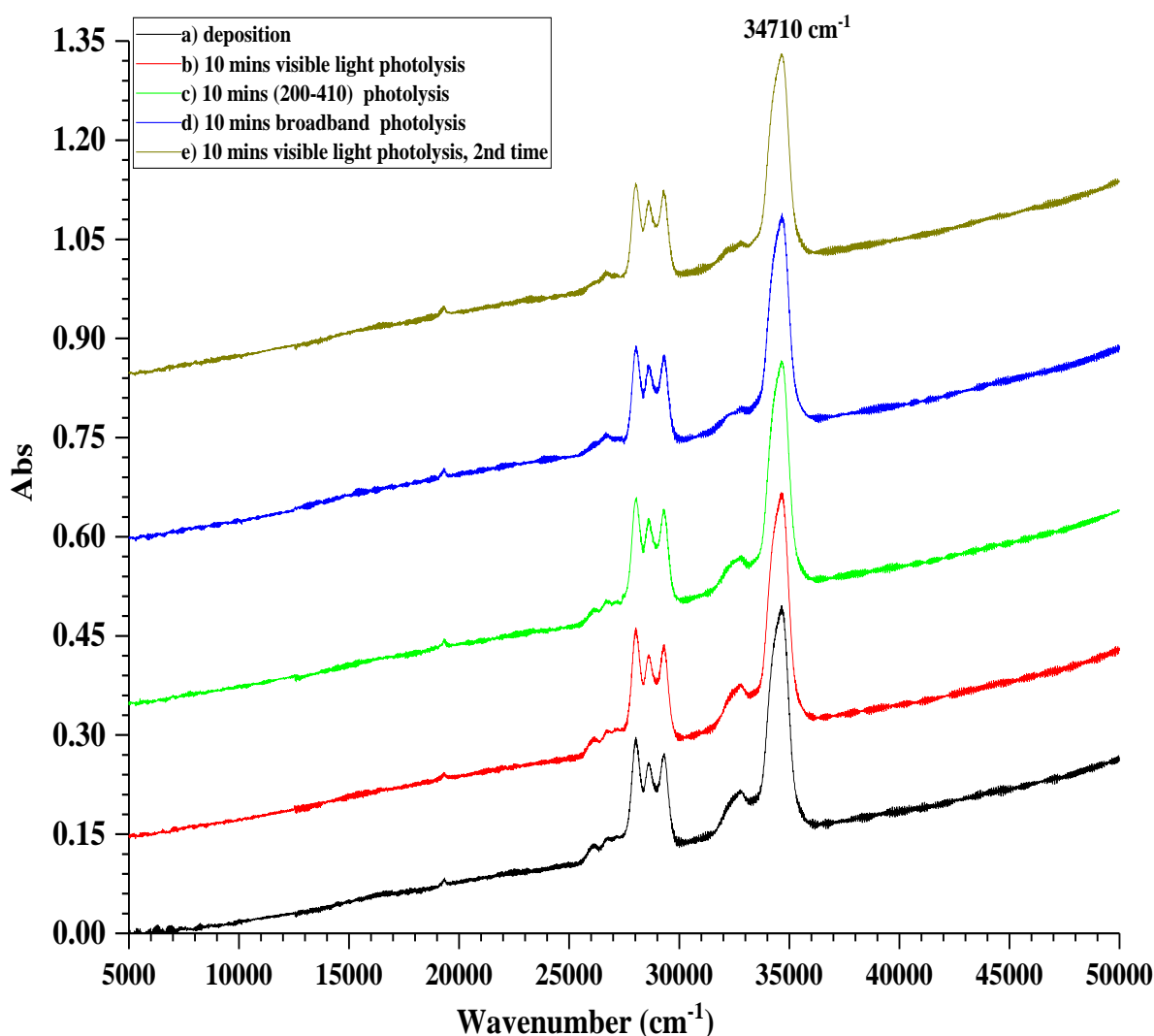
Figure 5.1: *UV/Vis spectra of atomic Mo in an Ar matrix (a) after deposition, (b) after 10 mins visible light photolysis, (c) after 10 mins 200−410 nm photolysis, (d) after 10 mins broadband photolysis, (e) after further 10 mins further visible light photolysis.*

The matrix was annealed to different temperatures progressively. Figure 5.2b illustrates the UV–visible spectrum of the matrix after 5 minutes of annealing to 15 K, no change in peak intensity was observed. There was a marginal increase in scattering at high energy in the spectrum. The intensity of the peaks at 28020, 28600, 29300, and 34710 cm^{-1} was reduced when the matrix was warmed to 20 K for 5 minutes (Figure 5.2c) and there is an increase in scattering of the light at high energy after annealing because the matrix is more likely to be microcrystalline, and more misty. As a result, the baseline in the spectra rose again, as indicated in Figure 5.2c. After further annealing at 25 K, (Figure 5.2d), the absorption bands related to matrix isolated Mo atoms decreased, and also the two bands at 19300 and 32800 cm^{-1} due to Mo$_2$ species were reduced, with more scattering in the spectrum. The optical spectrum presented in Figure 2.5e shows the matrix upon annealing for 5 minutes at 30 K. As expected the intensity of all peaks decreased, the spectrum was considerably scattered. The Mo in solid Ar matrix may be lost as the

argon evaporates. Despite the high temperature required to evaporate Mo atoms, the spectra contain predominantly atoms, with only a small fraction of dimers.
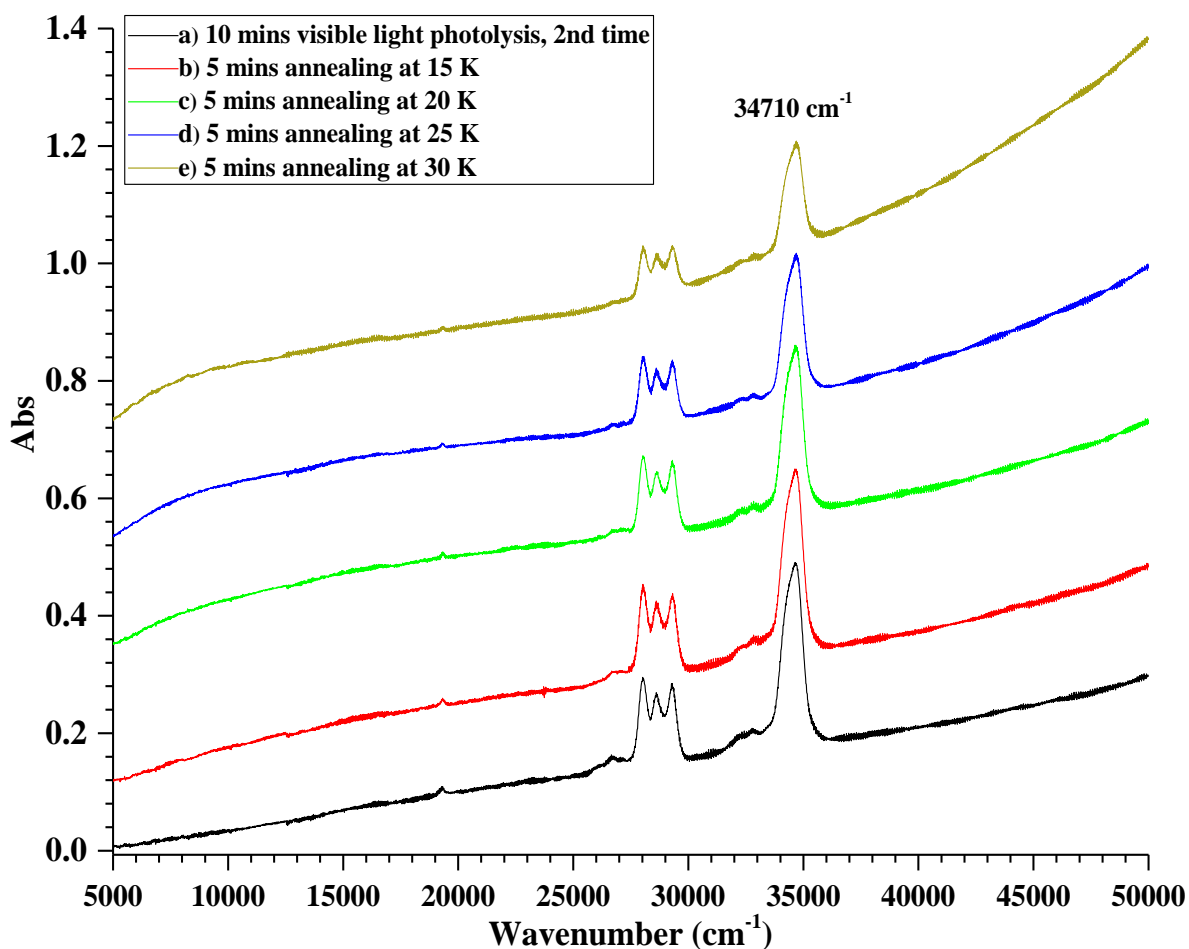
Figure 5.2: *UV/Vis spectra of atomic Mo in an Ar matrix (a) after further 10 mins visible light photolysis, (b) after 5 mins annealing at 15 K, (c) 5 mins annealing at 20 K, (d) after 5 mins annealing at 25 K, (e) after 5 mins annealing at 30 K.*

5.2.2 UV/Vis Spectra of 2.5% Cl₂ in Ar

The optical spectrum of 2.5% Cl_2 doped in Ar gas matrix was recorded after 100 minutes of depositing the gas mixture, the temperature of the deposition surface of the cryostat was at 11.3 K. The purpose of this experiment was to detect any impurities or chemical substances in the gas mixture. As displayed in Figure 5.3, a strong broad band at 30500 cm^{-1} can be assigned to Cl_2 in solid argon matrix based on previous work,[65] together with the intense band in the UV part of the spectrum. Cl_2 trapped in an argon lattice is known to suffer from a cage effect, when irradiated in the band at 33333–30303 cm^{-1} (300–330 nm). The chlorine bond strength of 240 kJ mol^{-1} in Cl_2 is higher than that of 155 kJ mol^{-1} of F_2. Fluorine, and so it is more thermodynamically stable. The photolysis does liberate chlorine atoms, but the atoms produced upon photolysis are

trapped in the same site, so recombination is much easier than in the gas phase. This was first observed for Cl_2/Ar by Bondybey and Fletcher,[66] and then confirmed by Kunz *et al.*[67] Therefore, there are far fewer mobile Cl atoms than F atoms after photolysis.
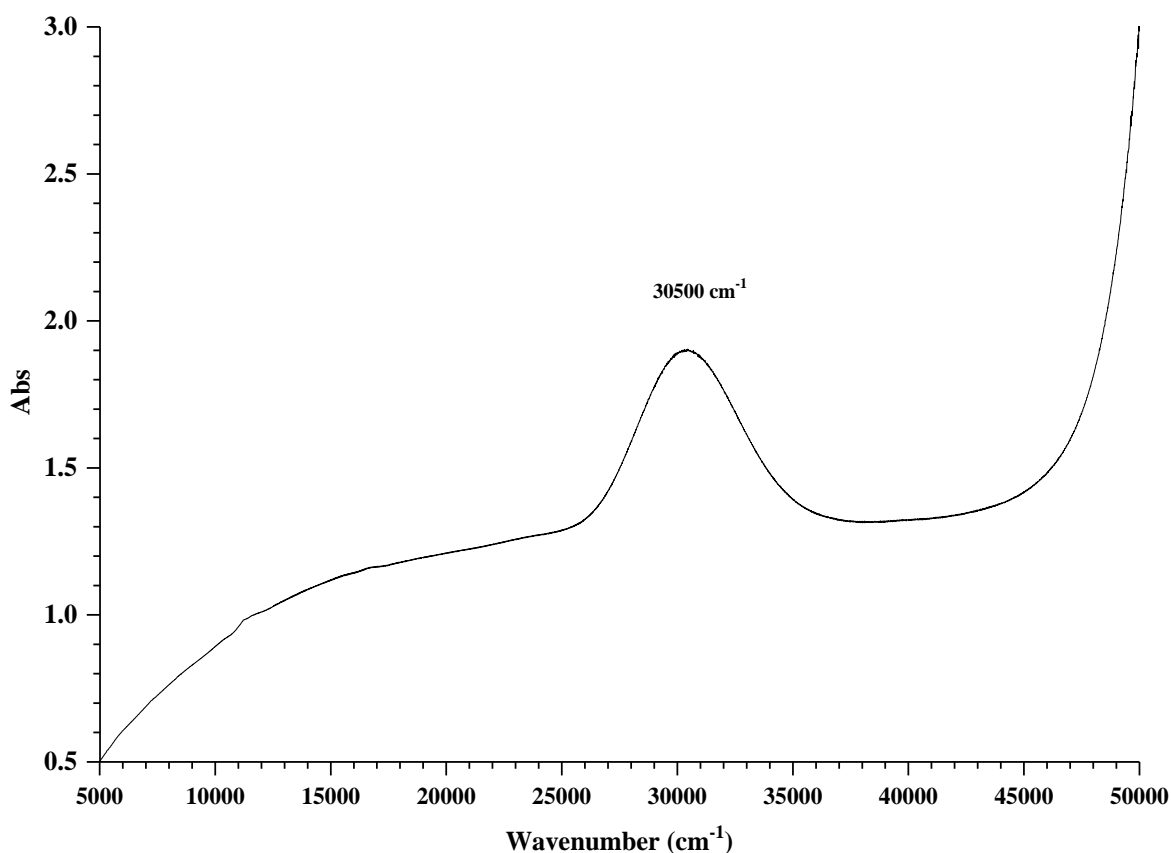
Figure 5.3: *UV/Vis spectrum of a 2.5% Cl_2/Ar matrix after deposition.*

5.2.3 UV/Vis Spectra of Mo in 1% Cl_2/Ar

1% of chlorine doped in the argon gas matrix was used throughout this experiment. The same experimental conditions have been employed to investigate the formation of molybdenum chlorides in a matrix of solid argon; the cryostat used cooled down the deposition window at 10.6 K and the pressure of the vacuum chamber was 2×10^{-6} mbar. A 10 A electrical current at 0.948 V was used to evaporate molybdenum atoms. 1% Cl_2 in Ar gas matrix was laid down for 8 minutes on the deposition surface of the cryostat to protect the surface. The optical spectrum was collected after 60 minutes of deposition of molybdenum and the 1% Cl_2/Ar matrix as presented in Figure 5.4a. The spectrum looks similar to the spectrum recorded for Mo in a solid Ar matrix; where three peaks were observed at 28030, 28600, and 29300 cm^{-1} alongside a strong asymmetric peak at 34710 cm^{-1}, also two weak absorption bands at 19300 and 32810 cm^{-1} are recorded. The matrix was exposed to 10 minutes of visible light photolysis. As presented in Figure 5.4b, the

intensity of the peaks remained the same. Figure 5.4c demonstrates the matrix after 10 minutes of 200–410 nm photolysis, the intensity of all peaks have been reduced. The matrix was exposed to broadband photolysis for 10 minutes, the spectrum located in Figure 5.4d displays that the intensity of all peaks decreased again to some extent. An additional 10 minutes of visible light photolysis was employed and the optical spectrum shows that all peaks have the same intensity, as seen in Figure 5.4e. As the spectra are essentially identical to those obtained for Mo atoms in Ar, there does not appear to be any evidence for the formation of molybdenum chlorides on photolysis.
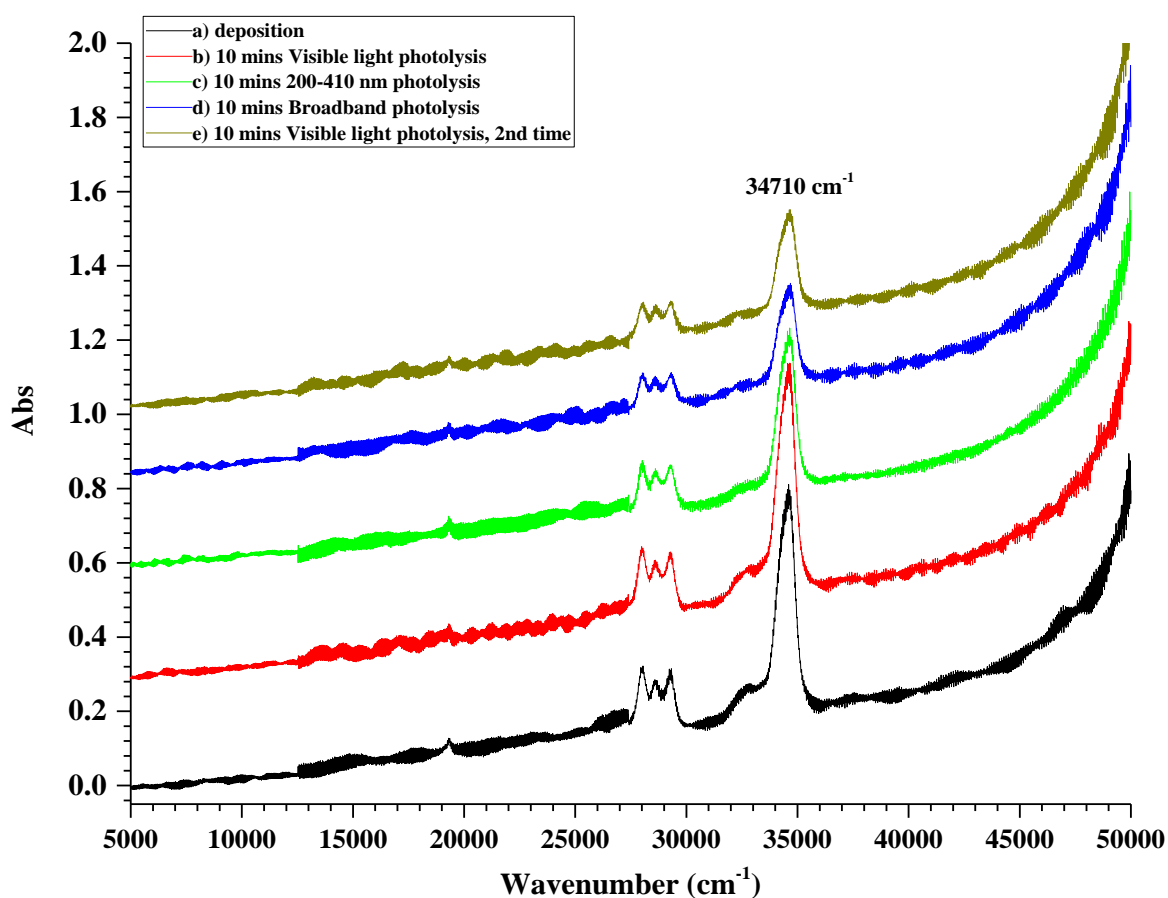
Figure 5.4: *UV/Vis spectra of Mo in a 1% Cl_2/Ar matrix (a) after deposition, (b) after 10 mins visible light photolysis, (c) after 10 mins 200−410 nm photolysis, (d) after 10 mins broadband photolysis, (e) after further 10 mins visible light photolysis.*

The matrix was progressively warmed up for 5 minutes to 15 K and 20 K, the UV/vis spectra are given in Figure 5.5b and 5.5c, respectively. All observed bands have the same intensity; it indicates that no change was happened. Moreover, the spectra were scattered to 10.0 Abs from 49400 cm^{-1} onwards, as the baseline has risen extremely and because of chlorine gas or the formation of a $MoCl_n$ compound which is very absorbing. A spectroscopic study conducted by Brisdon *et al.* stated that the UV/vis spectrum of $MoCl_5$ in nitrogen matrix exhibits a broad band at 21700 cm^{-1}, followed by three weak

bands at 26000, 29000, and 32700 cm^{-1}, and three intense bands at 37000, 40300, and 43710 cm^{-1}.[20] As none of these bands have been observed, the intense feature is most likely due to chlorine gas in matrix. Further annealing at 25 K for 5 minutes was implemented, the UV–visible absorption data are shown in Figure 5.5d. The intensity of peaks decreased slightly. Upon annealing to 30 K for 5 minutes; Figure 5.5e indicates that the intensity of all peaks reduced again, the spectrum became more noisy and scattered to 10.0 Abs from 48400 cm^{-1} onwards. The same experiments have been repeated several times and the same results were obtained. Surprisingly, there appears to be no evidence for a reaction between Mo atoms and chlorine molecules or atoms at cryogenic temperatures. Far−IR spectroscopy would be helpful to study the isolation of molybdenum chloride molecules later.
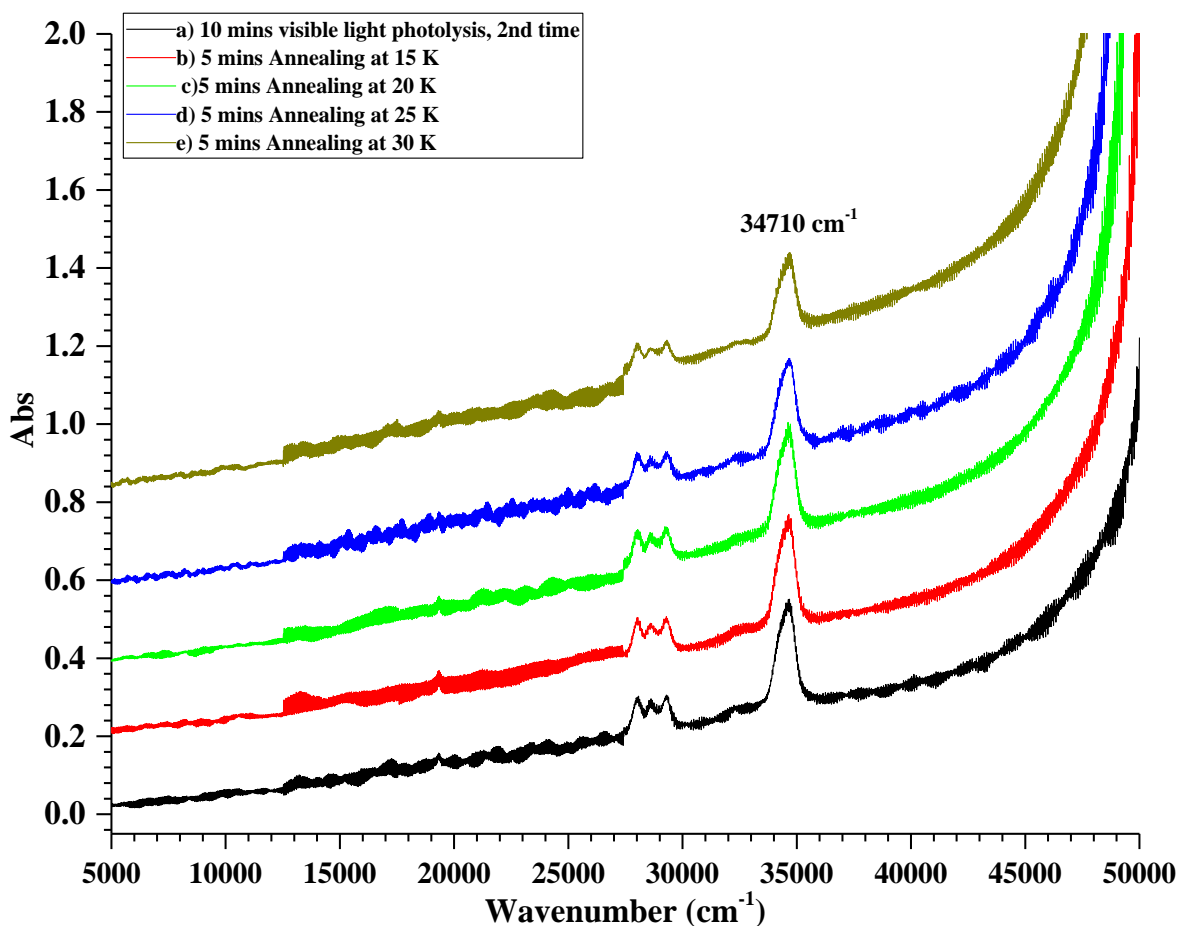
Figure 5.5: *UV/Vis spectra of Mo in a 1% Cl$_2$/Ar matrix (a) after further 10 mins visible light photolysis, (b) after 5 mins annealing at 15 K, (c) after 5 mins annealing at 20 K, (d) after 5 mins annealing at 25 K, (e) after 5 mins annealing at 30 K.*

5.2.4 FIR spectroscopy of Mo in a 10% Cl$_2$/Ar matrix

Infrared spectroscopy in the far−IR range was used to study the isolation of molybdenum chloride species in a solid argon matrix; molybdenum−chlorine stretching

modes are in the far−infrared region. The experiment was completed using 10% of Cl_2 in Ar gas mixture. The evaporation of molybdenum atoms was conducted at 3.38 V using 10 A of current. At first, a thin layer of 10% Cl_2/Ar gas matrix was laid down for 6 minutes onto the cooled inner window. The experiments were run at 9.9 K and at a pressure of 4 $\times 10^{-6}$ mbar. The vibrational spectrum was collected every 20 minutes, and the deposition process was carried out for a total of 110 minutes. The far−IR spectrum has no IR absorptions for molybdenum chlorides species. The matrix was photolysed and annealed to different temperature, no features for molybdenum chlorides species were observed. The experiment was repeated several times using a 2% Cl_2 in Ar gas mixture as well, yet no vibrational bands were observed. The lack of evidence for the formation of molybdenum chlorides from either the UV−vis or FIR spectra might be due to different potential explanations. The first explanation is that Mo atoms and Cl_2 do not react under cryogenic conditions. Moreover, there is a cage effect for chlorine in an argon lattice, where photolysis does not liberate many chlorine atoms. This is because the atoms produced upon photolysis are trapped in the same site as each other and because the chlorine bond strength is higher than fluorine, and so it is much thermodynamically stable. This was first observed for Cl_2/Ar by Bondybey and Fletcher,[66] and then confirmed by Kunz *et al.*[67] Another explanation is that the bands are very weak in the UV−vis spectra, and there is a possibility that the FIR instrument was not working properly as not long afterwards it failed to function at all.

5.2.5 FTIR spectroscopy of Mo in a 1% F_2/Ar matrix

FTIR spectroscopy was employed to investigate matrix isolated MoF_n molecules. Unfortunately, it was not possible to record the UV/vis spectra for the reaction of Mo atoms and F_2/Ar matrix, as the cryostat was not working properly. Molybdenum atoms were trapped in F_2 diluted in an Ar matrix so as to prepare different molybdenum fluoride molecules. A molybdenum filament was heated at 3.45 V with 19.5 A of electrical current. The experiments were carried out at a pressure of 8 $\times$ 10^{-6} mbar and the temperature of the matrix was 9.3 K. All evaporation conditions were very similar. Furthermore, all spectra were recorded at 2 cm^{-1} resolution and contained common impurity bands as described before in chapters 3 and 4.[68-71] Initially, a thin layer of 1% F_2/Ar gas matrix was placed down onto the cooled window of the cryostat; experiments were conducted with the filament of molybdenum exposed to 1% F_2/Ar matrix as well as protected from the 1% F_2/Ar gas by the 6 mm Cu disc, as presented in Figure 5.6. The peak at 737.4 cm^{-1} is common to both, and this peak can be assigned to MoF_6 molecules

based on previous work, where bands were observed at 737 cm^{-1} for an Ar matrix,[40, 42] and at 735 cm^{-1} by Acquista and Abramowitz.[47] The other features are very different, bands at 784, 767, 719, 707, 695, and 675 cm^{-1} were only observed when an exposed filament was used. The feature observed at 675 cm^{-1} can be due to MoF$_4$ species, which is in a good agreement with previous studies.[40, 42] The IR bands located at 767, 719, 707, and 695 cm^{-1} are most likely due to the formation of trimeric structures of molybdenum pentafluoride molecules; these bands were previously assigned to polymer of MoF$_5$ by Blinova and Predtechenskii,[42] and then assigned by Osin *et al.* to trimers of MoF$_5$ species.[40] The band at 784 cm^{-1} was observed by Blinova and Predtechenskii and assigned to a polymer form of MoF$_4$.[42] Bands at 573.6, 608.2, 617.1, 648.8, and 652.1 cm^{-1} are only observed when protected filament were observed cm^{-1} It seems that when the exposed Mo filament is used, F$_2$ molecules react with Mo on the hot surface of the filament and the species formed evaporate and are condensed with the F$_2$/Ar matrix at the cooled surface of the cryostat. Therefore, the protected filament was used for future experiments.
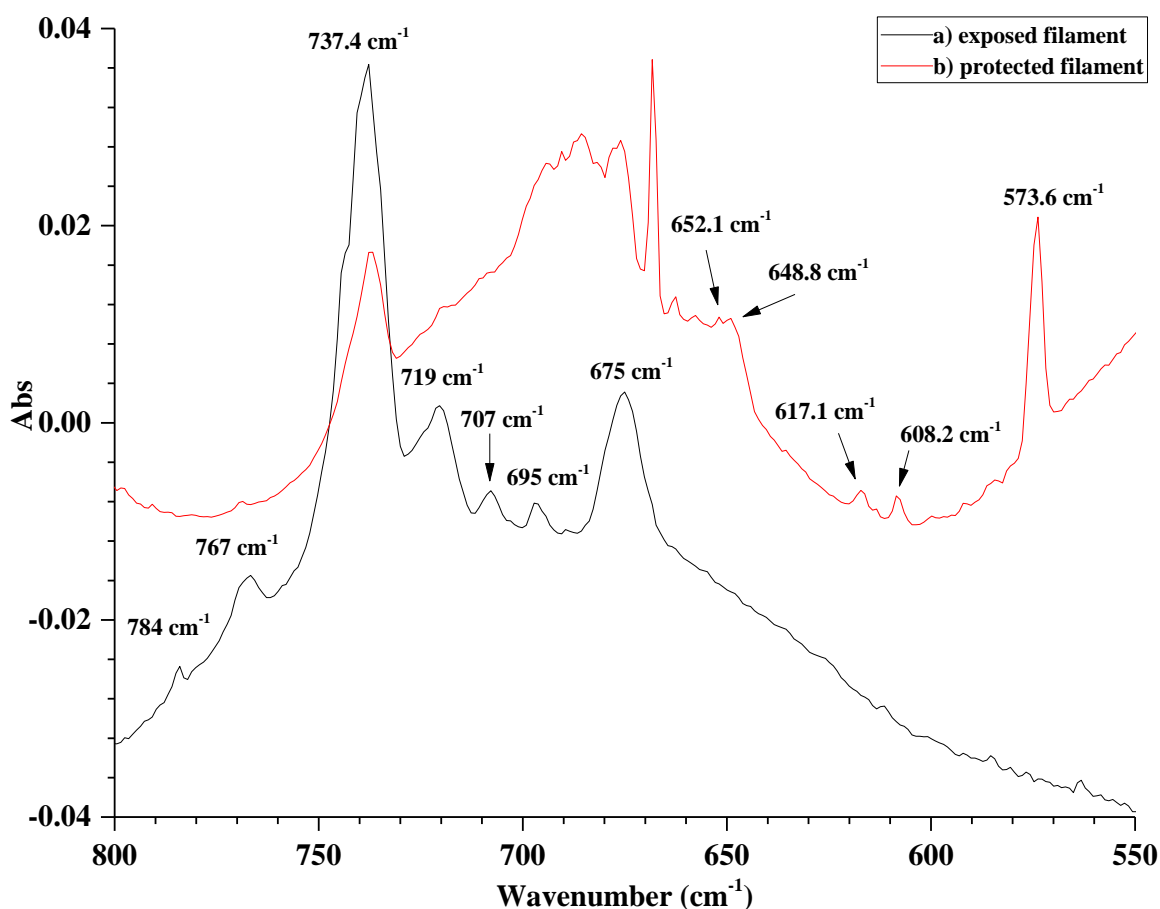
Figure 5.6: *FTIR spectra of atomic Mo isolated in 1% F$_2$/Ar matrix (a) exposed filament, (b) protected filament.*

Different concentrations of F_2 in argon gas were used to study the formation of molybdenum fluoride species in solid Ar matrices. Figure 5.7 shows the difference in interaction of molybdenum atoms with 2% F_2/Ar, 1% F_2/Ar, 0.5% F_2/Ar, and 0.2% F_2/Ar at 10 K using a protected filament. It would normally be expected that the higher oxidation state fluorides are more likely to be formed with higher concentrations of F_2 in the argon. The peak due to MoF_6 molecules at 737.4 cm^{-1} is present in 2% F_2/Ar and 1% F_2/Ar gas matrices, is only very weak in 0.5% F_2/Ar matrices and is absent in 0.2% F_2/Ar matrices.[40, 42, 47] Three IR absorption bands located at 694, 685, and 675 cm^{-1} with different intensity have been observed for 2% and 1% F_2/Ar matrices, while the band at 694 cm^{-1} has not been observed when a 0.5% F_2/Ar mixture was used (Figure 5.7c). In contrast, these features have not be found when an argon matrix doped with a low concentration (0.2%) of F_2 was used, as given in Figure 5.6d. It is most likely that these bands belong to different species of molybdenum, the feature observed at 675 cm^{-1} has previously been assigned to MoF_4 species,[40, 42] The feature at 573.6 cm^{-1} is observed for all concentration of F_2/Ar, but its relative intensity to the other features is highest for the lower concentrations of F_2 in the argon matrix. Furthermore, the bands at 608.2, 617.1, 648.8, and 652.1 cm^{-1} are observed for all concentration of F_2/Ar matrices, but their relative intensity is lowest for 2% F_2/Ar matrix. Therefore, the bands observed at 573.6, 608.2, 617.1, 648.8, and 652.1 cm^{-1} are most likely to be due to low valent molybdenum fluoride species, as they are observed when all concentration of F_2 in the argon matrix is used.
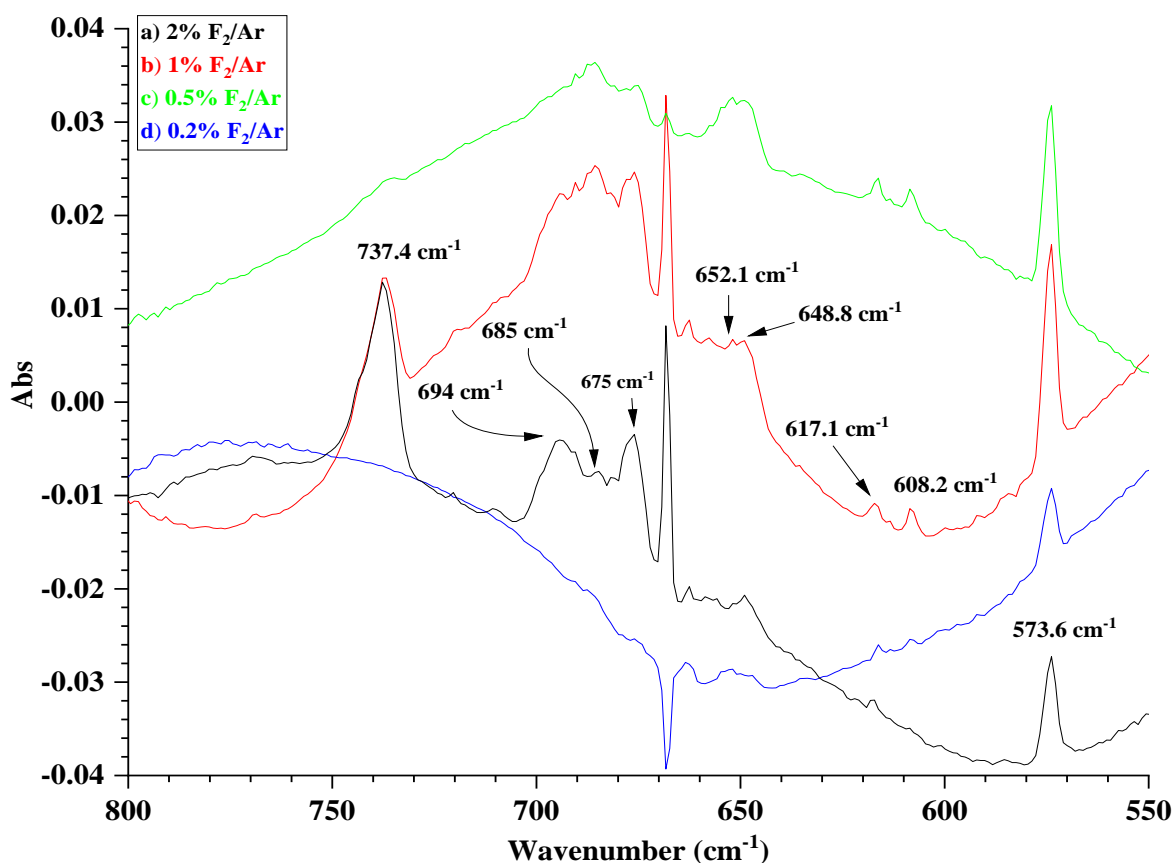
Figure 5.7: *FTIR spectra of atomic Mo isolated in (a) 2% F_2/Ar matrix, (b) 1% F_2/Ar matrix, (c) 0.5% F_2/Ar matrix, (d) 0.2% F_2/Ar matrix.*

An infrared spectrum recorded after 100 minutes of interaction of Mo atoms with an argon matrix doped with a low concentration (0.2%) of F_2 is presented in Figure 5.8a below. The spectrum shows an intense peak at 573.6 cm^{-1} and four less intense peaks at 608.2, 617.1, 648.8, and 652.1 cm^{-1}. Figure 5.8b represents the matrix after 10 minutes of visible light photolysis; there is no change in the intensity observed. The matrix was exposed to 200–410 nm and broadband photolysis as shown in Figures 3.8c and 3.8d, respectively. The intensity of peaks at 608.2, 617.1, 648.8, and 652.1 cm^{-1} increased slightly. Figure 3.8d demonstrates that all peaks have the same intensity when the matrix was photolysed with visible light again. The matrix was annealed to 15 K for 5 minutes, as illustrated in Figure 3.8e. The intensity of all observed features is the same. Figure 3.8f shows the matrix after 5 minutes of annealing to 20 K, the intensity of bands at 573.6, 617.1, and 652.1 cm^{-1} reduced. Nonetheless, the features at 608.2 and 648.8 cm^{-1} grew slightly, and also a new peak is observed at 737.4 cm^{-1} due to the formation of MoF_6 species.[40, 42, 47] The spectrum recorded after further 5 minutes of annealing to 25 K is displayed in Figure 3.8h. The intensity of the IR bands at 573.6, 608.2, 617.1, 648.8, and 652.1 cm^{-1} was diminished, while the peak at 737.4 cm^{-1} becomes more intense. Upon annealing the matrix to 30 K for minutes, the vibrational spectrum in Figure 3.8i displays

that the intensity of the peak at 573.6, 608.2, 617.1, 648.8, and 652.1 cm^{-1} decreased. On the other hand, the band at 737.4 cm^{-1} increased. It seems that the bands observed at 608.2 and 648.8 cm^{-1} belongs to same species. Similarly, the bands located at 617.1 and 652.8 cm^{-1}, exhibit persistent behaviour in intensity on photolysis and annealing. Furthermore, no bands were detected at 675, 685, 694 cm^{-1}, the feature at 737.4 cm^{-1} indicates that the formation of MoF$_6$ is very favourable with no evidence for peaks previously assigned to MoF$_3$, MoF$_4$, or MoF$_5$.
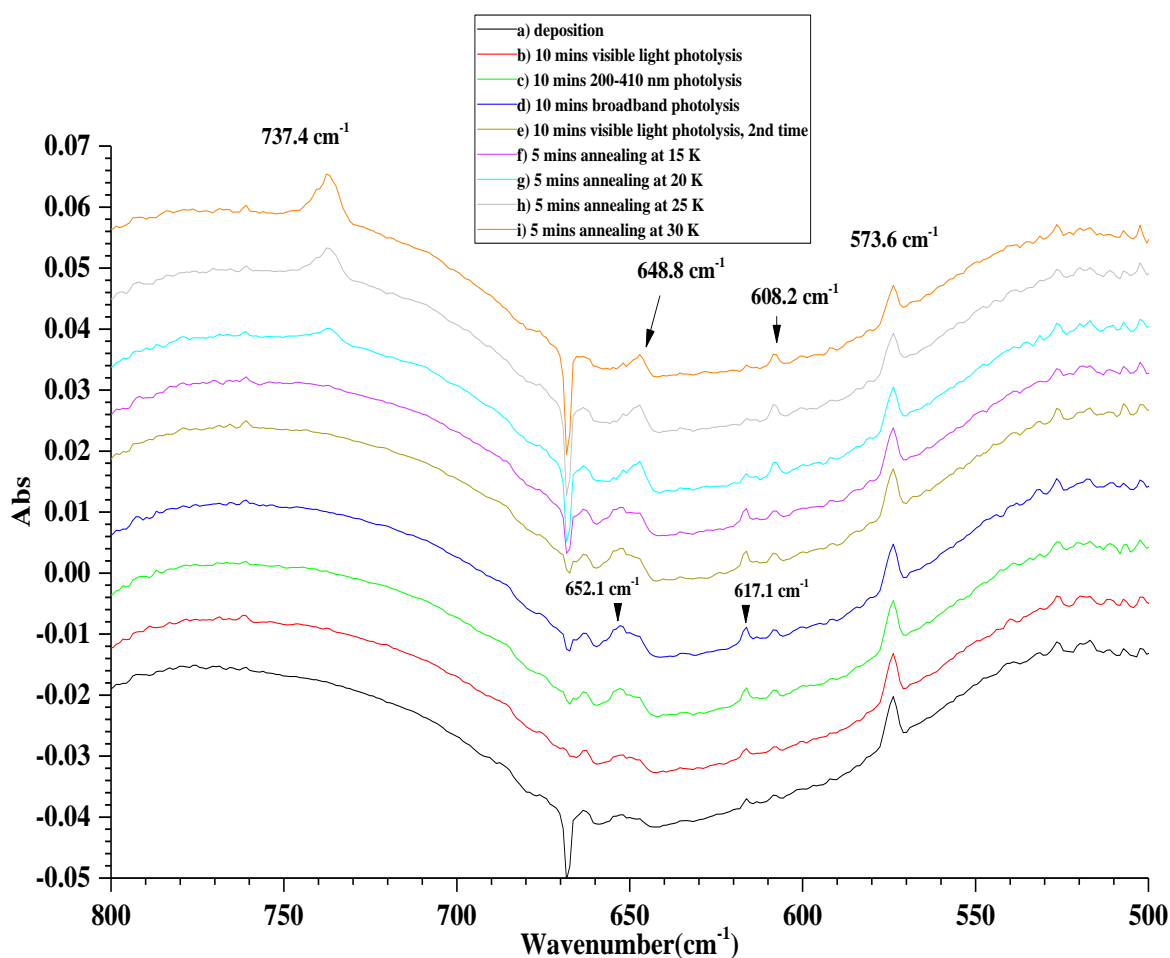
Figure 5.8: *FTIR spectra of atomic Mo in 0.2% F$_2$/Ar matrix (a) after deposition, (b) after 10 mins visible light photolysis, (c) after 10 mins 200−410 nm photolysis, (d) after 10 mins broadband photolysis, (e) after further 10 mins visible light photolysis, (f) after 5 mins annealing at 15 K, (g) after 5 mins annealing at 20 K, (h) after 5 mins annealing at 25 K, (i) after 5 mins annealing at 30 K.*

1% F$_2$/Ar was found to be the best concentration of matrix gas to be used, where it is optimum regarding to intensity and sharpness of peaks as well as containing all the peaks. An infrared spectrum run after 150 minutes of deposition is shown in Figure 5.9a. The observed peaks are tabulated in Table 5.2 below. The spectrum contains a strong sharp peak at 573.6 cm^{-1}, two weak bands are observed at 617 and 608 cm^{-1}, two medium bands at 648 and 652 cm^{-1}, a strong band at 675 cm^{-1}, three peaks are located at 675, 682,

94

and 694 cm^{-1}, the peak located at 737.4 cm^{-1} is attributed to the asymmetric stretching mode of MoF$_6$,[40, 42, 47] together with a very weak IR band at 769 cm^{-1}. Photolysis was carried out to produce more free fluorine atoms which disseminate throughout the matrix and react with both molybdenum and molybdenum fluoride species. As seen in Figure 5.9b, when the matrix was exposed to 10 minutes of visible light photolysis; the intensity of peak at 573.6 cm^{-1} was reduced slightly, while the band at 737.4 cm^{-1} increased. Figure 5.9c demonstrates the vibrational spectrum after 10 minutes of 200–410 nm photolysis. The IR bands have the same intensity; no change was noticed. The matrix was exposed to 10 minutes of broadband photolysis; the IR spectrum is presented in Figure 5.9d, the peak at 573.6 cm^{-1} decreased again, but the absorption bands at 685 and 737.4 cm^{-1} grew. Figure 5.9e illustrates the IR spectrum after exposure to visible light photolysis for 10 minutes; the intensity of all bands remained the same and no change was detected.

Table 5.2: Vibrational frequencies (cm^{-1}) observed and calculated of MoF$_n$ molecules in a matrix of Ar.

Assignments	Observed	Ref [47]	Ref [40]	Ref [42]	Calculated B3LYP/def2tzvpp
MoF	573.6 cm^{-1}	—	—	—	620.0 cm^{-1}
MoF$_2$	608.2 cm^{-1}, 648.8 cm^{-1}	—	—	—	635.0 cm^{-1}, 665.4 cm^{-1}
MoF$_3$	685.0 cm^{-1}	—	633 cm^{-1}	—	692.0 cm^{-1}
MoF$_4$	675.0 cm^{-1}	733 cm^{-1}	675 cm^{-1}	674.0 cm^{-1}	678.0 cm^{-1}
MoF$_5$	694.0 cm^{-1}	713 cm^{-1}, 683 cm^{-1}	694 cm^{-1}, 658 cm^{-1}	694.5 cm^{-1}, 658.0 cm^{-1}	650.0 cm^{-1}, 689.54 cm^{-1}, 761.51 cm^{-1}
MoF$_6$	737.4 cm^{-1}	735 cm^{-1}	736 cm^{-1}	737.0 cm^{-1}	734.1 cm^{-1}
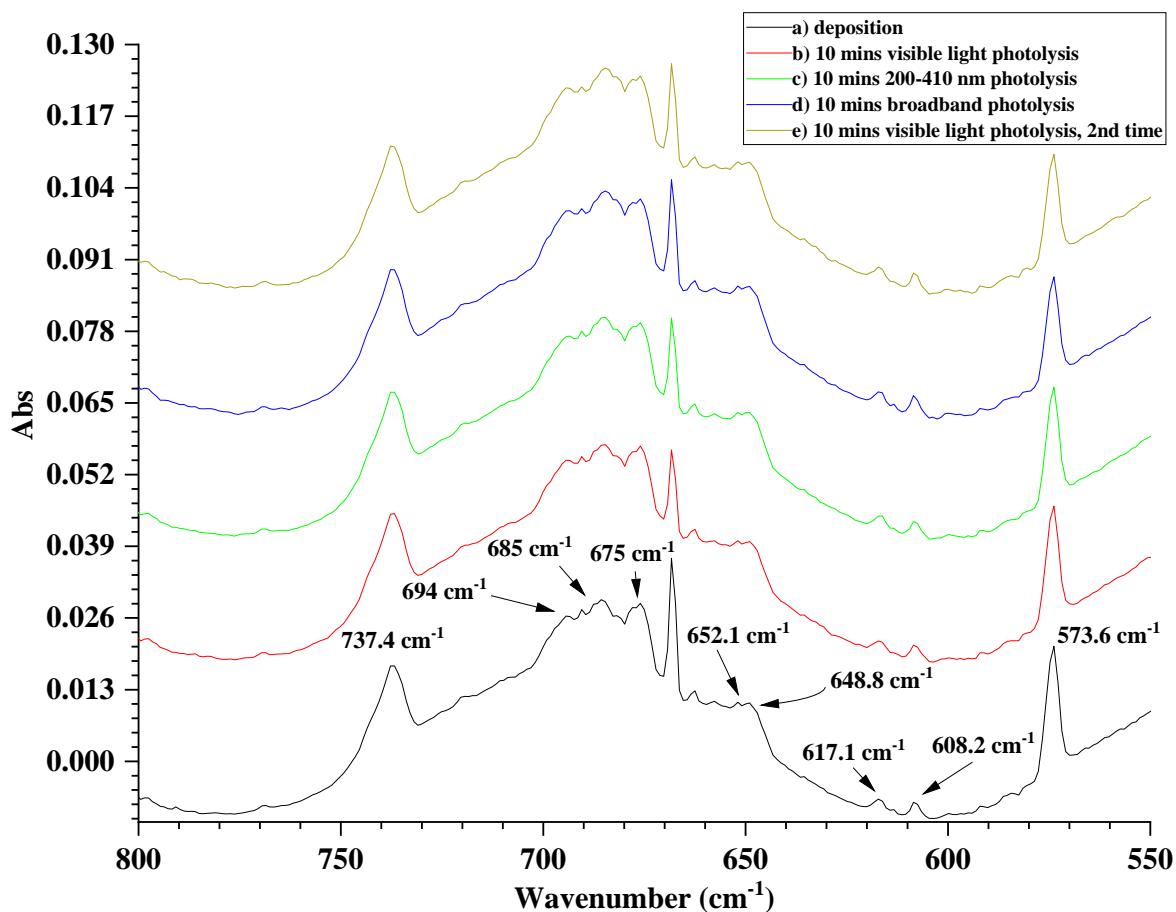
Figure 5.9: *FTIR spectra of atomic Mo in 1% F_2/Ar matrix (a) after deposition, (b) after 10 mins visible light photolysis, (c) after 10 mins 200−410 nm photolysis, (d) after 10 mins broadband photolysis, (e) after further 10 mins visible light photolysis.*

       The annealing process was undertaken after photolysis. The matrix becomes slightly soft allowing trapped molecules to either reorient or migrate through the matrix. Figure 5.10b displays the matrix after annealing to 15 K for 5 minutes, the bands at 652.1, 648.8, 617.1 and 608.2 cm^{-1} reduced in intensity. Oppositely, the peak at 737.4 cm^{-1} grew. Figure 5.10c demonstrates the IR spectrum after 5 minutes of annealing at 20 K. The features located at 573.6, 617.1, and 652.1 cm^{-1} decreased in intensity, whilst peaks at 608.2 and 648.8 cm^{-1} increased. Furthermore, the band at 737.4 cm^{-1} significantly increased in intensity. Upon annealing at 25 K for 5 minutes; the IR spectrum in Figure 5.10d reveals that the intensity of the IR peaks at 573.6, 608.2 and 648.8 cm^{-1} diminished. However, the bands at 694 cm^{-1} became bigger. Also, the band at 737.4 cm^{-1}, assigned to matrix isolated MoF_6 molecules, increased considerably.[40] Further annealing at 30 K for 5 minutes is seen in Figure 5.10e, the absorptions at 573.6, 608.2, and 648.8 cm^{-1} decreased. Additionally, the intensity of the peak at 685 cm^{-1} decreased, whereas, the band at 737.4 cm^{-1} increased. Figure 5.10f displays the IR spectrum of the matrix after it was warmed to 35 K for 5 minutes, the features located at 737.4 and 694 cm^{-1} became

more intense, whereas peaks at 573.6, 608.2 and 648.8 cm^{-1} were reduced in intensity. The peak at 685 cm^{-1} disappeared. It is noteworthy that the band at 737.4 cm^{-1} due to MoF$_6$ increased the most on annealing.
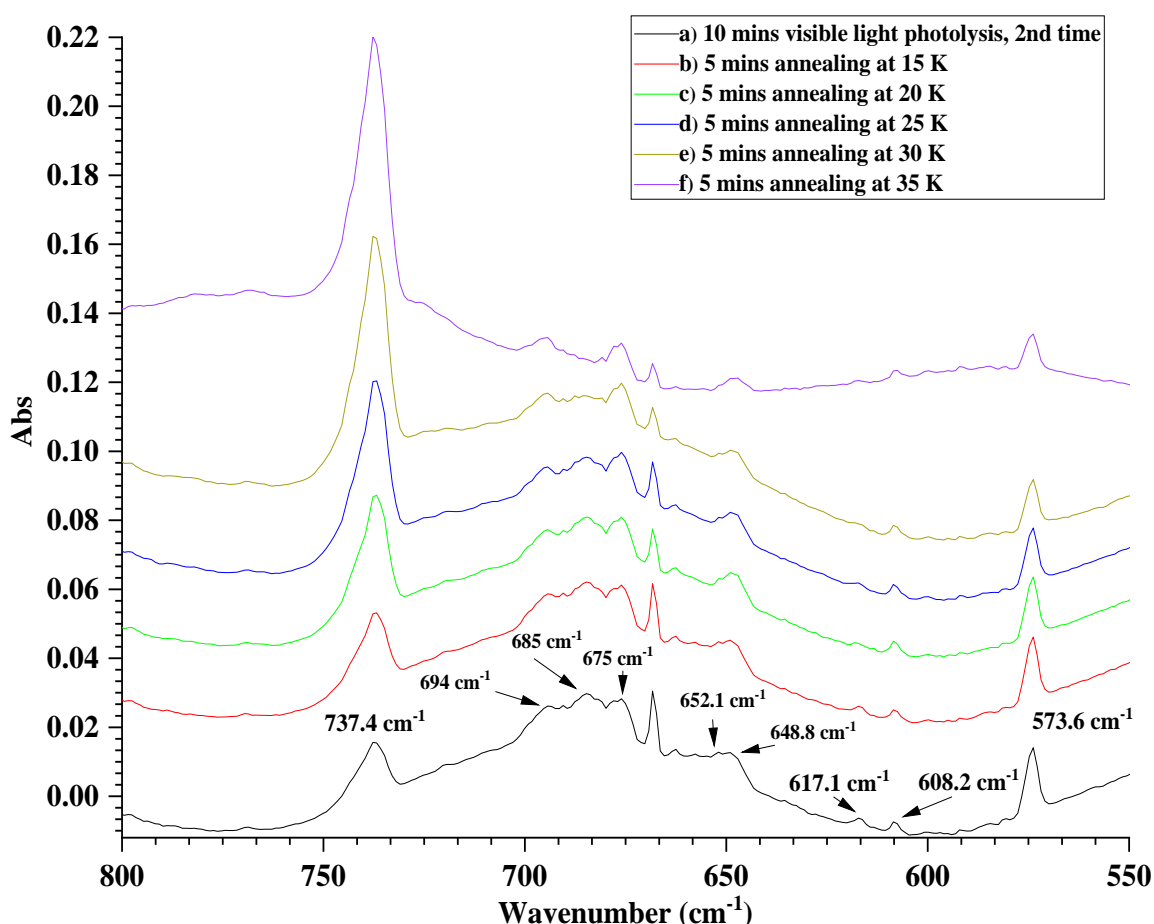
Figure 5.10: *FTIR spectra of atomic Mo in 1% F$_2$/Ar matrix (a) after further 10 mins visible light photolysis, (b) after 5 mins annealing at 15 K, (c) after 5 mins annealing at 20 K, (d) after 5 mins annealing at 25 K, (e) after 5 mins annealing at 30 K, (f) after 5 mins annealing at 35 K.*

Computational calculations were carried out for each molybdenum fluoride using B3LYP/def2tzvpp within G09W to help with the assignment of the peaks in the IR spectrum. The calculated data (Table 5.2) suggest that MoF molecules have one peak at 620 cm^{-1}, molybdenum difluoride has two bands located at 665.4 and 635.0 cm^{-1}. MoF$_3$ has one feature at 692.0 cm^{-1} and MoF$_4$ has also one band observed at 678.0 cm^{-1}, these calculations are in line with a recent computational work undertaken by Sliznev and Belova who calculated the vibrational frequencies of MoF$_3$ and MoF$_4$ at 706.0 and 684.0 cm^{-1}, respectively.[25] The authors predicted the difference value between calculated and experimental bands equals 10 wavenumbers, and so suggesting the experimental IR bands for MoF$_3$ and MoF$_4$ at 696.0 and 674.0 cm^{-1}, respectively. Therefore, Sliznev and Belova

assigned the band observed at 694.0 cm^{-1} by Osin *et al.*[40, 41] to MoF$_3$ in solid Ar Matrix rather than 633 cm^{-1}.

The calculations of MoF$_5$ were very complicated and took a long time to reach the ground state minimum. MoF$_5$ was suggested to have three bands at 761.51, 689.54, and 650.0 cm^{-1}. The theoretical data suggested the vibrational frequency of MoF$_6$ species as a single IR absorption band at 734.1 cm^{-1}. Additionally, the computational calculations confirmed that the geometry of MoF$_6$ molecules is (O$_h$) octahedral symmetry, see Table 5.3, and the configuration of MoF$_5$ species to be distorted trigonal bipyramid (C$_{2v}$) as reported before (Figure 5.11).[50, 51] Moreover, the molecular structure of MoF$_4$ as well as MoF$_3$ molecules was predicted to be tetrahedral and trigonal planar, respectively. These results were also found consistent with previous work.[25, 51, 53, 55] The bond angle in MoF$_2$ species was calculated as 132° suggested that the symmetry of molybdenum difluorides is bent. This unusual geometry has been predicted previously by Siegbahn who predicted a bond angle of 140° for MoF$_2$ while all the rest of the difluorides of the second row transition metals were linear, apart from YF$_2$.[24] The unusual geometry is most likely due to a Renner−Teller effect as observed for CrF$_2$[72] and CrCl$_2$.[73]

The position of the molybdenum fluoride peaks, as well as the characteristic isotope patterns of molybdenum fluoride molecules at two different half−widths, 0.5 cm^{-1} and 1.0 cm^{-1}, are illustrated in Figures 5.12 and 5.13 below. Additionally, the computer simulated IR spectrum for all molybdenum fluoride species is given in Figure 5.14. Furthermore, the bond lengths, bond angles and the electronic ground state are calculated and the data are listed in Table 5.2 below.

Table 5.3: The calculated geometry of molybdenum fluoride molecules

Assignments	Molecular structure	Electronic ground state	F–Mo–F Bond angles	Mo–F Bond lengths (Å)
MoF	–	$^6\Sigma$	–	1.898
MoF_2	Bent	$^5B_2$	132º	(1.878)×2
MoF_3	Trigonal planar	$^4A_1{}'$	(120º)×3	(1.861)×3
MoF_4	Tetrahedral	$^3A_1$	(109.47º)×6	(1.86)×4
MoF_5	Distorted trigonal bipyramid	^2A	110.46º, 125.81º, 123.71º, 90.00º, 90.23º, 89.71º, 90.01º, 90.22, 89.73º, 179.42 º	1.819, 1.801, 1.822, 1.876, 1.876
MoF_6	Octahedral	$^1A_{1g}$	(90º)×12	(1.829)×6
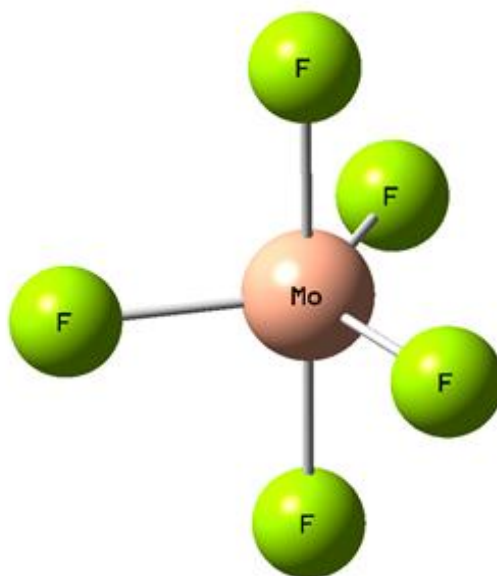
Figure 5.11: *Calculated (B3LYP/def2tzvpp) geometric structure of MoF₅.*
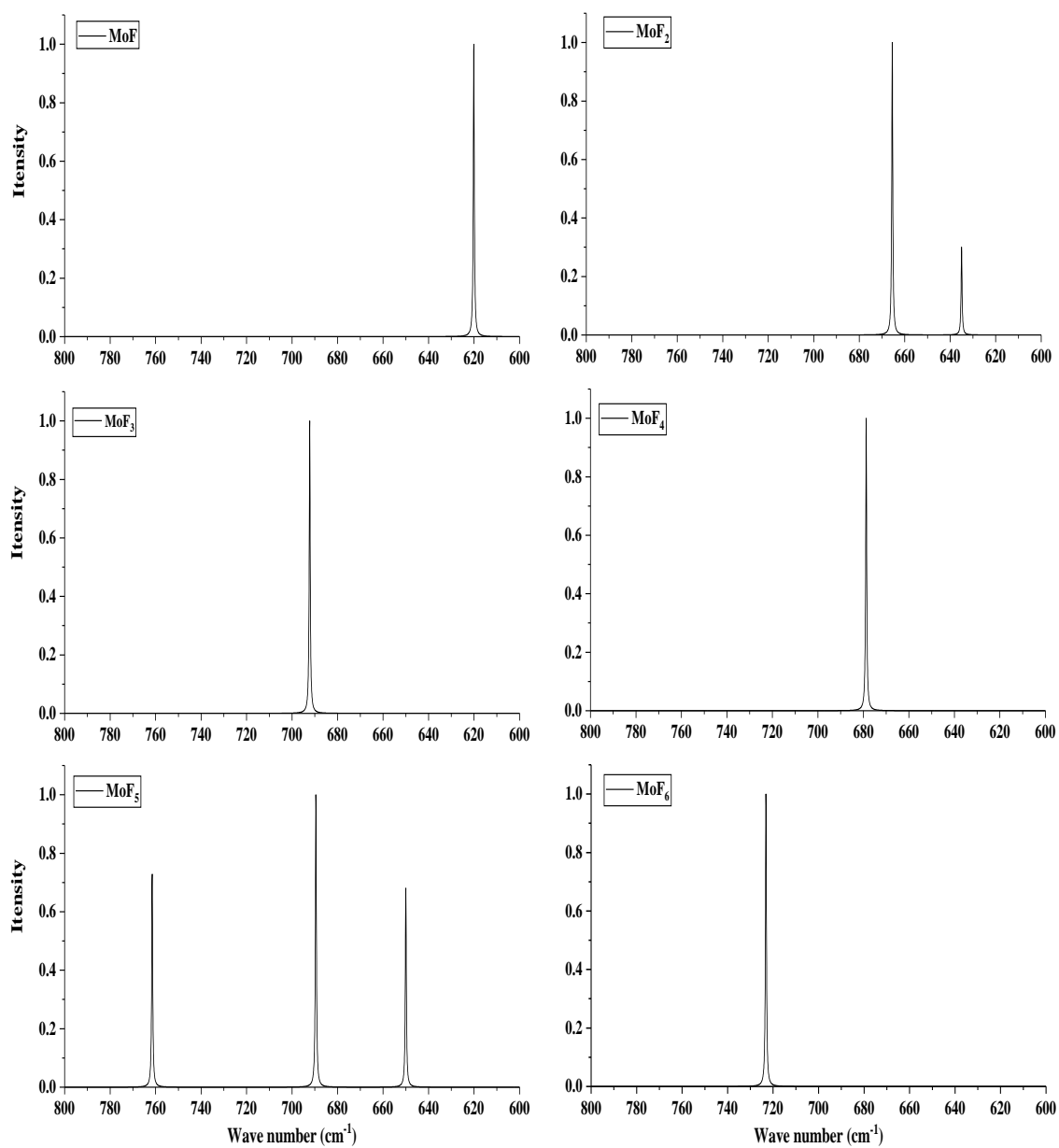
Figure 5.12: *Calculated (B3LYP/def2tzvpp) IR spectra of Mo fluoride molecules for ^{98}Mo as most intense isotope.*
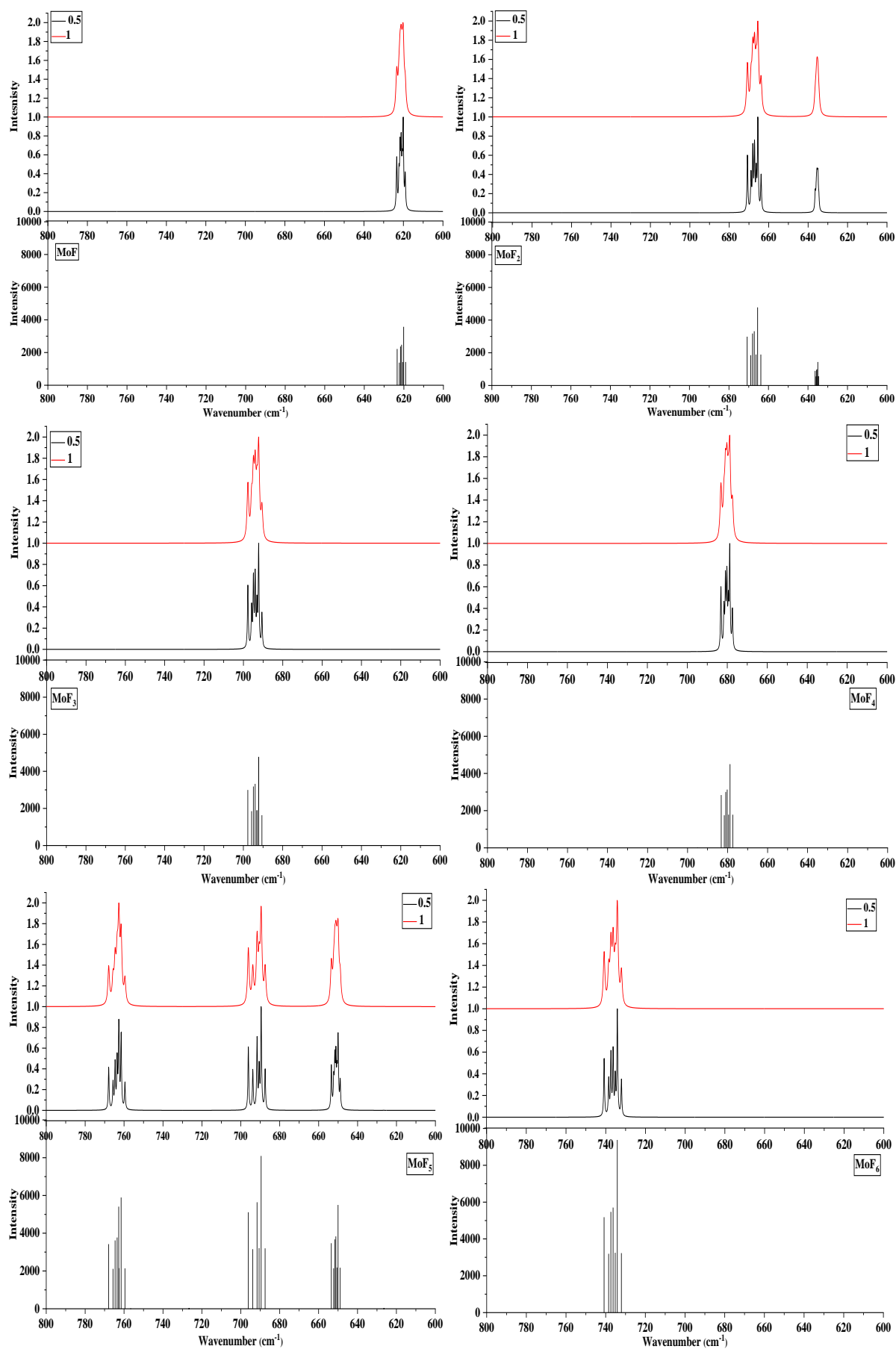
Figure 5.13: *Calculated (B3LYP/def2tzvpp) IR spectra of isotopes of Mo fluoride molecules at two different half−widths 0.5 and 1.0 cm^{-1}.*
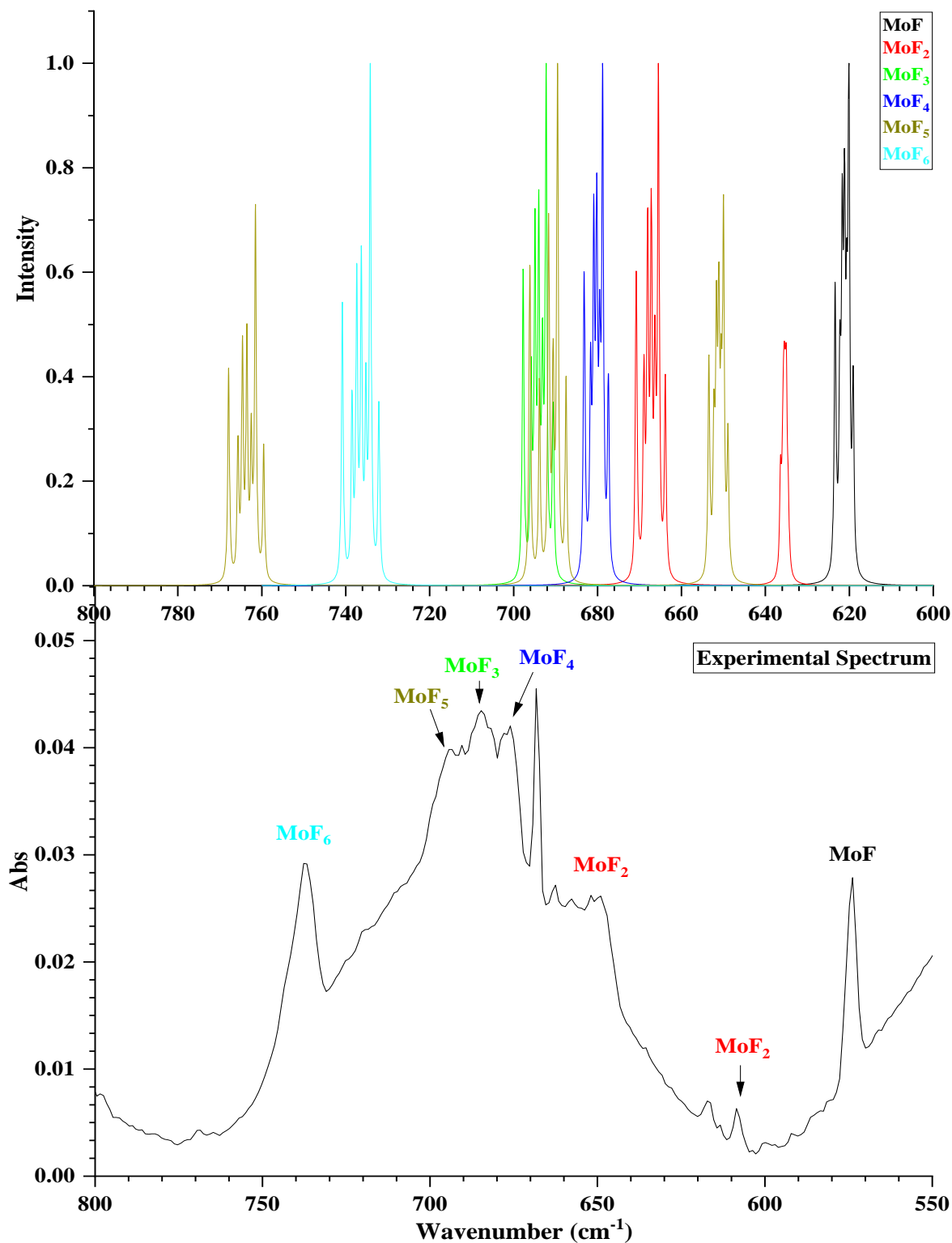
Figure 5.14: *Calculated (B3LYP/def2tzvpp) IR spectra of all Mo fluoride molecules and their isotope patterns at half−width 0.5 cm⁻¹ and experimental FTIR spectrum of atomic Mo in 1% F₂/Ar matrix.*

The experimental as well as the theoretical work indicates that the IR absorption peak observed at 737.4 cm^{-1} is due to the asymmetric stretching mode of MoF$_6$, and this assignment is consistent with previous studies.[40, 42, 47] The splitting of this peak as seen in Figure 5.15a is related to the isotope fine structure for MoF$_6$; ^{100}MoF$_6$, ^{98}MoF$_6$, ^{97}MoF$_6$,

$^{96}MoF_6$, $^{95}MoF_6$, and $^{92}MoF_6$. The band observed at 573.6 cm^{-1} with very limited molybdenum isotopic structure is most likely due to MoF molecules as this is expected to be the molybdenum fluoride with the lowest Mo−F stretching frequency. This band has not been reported in any previous study, athough it looks like the band labelled F and unassigned in the recent experimental work conducted by Wei *et al.* which they claim it was observed in the reaction of Mo and OF$_2$ experiments.[57] The consistent change in intensity of the bands at 648.8 and 608.2 cm^{-1} on photolysis and annealing implies that these bands belong to same species, which on the basis of the calculations is most likely to be a bent MoF$_2$ species. The vibrational frequency at 608.2 cm^{-1} shows a lack of molybdenum isotopic structure (Figure 5.15c), as it is the symmetric stretching mode which involves limited motion of the molybdenum atom. Furthermore, the bands at 652.1 and 617.1 cm^{-1} which have similar relative intensity and isotope patterns to those at 648.8 and 608.2 cm^{-1}, but which decreased after annealing to 20 K, are most probably due to site effects of MoF$_2$ molecules, which have also been observed for TiF$_2$ [74] and PdF$_2$.[75] This is the first observation of the vibrational modes for MoF and MoF$_2$ in matrices, or the first time in any phase. The literature data for the remaining MoF$_3$, MoF$_4$ and MoF$_5$ species are not unambiguous. The features between 694.0 and 675.0 cm^{-1} in the experimental spectra are assigned to MoF$_5$, MoF$_4$, and MoF$_3$ species and their characteristic isotope patterns (Figure 5.15c). The band at 685.0 cm^{-1} has a higher relative intensity during deposition using 0.5%, and 1% F$_2$/Ar gas matrices, and also disappeared on annealing suggested that this peak is due MoF$_3$ species, which is in agreement with the calculated band at 692.0 cm^{-1} for MoF$_3$, where the value of calculation error equals 7 cm^{-1}. Moreover, this band has not been reported previously in literature data, and the assignment is compatible with the theoretical work by Sliznev and Belova predicted the IR absorption band of MoF$_3$ at 694.0 cm^{-1}.[25] The band at 675.0 cm^{-1} could be due to MoF$_4$ molecules, as this has a higher relative intensity in the more concentrated matrices, and on annealing. Furthermore, the assignment is corresponding to previous literature data.[25, 40, 42] The feature at 694.0 cm^{-1} was observed during deposition using high concentration (1% and 2%) of F$_2$/Ar gas matrices, and its behaviour on annealing indicated that this band is related to one molecule and it could molybdenum pentafluoride. This band grew after annealing as well as the band of MoF$_6$ at the 737.4 cm^{-1}; it is more likely because of reaction of free fluorine atoms with trapped low valent molybdenum fluoride molecules. This result is in very good agreement with previous work carried out by Blinova and Predtechenskii who stated that the monomer form of MoF$_5$ molecules exhibits frequencies at 693.5 and 658.0 cm^{-1},[42] which was then confirmed by Osin *et al.*[40] It is

103

noteworthy that in previous studies the relative intensity of the peak obtained at 658.0 cm^{-1} is very weak comparing with the band at 693.5 cm^{-1}.[40, 42] Therefore, the peak with high relative intensity is only observed in the spectrum at 694.0 cm^{-1}, while the weak vibrational band at 658.0 cm^{-1} does not appear in the spectrum. Nonetheless, a previous experiment study conducted by Acquista *et al.* indicated that the vapour of MoF$_5$ consists of trimers, but by superheating they obtained monomeric MoF$_5$.[47] The study suggested that vibrational frequencies of monomeric MoF$_5$ are located at 713, and 683 cm^{-1} and the trimer forms of molybdenum pentafluorides at 768, 716, and 704 cm^{-1}.[47] The result is not in agreement with this study. The calculations suggested that MoF$_5$ has three absorptions at 761.51, 689.54, and 650.0 cm^{-1}, which are mismatching with the experimental data obtained.
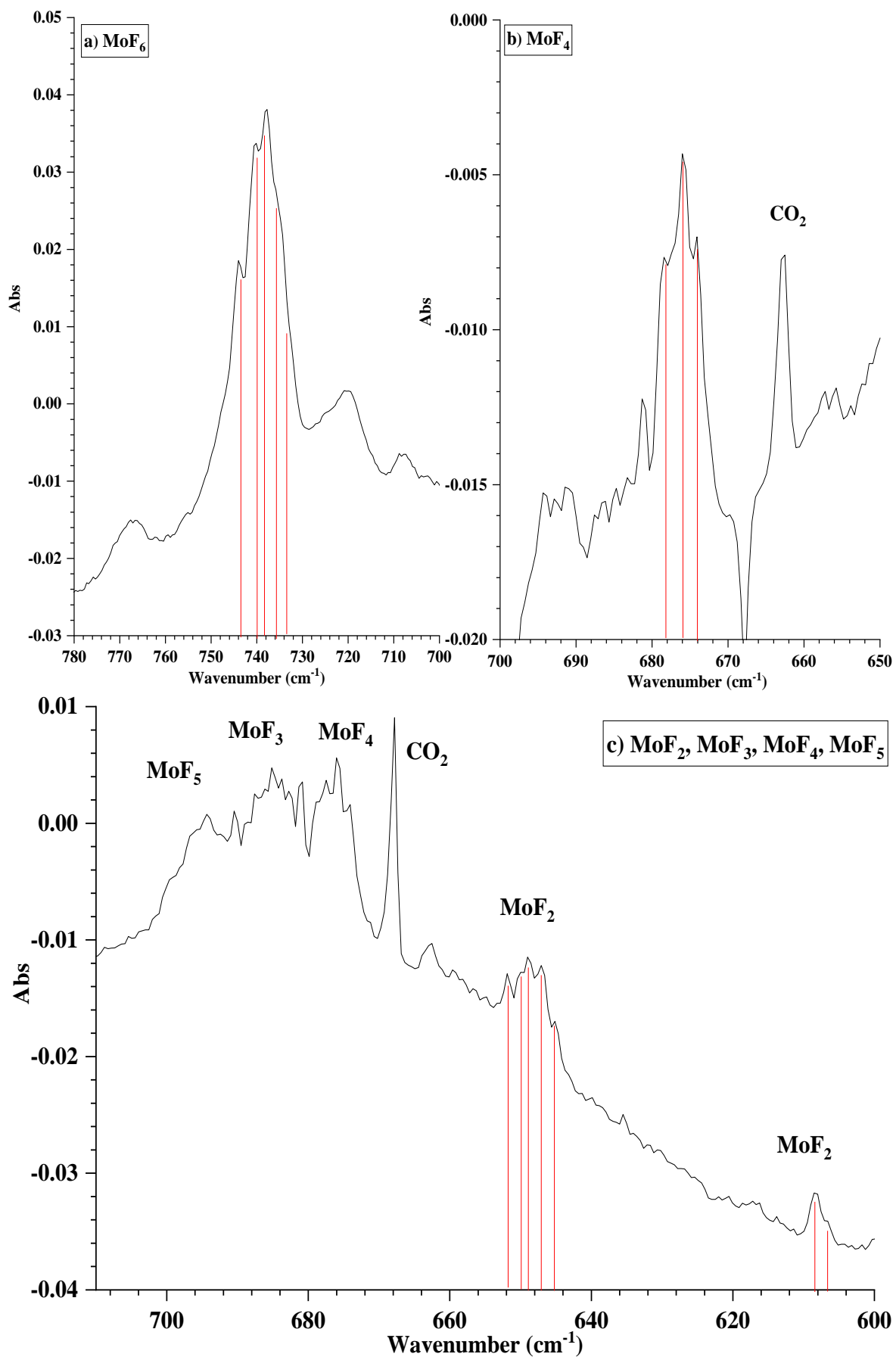
Figure 5.15: *IR spectra of MoF$_n$ molecules and their isotope patterns at 1 cm^{-1} resolution.*

5.2.5.1 Thermodynamic study

Thermodynamic calculations have been carried out to study the relative stability of molybdenum fluoride species regarding to the reaction between Mo atoms and F_2 molecules. As illustrated in Figure 5.16, the overall reaction enthalpy of Mo atoms and F_2 molecules indicates that the MoF_6 species have the lowest energy. Basically, if there is enough fluorine, we expect MoF_6 molecules to be formed, and this explains the rapid increase in intensity of the 737.4 cm^{-1} peak on annealing. The stepwise reaction enthalpy for reaction between Mo atoms and F_2 molecules is given in Figure 5.17, the results manifest that MoF_2 lies at a point above MoF and MoF_3. According to disproportionation phenomenon, it is less stable compared to MoF and MoF_3. On the other hand, MoF_3 lies on a point below MoF_2 and MoF_4, it is more stable than MoF_2 and MoF_4. Both MoF_2 and MoF_4 molecules have a tendency to comproportionate to MoF_3, while MoF_4 is above the line that connects MoF_3 and MoF_4. Similarly, MoF_5 lies above the line that connects MoF_4 and MoF_6. The thermodynamics of the reactions were also achieved using one fluorine atom instead of half fluorine molecules; it was found that the reaction enthalpy tends to decrease.
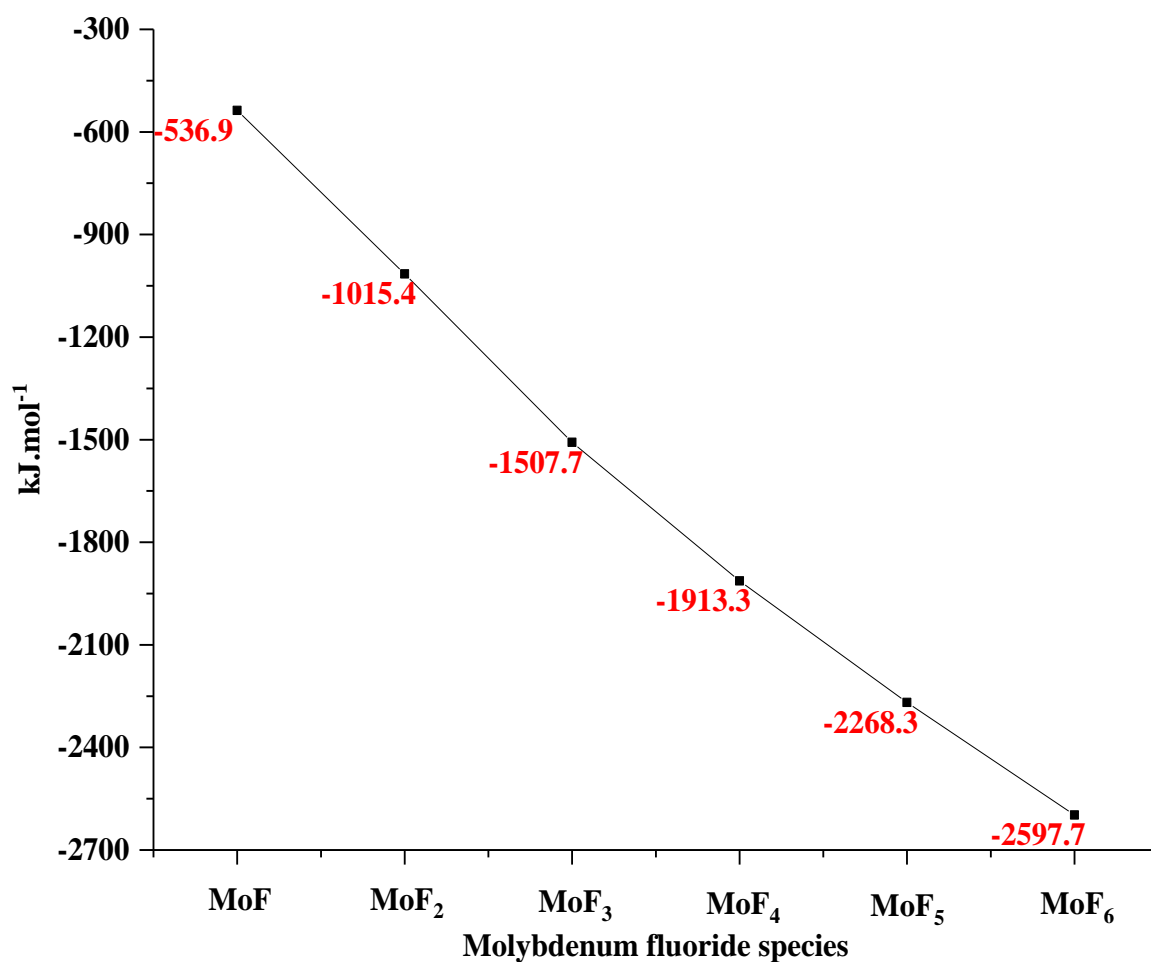
Figure 5.16: *Overall reaction enthalpy of MoF$_n$ species for the reaction of Mo atoms and F$_2$ molecules.*
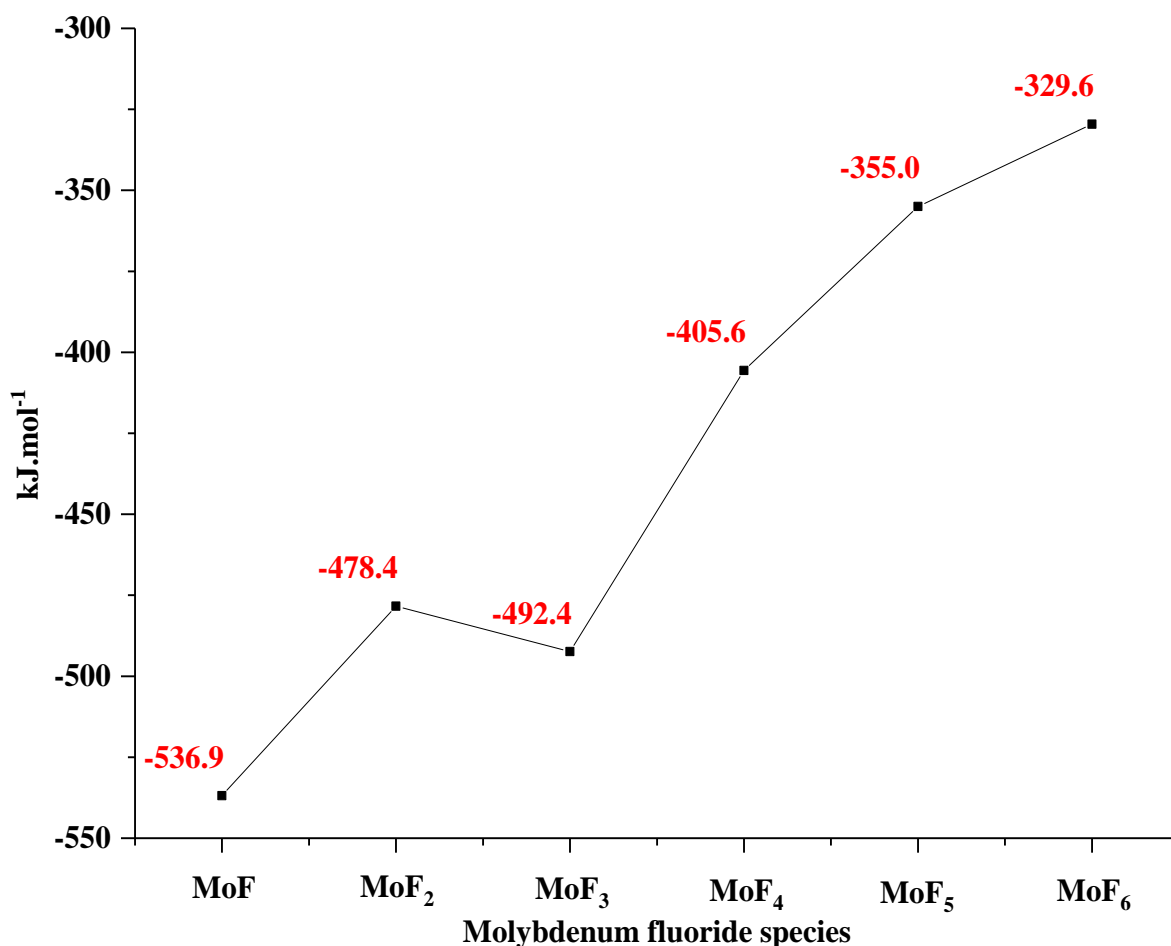
Figure 5.17: *Stepwise reaction enthalpy of MoF$_n$ species for the reaction of Mo atoms and F$_2$ molecules.*

5.3 Conclusion

The optical spectrum of molybdenum atoms isolated in a matrix of solid argon contains three medium intensity peaks at 28020, 28600, 29300 cm^{-1} and a strong asymmetric peak at 34710 cm^{-1}, the spectrum obtained is in a good agreement with literature data.[1, 2] Additionally, the two very weak bands at 19300 and 32800 cm^{-1} are related to Mo$_2$ dimers.[2, 5, 6] The ground state of molybdenum is $^7S_3$ (4d^{5}5s^1).[2] The photolysis process has no effect on the UV/vis spectrum. Nonetheless, the annealing process led to the reduction of intensity of peaks. UV/vis spectroscopy and FIR spectroscopy were used to identify any interaction between Mo atoms and Cl$_2$ in a matrix of solid argon, both techniques indicate that there are no bands characteristic of molybdenum chlorides. It seems that Mo atoms and Cl$_2$ do not react under cryogenic conditions because of the spin states of Mo as well as Cl$_2$. Moreover, the cage effect for chlorine in an argon lattice, where photolysis does not liberate many chlorine atoms because the chlorine band strength is higher than fluorine, and so it is much less

thermodynamically favourable.[66, 67] Also, it could be that the absorption bands are very weak in the UV−vis spectra, and that the FIR instrument was not working properly.

The vibrational spectra of molybdenum atoms trapped in a matrix of argon doped with different concentrations of fluorine were obtained. The IR absorption band assigned to the MoF species was detected at 573.6 cm^{-1}, the bands observed at 648.8 and 608.2 cm^{-1} are assigned to MoF_2 in conjunction with site effects observed at 652.1 and 617.1 cm^{-1}. The band at 685.0 cm^{-1} has been assigned to MoF_3, while the band at 675.0 cm^{-1} is due to MoF_4.[40, 42] The features observed at 694.0 cm^{-1} are probably for MoF_5 molecules, the asymmetric stretching mode of MoF_6 molecules was recorded at 737.4 cm^{-1}.[40, 42, 47] The computational calculations defined the geometry of MoF_6 molecules as O_h octahedral symmetry, and the configuration of MoF_5 species to be distorted trigonal bipyramid (C_{2v}). Moreover, the symmetry of MoF_4 molecules was predicted to be tetrahedral, while MoF_3 species was suggested as trigonal planar. The bond angle in MoF_2 molecules was 132° indicating the geometrical structure is bent.

5.4 Summary

First observation of MoF in solid Ar matrix; the IR absorption band was detected at 573.6 cm^{-1}. First observation of MoF_2 in solid Ar matrix. The two bands due to MoF_2 were observed at 648.8 and 608.2 cm^{-1}. The geometry of MoF_2 is bent. A band at 685.0 cm^{-1} was assigned to MoF_3 in line with some previous calculations.

5.5 References

1.   F. Schoch and E. Kay, *J. Chem. Phys.*, 1973, **39**, 718-728.
2.   D. W. Green and D. M. Gruen, *J. Chem. Phys.*, 1974, **60**, 1797-1801.
3.   W. D. Hewett, Jr., J. H. Newton and W. Weltner, Jr., *J. Phys. Chem.*, 1975, **79**, 2640-2649.
4.   W. E. Klotzbücher and G. A. Ozin, *J. Am. Chem. Soc.*, 1978, **100**, 2262-2264.
5.   J. K. Bates and D. M. Gruen, *J. Mol. Spectrosc.*, 1979, **78**, 284-297.
6.   W. E. Klotzbücher and G. A. Ozin, *Inorg. Chem.*, 1980, **19**, 3776-3782.
7.   T. Foosnaes, M. J. Pellin and D. M. Gruen, *J. Chem. Phys.*, 1983, **78**, 2889-2898.
8.   M. J. Pellin, T. Foosnaes and D. M. Gruen, *J. Chem. Phys.*, 1981, **74**, 5547-5557.
9.   C. Steinbrüchel and D. M. Gruen, *Surf. Sci. Rep.*, 1981, **106**, 160-164.
10.   C. Steinbrüchel and D. M. Gruen, *J. Chem. Phys.*, 1981, **74**, 205-214.
11.   J. Lon B. Knight and J. Steadman, *J. Chern. Phys.* , 1982, **76**, 3378-3384.
12.   M. J. Pellin, D. M. Gruen, T. Fisher and T. Foosnaes, *J. Chem. Phys.*, 1983, **79**, 5871-5886.
13.   G. H. Jeong and K. J. Klabunde, *J. Chem. Phys.*, 1989, **91**, 1958-1971.
14.   M. J. Pellin, T. Foosnaes and D. M. Gruen, *ACS Symp. Ser.*, 1982, **179**, 219-227.
15.   D. Roser and M. Vala, *Chem. Phys.*, 1993, **173**, 267-273.
16.   M. Frankowski, G. Sliwinski and N. Schwentner, *Proc. SPIE-Int. Soc. Opt. Eng.*, 2001, **4397**, 104-108.
17.   L. Fang, B. Davis, H. Y. Lu, X. Y. Chen, X. L. Shen and J. R. Lombardi, *Chem. Phys. Lett.*, 2002   **352**, 70-74.
18.   I. A. Topol, V. M. Kovba and E. L. Osina, *Theor. Chim. Acta*, 1984, **64**, 217–228.
19.   J. S. Ogden, W. Levason, E. G. Hope, J. T. Graham, D. M. Jenkins and R. M. Angell, *J. Mol. Struct.*, 1990, **222**, 109-119.
20.   A. K. Brisdon, J. T. Graham, E. G. Hope, D. M. Jenkins, W. Levason and J. S. Ogden, *J. Chem. Soc., Dalton Trans.*, 1990, 1529-1532.
21.   R. K. Bellingham, J. T. Graham, P. J. Jones, J. R. Kirby, W. Levason, J. S. Ogden, A. K. Brisdon and E. G. Hope, *J. Chem. Soc., Dalton Trans.*, 1991, 3387-3392.
22.   K. Fægri, K. G. Martinsen, T. G. Strand and H. V. Volden, *Acta Chem. Scand.* , 1993, **47**, 547-553.
23.   M. Mercer *Chem. Commun. (London)*, 1967, 119.
24.   P. E. M. Siegbahn, *Theor. Chim. Acta*, 1994, **87**, 441-452.
25.   V. V. Sliznev and N. V. Belova, *J. Mol. Struct.*, 2017, **1132**, 73-87.
26.   H. H. Claassen, G. L. Goodman, J. H. Holloway and H. Selig, *J. Chem. Phys.*, 1970, **53**, 341-348.
27.   H. E. Bass, V. Jensen and J. Ezell, *J. Chem. Phys.*, 1982, **77**, 4164-4168.
28.   D. E. Onopko, *Khimicheskaya Fiz.*, 1986, **5**, 1572-1574.
29.   A. Y. Borshchevskii, O. V. Boltalina, I. D. Sorokin and L. N. Sidorov, *J. Chem. Thermodyn.*, 1988, **20**, 523-537.
30.   P. Mercea, V. Tosa and Z. Gulacsi, *Rev. Roum. Phys.*, 1988, **33**, 289-308.
31.   E. Miyoshi, Y. Sakai, A. Murakami, H. Iwaki, H. Terashima, T. Shoda and T. Kawaguchi, *J. Chem. Phys.*, 1988, **89**, 4193-4299.
32.   M. Takami and Y. Matsumoto, *Mol. Phys.*, 1988, **64**, 645-658.
33.   R. D. Hunt, L. Andrews and L. Mactoth, *J. Phys. Chem.*, 1991, **95**, 1183-1188.
34.   R. D. Hunt, L. Andrews and L. M. Toth, *Inorg. Chem.*, 1991, **30**, 3829-3832.
35.   J. W. Hovick and L. S. Bartell, *J. Phys. Chem. B*, 1998, **102**, 534-539.

36. L. Zarkova and P. Pirgov, *J. Phys. B-At. Mol. Opt. Phys.*, 1996, **29**, 4411-4422.
37. F. Guillot, C. Dezarnauddandine, M. Tronc, A. Lisini, P. Decleva and G. Fronzoni, *Chem. Phys.*, 1995, **191**, 289-302.
38. H. Nakai, H. Morita, P. Tomasello and H. Nakatsuji, *J. Phys. Chem. A*, 1998, **102**, 2033-2043.
39. M. I. Nikitin, *High Temp.*, 1989, **27**, 681-688.
40. S. B. Osin, D. I. Davlyashin and J. S. Ogden, *Russ. J. Phys. Chem.*, 2001, **75**, 294-302.
41. S. B. Osin, D. I. Davlyatshin and D. S. Ogden, *Zh. Fiz. Khim.*, 2001, **75**, 294-302.
42. O. V. Blinova and Y. B. Predtechenskii, *Opt. Spektrosk.*, 1979, **47**, 1120-1125.
43. V. V. Sliznev and V. G. Solomonik, *Russ. J. Inorg. Chem.*, 2000, **45**, 1060-1062.
44. G. S. Quiñones, G. Hägele and K. Seppelt, *Chem.-Eur. J.*, 2004, **10**, 4755-4762.
45. M. J. Molski and K. Seppelt, *Dalton Trans.*, 2009, 3379–3383.
46. A. K. Brisdon, J. H. Holloway, E. G. Hope, W. Levason, J. S. Ogden and A. K. Saad, *J. Chem. Soc., Dalton Trans.*, 1992, 447-449.
47. N. Acquista and S. Abramowitz, *J. Chem. Phys.*, 1973, **58**, 5484-5488.
48. A. M. Panich, V. K. Goncharuk, S. P. Gabuda and N. K. Moroz, *J. Struct. Chem.*, 1979, **20**, 45-47.
49. Y. B. Predtechenskii, *Opt. Spectrosc.*, 1979, **47**, 622.
50. N. I. Giricheva, O. G. Krasnova and G. V. Girichev, *J. Struct. Chem.*, 1997, **38**, 54-61.
51. G. V. Girichev, N. I. Giricheva and O. G. Krasnova, *J. Molec. Struct.*, 2001, **567**, 203-210.
52. E. I. Voit, A. V. Voit, V. K. Goncharuk and V. I. Sergienko, *J. Struct. Chem.*, 1999, **40**, 380-386.
53. V. V. Sliznev and V. G. Solomonik, *J. Struct. Chem.*, 2000, **41**, 11-18.
54. A. S. Alikhanyan, A. V. Steblevskii, I. P. Malkerova, V. S. Pervov, V. D. Butskii and V. I. Gorgoraki, *Zh. Neorg. Khim.*, 1978, **23**, 1477-1482.
55. V. V. Sliznev and V. G. Solomonik, *Zh. Neorg. Khim.*, 2000, **45**, 513-522.
56. W. Levason, R. Narayanaswamy, J. S. Ogden, A. J. Rest and J. W. Turff, *J. Chem. Soc., Dalton Trans.*, 1981, 2501-2507.
57. R. Wei, Q. Li, Y. Gong, L. Andrews, Z. Fang, K. S. Thanthiriwatte, M. Vasiliu and D. A. Dixon, *J. Phys. Chem. A*, 2017, **121**, 7603-7612.
58. L. Andrews, P. F. Souter, W. D. Bare and B. Liang, *J. Phys. Chem. A*, 1999, **103**, 4649-4658.
59. W. D. Bare, P. F. Souter and L. Andrews, *J. Phys. Chem. A*, 1998, **102**, 8279-8286.
60. W. E. Falconer, G. R. Jones, W. A. Sunder, I. Haigh and R. D. Peacock, *J. Inorg. Nucl. Chem.*, 1973, **35**, 751-753.
61. D. L. Hildenbrand, *J. Chem. Phys.*, 1976, **65**, 614-618.
62. I. P. Malkerova, A. S. Alikhanyan, V. D. Butskii, V. S. Pervov and V. I. Gorgoraki, *Zh. Neorg. Khim.*, 1985, **30**, 2761-2765.
63. M. Moskovits and G. A. Ozin, *Cryochemistry, Wiley-Interscience, New York*, 1976.
64. G. A. Ozin and W. E. Klotzbücher, *J. Mol. Catal.*, 1977, **3**, 195-206.
65. I. J. Blackmore, A. J. Bridgeman, N. Harris, M. A. Holdaway, J. F. Rooms, E. L. Thompson and N. A. Young, *Angew. Chem., Int. Ed.*, 2005, **44**, 6746-6750.
66. V. E. Bondybey and C. Fletcher, *J. Chem. Phys.*, 1976, **64**, 3615-3620.
67. H. Kunz, J. G. McCaffrey, R. Schriever and N. Schwentner, *J. Chem. Phys.*, 1991, **94**, 1039-1045.

68. P. D. Mallinson, D. C. Mckvan, J. H. Holloway and I. A. Oxto, *Spectrochim. Acta, Part A*, 1975, **31A**, 143-159.

69. S. K. Ignatov, T. D. Kolomiistova, Z. Mielke and A. G. Razuvaaev, *Chem. Phys.*, 2006, **324**, 753-766.

70. A. V. Cherevatova, T. D. Kolomiistova, D. N. Shchepkin, K. G. Tokhadze, Z. Mielke, S. Coussan and P. Roubin, *J. Mol. Spec.*, 2006, **238**, 64-71.

71. R. L. Redington and D. E. Milligan, *J. Chem. Phys.*, 1963, **39**, 1276-1284.

72. B. Vest, P. Schwerdtfeger, M. Kolonits and M. Hargittai, *Chem. Phys. Lett.*, 2009, **468**, 143-147.

73. B. Vest, Z. Varga, M. Hargittai, A. Hermann and P. Schwerdtfeger, *Chem. Eur. J.*, 2008, **14**, 5130-5143.

74. I. R. Beattie, P. J. Jones and N. A. Young, *Angew. Chem.*, 1989, **101**, 322-324.

75. A. V. Wilson, T. Nguyen, F. Brosi, X. Wang, L. Andrews, S. Riedel, A. J. Bridgeman and N. A. Young, *Inorg. Chem.*, 2016, **55**, 1108-1123.

Chapter 6

Chromium fluorides: does CrF$_6$ exist?

6.1 Introduction

Although this chapter is principally concerned with the existence of chromium hexafluoride, the known matrix and vapour phase chemistry of chromium atoms and the lower valent fluorides will be considered first. Chromium atoms isolated in solid Ar matrix were first reported by Mann and Broida.[1] The UV/vis spectrum showed absorption bands at 29650, 30190, 30620, 33350, and 33920 cm^{-1} and the ground state of chromium is $^7S_3$ (3d^5 4s^1).[1] Another spectroscopic study was carried out by Kündig et al. to trap Cr atoms in rare gas matrices; the study revealed the presence of dimer species in Cr/Ar matrix.[2] An investigation was performed by Ozin and Klotzbücher to investigate Cr isolated in an Ar matrix at 10 K;[3] the UV–visible spectrum displayed peaks at 24930, 25641, 28571, and 30120 cm^{-1} which were assigned to atomic Cr in an Ar matrix and the bands at 21739 and 38461 cm^{-1} were related to Cr$_2$. 366 nm (27300 cm^{-1}) irradiation led to the decay of peaks due to Cr and Cr$_2$ species and the formation of two different species. Cr$_3$ species exhibited bands at 20964, 21367, and 27247 cm^{-1}, while the other weak features observed at 33333, 33898, and 34965 cm^{-1} were assigned to higher Cr clusters in Ar.[3] Further 460 nm (21735 cm^{-1}) irradiation led to photodissociation of the higher Cr clusters to Cr/Cr$_2$/Cr$_3$. Another spectroscopic study was performed by Pellin et al. who recorded the same absorption spectrum for matrix isolated Cr/Ar as previous workers and assigned the band at 460 nm (21735 cm^{-1}) to Cr$_n$.[4] The laser ablation technique was used to generate Cr atoms which were allowed to react with O$_2$ and the products trapped in an Ar matrix; the bands due to CrO$_2$ molecules were centred around 1869.7, 965.4 and 914.4 cm^{-1}. The IR band observed at 968.44 cm^{-1} was assigned to CrO$_3$ molecules, and the feature located at 846.3 cm^{-1} was related to CrO species in Ar matrix.[5] A recent study investigated the reaction of laser ablated Cr atoms with OF$_2$ diluted in Ar gas mixture by matrix isolation infrared spectroscopy; the IR absorptions of OCrF$_2$ isolated in solid Ar matrix were obtained, and the vibrational spectrum demonstrated three bands. The band at 1017.3 cm^{-1} is due to Cr–O stretching mode and the features at 735.3 and 622.1 cm^{-1} are assigned to the antisymmetric and symmetric stretching modes of F–Cr–F, respectively. Furthermore, the band observed at 965.3 cm^{-1} is related to CrO$_2$, while OCrF has two bands, one at 935.5 cm^{-1} due to Cr–O stretching mode, and at 646.0 cm^{-1} due to Cr–F stretching mode.[6]

The fluorides of chromium have been widely explored and reported in the literature. Few studies were performed to investigate the ground electronic state of CrF. The band observed at 8000 cm^{-1} in the near infrared region was assigned to CrF, while the CrF was produced through a thermal evaporation of a mixture of Cr, CrF$_3$, and NaF at 1227 °C (1500 K).[7, 8] The vibrational frequency of CrF was calculated as 655.68 cm^{-1} using anharmonicity equation, and the spin of CrF was suggested as sextet.[8] A theoretical study using the RCCSD(T) method also proposed the electronic configuration of CrF as $X^6\sum{}^+$.[9] The fluorescence excitation spectrum of CrF in the gas phase was recorded by Koivisto *et al.* in 2001. The spectrum showed a band at 31700 cm^{-1}.[10] In 2005, Popove studied the fluorides of 3d transition metals theoretically. The study proposed the IR band of CrF was located at 1281 cm^{-1} and the bond length as 1.73 Å.[11] In the same year, Nielsen and Allendorf in their theoretical investigation for chromium halides calculated the absorption band of CrF at 621 cm^{-1}.[12] A further theoretical study was conducted by Hamdan and Korek using the CASSCF method; the study investigated seven electronic states for the low lying sextet states of CrF, and calculated the vibrational frequency of CrF at 627.57 cm^{-1}.[13] A year later, a similar theoretical study was carried out by Hamdan and Korek for the low–lying quartet states of the CrF.[14]

The early studies of CrF$_2$ in the gas phase were achieved by matrix isolation IR spectroscopy.[15] The asymmetric stretching modes were observed at 654.5 cm^{-1} and at 679.6 cm^{-1} in solid Ar and Ne matrices, respectively.[16, 17] The geometry of CrF$_2$ was reported to be linear. A further study was conducted to characterise CrF$_2$ and CrF$_3$ isolated in solid argon matrix by Van Leirsburg, *et al.*[18] The vibrational frequency of the asymmetric stretching mode of CrF$_2$ was recorded at 654.4 cm^{-1}, while a band at 749.3 cm^{-1} was assigned to CrF$_3$ species.[18] In addition, the study proposed that CrF$_3$ has D$_{3h}$ symmetry with bond angles of 120°. The matrix isolation infrared technique was used by Bukhmarina *et al.* to characterise CrF$_2$. The infrared absorption spectrum of CrF$_2$ matrix isolated in solid argon and neon matrices displayed peaks at 654.5 and 679.8 cm^{-1}, respectively.[19] The geometry of CrF$_2$ is contentious; some studies reported it is linear while it was reported as bent by other studies. The IR spectrum showed only one peak, while the symmetric stretching mode is not observable. Bukhmarina *et al.* in their study observed the symmetric stretch in the Raman spectrum at 565 cm^{-1}.[19] A further, theoretical study completed a by Wang and Schwarz suggested CrF$_2$ as quasi–linear, with large amplitude vibrations over the linear energy saddle point.[20] This result corresponds to a combined theoretical and electron diffraction study carried out by Vest *et al.* which

indicated that CrF_2 is bent.[21] Research completed by Osin *et al.* investigated the reaction of Cr and F_2 molecules by passing fluorine gas over heated chromium and trapping the chromium fluoride molecules in an Ar matrix at cryogenic temperature. The vibrational frequencies of $^{52}CrF_2$ and $^{52}CrF_3$ were observed at 653.8 and 748.7 cm^{-1}, respectively.[22] Several studies were carried out using vibrational spectroscopy to reinvestigate the absorptions of matrix–isolated CrF_3 species. The IR absorption of CrF_3 molecules isolated in Ar matrix was recorded at 749.51 cm^{-1}, whereas the absorption was located at 762.90 cm^{-1} for a matrix of Ne.[19] The configuration of CrF_3 was defined as D_{3h} planar symmetry.[22-24] These data were in agreement with work done by Van Leirsburg *et al.*[18] In 2014, a laser ablation study performed by Schlöder *et al.* indicated that the asymmetric stretching mode of $^{52}CrF_2$ is at 654.4 cm^{-1} and 679.5 cm^{-1} in solid Ar and Ne matrices, respectively, and reported the geometry of CrF_2 as bent, while the IR absorption band of CrF_3 was located at 749.3 cm^{-1} in solid Ar matrix and 762.8 cm^{-1} in a matrix of solid Ne.[25]

Higher binary chromium fluorides, for example, CrF_4, CrF_5 and the much talked about CrF_6 have been reported. The earliest investigations of chromium fluorides identified how to prepare and detect CrF_4 and CrF_5 species. The molecular geometry of CrF_4 was resolved to be tetrahedral (T_d symmetry) by Hedberg *et al.* utilizing electron diffraction.[26] This was consistent with infrared spectra recorded at the University of Southampton by Hope *et al.* just a few years prior, indicating the configuration of CrF_4 as T_d symmetry.[27] The IR spectra had a group of bands in the area of 784.3 cm^{-1} for CrF_4 isolated in a solid argon matrix and for CrF_4 isolated in nitrogen matrix the bands were observed at 790.0 and 780.7 cm^{-1}.[27] Furthermore, for $CrOF_4$ in a nitrogen matrix the vibrational frequencies detected at 746.3 and 741.6 cm^{-1} were due to stretching mode of doublet degenerate mode of Cr–F, and the band at 1027.7 cm^{-1} was related to the Cr=O stretching mode.[27, 28] A study carried out by Jacobs *et al.*; where CrF_4 molecules were isolated in a matrix of neon were found to have the most intense IR peak at 790.17 cm^{-1},[29] and the molecular structure of CrF_4 was suggested as tetrahedral (T_d) symmetry as well.[29] The shifting of vibrational frequencies in both spectra is a matrix shift because of different matrix gases used. Osin *et al.* in their study to investigate the reaction of the formation of chromium fluoride molecules detected the IR band related to $^{52}CrF_4$ at 783.8 cm^{-1}, and also the calculations proposed CrF_4 to have a tetrahedral configuration.[22] Hope *et al.* assigned the bands due to CrF_5 molecules at 763.2 cm^{-1} for a solid Ar matrix and at 758.9 cm^{-1} for a N_2 matrix.[27] Jacobs *et al.* in their study found that matrix isolated $^{52}CrF_5$

in a neon matrix has IR peaks located at 767.71 cm^{-1} and 792.2 cm^{-1}.[29] The splitting of these peaks is related to the characteristic isotope patterns of CrF_5. The symmetry of CrF_5 molecule was determined to be distorted trigonal bipyramid C_{2v}, rather than D_{3h}. In 2014, a study was conducted by Schlöder *et al*. to investigate CrF_4 as well as CrF_5 molecules isolated in inert gas matrices using laser ablation technique; the IR spectra had absorption bands at 767.7, 763.1, and 758.9 cm^{-1} for $^{52}CrF_5$ isolated in Ne, Ar, and N_2 matrices, respectively.[25, 30] This study also assigned the bands at 750.4 and 754.9 cm^{-1} to $CrOF_4$ in an Ar matrix.[25]

The first case of CrF_6 being synthesised was made in 1963 considering the information accumulated through low temperature infrared spectroscopy.[31] However, the spectral features were later found to be due to CrF_5, $CrOF_4$ and further compounds.[22, 25] In 1984, Hope *et al*. carried out experimental work to identify CrF_6 produced through the reaction of CrO_3 with high pressure of F_2 gas at 170 °C and trapping the yellow vapour in a nitrogen matrix at cryogenic temperatures.[32] The observed IR absorption band at 758.9 cm^{-1} was assigned to the asymmetric stretching mode of $^{52}CrF_6$ and the geometry of CrF_6 molecules was suggested as O_h symmetry.[32] A year later, Hope *et al*. used the same procedures to isolate CrF_6 in Ar and N_2 matrices as well as CrF_4.[27] A peak recorded at 769.6 cm^{-1} was assigned to $^{50}CrF_6$ in solid Ar matrix, a band present at 763.2 cm^{-1} was assigned to $^{52}CrF_6$, a band located at 760.0 cm^{-1} was assigned to $^{53}CrF_6$ and absorption of $^{54}CrF_6$ was at 757.1 cm^{-1}. Moreover, the UV–vis spectrum of CrF_6 molecules demonstrated three peaks at 38450 cm^{-1}, 31250 cm^{-1} (shoulder), and 26700 cm^{-1}. The molecular geometry of CrF_6 was O_h (octahedral symmetry).[27, 33] A theoretical study was conducted by Miyoshi *et al*. which calculated the electron affinity (EA) of CrF_6 as 8.24 eV.[34] In 1991, another study conducted by Hope *et al*. confirmed the preparation of CrF_6 and revealed that molecular CrF_6 has octahedral symmetry.[33] Additionally, a study in the same year was undertaken by Jorgensen using photoelectron spectroscopy which claimed that the lemon yellow product is due to CrF_6 and it is thermally unstable and decomposed by heating above 100 °C.[35] The suggestion of the presence of CrF_6 was very controversial., Jacob *et al*. employed matrix isolation IR spectroscopy to detect CrF_6 in noble gas matrices, however, the study assigned the band observed at 763.0 cm^{-1} to the $^{52}CrF_5$ species in a solid Ar matrix rather than CrF_6 and claiming no evidence for CrF_6 species.[36] Also, Jacobs *et al*. in their study were not able to detect matrix isolated CrF_6 in Ne or N_2 matrices.[29] A recent report by Schlöder *et al*. using laser ablation technique claimed that bands between 769.6 and 757.1 cm^{-1} were attributed to CrF_5 species in inert

gas matrices and were not from CrF_6.[25] They assigned the bands at 763.1 and 785.9 cm^{-1} to CrF_5, and the bands related to dimeric CrF_5 observed at 672.8, 731.9, 763.1, and 812.6 cm^{-1}.[25] This result was completely inconsistent with results reported previously by Hope *et al.*[27, 33] and the study did not succeed in the characterisation of CrF_6 molecules. As a consequence, the existence of matrix isolated CrF_6 molecules is still contentious.

The aim of this study is to investigate the formation of CrF and CrF_6 molecules in a solid Ar matrix.

6.2 Results and Discussion

6.2.1 FTIR spectroscopy of 1% F_2 in Ar

A blank experiment with just F_2/Ar was carried out to investigate the purity of 1% F_2/Ar gas mixture and to identify any spectral features due to the gas mixture. A layer of 1% F_2 in Ar gas matrix was deposited on the cooled window of the cryostat for 200 minutes at 9.2 K . As seen in Figure 6.1a, only two tiny absorption bands at 662 and 667 cm^{-1} are present which can be assigned to matrix isolated and atmospheric CO_2, respectively. Additionally, the photolysis processes were performed for 10 minutes using visible light, 200–410 nm, broadband, and further visible light. The IR spectra were collected after every process and are presented in Figures (5.1b–5.1e) successively and no change was found.
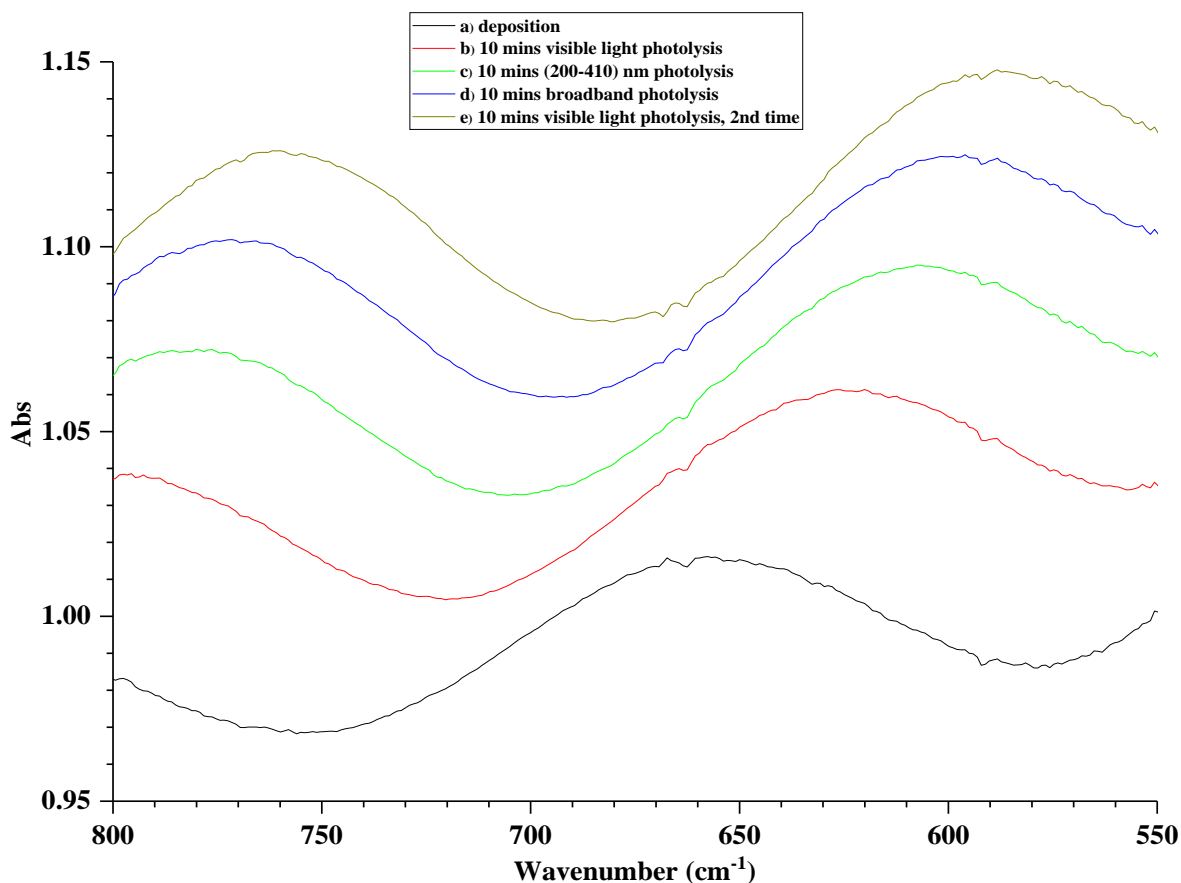
Figure 6.1: *FTIR spectra of a 1% F$_2$/Ar matrix (a) after deposition, (b) after 10 mins visible light photolysis, (c) after 10 mins (200-410) nm photolysis, (d) after 10 mins broadband photolysis, (e) after further 10 mins visible light photolysis.*

Furthermore, the matrix was warmed up to 15, 20, and 25 K for 5 minutes and after recooling to *ca*. 10 K the IR spectra were run and are displayed in Figure (6.2b–6.2d). No obvious change was observed. Figure 6.2e shows the matrix after exposure to a further 10 minutes of broadband photolysis, again no change was observed. Upon 5 minutes of further annealing at 30 K; no change was observed as indicated in Figure 6.2f. Similar experiments were conducted using 10% of F$_2$ in Ar gas mixture and the same results were found.

118
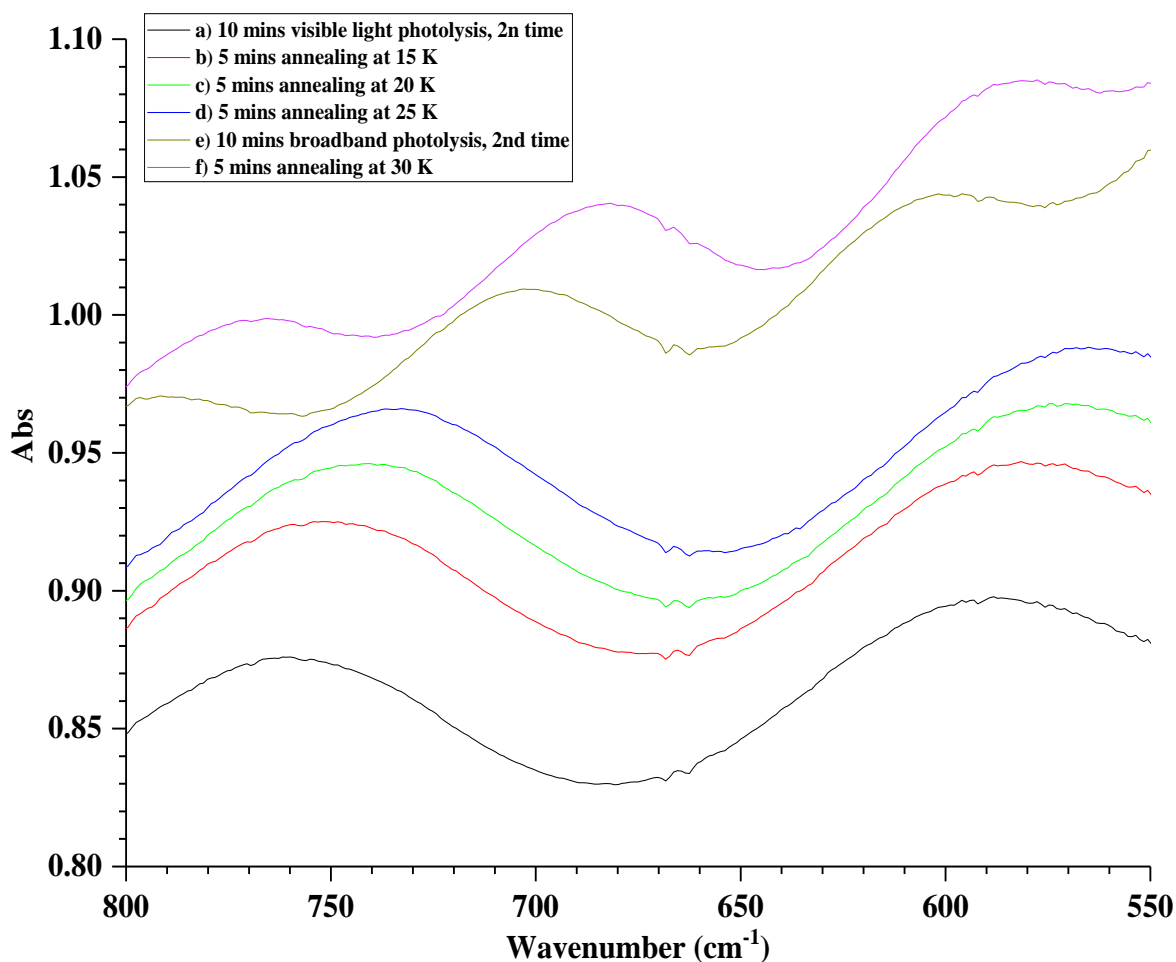
Figure 6.2: *FTIR spectra of a 1% F$_2$/Ar matrix (a) after deposition, (b) after 5 mins annealing at 15 K, (c) after 5 mins annealing at 20 K, (d) after 5 mins annealing at 25 K, (e) after further 10 mins broadband photolysis, (f) after 5 mins annealing at 30 K.*

6.2.2 FTIR spectroscopy of Cr in a 1% F$_2$/Ar matrix

The melting point of Cr is 1903 °C, and the temperature required to get a vapour pressure 1×10^{-3} torr is 1265 °C.[37] A filament of a Cr bar supported in a Ta wound filament as described in Chapter 2 was heated at 1.88 V with 24 A of electrical current to evaporate Cr atoms which were allowed to react with different concentrations of F$_2$ diluted in an Ar matrix. The temperature of the matrix was 9.2 K, and a pressure of 4 x 10^{-5} mbar during deposition. All evaporation conditions conducted later were very similar. In the beginning, a thin layer of F$_2$ in Ar gas matrix was laid down onto the deposition window of the cryostat. All spectra were recorded at 1 cm^{-1} resolution and contained common impurity bands as described before in previous chapters.[38-41] Also, the features detected at 662 and 667 cm^{-1} are because of CO$_2$ isolated in the matrix as well as atmospheric CO$_2$. Due to several oxidation states of Cr, different chromium fluoride species were expected to be observed. Furthermore, the higher oxidation state fluorides

are more likely to be formed when using higher concentration of F_2 doped in the Ar gas matrix. As seen in Figure 6.3, peaks located at 784.3 and 749.3 cm^{-1} have been observed in all cases using 10% F_2/Ar, 5% F_2/Ar, and 1% F_2/Ar gas matrices but with different relative intensities. These features have been previously assigned to $^{52}CrF_4$ and $^{52}CrF_3$ molecules, respectively.[6, 19, 22, 23, 25, 27] The IR absorption band assigned to the most intense band of isotopic patterns for $^{52}CrF_2$ species was observed at 654.4 cm^{-1}, but only for low concentrations such as 1% F_2/Ar as shown in Figure 6.3c.[6, 16, 18, 19, 22, 23, 25, 42] A weak broad peak at 757.3 cm^{-1} has been obtained in case of using 10% and 5% F_2/Ar mixture only. It is very clear in the 10% F_2/Ar spectrum, but is not so obvious in the 5% F_2/Ar spectrum as given in Figures 6.3a and 6.3b. Furthermore, a sharp strong band was recorded at 591.9 cm^{-1} in case of using 1% F_2/Ar gas matrix only, as presented in Figure 6.3c. It is most likely to be due to a low valent chromium fluoride molecules. It looks to be the same band labelled F and unassigned in the recent study conducted by Wei *et al.* in their experiments using Cr and OF_2,[6] but it does not look like there is any sign of it in the published paper by Schlöder *et al.*[25] In addition, a weak peak at 733 cm^{-1} is present in 1% F_2/Ar gas matrix, this is only very weak in 1% F_2/Ar matrices and is absent in 5% and 10% F_2/Ar matrices. This band was not reported in the literature data.
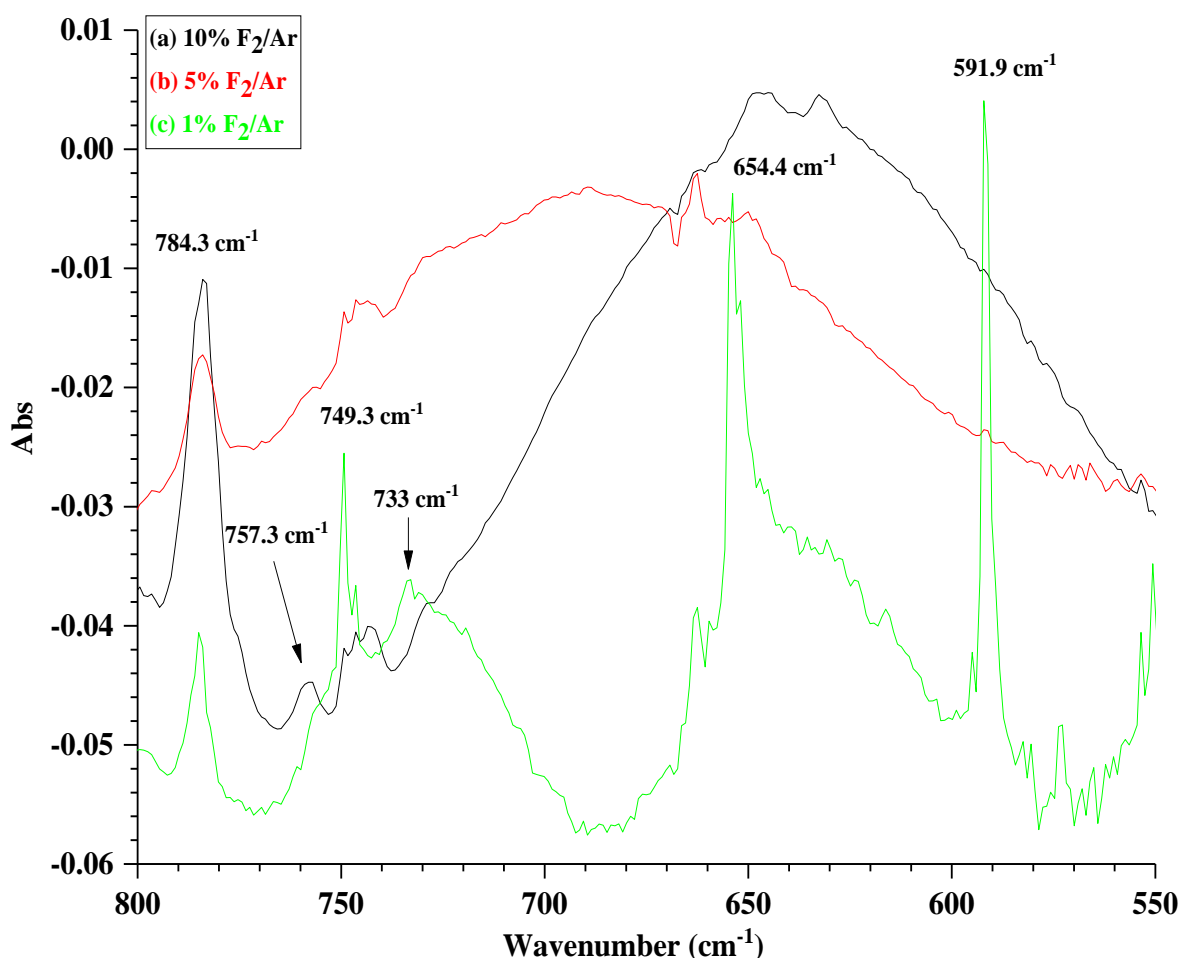
Figure 6.3: *FTIR spectra of atomic Cr isolated in (a) 10% F₂/Ar matrix, (b) 5% F₂/Ar matrix, (c) 1% F₂/Ar matrix.*

The low concentration of F_2 in an Ar matrix was found most suitable to study the interaction between Cr atoms and F_2 and the formation of chromium fluoride species in more detail. The peaks observed are presented in Table 6.1 below. The IR spectrum in Figure 6.4a shows a sharp peak located at 654.4 cm⁻¹ is related to CrF_2 molecules and the shoulder peak at 652.2 cm⁻¹ is due to the presence of isotopes of Cr; $^{53}CrF_2$ (Figure 6.5b). The relative intensity of this band looks bigger than expected regarding to the abundance of chromium isotopes (^{50}Cr: 4.35%, ^{52}Cr: 83.78%, ^{53}Cr: 9.50%, and ^{54}Cr: 2.36%), because it is super imposed on broad feature.[6, 16, 18, 19, 22, 23, 25, 42] A sharp medium band at 749.3 cm⁻¹ in conjunction with a shoulder peak at 746.6 cm⁻¹ were previously documented as CrF_3 species and isotope fine structure (Figure 6.5c),[6, 19, 22, 23, 25] while the weak peak at 784.3 cm⁻¹ is due to CrF_4 molecules with isotopic patterns (Figure 6.5d).[6, 22, 25, 27] In addition, a sharp strong absorption band located at 591.9 cm⁻¹ with very limited isotopic structure (Figure 6.5a), was not reported before, this band could be due to CrF molecules. It is in agreement with computational study undertaken by Nielsen and Allendorf that proposed the IR feature of CrF is located at 621 cm⁻¹,[12] as well as the theoretical study of

121

Hamdan and Korek which suggested CrF molecules exhibit a band at 627.57 cm^{-1}.[13] Figure 6.4b illustrates the IR spectrum after 5 minutes of exposure to visible light photolysis, the IR band at 591.9 cm^{-1} has shrunk slightly, while the intensity of the peak at 784.3 cm^{-1} has increased to some extent. In addition, two new tiny features at 756 and 757 cm^{-1} were observed. The matrix was photolysed by 200–410 nm light for 10 minutes; the IR spectrum is displayed in Figure 6.4c, the peaks at 654.4, 756, 757, and 784.3 cm^{-1} grew marginally, where free F atoms are generated by photolysis and react with chromium atoms as well as chromium fluorides to form new chromium fluoride species. Figure 6.4d demonstrates the vibrational spectrum after 10 minutes of broadband photolysis; the vibrational frequency at 591.9 cm^{-1} decreased. In return, there was a small increase in intensity of absorption bands at 654.4, 756, and 757 cm^{-1}. The matrix was exposed to further 10 minutes of visible light photolysis, as stated in Figure 6.4e. All the absorption bands have the same intensity and no change has been observed.

Table 6.1: Vibrational frequencies (cm^{-1}) observed of CrF$_n$ molecules in a matrix of Ar.

Assignments	Observed	Ref [25]	Ref [22]	Ref [36]	Ref [27]
^{52}CrF	591.9 cm^{-1}	—	—	—	—
^{52}CrF$_2$	654.4 cm^{-1}	654.4 cm^{-1}	653.8 cm^{-1}	—	—
^{52}CrF$_3$	749.3 cm^{-1}	749.3 cm^{-1}	748.7 cm^{-1}	—	—
^{52}CrF$_4$	784.3 cm^{-1}	784.3 cm^{-1}	783.8 cm^{-1}	–	784.3 cm^{-1}
^{52}CrF$_5$	—	763.1 cm^{-1}, 785.9 cm^{-1}	—	763.0 cm^{-1}	763.2 cm^{-1}
^{52}CrF$_6$	757 cm^{-1}	—	—	—	763.2 cm^{-1}
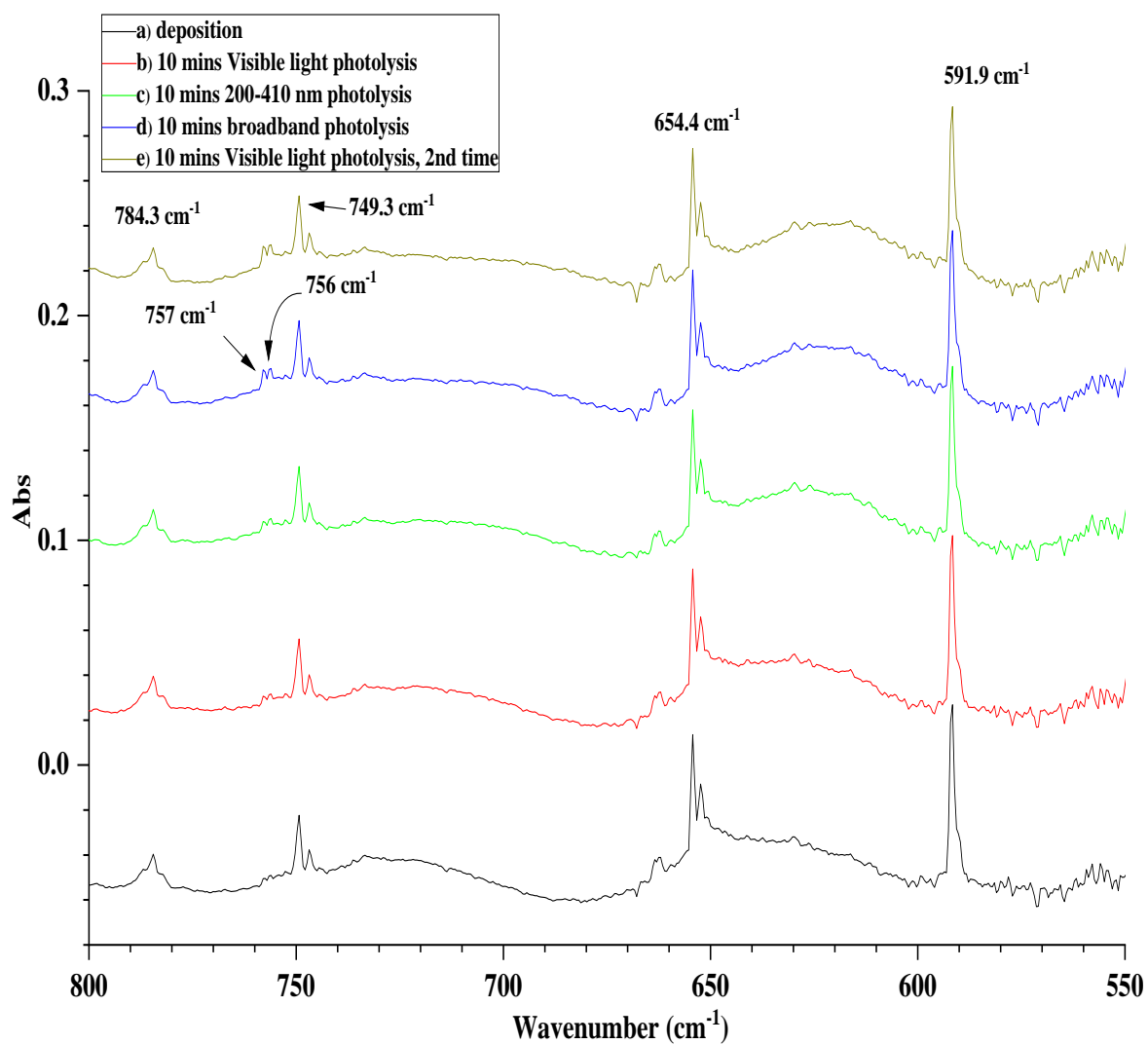
Figure 6.4: *FTIR spectra of atomic Cr in 1% F$_2$/Ar matrix (a) after deposition, (b) after 10 mins visible light photolysis, (c) after 10 mins 200−410 nm photolysis, (d) after 10 mins broadband photolysis, (e) after further 10 mins visible light photolysis.*
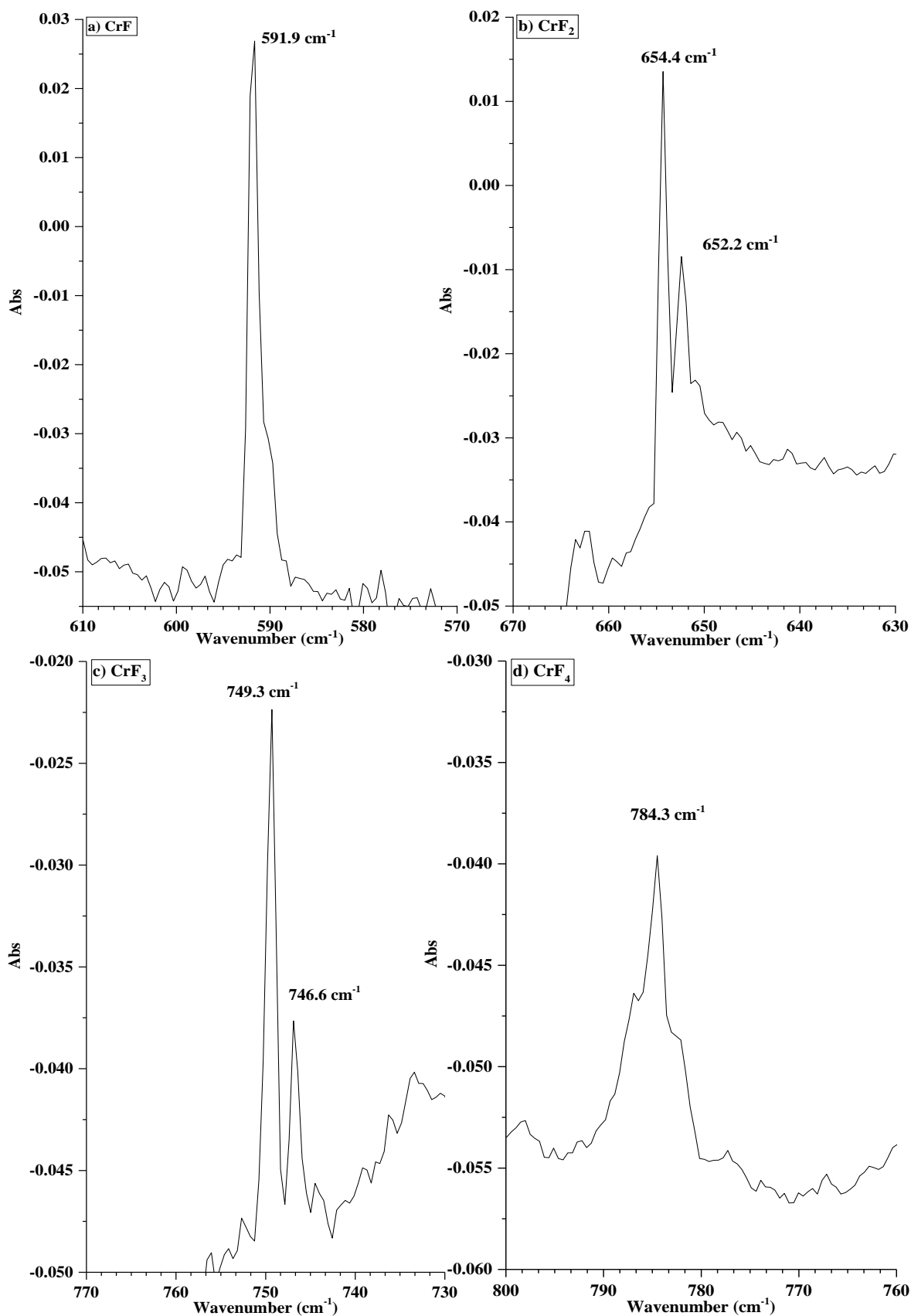
Figure 6.5: *FTIR spectra of atomic Cr in 1% F₂/Ar matrix after deposition for (a) CrF with its characteristic isotope patterns, (b) CrF₂ with its characteristic isotope patterns, (c) CrF₃ with its characteristic isotope patterns, (d) CrF₄ with its characteristic isotope patterns.*

The matrix was warmed up to different temperature gradually after photolysis, in order to soften the matrix slightly and allow the molecules in the matrix to either react with each other or decompose. As seen in Figure 6.6b, the matrix was annealed to 15 K for 5 minutes, the peak at 654.4 cm^{-1} decreased slightly. After annealing at 20 K for 5 minutes, the IR spectrum in Figure 6.6c reveals that the intensity of IR bands at 591.9 and 654.4 cm^{-1} was reduced. Oppositely, the intensity of peak at 784.3 cm^{-1} grew slightly. Furthermore, a shoulder peak grew at 787.2 cm^{-1}. Upon annealing the isolated matrix at 25 K for 5 minutes, as presented in Figure 6.6d. The vibrational frequencies located at 591.9 and 654.4 cm^{-1} were diminished once more. On the other hand, the feature at 749.3 cm^{-1} assigned to matrix isolated CrF_3 molecules was augmented. Also, the IR band at 784.3 cm^{-1} due to matrix isolated CrF_4 species became bigger and the intensity of the shoulder peak at 787.2 cm^{-1} increased as well. Figure 6.6e shows the matrix after exposure to broadband photolysis for 10 minutes; the intensity of the peak at 591.9 cm^{-1} became less, whereas the IR absorptions at 654.4, 756 and 757 cm^{-1} became more intense. After further annealing to 25 K for 5 minutes, the IR spectrum in Figure 6.6f indicates an insignificant reduction in intensity of the peak located at 591.9 cm^{-1}. Nonetheless, the absorptions at 749.3, 756 and 757 cm^{-1} decreased. The shoulder peak at 787.2 cm^{-1} became more intense.
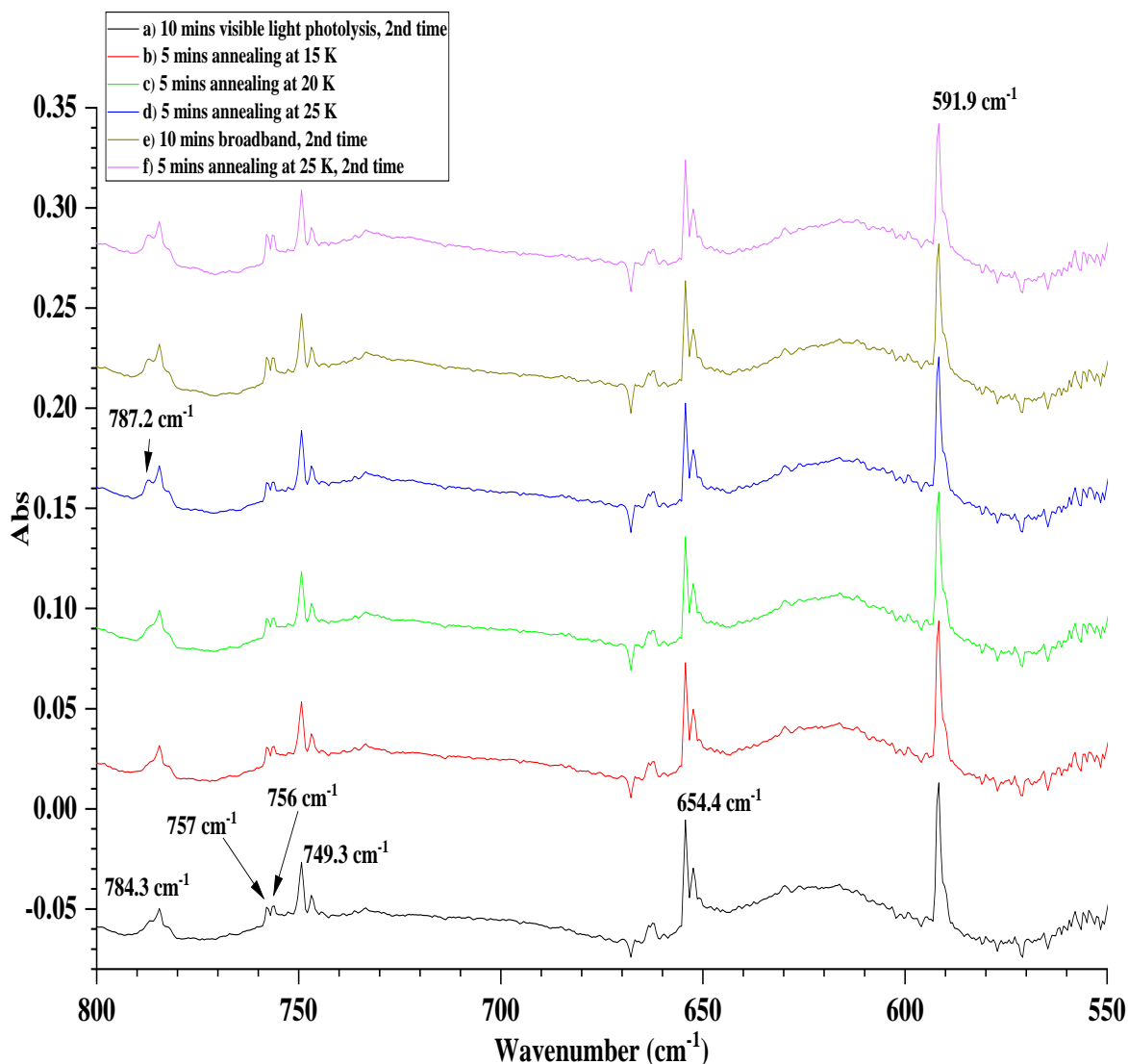
Figure 6.6: *FTIR spectra of atomic Cr in 1% F$_2$/Ar matrix (a) after further 10 mins visible light photolysis, (b) after 5 mins annealing at 15 K, (c) after 5 mins annealing at 20 K, (d) after 5 mins annealing at 25 K, (e) after further 10 mins broadband photolysis, (f) after further 5 mins annealing at 25 K.*

Figure 6.7b illustrates the spectrum of the matrix after 5 minutes of annealing to 30 K, the bands at 591.9, 654.4, 756 and 757 cm^{-1} became less intense. On the contrary, the intensity of peaks located at 749.3, 784.3, and 787.2 cm^{-1} was increased. Also, a weak peak at 733.4 cm^{-1} grew a little. The vibrational spectrum of the matrix after annealing to 35 K for 5 minutes is seen in Figure 6.7c, new feature observed at 730.5 cm^{-1}, while the vibrational frequency at 733.4 cm^{-1} grew slightly. In addition, the feature at 749.3 cm^{-1} due to matrix isolated CrF$_3$ species increased as well, whereas the absorption bands at 591.9, 654.4, 756, and 757 cm^{-1} were reduced. The shoulder peak observed at 787.2 cm^{-1} disappeared. Further warming up the matrix to 40 K for 5 minutes is given in Figure 6.7d below, the IR bands at 730.5, 733.4, 749.3 and 784.3 cm^{-1} increased. In contrast, the peaks

at 591.9 and 654.4 cm^{-1} shrank remarkably. Additionally, the peaks at 756 and 757 cm^{-1} disappeared.
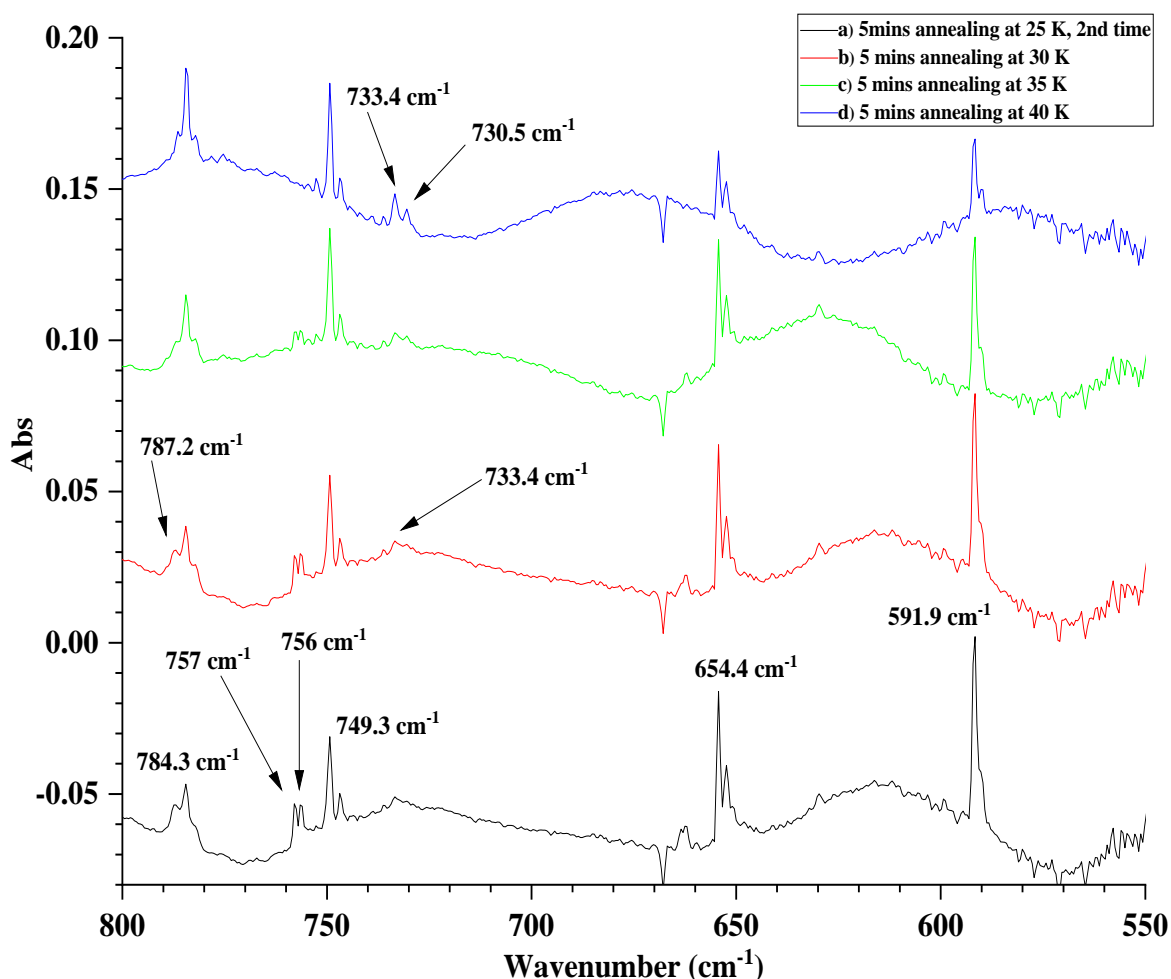
Figure 6.7: *FTIR spectra of atomic Cr in 1% F$_2$/Ar matrix (a) after further 5 mins annealing at 25 K, (b) after 5 mins annealing at 30 K, (c) after 5 mins annealing at 35 K, (d) after 5 mins annealing at 40 K.*

The experimental study points to the vibrational frequency observed at 591.9 cm^{-1} with very limited chromium isotopic structure is related to a matrix isolated CrF species, where it is expected that the lowest chromium fluoride species have the lowest Cr−F stretching frequency. This band has not been stated in any previous study and is the first observation for CrF molecules in a matrix, athough it looks like the band labelled F and unassigned in the recent study carried out by Wei *et al*. which was observed in Cr and OF$_2$ experiments.[6] The SVFF bond angle calculator for XY$_2$ molecules using the experimental wavenumbers of CrF$_2$ at 654.4 and 652.2 cm^{-1}, suggested the geometry of CrF$_2$ as bent with a F−Cr−F angle of 120.45° assuming no interaction between stretching and bend modes.[37] This result corresponds with literature data reported by Nielsen and Allendorf,[12] Vest *et al*.,[21] and Schlöder *et al*.[25] The reason for only one IR band detected

is the other band is potentially too weak to be observed, as Bukhmarina *et al.* performed Raman spectroscopy to detect the symmetric stretch of CrF_2 at 565 cm^{-1}.[19]

The shoulder peak observed at 787.2 cm^{-1} on annealing to 20 K and which disappeared on high temperature annealing (35 K) could be site effect of CrF_4. Surprisingly, there is no band observed at 763.1 cm^{-1} which is reported as the most intense absorption of isotopic $^{52}CrF_5$ isolated in solid Ar matrix by Schlöder *et al.*,[25] Jacob *et al.*,[36] and Hope *et al.*[27] Furthermore, there are no bands detected at 812.6, 763.1, 731.9, and 672.8 cm^{-1} assigned to Cr_2F_{10} as reported by Schlöder *et al.*[25] The apparent increase in intensity of the frequencies at 730.5 and 733.4 cm^{-1} at high temperature of annealing (30−40 K) indicates that these bands are more likely to be due to aggregation of chromium fluoride species, which could be dimer species for either CrF_3 or CrF_4 molecules.

The existence of CrF_6 species is debatable. Former investigations conducted by Hope, *et al.* in 1985 and 1991 assumed the formation of CrF_6 molecules and assigned the absorption recorded at 763.2 cm^{-1} to matrix isolation CrF_6 species is Ar matrix.[27, 33] Nevertheless, a published work performed by Jacob *et al.* proposed that the formation of CrF_6 molecules does not exist and the frequency at 763.0 cm^{-1} corresponds to chromium pentafluoride isolated in solid Ar matrix,[36] and also, another study carried out by Schlöder *et al.* claimed that CrF_6 does not exist and assigned the band at 763.1 cm^{-1} to CrF_5 species.[25] The two IR absorption bands located at 757 and 756 cm^{-1} have not been reported in the former literature data, although they appear as an unassigned side product in the supplementary information of Schlöder *et al.*[25] The intensity of these two bands grew after photolysis and decreased in intensity after annealing. What is more, a weak broad peak at 757.3 cm^{-1} is observed after evaporation of Cr atoms in the presence of high concentrations (10% and 5%) of F_2 in Ar gas mixture, it is very obvious in the 10% F_2/Ar spectrum, but its relative intensity is lowest for 5% F_2/Ar matrix, supporting the idea that these bands are due to chromium fluoride species. In addition, this conclusion is supporting because the spectra have no bands located at 1017.3, 735.3, and 622.1 cm^{-1} due of $OCrF_2$, or at 935.5 and 646.0 cm^{-1} for OCrF isolated in solid Ar matrix,[6] and also, no features related to $CrOF_4$ in Ar matrix at 750.4 and 754.49 cm^{-1}.[25] Therefore, the bands at 757 cm^{-1} could be assigned to CrF_6 species. It is evident that the most abundant isotope is $^{52}CrF_6$ which exhibits the vibrational frequency at 757 cm^{-1}, while the band at 756 cm^{-1} which have similar relative intensity is its site effect. These data indicate the existence of CrF_6.

Theoretical calculations were not carried out as part of this work as detailed calculations have been reported in the published paper by Schlöder *et al.*[25] but the calculations missed CrF. Unfortunately, the UV/vis spectrum of Cr atoms F_2/Ar matrix was not recorded because the cryostat was not working properly.

6.3 Conclusion

The ground state of chromium is $^7S_3$ ($3d^5\ 4s^1$).[1] Thermally evaporated Cr atoms reacted with different concentrations of fluorine diluted in a matrix of argon and the reaction products were trapped at cryogenic temperature. The vibrational spectrum shows a sharp strong band at 591.9 cm^{-1} assigned to CrF species, which was a band labelled F and unassigned in the recent study conducted by Wei *et al.*[6] The feature of $^{52}CrF_2$ species is located at 654.4 cm^{-1},[6, 16, 18, 19, 22, 23, 25, 42] and the geometry of CrF_2 is bent. The absorption bands observed at 749.3 and 784.3 cm^{-1} are assigned to $^{52}CrF_3$ and $^{52}CrF_4$ species, respectively.[6, 19, 22, 23, 25, 27] The vibrational frequencies at 730.5 and 733.4 cm^{-1} are due to dimer form of either CrF_3 or CrF_4 molecules, while the band related to CrF_6 is observed at 757 cm^{-1} with its site effect at 756 cm^{-1}.

6.4 Summary

First observation of CrF in solid Ar matrix; the FTIR band was obtained at 591.9 cm^{-1}. There is strong evidence for the existence of CrF_6; the IR band related to CrF_6 was observed at 757 cm^{-1} with its site effect at 756 cm^{-1}. These bands reproducibly grow upon photolysis and diminish upon annealing.

6.5 References

1.   D. M. Mann and H. P. Broida, *J. Chem. Phys.*, 1971, **55**, 84-94.
2.   E. P. Kündig, M. Moskovits and G. A. Ozin, *Nature (London)*, 1975, **254**, 503-504.
3.   G. A. Ozin and W. E. Klotzbücher, *J. Mol. Catal.*, 1977, **3**, 195-206.
4.   M. J. Pellin, D. M. Gruen, T. Fisher and T. Foosnaes, *J. Chem. Phys.*, 1983, **79**, 5871-5886.
5.   G. V. Chertihin, W. D. Bare and L. Andrews, *J. Chem. Phys.*, 1997, **107**, 2798-2806.
6.   R. Wei, Q. Li, Y. Gong, L. Andrews, Z. Fang, K. S. Thanthiriwatte, M. Vasiliu and D. A. Dixon, *J. Phys. Chem. A*, 2017, **121**, 7603-7612.
7.   R. Koivisto, S. Wallin and O. Launila, *J. Mol. Spectrosc.*, 1995, **172**, 464-468.
8.   O. Launila, *J. Mol. Spectrosc.*, 1995, **169**, 373-395.
9.   J. F. Harrison and J. H. Hutchison, *Mol. Phys.*, 1999, **97**, 1009-1027.
10.   R. Koivisto, O. Launila, B. Schimmelpfennig, B. Simard and U. Wahlgren, *J. Chem. Phys.*, 2001, **114**, 8855-8866.
11.   A. V. Popov, *Russ. J. Phys. Chem.*, 2005, **79**, 732-735.
12.   I. M. B. Nielsen and M. A. Allendorf, *J. Phys. Chem. A*, 2005, **109**, 928-933.
13.   A. Hamdan and M. Korek, *Chem. Phys.*, 2010, **369**, 13-18.
14.   A. Hamdan and M. Korek, *Can. J. Chem.*, 2011, **89**, 1304-1311.
15.   M. J. Linevsky, *Spectroscopic studies of the vaporization of high temperature materials*, Gen. Elec. Co., 1968.
16.   J. W. Hastie, R. H. Hauge and J. L. Margrave, *J. Chem. Soc. D*, 1969, 1452-1453.
17.   J. L. Margrave, J. W. Hastie and R. H. Hauge, *Amer. Chem. Soc., Div. Petrol. Chem., Prepr.*, 1969, **14**, E11-E13.
18.   D. A. Van Leirsburg and C. W. DeKock, *J. Phys. Chem.*, 1974, **78**, 134-142.
19.   V. N. Bukhmarina, A. Y. Gerasimov, Y. B. Predtechenskii and V. G. Shklyarik, *Opt. Spektrosk.*, 1988, **65**, 876-881.
20.   S. G. Wang and W. H. E. Schwarz, *J. Chem. Phys.*, 1998, **109**, 7252-7262.
21.   B. Vest, P. Schwerdtfeger, M. Kolonits and M. Hargittai, *Chem. Phys. Lett.*, 2009, **468**, 143-147.
22.   S. B. Osin, D. I. Davliatshin and J. S. Ogden, *J. Fluorine Chem.*, 1996, **76**, 187-192.
23.   O. V. Blinova, V. G. Shklyarik and L. D. Shcherba, *Russ. J. Phys. Chem.*, 1988, **62**, 831-833.
24.   N. B. Balabanov, V. G. Solomonik and V. V. Sliznev, *Zh. Neorg. Khim.*, 1997, **42**, 1173-1179.
25.   T. Schlöder, F. Brosi, B. J. Freyh, T. Vent-Schmidt and S. Riedel, *Inorg. Chem.*, 2014, **53**, 5820-5829.
26.   L. Hedberg, K. Hedberg, G. L. Gard and J. O. Udeaja, *Acta Chem. Scand.*, 1988, **42A**, 318-323.
27.   E. G. Hope, P. J. Jones, W. Levason, J. S. Ogden, M. Tajik and J. W. Turff, *J. Chem. Soc., Dalton Trans.*, 1985, 1443-1449.
28.   E. G. Hope, P. J. Jones, W. Levason, J. S. Ogden, M. Tajik and W. J. Turff, *J. Chem. Soc., Dalton Trans.*, 1985, 529-533
29.   J. Jacobs, H. S. P. Mueller, H. Willner, E. Jacob and H. Buerger, *Inorg. Chem.*, 1992, **31**, 5357-5363.
30.   F. Brosi, T. Vent-Schmidt, S. Kieninger, T. Schlöder, H. Beckers and S. Riedel, *Chem. - Eur. J.*, 2015, **21**, 16455-16462.
31.   O. Glemser, H. Roesky and K. H. Hellberg, *Angew. Chem., Int. Ed. Engl.*, 1963, **2**, 266-267.

32. E. G. Hope, P. J. Jones, W. Levason, J. S. Ogden and M. Tajik, *J. Chem. Soc., Chem. Commun.*, 1984, 1355-1356.
33. E. G. Hope, W. Levason and J. S. Ogden, *Inorg. Chem.*, 1991, **30**, 4873-4874.
34. E. Miyoshi, Y. Sakai, A. Murakami, H. Iwaki, H. Terashima, T. Shoda and T. Kawaguchi, *J. Chem. Phys.*, 1988, **89**, 4193-4299.
35. C. K. Joergensen, *Eur. J. Solid State Inorg. Chem.*, 1991, **28**, 799-808.
36. E. Jacob and H. Willner, *Chem. Ber.*, 1990, **123**, 1319-1321.
37. M. Moskovits and G. A. Ozin, *Cryochemistry, Wiley-Interscience, New York*, 1976.
38. A. V. Cherevatova, T. D. Kolomiistova, D. N. Shchepkin, K. G. Tokhadze, Z. Mielke, S. Coussan and P. Roubin, *J. Mol. Spec.*, 2006, **238**, 64-71.
39. P. D. Mallinson, D. C. Mckvan, J. H. Holloway and I. A. Oxto, *Spectrochim. Acta, Part A*, 1975, **31A**, 143-159.
40. S. K. Ignatov, T. D. Kolomiistova, Z. Mielke and A. G. Razuvaaev, *Chem. Phys.*, 2006, **324**, 753-766.
41. R. L. Redington and D. E. Milligan, *J. Chem. Phys.*, 1963, **39**, 1276-1284.
42. J. W. Hastie, R. H. Hauge and J. L. Margrave, *High Temp. Sci.*, 1969, **1**, 76-85.

Chapter 7

Palladium halides

7.1 Introduction

The reaction of palladium in atomic form with a variety of molecules, usually at cryogenic temperatures, is considered an interesting source to investigate the formation of new chemical species. The spectrum of Pd atoms has been complex and contentious; several studies have been conducted to investigate the matrix isolation of palladium atoms in rare gas matrices. In 1976, an optical study was used to characterise palladium atoms isolated in different rare gases matrices.[1] The assignments of the Pd spectrum was controversial, as the previous study indicated that Pd atoms isolated in neat Ar matrix exhibit four absorptions at 29600, 31260, 31940, and 33680 cm^{-1}. This discrepancy may be due to depending only on data presented by UV/vis spectroscopy. Later, vibrational spectroscopy study assigned these features to PdN$_2$.[2, 3] The UV/vis spectra of matrix isolated Pd atoms demonstrated bands between 36360 and 50000 cm^{-1} (200 and 275 nm).[4, 5] The isolation of Pd atoms in both argon and krypton matrices was reported using a magnetic circular dichroism (M.C.D) instrument.[6] The electronic spectra after photolysis revealed that the spectral features are due to an excited state of palladium atoms in Ar matrix, which is long−lived instead of chemically produced species. The absorption, emission, and emission–yield spectroscopy techniques were employed to study Pd atoms isolated in Ar, Xe, Ne, and Kr solid matrices. The study revealed that Pd atoms are in octahedral structure in Ne, Ar, and Kr matrices, and tetrahedral interstitial sites in solid Xe matrix.[7] Furthermore, palladium atoms isolated in an Ar solid matrix were reinvestigated again;[8] the studies confirmed the same peak positions of Pd atoms and Pd(N$_2$) species reported previously.[4] Additionally, further study recorded the optical spectra of palladium atoms isolated in a matrix of solid Ar, indicating that Pd atoms in solid Ar matrix can be in the ^{3}D$_3$ metastable electronic state, whilst the gas phase ground state is (4d^{10}; ^{1}S$_0$).[9] In 1997, the optical data recorded by Garcia−Prieto *et al.* for Pd atoms isolated in rare matrices revealed similar results.[10] A theoretical study using the CCSD(T) method predicted the interaction of Pd atoms with rare gas; the calculated data predicted a bond length for Pd–Ar$_2$ as 2.544 Å. The short Pd–Ar bond indicates a stronger binding between Pd and Ar atoms.[11]

The reaction of Pd atoms with pure CO was investigated as well. In 1972, Kündig *et al.* conducted research to investigate the interaction of palladium with carbon monoxide in solid argon matrix at 10 K.[12, 13] The infrared absorption spectrum demonstrated peaks at 2070, 2060, 2044, and 2050 cm^{-1} for Pd(CO)$_4$, Pd(CO)$_3$, Pd(CO)$_2$, and PdCO, respectively. In addition, the data implied that the geometry of Pd(CO)$_2$ is linear (D$_{\infty h}$), whereas Pd(CO)$_3$ has trigonal planar shape (D$_{3h}$), and the structure of Pd(CO)$_4$ is tetrahedral (T$_d$). One year later, another study was carried out to determine the geometric structure of palladium carbonyl species using IR spectroscopy.[14] This study confirmed that the shapes of Pd(CO)$_2$, Pd(CO)$_3$, and Pd(CO)$_4$ are linear, trigonal planar, and tetrahedral, respectively. Another study was undertaken by Kuendig *et al.* using matrix infrared spectroscopy; the IR absorption spectrum of Pd(CO)$_4$ displayed peak at 2070 cm^{-1}.[15] The reinvestigation of PdCO trapped in solid argon matrix was undertaken in another experimental work. The study reassigned the bands observed at 2050 and 2044 cm^{-1} to PdCO and confirm the linearity of PdCO molecule.[16] IR absorption spectroscopy was used to study the reaction of laser ablated Pd atoms and CO doped in neon gas mixture. The IR bands observed at 2074.6 and 2060.7 cm^{-1} were related to Pd(CO)$_4$ and Pd(CO)$_3$, respectively. The vibrational frequency at 2065.8 cm^{-1} is due the antisymmetric CO stretching mode of Pd(CO)$_2$, while the peak located at 2056.4 cm^{-1} belongs to PdCO species. Furthermore, the geometry of Pd(CO)$_2$ was determined to be nonlinear.[17] A theoretical study was carried out by Wu *et al.* using different density functional methods found that the ground electronic state for PdCO is $^1\Sigma^+$.[18] In addition, another computational study using QCISD(T) method suggested the bending energy of PdCO in Ar matrix as 22.2 kJ.mol^{-1}; the calculations proposed the M–C bond length as 1.833 Å and 1.146 Å for C–O.[19]

Moreover, the reaction of Pd atoms and neat N$_2$ was studied at 4–10 K. The IR and Raman spectroscopic data indicated the formation of Pd(N$_2$)$_2$ as well as Pd(N$_2$)$_3$ species.[20] The absorptions of mono– and di–Pd(N$_2$) molecules were also recorded at 27320 and 34965 cm^{-1}.[8] The vibrational frequency for Pd(N$_2$)$_3$ was observed at 2241 cm^{-1}.[21] Two years later, a study assigned the IR absorption bands observed at 2213, 2234, and 2242 cm^{-1} to Pd(N$_2$), Pd(N$_2$)$_2$, and Pd(N$_2$)$_3$, respectively.[2] Another study completed by Souvi *et al.* found that the geometry of Pd$_2$N$_2$ molecules trapped in Ar and Ne matrices have a linear structure (D$_{\infty h}$).[22] Matrix isolation infrared spectroscopy was employed to study the reaction of Pd atoms with a mixture of N$_2$ and O$_2$ doped in Ar gas at 6 K. The split band at 2246/2238 cm^{-1} is related to Pd(N$_2$)$_3$, the split band at 2212/2208 cm^{-1} is for

Pd(N$_2$), and band at 2232 cm^{-1} is due to Pd(N$_2$)$_2$.[3] The vibrational frequency of PdO$_2$ molecules was observed at 1022 cm^{-1}, the peak for Pd(O$_2$)$_2$ was located at 1108 cm^{-1}, while the features at 1014 and 988 cm^{-1} are due to (O$_2$)Pd(N$_2$) and (O$_2$)Pd(N$_2$)$_2$, respectively.[3, 23] The reinvestigation of Pd(O$_2$) and Pd(O$_2$)$_2$ molecules in solid neon matrix showed the IR absorptions at 1030 and 1112.5 cm^{-1}, respectively.[24] A study was carried out by Yang *et al.* to investigate the formation of dipalladium dioxygen complexes, and the infrared absorption spectrum of PdO$_2$ and Pd$_2$O$_2$ matrix isolated in solid argon matrix revealed peaks in the range between 920–1050 cm^{-1}. The BPW91 calculations were consistent with the IR bands recorded as well.[25] In 2006, IR spectroscopy studied matrix isolated Pd(N$_2$O) in solid Ar; the vibrational frequency observed at 1226.8 cm^{-1} was attributed to the asymmetric stretching mode of N–O in the Pd(N$_2$O) complex. New IR absorption bands were also recorded at 2257.6, 2254.2, and 1230.4 cm^{-1} after warming up the matrix and were assigned to N−N and N−O stretching modes of the Pd(N$_2$O)$_2$ complex.[26]

Knight and Weltner used the ESR technique to study the interaction of Pd atoms and H$_2$ in Ar and Kr matrices in 1971.[27] Laser ablation techniques were used to vaporise palladium atoms to interact with H$_2$ diluted in both Ar and Ne gas mixtures; the matrices were characterised by electron spin resonance (ESR) spectroscopy.[28] The study indicated that the H atoms are equivalent in PdH^{2+} and the energy of low–lying electronic states is 38 kJ.mol^{-1} (9 kCal/mol), corresponding with Pd$^+$ + H$_2$.[28] The IR spectrum of Pd(H$_2$) isolated is solid argon matrix was recorded by Andrews *et al.* The bands observed at 2971, 1507, and 950 cm^{-1} are corresponding to Pd(H$_2$), Pd(HD), and Pd(D$_2$), respectively. Furthermore, Pd(H$_2$)$_2$ displayed peaks at 3038 and 778 cm^{-1} and the features located at 2909, 730, 319 cm^{-1} are due to Pd(H$_2$)$_3$ complex.[29, 30] A theoretical study achieved by Alikhani and Minot using the B3LYP functional found the activation energy of PdH$_2$ molecule is very low at 25 kJ.mol^{-1}.[31] IR spectroscopy was used to investigate the interaction between Pd atoms and C$_2$H$_4$ diluted in Xe gas mixture at 15 K; the data indicated the formation of a (1:1) (C$_2$H$_4$)Pd complex.[32] Furthermore, a study was carried out by Wang and Andrews to investigate the interaction of laser ablated Pd atoms and (C$_2$H$_2$) diluted in an argon gas mixture; the vibrational bands at 3171.7, 1714.6, and 678.4 cm^{-1} are assigned to stretching and deformation modes of Pd(C$_2$H$_2$) molecules.[33]

Recently, a study was carried out at the University of Hull in collaboration with Freie Universität Berlin, University of Sydney, and University of Virginia to detect the matrix isolation palladium fluorides species. The IR spectrum displayed bands at 450,

617, 624, and 692 cm^{-1} were attributed to PdF, PdF_2, PdF_3, and PdF_4 in a matrix of solid Ar, respectively. Additionally, the study proposed that matrix isolated palladium hexafluoride molecules does not form.[34] Matrix isolation IR spectroscopy was employed to study the vibrational bands of $PdCl_2$ and $(PdCl_2)_n$ isolated in solid Ar matrix. The molecular arrangement of $PdCl_2$ was resolved to be hexameric with a distorted $(PdCl_2)_6$ cluster.[35] The geometry of $PdCl_2$ is disputed; a theoretical study was conducted by Siegbahn suggested the molecular structure of $PdCl_2$ as bent with Cl–Pd–Cl bond angle of 98.4°.[36] A study was conducted at The University of Hull to investigate the formation of monomeric $PdCl_2$ molecules.[37] Harris tried to use sputtering of Pd foil with 5% Cl_2/Ar gas mixture. The study failed to isolate the monomeric vapour phase palladium chlorides molecules, as Pd_6Cl_{12} cluster was formed only on the Pd foil surface and was then sputtered into the matrix.[37] In 2004, further research was done at The University of Hull to reinvestigate the configuration of $PdCl_2$. Dixon tried the vaporisation of solid $PdCl_2$, however only the Pd_6Cl_{12} cluster was observed.[38]

Therefore, the aim of these experiment is to generate Pd atoms by thermal evaporation and react them with Cl_2 to try to make monomeric $PdCl_2$ species and to confirm whether the molecular structure as bent or linear. In addition, to study the interaction between palladium atoms and bromine in a solid argon matrix, as there is no information available for the palladium bromides, either experiment or calculated.

7.2 Results and Discussion

7.2.1 UV/Vis Spectra of Pd in Ar

The melting point of palladium is 1552 °C, while the temperature required to get vapour pressure 1×10^{-3} torr is 1315 °C.[39] A filament of palladium and tantalum metal wound together was thermally heated to evaporate palladium atoms using a 33 A / 1.128 V electrical supply and the argon gas was introduced at a pressure of 4 x 10^{-6} mbar; the deposition temperature was *ca.* 11 K. A UV/vis spectrum was recorded after 40 minutes as displayed in Figure 7.1a, two medium intense absorptions were located at 40220 and 42450 cm^{-1}, one strong peak was seen at 45340 cm^{-1} as well as a very weak peak at 49650 cm^{-1}.[1, 4, 5, 7-9] The optical spectrum is compatible with data presented in the literature for Pd atoms isolated in solid argon matrix, see Table 7.1.[5] No bands located at 37750 cm^{-1} were found, indicating that the matrix does not contain dimer species of palladium.[5] That is because the ground state (4d^{10}; $^1S_0$) of Pd atoms makes dimer formation unlikely.[5]

Moreover, no absorptions were observed in the range of 27300−35000 cm^{-1} which have been previously reported for monomer and dimer species of Pd(N$_2$).[4, 8] The matrix was photolysed for 10 minutes using visible light (400–700 nm) and the spectrum is presented in Figure 7.1b. All bands have the same intensity without any change noticed. Figure 7.1c illustrates the matrix after 10 minutes of 200−410 nm irradiation, the absorption band at 45350 cm^{-1} was reduced slightly. The matrix was exposed to 10 minutes of broadband photolysis; the UV/vis spectrum in Figure 7.1d shows barely any reduction in the peak at 45350 cm^{-1}. Further visible light photolysis has no impact on the matrix, as shown in Figure 7.1e.

Table 7.1: Absorptions (cm^{-1}) observed and previous studies of Pd atoms isolated in Ar matrix.

Experiment	Ref [4, 5]	Assignments/ Ground state
40220 cm^{-1}	40322 cm^{-1}	$^3P_1 \leftarrow {}^1S_0$
42450 cm^{-1}	42400 cm^{-1}	$^3D_1 \leftarrow {}^1S_0$
45340 cm^{-1}	45454 cm^{-1}	$^1P_1 \leftarrow {}^1S_0$
49650 cm^{-1}	—	$^1S_0$
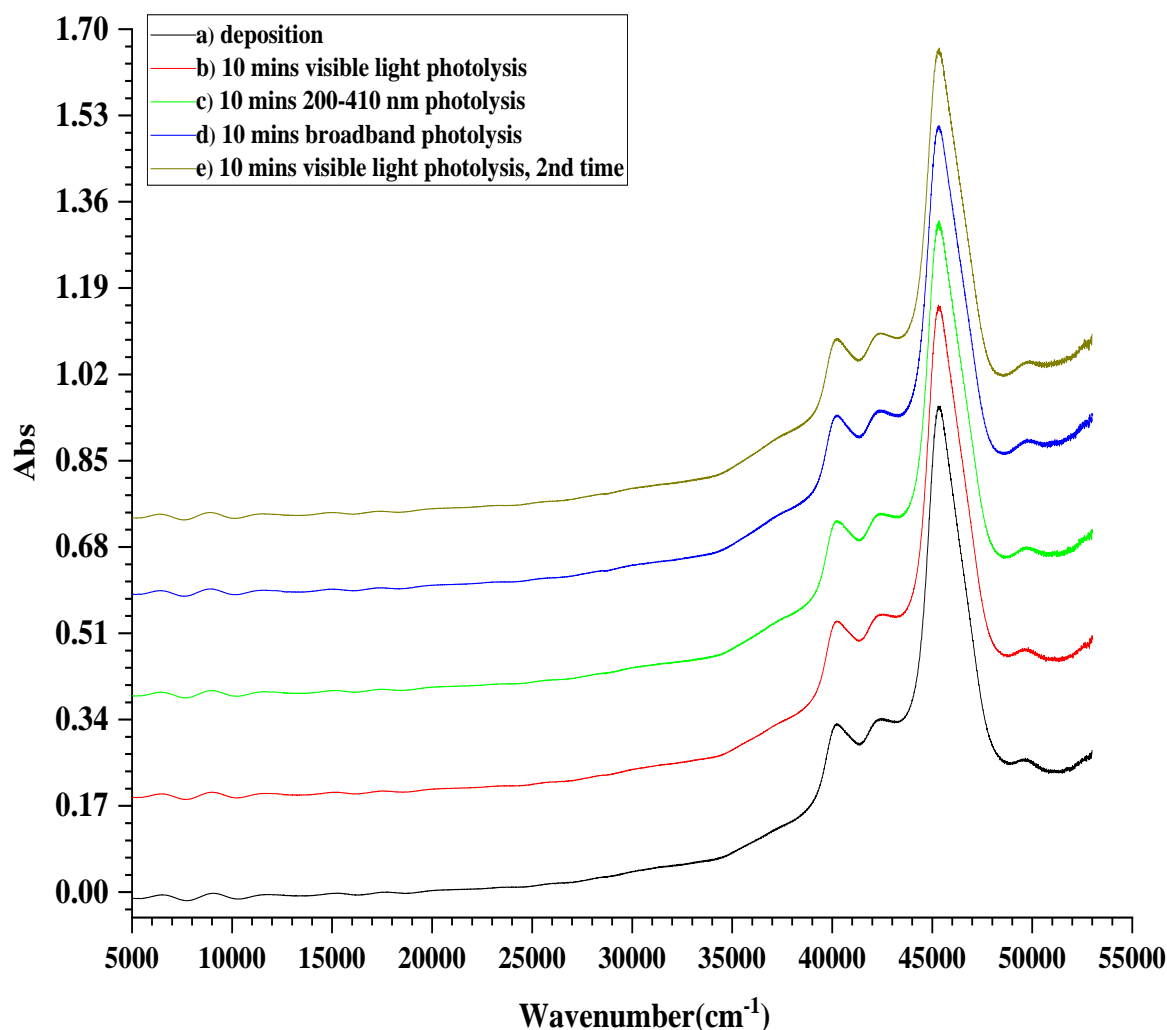
Figure 7.1: *UV/Vis spectra of atomic Pd in an Ar matrix (a) after deposition, (b) after 10 mins visible light photolysis, (c) after 10 mins 200−410 nm photolysis, (d) after 10 mins broadband photolysis, (e) after further 10 mins visible light photolysis.*

The matrix was annealed at different temperature; the matrix becomes soft and with high temperature solid argon starts to evaporate. The optical spectrum in Figure 7.2b is of the matrix after 15 minutes of annealing at 15 K. It was observed that the intensity of all peaks decreased, the bands at 40220 and 49650 cm^{-1} disappeared and no evidence for dimer forms of palladium was observed. Upon annealing to 20 K for 5 minutes, Figure 7.2c demonstrates an observable reduction in intensity of the peak at 45340 cm^{-1}. When the matrix was warmed up to 25 K and 30 K (Figures 7.2d and 7.2e, respectively), the intensity of peaks decreased more, and the spectra became noisier at the high energy end, where the baseline in the spectra increased corresponding to an increase in scattering of the light by the matrix at high energies. Surprisingly, no band related to Pd$_2$ was observed on annealing the matrix to 25 K. The UV−visible spectrum collected after 5 minutes of annealing at 35 K, shows no distinct peaks due to the evaporation of argon as demonstrated in Figure 7.2f. The loss in intensity of the peaks on annealing has been

observed in previous studies,[5] as there is a mixture of Pd atoms present, one set with a well defined Pd–Ar distance of 2.53(3) Å, and a second set with a wide range of Pd–Ar distances, and that on annealing the first is converted to the second, accompanied by the emission of blue/green light.[7, 8]
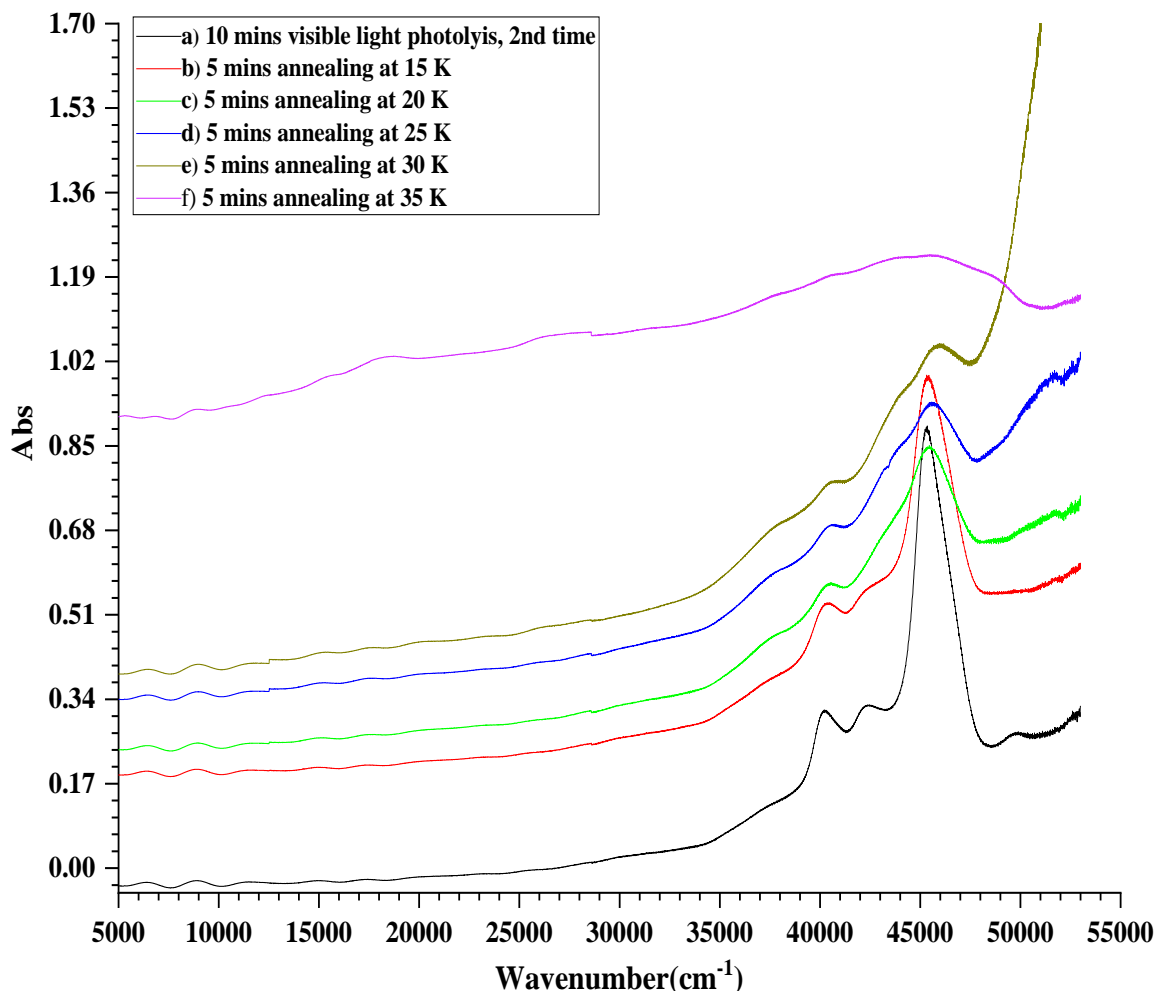
Figure 7.2: *UV/Vis spectra of atomic Pd in an Ar matrix (a) after further 10 mins visible light photolysis, (b) after 5 mins annealing at 15 K, (c) 5 mins annealing at 20 K, (d) after 5 mins annealing at 25 K, (e) after 5 mins annealing at 30 K, (f) after 5 mins annealing at 35 K.*

7.2.2 UV/Vis Spectra of 2.5% Cl_2 in Ar

The optical spectrum of 2.5% Cl_2 doped in Ar gas matrix was recorded after 100 minutes of depositing the gas mixture, the temperature of the deposition surface of the cryostat was at 11.3 K. The purpose of this experiment was to detect any impurities or chemical substances in the gas mixture. As displayed in Figure 7.3, a strong broad band at 30500 cm^{-1} was assigned to Cl_2 in solid argon matrix,[40] together with the intense band in the UV part of the spectrum.
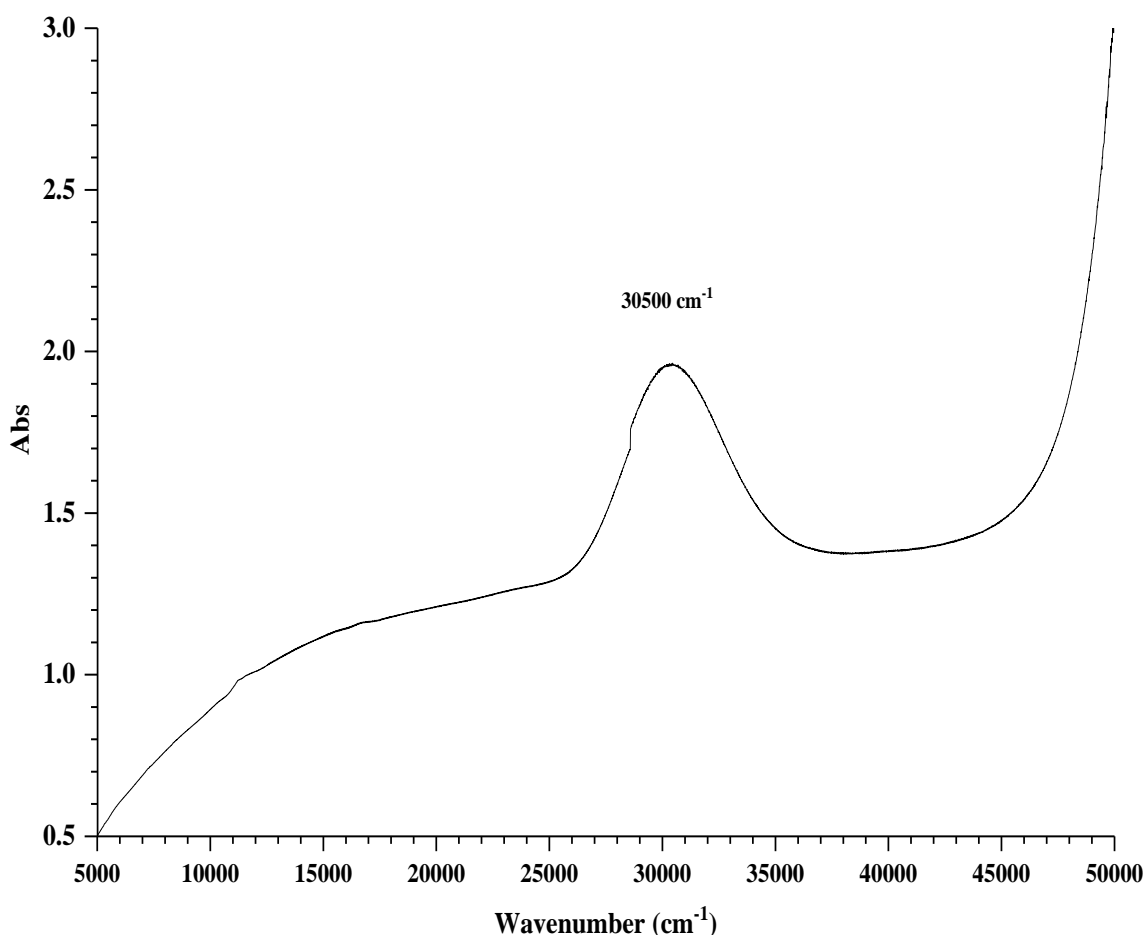
Figure 7.3: *UV/Vis spectrum of a 2.5% Cl$_2$/Ar matrix after deposition.*

7.2.3 UV/Vis Spectra of of Pd in 2.5% Cl$_2$ in Ar

The evaporation of the Pd atoms was performed using a 32.5 A / 1.315 V electrical supply and the 2.5% Cl$_2$/Ar gas mixture was introduced at a pressure of 2×10^{-6} mbar and a deposition temperature of 11.4 K. A UV/vis spectrum was obtained after 75 minutes and is illustrated in Figure 7.4a. Two tiny peaks are observed at 10900 and 11400 cm^{-1}, four weak features are located at 16700, 20880, 22640, and 25300 cm^{-1}, together with a broad peak at 30500 cm^{-1} for unreacted Cl$_2$ in the matrix. In addition, three peaks that were previously assigned to palladium atoms are observed at 40200, 42100, and 45300 cm^{-1}. The photolysis process was implemented to study the reaction between palladium species and chlorine atoms and molecules. Figure 7.4b shows the spectrum of the matrix after exposure to 10 minutes of visible light photolysis; the intensity of the peak at 45300 cm^{-1} decreased after visible light photolysis. The matrix was then exposed to 200–410 nm photolysis for 10 minutes, the intensity of absorption band at 30500 cm^{-1} decreased a little, indicating the destruction of Cl$_2$, and the band at 45300 cm^{-1} was reduced as well, as displayed in Figure 4.4c. After that, the matrix was photolysed using 10 minutes of

139

broadband photolysis, the UV/vis spectrum was collected and is shown in Figure 7.4d. It can be seen that the peak at 30500 cm^{-1} decreased in intensity. Moreover, the absorption bands at 40200, 42100, and 45300 cm^{-1} became less intense. It could be due to reaction between Pd atoms and the Cl$_2$ gas unreacted into the matrix. However, the UV/vis spectra do not indicate any other features related to the formation of new palladium chloride species. Figure 7.4e shows the UV–visible spectrum collected after further visible light photolysis, the spectrum has the same intensity without any change being observed. The bands observed at 10900, 11400, 16700, 20880, 22640, and 25300 cm^{-1} were not affected by photolysis.
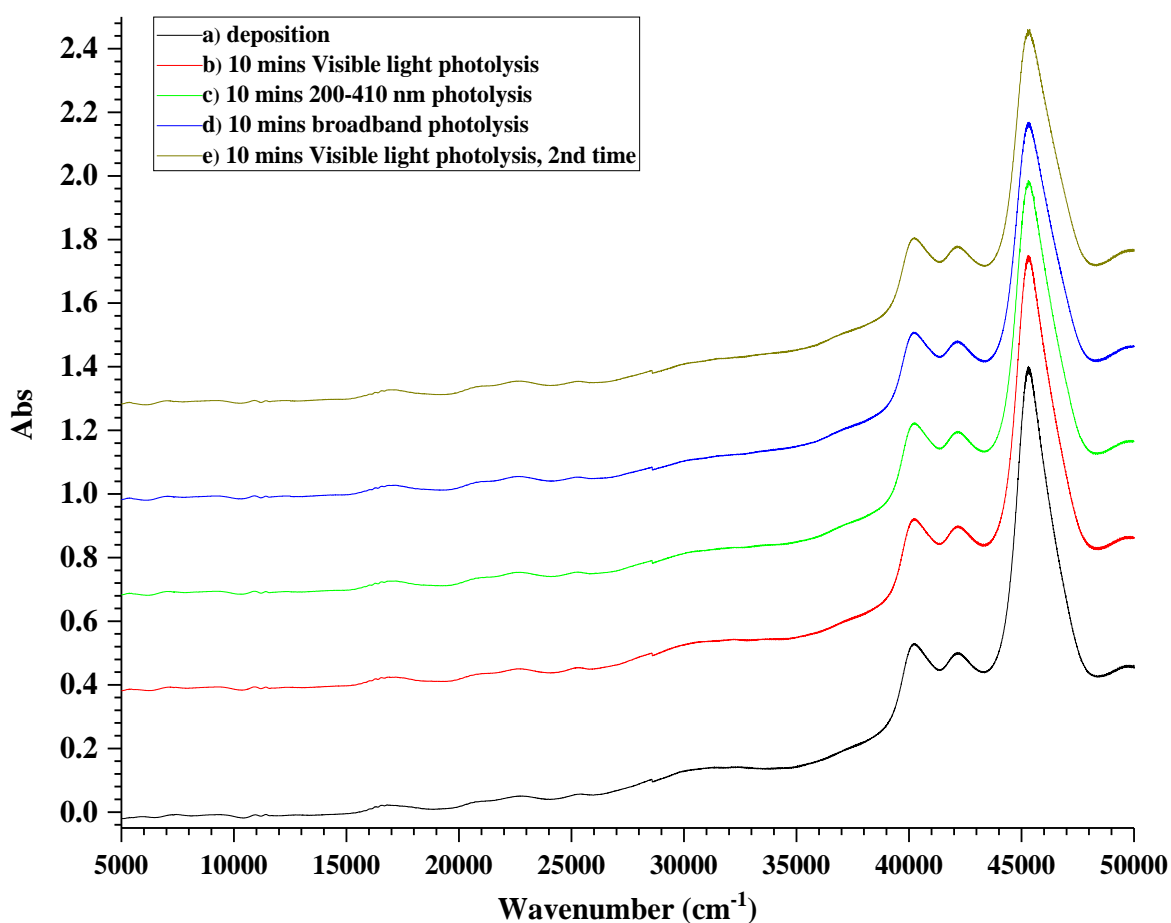
Figure 7.4: *UV/Vis spectra of Pd in a 2.5% Cl$_2$/Ar matrix (a) after deposition, (b) after 10 mins visible light photolysis, (c) after 10 mins 200–410 nm photolysis, (d) after 10 mins broadband photolysis, (e) after further 10 mins visible light photolysis.*

Annealing of the matrix was conducted after the photolysis process. As presented in Figure 7.5b, there is a distinct reduction in intensity of the peaks at 40200, 42100, and 45300 cm^{-1} after 5 minutes of annealing at 15 K. The optical spectrum was recorded after annealing the matrix to 20 K for 5 minutes; it is clear in Figure 7.5c that the peak at 42100 cm^{-1} disappeared, while the two absorption bands at 40200 and 45300 cm^{-1} decreased.

After a further five minutes of warming up the matrix to 25 K (Figure 7.5d), the intensity of the features at 16700, 20880, 22640, and 25300 cm^{-1} was slightly reduced. In addition, the band at 40200 cm^{-1} has disappeared and the intensity of the peak at 45300 cm^{-1} was weakened. The increase in the baseline at high energies is due to increased scattering of the light by the matrix after annealing. Furthermore, the matrix was annealed to 30 K for 5 minutes. Figure 7.5e demonstrates that the feature at 45300 cm^{-1} disappeared and the extent of scattering increased. Finally, the UV−visible spectrum in Figure 7.5f reveals the matrix after annealing at 35 K; the spectrum was scattered rather more than it was before. The intensity of the peaks at 16700, 20880, 22640, and 25300 cm^{-1} entirely shrunk. It is clear that Ar started to vaporise when annealed higher than 30 K. The bands at 16700, 20880, 22640, and 25300 cm^{-1} were considered as evidence of the generation of palladium chloride species, as these are different features that have not been observed in the spectrum of Pd atoms isolated in neat Ar matrices. Similar results were obtained using different concentrations of the Cl_2/Ar gas mixture; 1% Cl_2/Ar, 5% Cl_2/Ar, and 10% Cl_2/Ar. It is apparent that annealing and photolysis led to an increase/decrease in intensity of peaks, or formation of new bands. Consequently, additional work is required using matrix isolation Far−IR spectroscopy to differentiate among palladium chloride species formed. This will also allow for the identification of the molecular geometry of the deposited molecules.
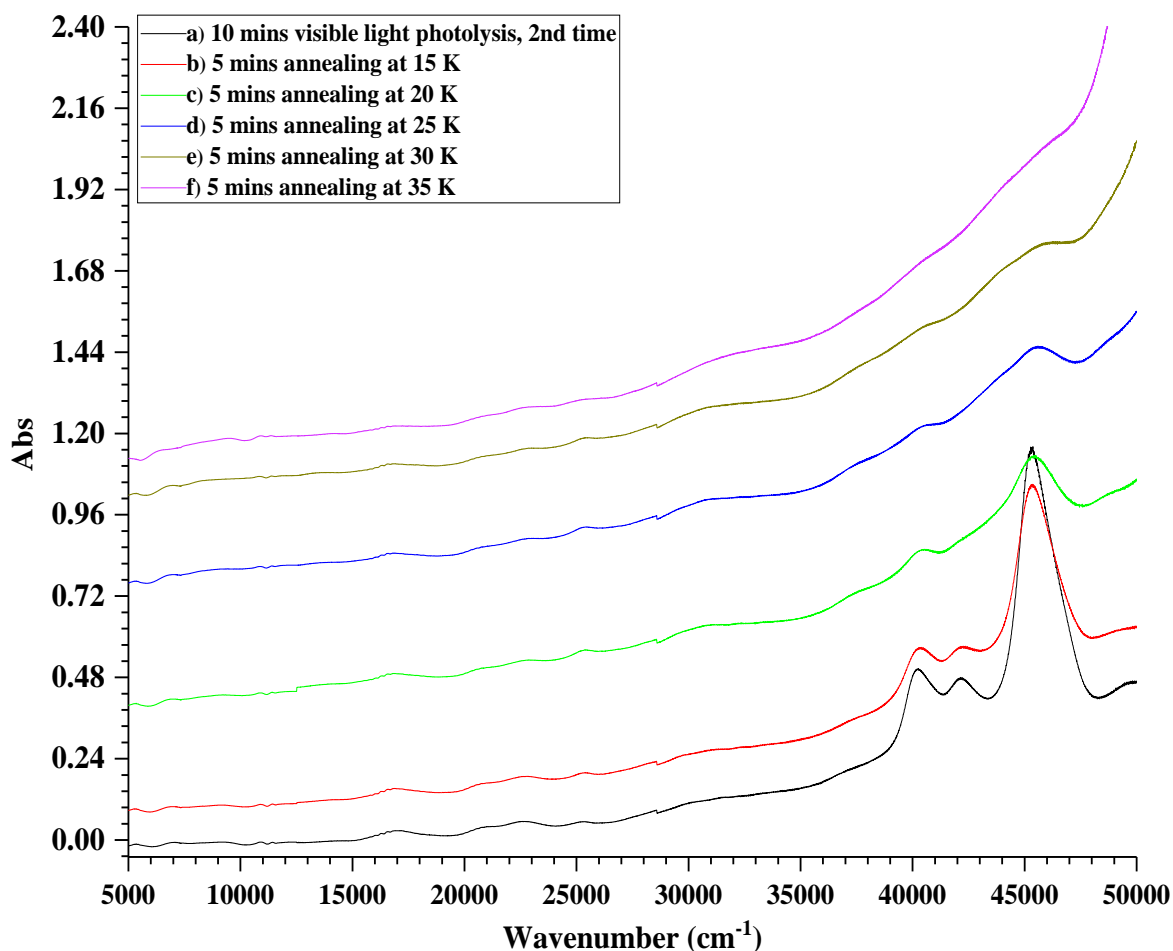
Figure 7.5: *UV/Vis spectra of Pd in a 2.5% Cl$_2$/Ar matrix (a) after further 10 mins visible light photolysis, (b) after 5 mins annealing at 15 K, (c) after 5 mins annealing at 20 K, (d) after 5 mins annealing at 25 K, (e) after 5 mins annealing at 30 K, (f) after 5 mins annealing at 35 K.*

7.2.4 UV/Vis Spectra of 1% Br$_2$ in Ar

The UV−visible spectrum in Figure 7.6a was recorded after a layer of the 1% Br$_2$ diluted in Ar gas matrix was introduced for about 90 minutes, while the temperature of the cooled CaF$_2$ window of the cryostat was at 11.2 K. Two weak peaks at 20800 and 24300 cm^{-1} accompanied by a strong broad absorption at 43900 cm^{-1} are observed from the 1% Br$_2$/Ar solid gas matrix. These features are at lower energy than Cl$_2$, which is expected for Br$_2$. The matrix was irradiated using different wavelengths of photolysis for 10 minutes and the UV/vis spectra were collected subsequently and are presented in Figures (7.6b–7.6e) below. It is apparent that the photolysis processes do not have an influence on the solid matrix.
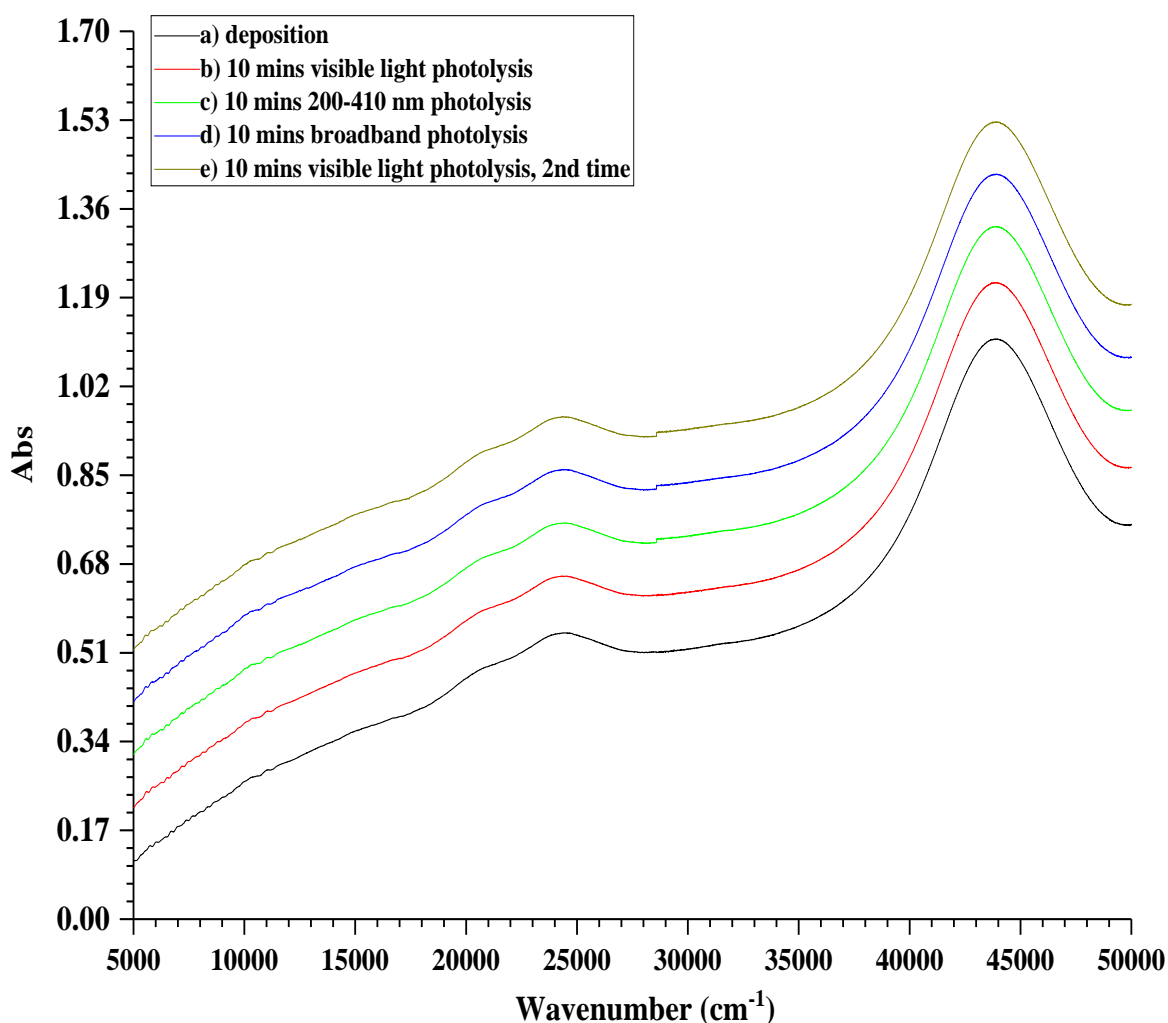
Figure 7.6: *UV/Vis spectra of a 1% Br$_2$/Ar matrix (a) after deposition, (b) after 10 mins visible light photolysis, (c) after 10 mins 200–410 nm photolysis, (d) after 10 mins broadband photolysis, (e) after 10 mins further visible light photolysis.*

The spectrum in Figure 7.7b was run after 5 minutes warming up the matrix to 15 K. Although no change was found in matrix, scattering was noticed slightly because the baseline had risen due to reduction of the throughput at high energy. The optical data presented in Figure 7.7c refers to the matrix after annealing to 20 K for 5 minutes; the strong peak at 43900 cm^{-1} grew and started to move a little to 43500 cm^{-1}. As shown in Figures 7.7d and 7.7e, a gradual decrease in intensity of peak at 20800 cm^{-1} was observed after 5 minutes of annealing the matrix at 25 and 30 K, respectively. Besides, the absorption peak at 43500 cm^{-1} increased and shifted slightly to 43300 cm^{-1}. The optical spectrum presented in Figure 7.7f shows the matrix upon annealing for 5 minutes at 35 K, the peak at 20800 cm^{-1} has disappeared, and the band at 43300 cm^{-1} continued to increase in intensity and to shift at 43000 cm^{-1}. The most likely explanations are that on annealing the Br$_2$ molecules migrate so the spectral features are due to small oligomers/aggregates, or that as Br and Ar have very similar van der Waals radii, so that

one Br atom will sit very well is a substitutional hole in the argon matrix and that on annealing the matrix, this allows both ends of the Br$_2$ molecule to be more favourably located so that there is only one band in each region.
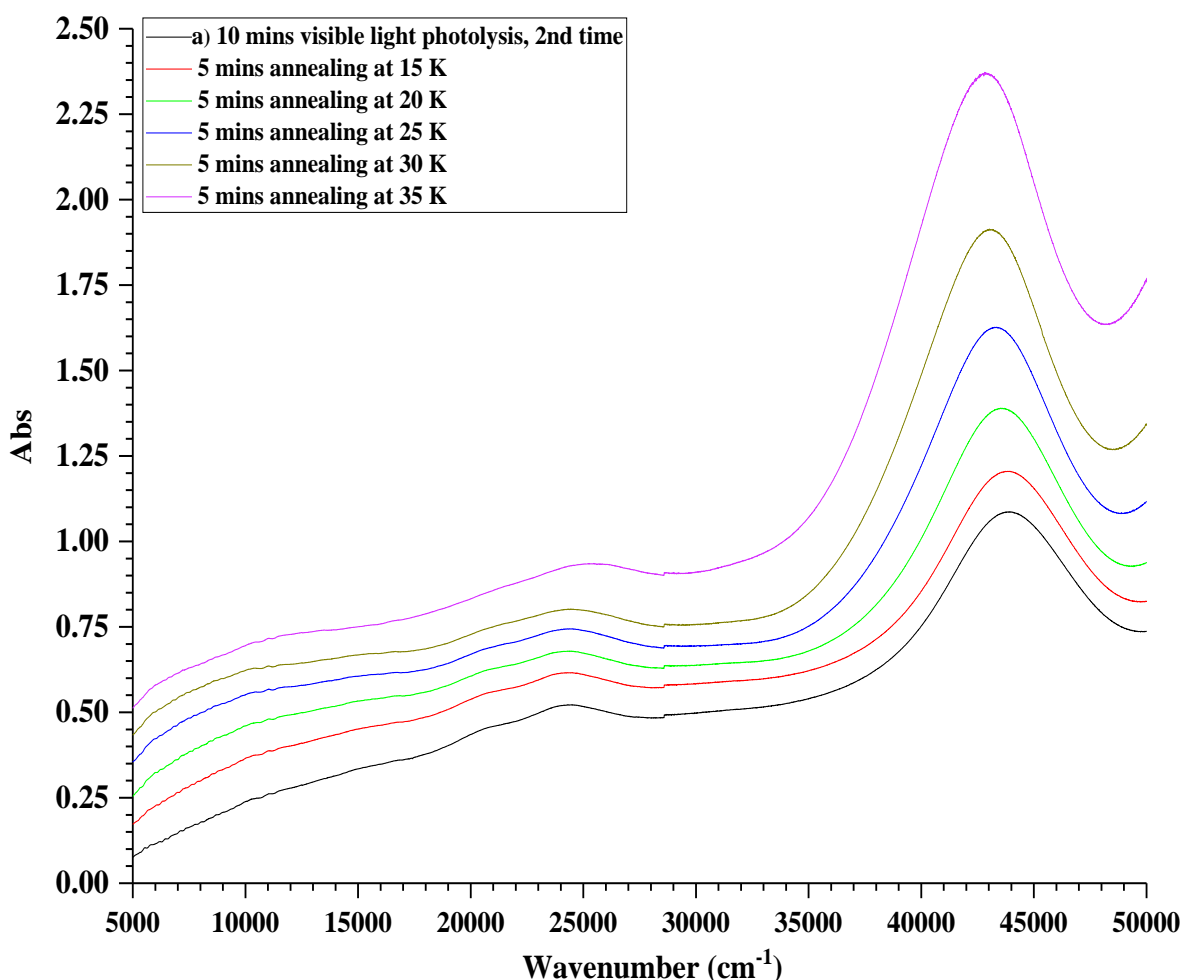
Figure 7.7: *UV/Vis spectra of a 1% Br$_2$/Ar matrix (a) after further 10 mins visible light photolysis, (b) after 5 mins annealing at 15 K, (c) after 5 mins annealing at 20 K, (d) after 5 mins annealing at 25 K, (e) after 5 mins annealing at 30 K, (f) after 5 mins annealing at 35 K.*

7.2.5 UV/Vis Spectra of Pd in 2% Br$_2$/Ar

The evaporation of the palladium atoms was obtained using 32.5 A and 1.359 V, the deposition surface in the cryostat was cooled to 11.5 K. The 2% Br$_2$ diluted in argon gas mixture was introduced at the beginning of the experiment for 7 minutes. The pressure in the vacuum chamber during the interaction with the palladium atoms was 4×10^{-6} mbar. The UV/vis spectrum was recorded after 60 minutes of deposition to characterise the interaction between palladium atoms and bromine in a solid argon matrix and is demonstrated in Figure 7.8a below. Three weak features are located at 12600, 18600, and 20500 cm^{-1} followed by a broad peak due to the unreacted Br$_2$ in solid Ar matrix at 25000

cm^{-1}. In addition, bands related to palladium were also observed at 40220, 42450, 45340, and shoulder at 49600 cm^{-1}, indicating the presence of some unreacted palladium atoms in the matrix. 10 minutes of photolysis was carried out using different wavelengths visible light (400–700 nm), 200–410 nm, broadband, and visible light, respectively. Consecutive scans were recorded after each process and are illustrated in Figures (7.8b–4.8e). The intensity of peak at 45300 cm^{-1} was marginally reduced only after exposure to broadand photolysis, while the other photolysis processes have no detectable effect.
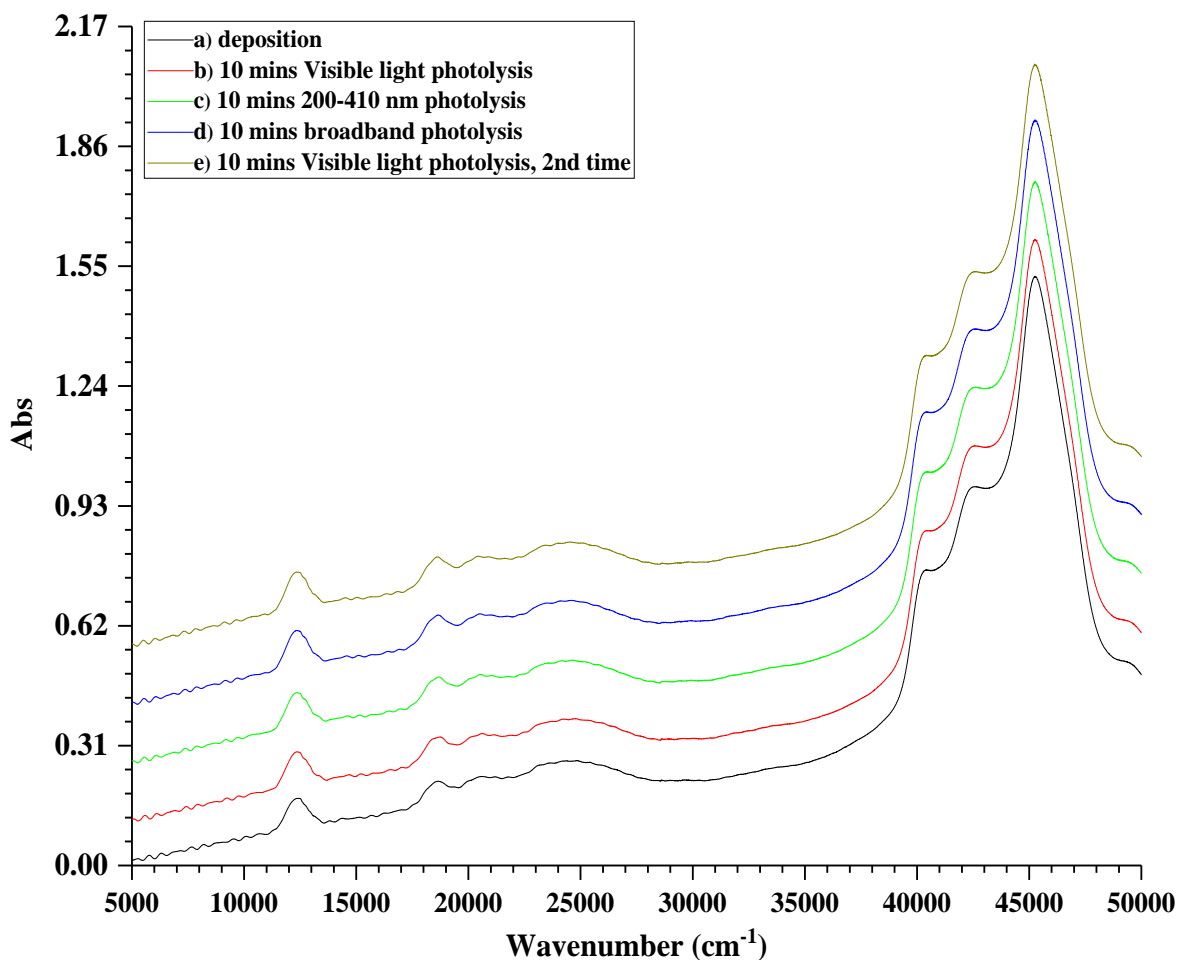
Figure 7.8: *UV/Vis spectra of Pd in a 2% Br$_2$/Ar matrix (a) after deposition, (b) after 10 mins visible light photolysis, (c) after 10 mins 200–410 nm photolysis, (d) after 10 mins broadband photolysis, (e) after further 10 mins visible light photolysis.*

The matrix was annealed to different temperatures to investigate the possibility of any reactions taking place. The optical spectrum shown in Figure 7.9b was recorded after 5 minutes of annealing the matrix at 15 K, the intensity of absorptions at 40200, 42300, and 45300 cm^{-1} broadened and decreased in intensity. The spectrum started to scatter; this is because the light of the spectrometer beam might be either scattered, or absorbed. Figure 7.9c was collected after 5 minutes of annealing at 20 K, the features at 40200, 42300, and 45300 cm^{-1} disappeared; new broad peak was formed at 44130 cm^{-1}. Upon

145

annealing to 25 K for 5 minutes (Figure 7.9d), the broad peak due to the unreacted Br_2 in solid Ar matrix observed at 25000 cm^{-1} decreased it is. Also, the new broad peak at 44130 cm^{-1} increased in intensity and shifted to 43500 cm^{-1}. The extent of scattering in the spectrum has increased. A further 5 minutes of annealing at 30 K was conducted and the UV–visible spectrum in Figure 7.9e illustrates that the peaks at 18600 and 20500 cm^{-1} decreased, while the broad peak at 25000 cm^{-1} has now disappeared. The strong peak at 43500 cm^{-1} shifted a little to 43300 cm^{-1} and became more intense. Lastly, when the matrix was warmed up to 35 K, the absorption bands at 12600 and 20500 cm^{-1} disappeared, the band located at 18600 cm^{-1} decreased, whereas the band at 43300 cm^{-1} increased in intensity and shifted once more to 43100 cm^{-1}. The optical spectrum was greatly affected by scattering and became noisier than before at the end, as the baseline has risen, as shown in Figure 7.9f. The similar results were obtained by using 1% of Br_2 in Ar gas mixture. It is clear the change comparing to the spectrum of Pd atoms in Ar matrix, where the peaks at 40220, 42450, 45340, and 49600 cm^{-1} disappeared on annealing, and the Br_2/Ar spectrum, where the broad peak at 44130 cm^{-1} grew in intensity. Therefore, these bands are not due to $PdBr_n$ molecules. Consequently, the features observed at 12600, 18600, and 20500 cm^{-1} might be from palladium bromide molecules. FIR might confirm this and provide strong evidence for the formation of palladium bromide species.
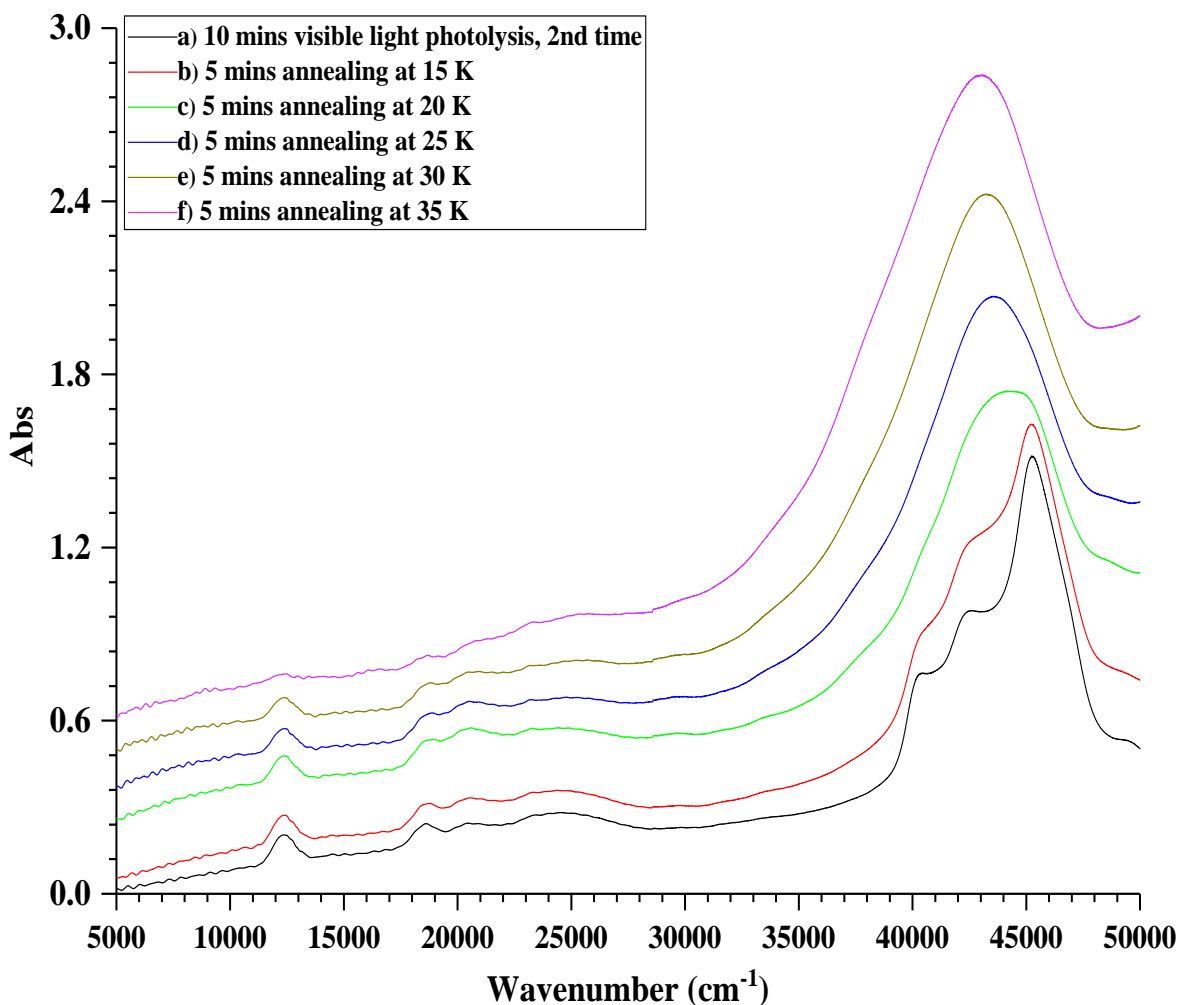
Figure 7.9: *UV/Vis spectra of Pd in a 2% Br$_2$/Ar matrix (a) after further 10 mins visible light photolysis, (b) after 5 mins annealing at 15 K, (c) after 5 mins annealing at 20 K, (d) after 5 mins annealing at 25 K, (e) after 5 mins annealing at 30 K, (f) after 5 mins annealing at 35 K.*

7.2.6 UV/Vis Spectra of 0.6% I$_2$ in Ar

The 0.6% I$_2$ in Ar matrix gas was prepared as a result of sublimation of solid I$_2$ in a fixed volume bulb (2 l) made up with 50 torr, of Ar gas.[41] Figure 4.10 was obtained after 60 minutes of 0.6% I$_2$/Ar gas mixture being introduced onto the cryostat at 11.8 K, whilst the pressure of the vacuum chamber was 8×10^{-6} mbar. The UV–visible spectrum shows only a broad peak at 19300 cm^{-1}, and two weak peaks at 35000 and 40000 cm^{-1}. The ripples are due to interference fringes as the layer is very thin.
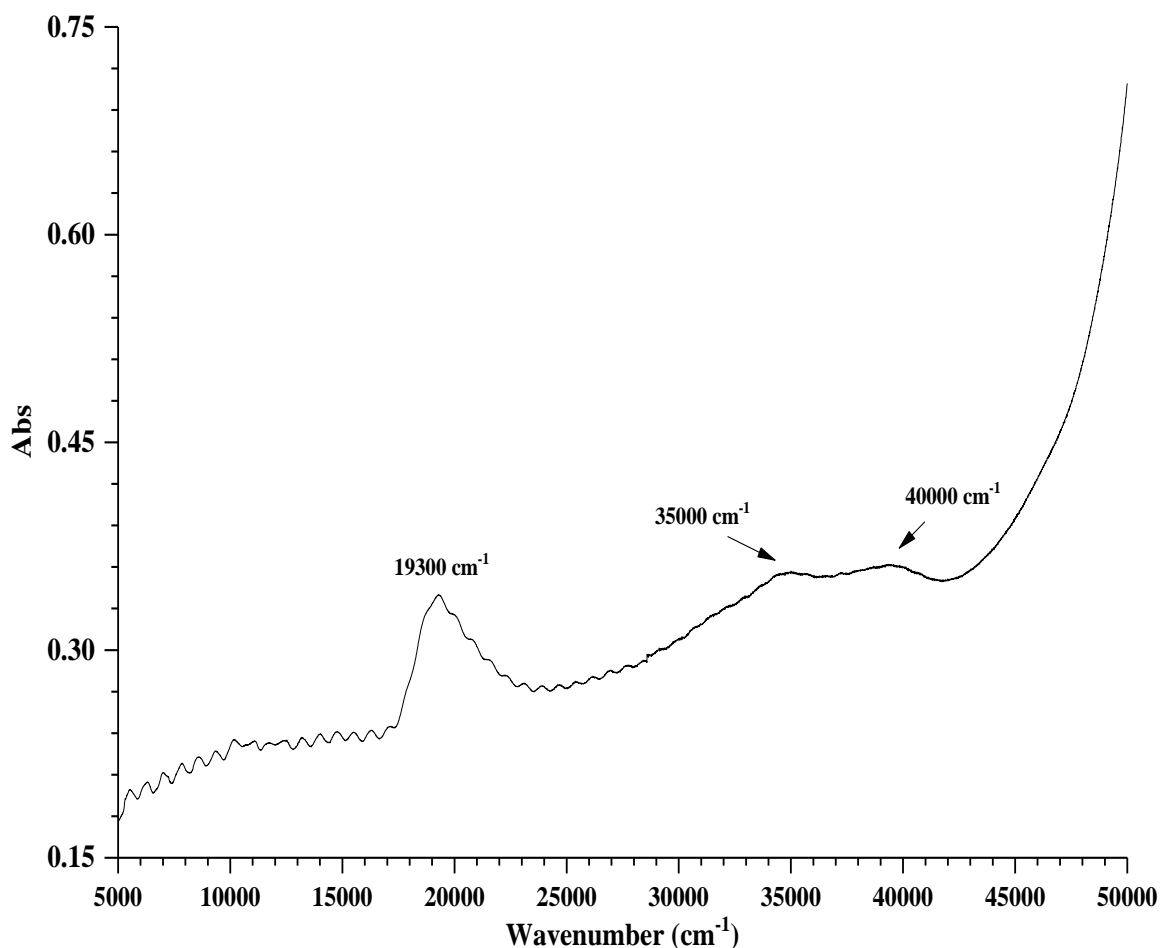
Figure 7.10: *UV/Vis spectrum of a 0.6% I$_2$/Ar matrix after deposition.*

7.2.7 UV/Vis Spectra of Pd in 1% I$_2$/Ar

Initially, 1% I$_2$/Ar gas matrix was introduced for 6 minutes, the thermal evaporation of Pd/Ta filament was obtained using a 34 A electrical current and the equivalent voltage was 1.289 V for 50 minutes and the temperature of the deposition surface of the cryostat was 11.2 K, while the pressure of the vacuum chamber was 4 × 10^{-6} mbar. As shown in Figure 7.11a, two tiny bands at 10400 and 11120 cm^{-1}, a broad peak at 19300 cm^{-1} from unreacted I$_2$ gas, two intense features are observed at 40200 and 42300 cm^{-1}, alongside a strong sharp absorption at 45400 cm^{-1}. The last three are characteristic of unreacted Pd atoms. The matrix was exposed to 10 minutes of visible light photolysis; the peak at 45400 cm^{-1} became more intense as shown in Figure 7.11b. The optical data collected after 200–410 nm photolysis are displayed in Figure 7.11c; the intensity of peak at 45400 cm^{-1} grew a little again. Figures 7.11d and 7.11e contain the UV/vis spectra after 10 minutes of broadband photolysis and further visible light photolysis; it is clear that the photolysis processes have no effect on the matrix.

148
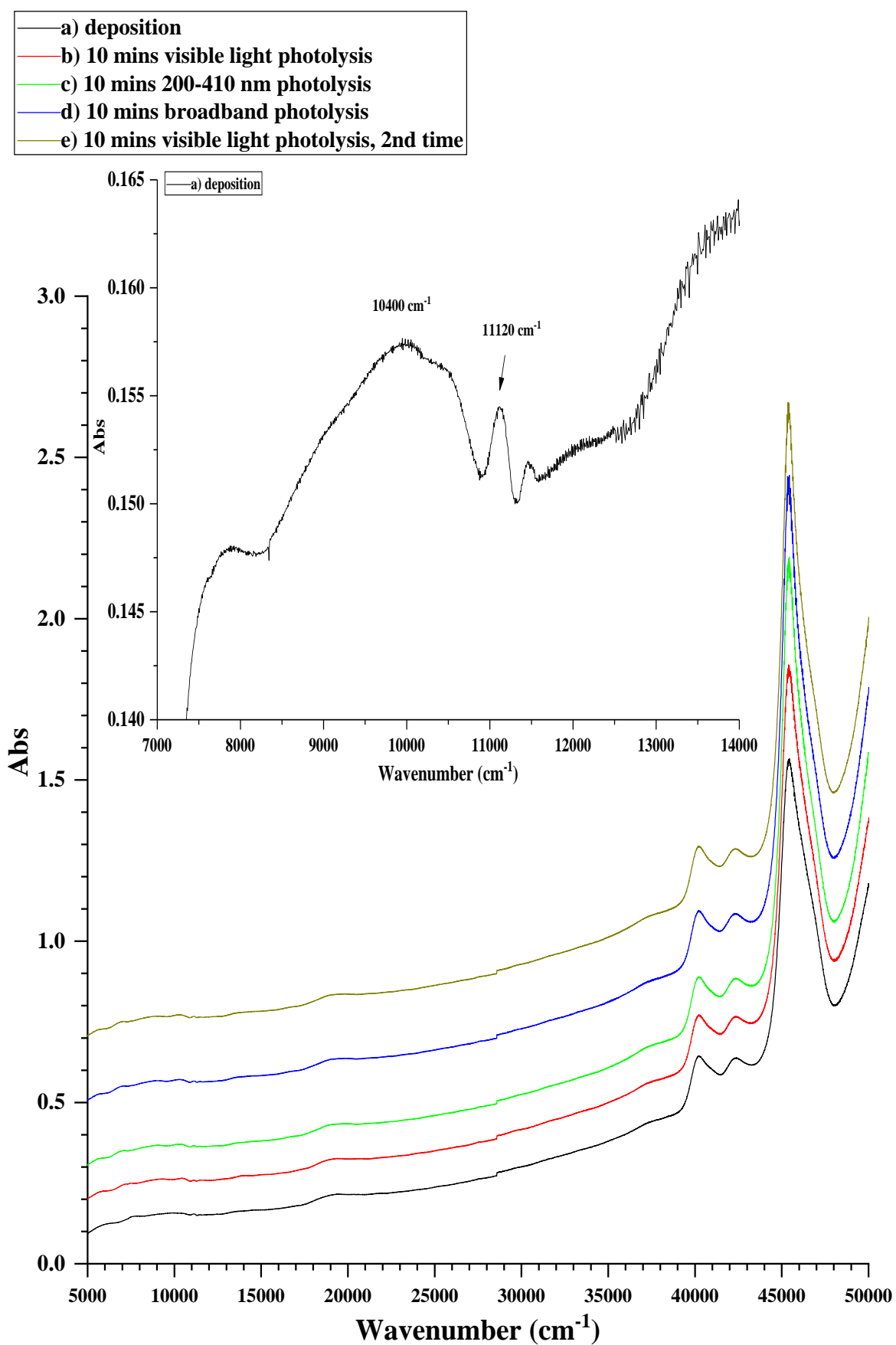
Figure 7.11: *UV/Vis spectra of Pd in a 1% I$_2$/Ar matrix (a) after deposition, (b) after 10 mins visible light photolysis, (c) after 10 mins 200–410 nm photolysis, (d) after 10 mins broadband photolysis, (e) after further10 mins visible light photolysis.*

The matrix was warmed up to 15 K for 5 minutes, from Figure 7.12b it can be seen that that intensity of the features at 40200, 42300, and 45400 cm^{-1} significantly decreased. Additionally, the spectrum was shifted up to an absorbance of 10.0 at high wavenumbers from 49400 cm^{-1} onwards, implying the presence of something very absorbing so that no light was reaching the detector. It could be a palladium iodide species or the formation of iodine, but there is no evidence for the I$_2$ peak at 19300 cm^{-1}. The matrix was annealed again to 20 K for 5 minutes; the UV–visible spectrum in Figure 7.12c, shows that the tiny peak at 11120 cm^{-1} decreased, and the peak at 19300 cm^{-1} decreased, this indicates reduction of I$_2$. Furthermore, a new broad peak was formed at 37600 cm^{-1} and the intensity of the bands at 40200, 42300, and 45400 cm^{-1} diminished. The spectrum rose to 10.0 Abs from 47900 cm^{-1} to the end, indicating an increase in the amount of the highly absorbing material. After further annealing for 5 minutes at 25 K, a successive decrease in intensity of the peak at 19300 cm^{-1} was observed as presented in Figure 4.12d, whereas the band at 45400 cm^{-1} disappeared, and the spectrum started to shift to 10.0 Abs from 46300 cm^{-1} to the end of spectrum. The matrix was exposed to further 10 minutes of broadband photolysis. As shown in Figure 7.12d, a new absorption at 13900 cm^{-1} was recorded, and the spectrum was scattered to 10.0 Abs from 47100 cm^{-1} onwards. Figure 7.12e was recorded after further 5 minutes of warming up the matrix to 25 K, as can be seen the peak at 13900 cm^{-1} was gone. The matrix was annealed at 30 K for 5 minutes, the optical spectrum shows that the intensity of the I$_2$ band at 19300 cm^{-1} decreased; it is probably that Ar started to evaporate and taking some I$_2$ with it. The spectrum began to scatter from 44700 cm^{-1} onwards to 10.0 Abs, as displayed in Figure 7.12f. The same experiments were conducted using 0.6% of I$_2$/Ar gas mixture and similar results were obtained. The absorption bands recorded at 10400, 11120, and 13900 cm^{-1} could be for palladium iodide species in solid matrix of argon. The UV/vis spectroscopy provides a good evidence for the formation of PdI$_n$ compounds. In all of the experiments between Pd atoms and the halogens, there is good evidence for a reaction as the Pd atomic features reduce and are replaced by others. Far−IR experiments are required to characterise different palladium iodide molecules fully.
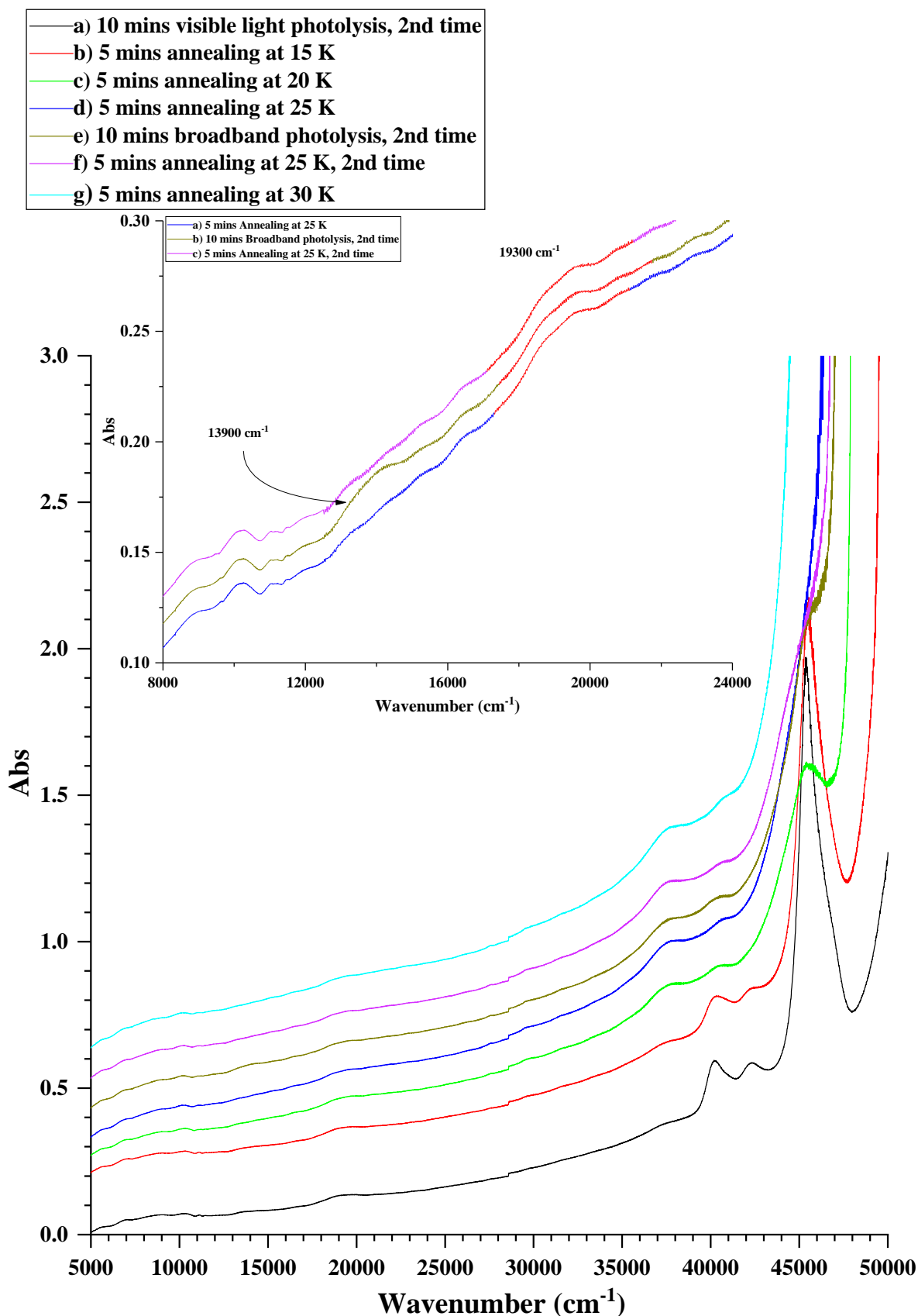
Figure 7.12: *UV/Vis spectra of Pd in a 1% I₂/Ar matrix (a) after further 10 mins visible light photolysis, (b) after 5 mins annealing at 15 K, (c) after 5 mins annealing at 20 K, (d) after 5 mins annealing at 25 K, (e) after 10 mins further broadband photolysis, (f) after further 5 mins annealing at 25 K, (g) after 5 mins of annealing at 30 K.*

7.2.8 FIR spectroscopy of Pd in a 1% Cl_2/Ar matrix

Far infrared spectroscopy was used to investigate the isolation of palladium chlorides in an Ar matrix with the aim of characterising species such as PdCl, $PdCl_2$, $PdCl_3$, and $PdCl_4$ in solid argon, that were hinted at in the UV/vis experiments. The experiment was carried out using 1% of Cl_2 in Ar gas mixture. Palladium atoms were thermally evaporated into the vacuum chamber by using a high current and low voltage furnace. The optimum conditions for evaporation of palladium atoms were achieved using 36 A at 1.351 V. As in all other experiments, a thin layer of 1% Cl_2 in Ar matrix gas was put down onto the cooled inner window before the filament was heated. The experiments of Pd in 1% Cl_2/Ar matrix were run at 10 K and at a pressure of 4×10^{-6} mbar. The far–IR spectra were recorded every 20 minutes for 120 minutes. Unfortunately, no IR bands for palladium chlorides species were detected. Different wavelengths of photolysis and annealing at different temperature were applied to the solid matrix formed. However, no peaks representative any of palladium chloride species were recorded. It was thought that the concentration of 1% of Cl_2 in Ar gas mixture was not enough to interact with palladium atoms. Therefore, the experiments were repeated again using a high concentration of Cl_2 in Ar (10% Cl_2/Ar) gas mixture. IR features due to palladium chlorides molecules were not observed as before. Astonishingly, a brownish rust coloured material was found during cleaning the window of the cryostat after the end of experiments, as seen in Figure 7.13 below. As solid state $PdCl_2$ has a similar colour, this indicates that $PdCl_2$ is formed from the interaction of Pd atoms with Cl_2 in solid Ar matrix, but for reasons that remain unclear was not detected by infrared spectroscopy in far–IR region. Unfortunately, the FIR instrument failed during this series of experiments, which also precluded any experiments using Br_2 or I_2 doped argon matrices.

Therefore, there is tantalising evidence for the formation of palladium halides from palladium atoms and halogens, but detailed characterisation has not been able to be carried out.
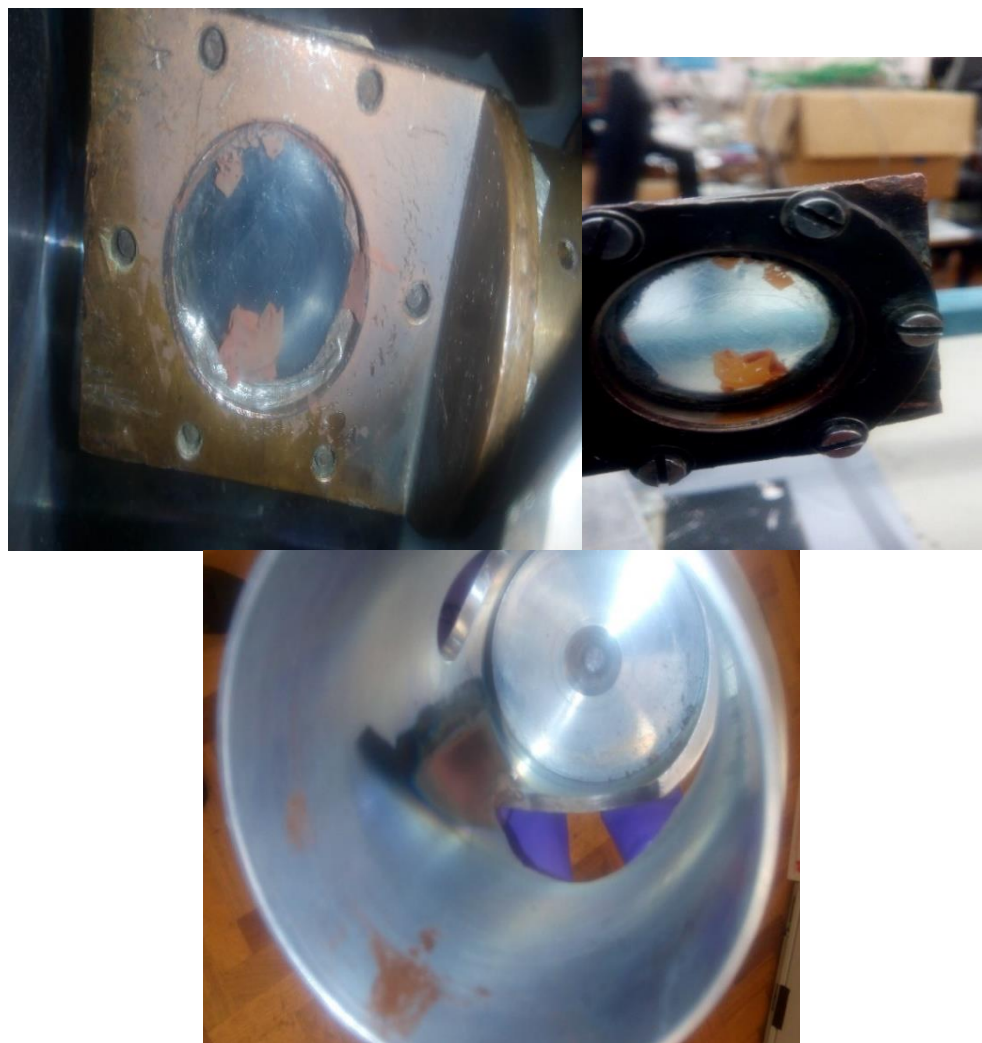
Figure 7.13: *Brownish rust coloured material on the spectroscopic window of cryostat and the radiation shield related to the formation of PdCl$_2$.*

7.2.8.1 Computational study

The theoretical calculations were completed for all palladium chlorides for the molecular arrangement of palladium dichloride molecules with bond angle 179.93° and high–spin configuration (Figure 7.14) this result does not match with previous calculations study by Siegbahn who proposed that PdCl$_2$ is bent with Cl–Pd–Cl bond angle of 98.4°.[42] It is noteworthy that some of the calculations suggested PdCl$_2$ as bent with total energy higher than the linear structure, the details of these calculations are displayed in appendix D. Furthermore, the molecular structure of PdCl$_3$ molecules was predicted as slightly distorted trigonal planar, and the spin state is high–spin electronic configuration. The geometry of PdCl$_4$ species was proposed as distorted seesaw, as the linearity of the molecular structure was completely lost. Also, the calculations indicated that high–spin PdCl$_4$ is lower in energy than low–spin. The bond lengths, electronic ground state, and bond angles for the ground state are presented in Table 4.2 below.

Figure 7.15 demonstrates the calculated IR bands of palladium chloride molecules with their isotopic patterns at half−widths of 0.5 and 1.0 cm^{-1}. Furthermore, the calculated FIR spectra for all palladium chloride molecules and their characteristic isotope patterns at half−width 0.5 cm^{-1} are displayed in Figure 7.16. The calculations suggest that palladium monochloride species and their isotope patterns has only one stretching mode centred at 343 cm^{-1}, PdCl$_2$ has two absorption bands, the antisymmetric stretching mode centred at 398 cm^{-1} and the bending mode at 29 cm^{-1}. The calculations show five peaks for PdCl$_3$, the stretching modes at 358, 335, and 324 cm^{-1} and the deformation modes at 60 and 49 cm^{-1}. The calculations for PdCl$_4$ species proposed four bands, the vibrational frequency centred at 368 cm^{-1} is due to the antisymmetric stretching mode and the symmetric stretching mode at 305 cm^{-1}, while the two peaks calculated at 122 and 104 cm^{-1} belong to the bending modes.

Table 7.2: The calculated geometry of palladium chloride species.

Assignments	Molecular structure	Electronic ground state	Cl–Pd–Cl Bond angles	Pd–Cl Bond lengths (Å)
PdCl	−	$^2\Sigma$	−	2.251
PdCl$_2$	Linear	$^3B_2$	179.93°	(2.232)×2
PdCl$_3$	Distorted trigonal planar	$^4B_1$	(114.06°)×2, 131.87°	(2.236) ×2, 2.283
PdCl$_4$	Distorted seesaw	$^3B_2$	(93.19°)×4, (152.73°)×2	(2.251)×4
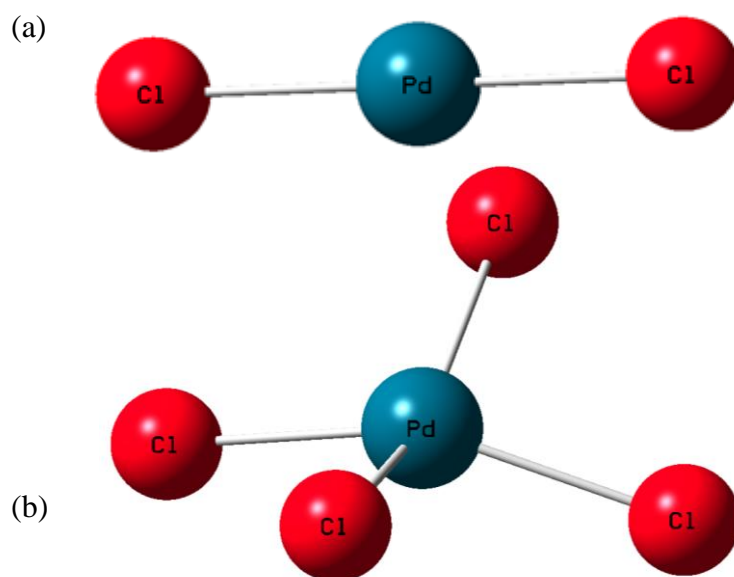
Figure 7.14: *Calculated (B3LYP/def2tzvpp) geometric structure of (a) PdCl$_2$, (b) PdCl$_4$.*
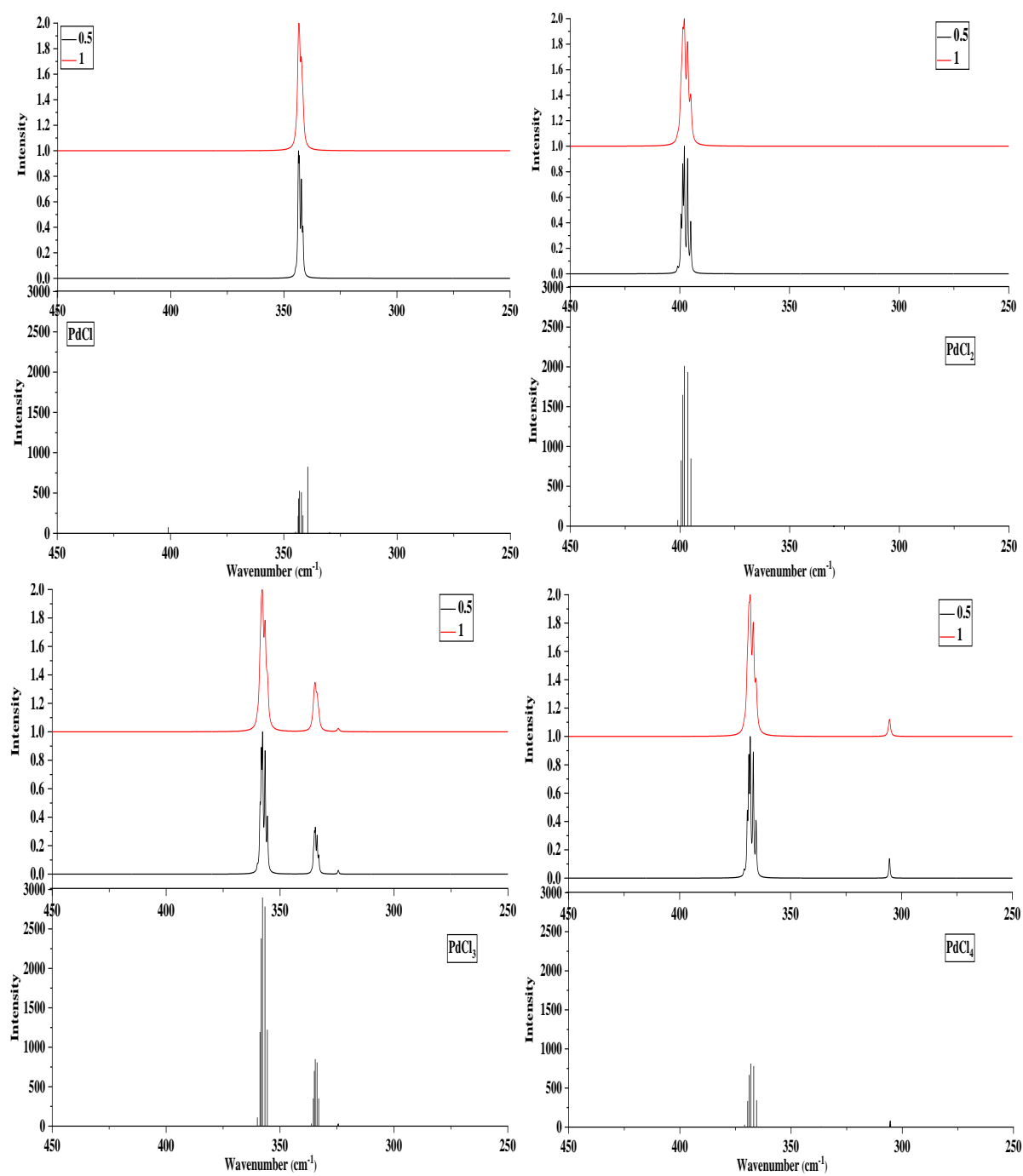
Figure 7.15: *Calculated (B3LYP/def2tzvpp) IR spectra of isotopes of Pd chloride molecules at two different half−widths 0.5 and 1.0 cm^{-1}.*
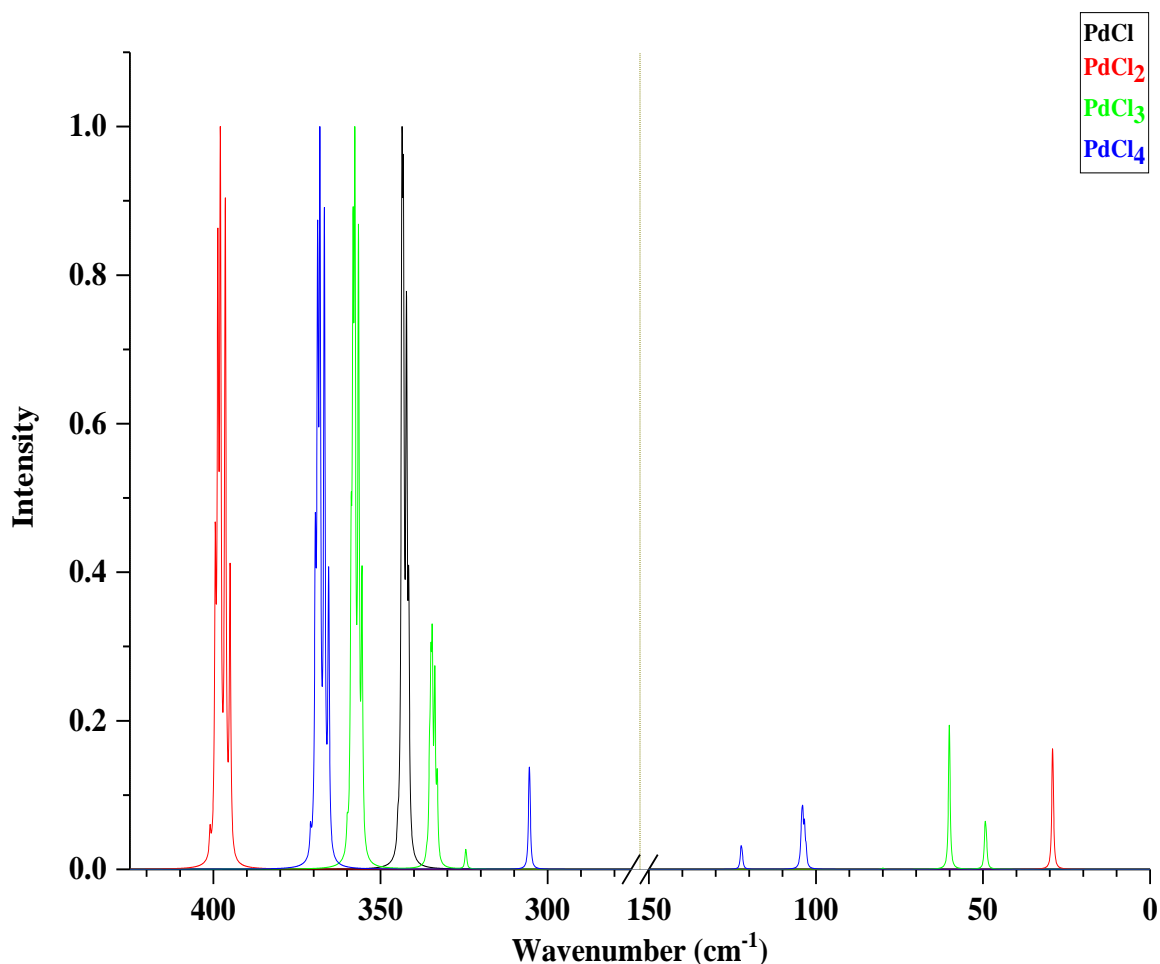
Figure 7.16: *Calculated (B3LYP/def2tzvpp) IR spectra of all Pd chloride molecules and their isotope patterns at half−width 0.5 cm^{-1}.*

The overall reaction enthalpy as well as stepwise reaction enthalpy calculations according to reaction between Pd and Cl_2 molecules have been undertaken to investigate the relative stability of palladium chlorides. The overall reaction enthalpy in Figure 7.17 shows that the enthalpy of formation of $PdCl_2$ and $PdCl_3$ species is close and palladium tetrachloride species have the largest enthalpy of formation. Based on that, the formation of $PdCl_4$ molecules is expected, if there is abundant chlorine in the matrix. Figure 7.18 represents the stepwise reaction enthalpy, and this shows that the formation of $PdCl_3$ is only just exothermic. $PdCl_3$ lies a point above $PdCl_2$ and $PdCl_4$; it is more unstable compared to $PdCl_2$ and $PdCl_4$ and has a propensity to disproportionate to $PdCl_2$ or $PdCl_4$ molecules. Whereas, $PdCl_2$ lies below the line connecting PdCl and $PdCl_3$, and this indicates that a comproportionation reaction is possible resulting in the formation of $PdCl_2$ from PdCl and $PdCl_3$.
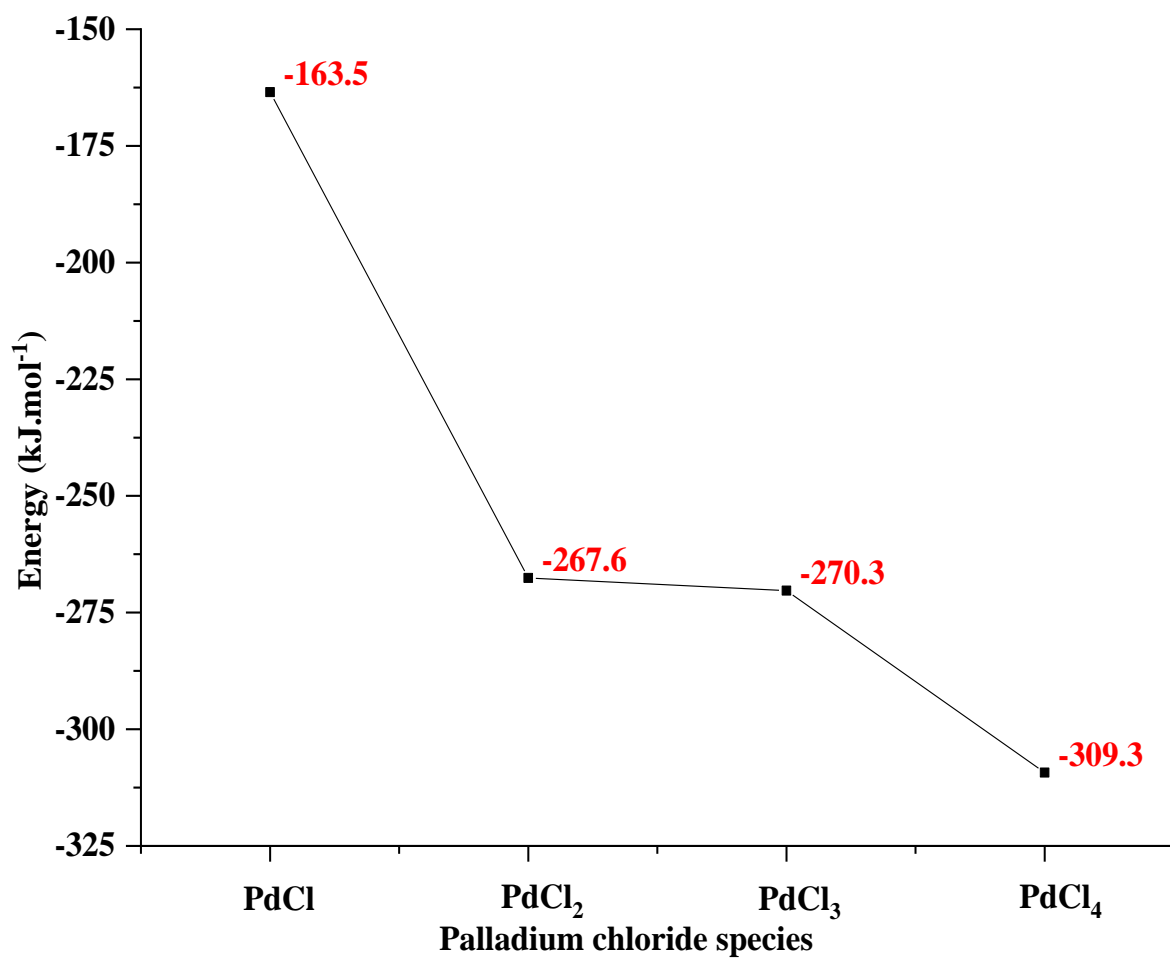
Figure 7.17: *Overall reaction enthalpy of PdCl$_n$ species.*
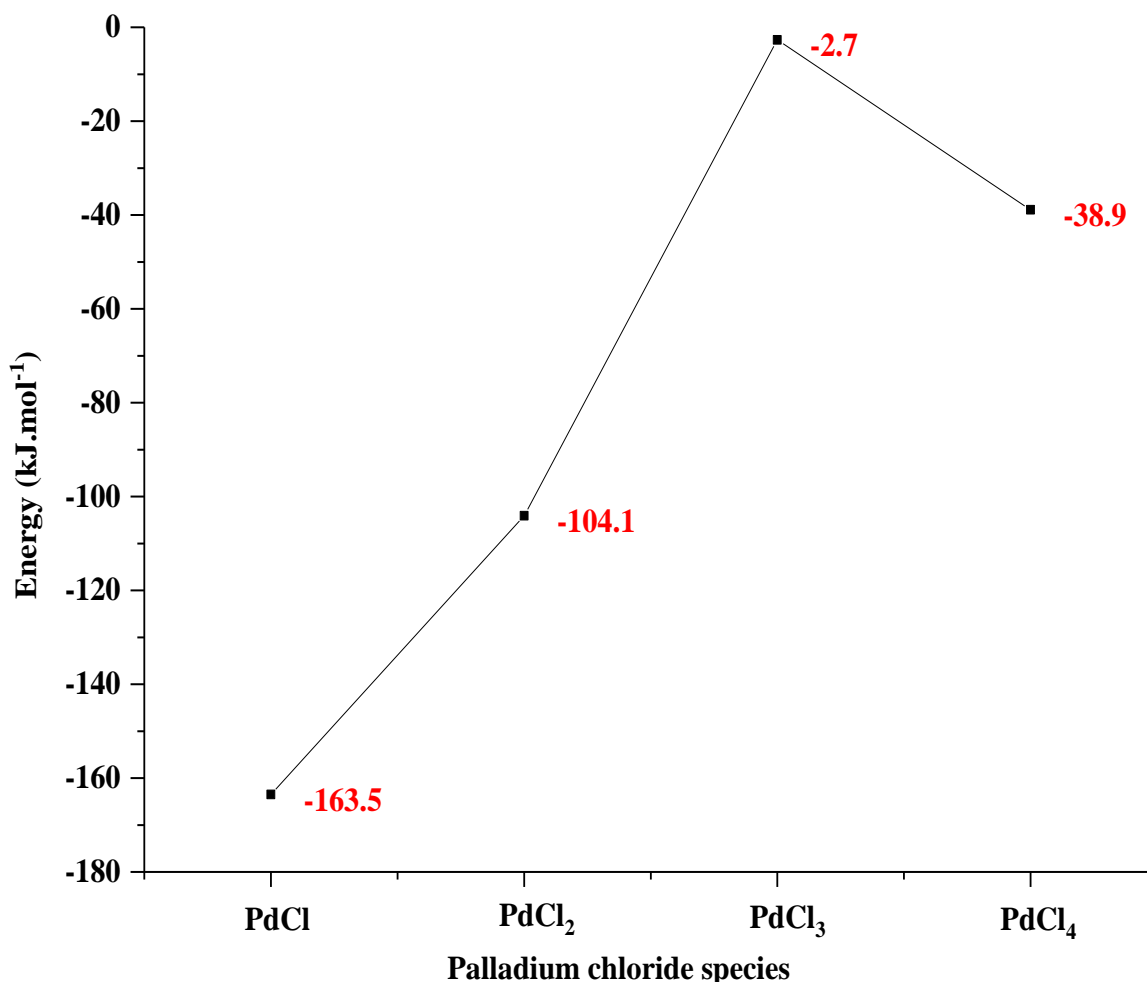
Figure 7.18: *Stepwise reaction enthalpy of PdCl$_n$ species.*

7.3 Conclusion

UV/vis spectroscopy has been used to determine the optimum conditions for producing atomic palladium in argon matrices as well as identifying the possible formation of new palladium halide species while matrix isolation infrared spectroscopy was employed to try to characterise the vibrational frequencies of the palladium chlorides. .

The UV/vis spectrum was recorded after 40 minutes of vaporising palladium atoms metal in the presence of neat argon gas. The spectrum is in agreement with data reported in the past for Pd atoms isolated in solid argon matrix.[4, 5] Photolysis had no impact on the matrix, while annealing up to different temperature did not provide any evidence for the formation of dimeric species of palladium.[5] The intensity of peaks decreased with annealing, as also reported in previous studies. The UV/vis spectrum obtained after 75 minutes of evaporating Pd in presence of 2.5% Cl$_2$ diluted in Ar matrix showed bands at 16700, 20880, 22640, and 25300 cm^{-1}, which were considered as

evidence of the generation of palladium chloride species, as they are different features that have not been observed in the spectrum of Pd atoms isolated in neat Ar matrix. The UV/vis spectra was recorded after 60 minutes of deposition to characterise the interaction between palladium atoms and bromine in a solid argon matrix. Three weak features are located at 12600, 18600, and 20500 cm^{-1} followed by a broad peak at 25000 cm^{-1} due to the unreacted Br_2. In addition, bands related to palladium were also observed. Photolysis with different wavelength visible light, 200–410 nm, and broadband, and annealing to 35 K by an interval of 5 K were also applied, the features observed at 12600, 18600, and 20500 cm^{-1} might due to palladium bromide molecules. The optical data of palladium isolated in solid argon matrix doped with 1% of iodine were obtained. Two tiny bands at 10400 and 11120 cm^{-1}, a broad peak at 19300 cm^{-1} from unreacted I_2 gas are observed accompanied by three intense features at 40200, 42300, and 45400 cm^{-1} from Pd atoms. A new peak at 13900 cm^{-1} appeared after broadband photolysis but disappeared on annealing to 25 K. The absorption bands at 10400, 11120, and 13900 cm^{-1} are more likely for palladium iodide species in solid matrix of argon. Infrared spectroscopy in the far−IR region was used to investigate the interaction of palladium with chlorine doped in an Ar matrix. Surprisingly, no IR features due to palladium chlorides species were observed for reasons that are not completely clear, but the instrument has now stopped working so it is not possible to reinvestigate the chlorine, or investigate the bromine and iodine reactions with Pd atoms. However, there was evidence of a reaction between Pd and Cl_2 as a brownish rust coloured material, very similar in appearance to solid state $PdCl_2$ was found during cleaning the window of the cryostat after the end of experiments.

7.4 Summary

The theoretical calculations suggested the geometry of molecular $PdCl_2$ was linear. The interaction of palladium atoms and bromine in a solid argon matrix was examines for the first time. The UV/vis spectrum showed features at 12600, 18600, and 20500 cm^{-1} which appeared on deposition of the Pd/Br_2 suggesting they due to palladium bromide molecules. No Further investigation of stoichiometry or geometry of these species was possible.

7.5 References

1.   D. M. Mann and H. P. Broida, *J. Chem. Phys.*, 1971, **55**, 84-94.
2.   W. E. Klotzbücher and G. A. Ozin, *J. Am. Chem. Soc.*, 1975, **97**, 2672-2675.
3.   G. A. Ozin and W. E. Klotzbücher, *J. Am. Chem. Soc.*, 1975, **97**, 3965-3974.
4.   W. E. Klotzbücher and G. A. Ozin, *Inorg. Chem.*, 1976, **15**, 292-295.
5.   W. E. Klotzbücher and G. A. Ozin, *Inorg. Chem.*, 1980, **19**, 3767-3776.
6.   R. Grinter and D. R. Stern, *J. Chem. Soc., Chem. Commun.*, 1982, 40-41.
7.   W. Schrittenlacher, H. H. Rotermund and D. M. Kolb, *J. Chem. Phys.*, 1985, **83**, 6145-6149.
8.   G. A. Ozin and J. Garcia-Prieto, *J. Phys. Chem.*, 1988, **92**, 325-337.
9.   G. A. Ozin and J. Garcia-Prieto, *J. Phys. Chem.*, 1988, **92**, 318-324.
10.   J. Garcia-Prieto and O. Novaro, *Rev. Mex. Fis.*, 1997, **43**, 130-158.
11.   Y. Taketsugu, T. Taketsugu and T. Noro, *J. Chem. Phys.*, 2006, **125**, 154308.
12.   E. P. Kündig, M. Moskovits and G. A. Ozin, *Can. J. Chem.*, 1972, **50**, 3587-3593.
13.   E. P. Kündig, M. Moskovits and G. A. Ozin, *J. Mol. Struct.*, 1972, **14**, 137-144.
14.   J. H. Darling and J. S. Ogden, *J. Chem. Soc., Dalton Trans.*, 1973, 1079-1085.
15.   E. P. Kündig, D. McIntosh, M. Moskovits and G. A. Ozin, *J. Amer. Chem. Soc.*, 1973, **95**, 7234-7241.
16.   B. Tremblay and L. Manceron, *Chem. Phys.*, 1999, **250**, 187-197.
17.   B. Liang, M. Zhou and L. Andrews, *J. Phys. Chem. A*, 2000, **104**, 3905-3914.
18.   Z. J. Wu, H. L. Li, H. J. Zhang and J. Meng, *J. Phys. Chem. A*, 2004, **108**, 10906-10910.
19.   Y. Taketsugu, T. Noro and T. Taketsugu, *Chem. Phys. Lett.*, 2010, **484**, 139-143.
20.   G. A. Ozin, M. Moskovits, E. P. Kündig and H. Huber, *Can. J. Chem.*, 1972, **50**, 2385-2387.
21.   H. Huber, E. P. Kündig, M. Moskovits and G. A. Ozin, *J. Amer. Chem. Soc.*, 1973, **95**, 332-344.
22.   S. M. Souvi, B. Tremblay, J. P. Perchard and M. E. Alikhani, *J. Chem. Phys.*, 2009, **130**, 074304.
23.   H. Huber, W. E. Klotzbücher, G. A. Ozin and A. Vander Voet, *Can. J. Chem.*, 1973, **51**, 2722-2736.
24.   X. Wang and L. Andrews, *J. Phys. Chem. A*, 2001, **105**, 5812-5822.
25.   R. Yang, Y. Gong and M. Zhou, *Chem. Phys.*, 2007, **340**, 134-140.
26.   X. Jin, G. Wang and M. Zhou, *J. Phys. Chem. A*, 2006, **110**, 8017-8022.
27.   L. B. Knight and W. Weltner, *J. Mol. Spectrosc.*, 1971, **40**, 317-327.
28.   L. B. Knight, S. T. Cobranchi, J. Herlong, T. Kirk, K. Balasubramanian and K. K. Das, *J. Chem. Phys.*, 1990, **92**, 2721-2732.
29.   L. Andrews, L. Manceron, M. E. Alikhani and X. Wang, *J. Am. Chem. Soc.*, 2000, **122**, 11011-11012.
30.   L. Andrews, X. Wang, M. E. Alikhani and L. Manceron, *J. Phys. Chem. A*, 2001, **105**, 3052-3063.
31.   M. E. Alikhani and C. Minot, *J. Phys. Chem. A*, 2003, **107**, 5352-5355.
32.   G. A. Ozin and W. J. Power, *Inorg. Chem.*, 1977, **16**, 212-213.
33.   X. Wang and L. Andrews, *J. Phys. Chem. A*, 2003, **107**, 337-345.
34.   A. V. Wilson, T. Nguyen, F. Brosi, X. Wang, L. Andrews, S. Riedel, A. J. Bridgeman and N. A. Young, *Inorg. Chem.*, 2016, **55**, 1108-1123.
35.   T. P. Martin, *J. Chem. Phys.*, 1978, **69**, 2036-2042.
36.   P. E. M. Siegbahn, *Theor. Chim. Acta,*, 1994, **87**, 441-452.
37.   N. Harris, *PhD Thesis, The University Of Hull*, 2001.

38. E. L. Dixon, *PhD Thesis, The University Of Hull*, 2004.
39. M. Moskovits and G. A. Ozin, *Cryochemistry, Wiley-Interscience, New York*, 1976.
40. I. J. Blackmore, A. J. Bridgeman, N. Harris, M. A. Holdaway, J. F. Rooms, E. L. Thompson and N. A. Young, *Angew. Chem., Int. Ed.*, 2005, **44**, 6746-6750.
41. J. H. Stern and N. W. Gregory, *J. Phys. Chem.*, 1957, **61**, 1226-1232.
42. P. E. M. Siegbahn, *Theor. Chim. Acta.*, 1994, **87**, 441-452.

Chapter 8

Lewis acid–base chemistry of silicon tetrafluoride and alkyl phosphines

8.1 Introduction

8.1.1 History

In 1927, Sidgwick revealed the ability of halides of groups 13 and 14 to react with other ligands and receive pairs of electrons to complete the electronic configuration. This process was known as coordination or coordinate bond formation, while the ligands are called donors and the term acceptor for the halides of groups 13 and 14 was adopted.[1]

Afterwards in 1932, G. N. Lewis proposed a new definition of acid and base. He indicated that in his definition an acid is a molecule capable of accepting an electron pair into an orbital of one of its atoms, whereas a base is a molecule which is able to donate an electron pair to another molecule forming an electron pair bond.[2] Moreover, he also defined the acid in a solvent system as a substance which either releases cations or reacts with the anion of the solvent, and defined the base as a substance which loses anions or combines with the cation in the solvent.[3, 4] In the same year a new definition known as the proton definition was developed by Lowry[5] and Brønsted.[6] Subsequently, the concept of Lewis acid/base has become common in chemistry.

8.1.2 Lewis Acids – SiF$_4$

Silicon tetrafluoride is one of the most important Lewis acids of group 14. The Si–F bond energy is about 590 kJ/mol.[7] It is one of the group 14, where the silicon atom is located in the centre, linked with four valence electrons and the outer shell contains eight electrons. In the last decade, scientists were concerned about the adducts from the reaction of SiX$_4$ (X = Cl, Br, I, or F) with N– and O– donor ligands.[8-12] The main reason of studying the complexes of silicon tetrahalide and neutral ligands are because the attained compounds are thermodynamically stable and the interesting configuration of the complexes as well. The bi– or poly–dentate ligands (Ethylenediamine, 1,3–diisopropyl–4,5–dimethylimidazol–2–ylidene, etc) have the ability to form inorganic complexes with silicon halide molecules through donating an electron pair into the orbital of silicon atom.[13, 14]

Whilst SiF$_4$ might be thought to be a strong Lewis acid because of the electronegativity of the fluorine atoms; it is in fact less reactive and considered a weak acceptor compared to the other SiX$_4$ species. This is because the Si–F bond length is shorter than other Si–X bonds and results in greater steric hindrance during reaction with phosphorus ligands.[7, 15] Beattie and Ozin stated that the reactivity of SiF$_4$ in reaction with NMe$_3$ is more than the reactivity in reaction with PMe$_3$, and so it forms stable adducts with NMe$_3$ compared to the reaction with PMe$_3$. In contrast, the reaction of silicon tetrachloride with trimethylphosphine is relatively preferred. This is because the size of the p orbital in fluorine is smaller than the size of p orbital in chlorine and so it is more preferable for the Si atom in SiF$_4$ to interact with N of NMe$_3$. Nonetheless, it is appropriate for the Si atom in SiCl$_4$ to react with P of trimethylphosphine.[15]

8.1.3 SiF$_4$ Adducts

Researchers began to investigate the reaction between group 14 tetrahalide (MX$_4$) and different ligands in 1960s.[15] SiF$_4$ reacts with N– donor ligands such as the Lewis base NH$_3$ to form SiF$_4$.NH$_3$ and SiF$_4$.(NH$_3$)$_2$ complexes.[7, 16-20] The reaction involves the formation of Si–N coordination bonds. Although, the six coordinate adduct of SiF$_4$ and NH$_3$ was discovered two centuries ago. he five coordinate (1:1) complex isolated in solid Ar matrix was first reported by Ault in 1981.[21] Two sets of absorption bands assigned to SiF$_4$.NH$_3$ complex were observed in the recorded IR data; sharp bands at 409, 456, 706, 854, and 1253 cm^{-1}, whilst the other group of broad vibrational frequencies was obtained at 416, 463, 839, 1260 cm^{-1}. The geometrical structure of SiF$_4$.NH$_3$ complex was suggested as C$_{3v}$ trigonal bipyramid shape, where the NH$_3$ ligand was connected to Si atom in an axial position and perpendicular to three Si–F bonds, instead of C$_{2v}$ geometry for an equatorial NH$_3$ ligand. This geometry did not obey Muetterties rule,[22] which states that the most electronegative ligand occupies the axial position.[22] Additional experimental and theoretically investigations indicated the same axial site of N– donor ligand and confirming the C$_{3v}$ symmetry.[23-28] Other studies revealed that the complex is only stable at temperatures lower than –40 °C; raising the temperature led to converting the complex into SiF$_4$ and *trans*–SiF$_4$(NH$_3$)$_2$ complex.[7, 29, 30] A recently published book indicated the reaction of SiF$_4$ with liquid ammonia and formation of SiF$_4$.(NH$_4$)$_2$.2NH$_3$ complex which decomposed to the *trans*–SiF$_4$(NH3)$_2$ complex by warming the adduct.[31] In 2018, a recent work was carried out by Hora *et al*. to investigate the reaction of SiF$_4$ with different N– donor ligands such as pyridine, nitrile, and fluoro–substituted pyridine using thin film IR spectroscopy.[32] The study revealed the formation of 1:1 complexes as

well as 1:2 complexes. Furthermore, the computational calculations were consistent with the experimental data obtained.

The first investigation of reaction between SiF_4 and O– donor ligands such as H_2O and MeOH was performed by Margrave *et al.* and the results indicated that no complex was formed.[33] Several trials were carried out by Ault to study the reaction of SiF_4 with MeOH, Me_2O, and H_2O and using the twin–jet matrix isolation method led to the formation of the 1:1 complexes $SiF_4.(OMe_2)$ and $SiF_4.(OH_2)$. The geometry of the adduct was proposed as distorted trigonal bipyramid.[21, 34] Later on, several studies were conducted confirming the suggested geometry of the adducts.[35-37] IR spectroscopy was used to investigate the reaction of SiF_4 within $O(CH_2)_2$ diluted in Ar gas matrix. The IR spectrum had no features relating to $O(CH_2)_2$ indicating the consumption of ligand and the reaction with SiF_4, while the band observed at 973 cm^{-1} was due to the Si–F stretching mode.[38] However, the structure of the complex was not able to be identified.

Silicon tetrachloride was a good example to study the reaction of SiX_4 with P– donor ligands, and some experiments were undertaken to study the reaction between $SiCl_4$ and PMe_3, indicating that both 1:1 and 1:2 adducts can be formed. It was easy to form the $SiCl_4.(PMe_3)_2$ (1:2) complex at room temperature, while the $SiCl_4.(PMe_3)$ (1:1) complex was not formed.[15] Another attempt to carry out the same experiment at very low temperature (–78 °C) led to the formation of both 1:1 and 1:2 adducts. The first reported complex between SiF_4 and PMe_3 was reported in the sixties of last century by Beattie and Ozin,[17, 20] but this was poorly characterised; and although there have been several attempts since, none have been successful. The symmetry of all 1:2 complexes for $SiX_4.(PMe_3)_2$ was proposed as *trans*–octahedral.[20] Research was undertaken by K. George *et al.* to investigate the reaction between silicon tetrafluoride and phosphine oxide ligands at room temperature, but this failed to produce any complexes.[39] The same experiments were successful when anhydrous CH_2Cl_2 was added, which supported the formation of the complexes at room temperature. A *trans*–isomer of $SiF_4.(OPMe_3)_2$ with octahedral configuration as well as *trans*–$SiF_4.(OPEt_3)_2$ were detected. A theoretical study proposed that the 1:1 adduct $SiX_4.(PMe_3)$ was less stable compared to the 1:2 adduct $SiX_4.(PMe_3)_2$.[40] A recent attempt to reinvestigate reaction of silicon tetrafluorides with phosphine ligands failed to isolate any adducts of SiF_4 with phosphine or diphosphine ligands, even though CH_2Cl_2 was added to expedite the reaction and the temperature of reaction was 190 K.[9] The NMR analysis did not provide any evidence for the formation of corresponding complexes. This result was in contrast to the previous work using

164

Raman spectroscopy by Beattie and Ozin.[20] Some experiments were carried out to investigate reaction between SiF_4 and PPh_3, but the reaction was ineffective because PPh_3 is a weak donor ligand. In addition, it is considered a bulky ligand as well, thus it would not be able to coordinate to SiF_4 to form complexes.[40] A theoretical work discussed the reaction between SiF_4 and HF as well as PH_3 and the geometry of both complexes was axial.[16] The HF complex was very weakly bound and there was doubt that it would be able to be observed experimentally, and the PH_3 complex only had marginal stability. In 2016, a recent attempt at the Department of Chemistry, University of Hull succeeded in forming complexes of SiF_4 with PMe_3 by conducting the experiment at 80 K using a cryogenic system.[41] The aim of this work is to investigate the reaction of silicon tetrafluoride with alkyl phosphines.

8.2 Experimental

8.2.1 Sample preparation

The stock supply of neat SiF_4 gas had been decanted from a metal cylinder into a 1 L glass bulb previously and was mounted on a glass vacuum line in a fume cupboard. PMe_3 and PEt_3 (Strem Chemicals) were supplied in glass ampoules and were decanted into tap ampoules in a glove box, and then subjected to three freeze-thaw degas cyles to remove dissolved gases using the glass vacuum line in the fume cupboard. A clean empty glass bulb was connected to a glass manifold and kept under dynamic vacuum for about an hour in a fume cupboard. It was heated smoothly using a heat gun to remove any volatile impurities or water vapour from inside. The experimental mixtures were made up using standard manometric procedures to produce the desired pressures in the appropriate ratios. In the case of mixed SiF_4 and PMe_3 and PEt_3 mixtures the phosphine was added first as it has a lower vapour pressure.

8.2.2 IR Spectroscopy

The same FTIR apparatus and vacuum chamber used in matrix isolation study of transition metals halides were used as described in chapter 2 before (Figure 2.6). Furthermore, the same closed cycle cryostat was used as well, details were provided in chapter 2. The prepared sample bulbs were mounted to the front port of the vacuum chamber instead of the evaporation furnace as illustrated in Figure 8.1. The cryostat was turned on to cool down the spectroscopic window and experiments were carried out at

temperature 10–80 K, as the preliminary studies had indicated that it 80 K was the optimum temperature.[41]
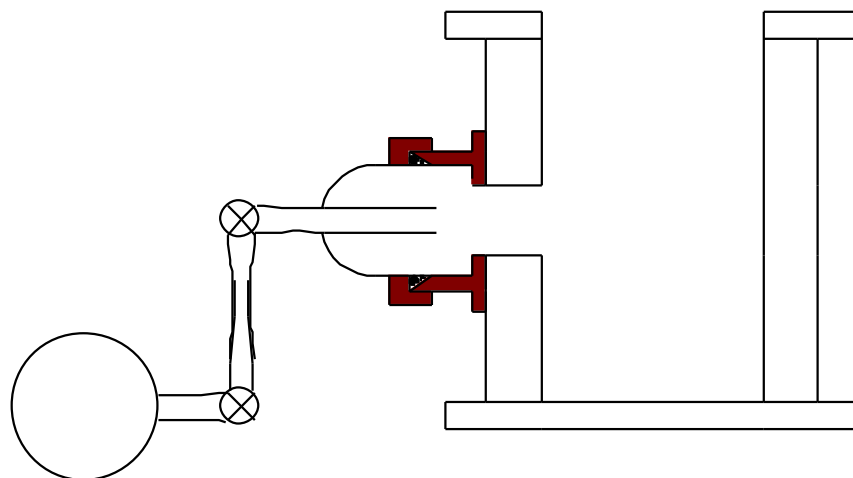
Figure 8.1: *Diagram shows the prepared sample bulb mounted to the front port of the vacuum.*

8.2.3 Computational Calculations

DFT calculations using G09W at the B3LYP/def2tzvpp level were carried out to identify the geometric and electronic ground state for the complexes formed. The calculated vibrational frequencies were also used to help with the assignment of the features in the IR spectra.

8.3 Results and Discussion

Earlier studies undertaken by undergraduate project students R. Brighouse (2014)[42] and A. Niculau (2016)[41] had shown that the most effective way to carry out the experiments was to use thin films at 80 K rather than dilute matrices. Therefore, spectra of the pure materials were collected before investigating the complexes.

8.3.1 FTIR spectroscopy of neat SiF₄

An 11 torr sample of neat SiF_4 gas in a *ca* 50 mL bulb was introduced to the deposition surface of the cryostat as sequential aliquots. Each aliquot was formed by evacuating the glass tubing between the bulb and the vacuum chamber, closing the valve on the vacuum chamber, opening the valve on the bulb to fill the tube and then closing the valve. The sample was then deposited by opening the valve on the vacuum chamber. This process was repeated as necessary. Figure 8.2a shows the infrared spectrum for SiF_4 gas condensed at 9.2 K. It displays a strong asymmetric broad peak centred at 993 cm^{-1}

alongside two shoulders at 988 and 1055 cm^{-1} which are assigned to Si–F asymmetric stretching mode.[32, 43, 44] A very weak peak at 835 cm^{-1} is attributed to the symmetric stretching mode of Si–F bonds (Table 8.1). In order to identify the changes associated with warming the sample up, the solid compound was warmed by 10 K intervals to 80 K and the peaks became narrower and taller as presented in Figure 8.2b. When the sample was warmed to 90 K, and as shown in Figure 8.2c, the intensity of all peaks was reduced. Figure 8.2d displays the IR spectrum after 5 minutes of annealing the SiF$_4$ compound to 100 K; and the feature located at 835 cm^{-1} disappeared completely, and the peak at 993 cm^{-1} decreased significantly. The spectrum in Figure 8.2e was run after annealing the compound to 120 K, no bands were obtained. It is obvious that the deposited SiF$_4$ was utterly evaporated at 120 K.

Table 8.1: Vibrational frequencies (cm^{-1}) observed and previous studies of neat SiF$_4$.

Experiment	Ref [43]	Assignments
993 cm^{-1}	991 cm^{-1}	Si–F asymmetric stretching mode
835 cm^{-1}	–	Si–F symmetric stretching mode
373 cm^{-1}	–	Si–F in plane scissoring bending mode
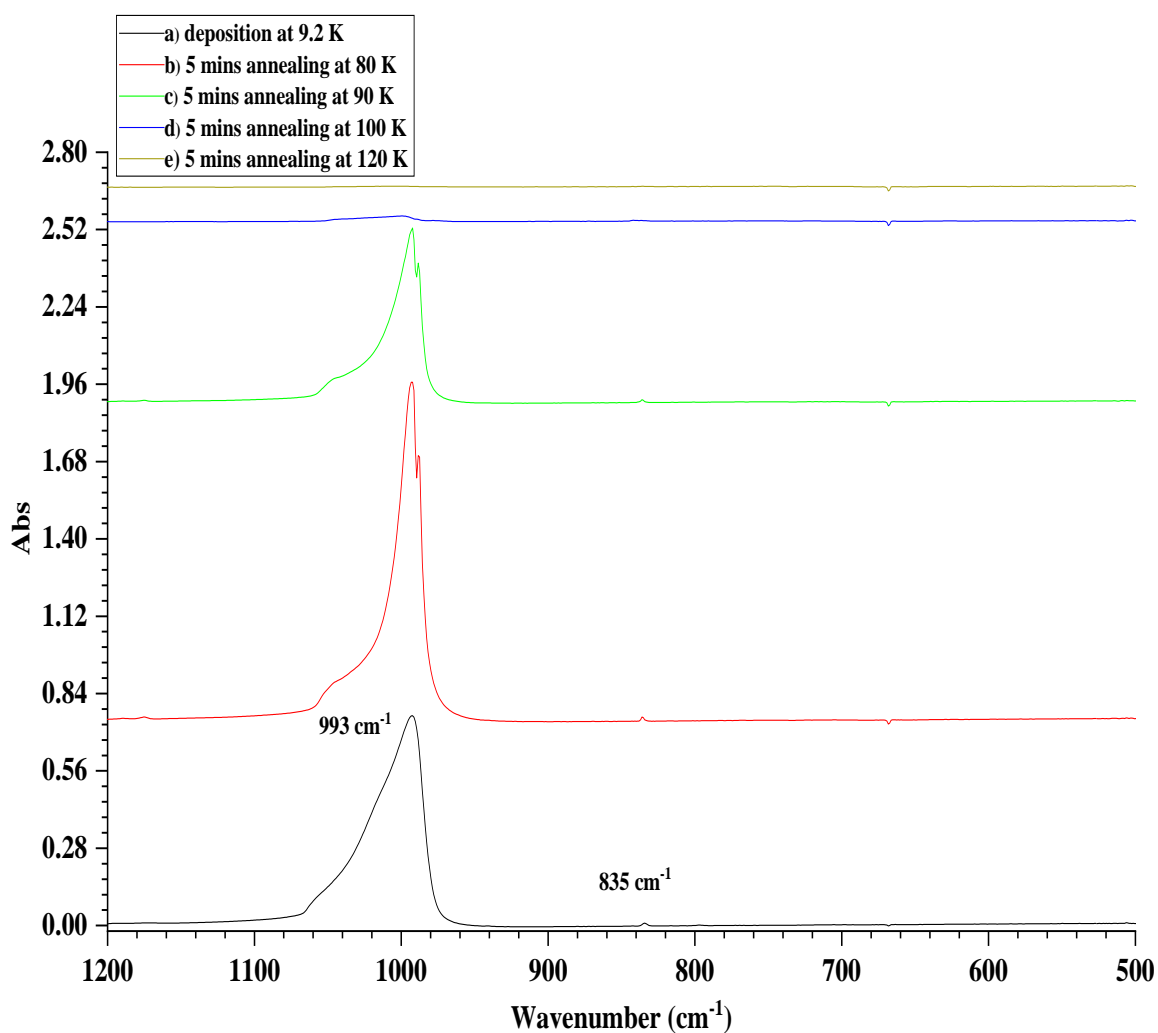
Figure 8.2: *FTIR spectra of neat SiF$_4$ (11 torr) (a) after deposition at 9.2 K, (b) after 5 mins annealing at 80 K, (c) after 5 mins annealing at 90 K, (d) after 5 mins annealing at 100 K, (e) after 5 mins annealing at 120 K.*

8.3.2 Far−IR spectroscopy of neat SiF$_4$

The FIR spectrum for neat SiF$_4$ compound condensed at 9.2 K was presented in Figure 8.3a; it demonstrates only a sharp strong peak in the far infrared region at 373 cm^{-1} which is related to the Si–F in plane scissoring bending mode, as listed in Table 8.1.[44] The solid sample was warmed by 10 K intervals to 80 K and the FIR spectrum was collected and is presented in Figure 8.3b, the peak became narrower and taller than before. After further 5 minutes of annealing to 90 K, the band at 369.6 cm^{-1} disappeared as seen in figure 8.3c.
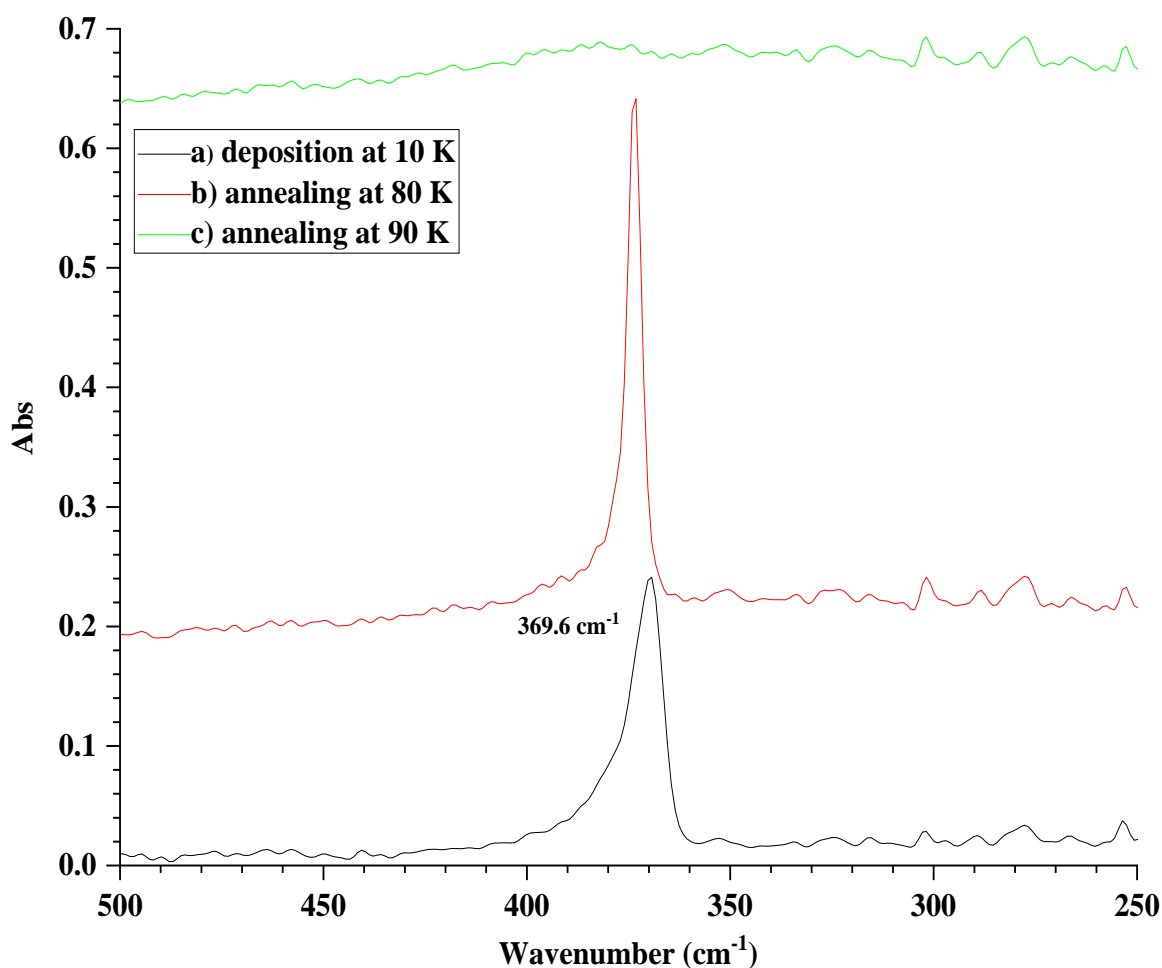
Figure 8.3: *Far–IR spectra of neat SiF₄ (11 torr) (a) after deposition at 9.2 K, (b) after 5 mins annealing at 80 K, (c) after 5 mins annealing at 90 K.*

8.3.3 FTIR spectroscopy of neat PMe₃

Four aliquots of the PMe₃ sample (5 torr in *ca* 50 mL flask) were introduced to the deposition surface of the cryostat at 80 K in the same way as for SiF₄, and the infrared spectrum of PMe₃ is given in Figure 8.4a. All bands are listed in Table 8.2, where bands at 2965, 2955, and 2895 cm⁻¹ are assigned to C–H asymmetric stretching mode, weak bands at 2810 cm⁻¹ are assigned to the C–H symmetric stretching mode.[44] Bands located at 1430, 1420 cm⁻¹ are assigned to C–H in–plane scissoring bending modes;[44] peaks at 1310 (weak), 1290, and 1270 (weak) cm⁻¹ are due to C–H out of plane wagging bending modes,[44] the vibrational frequency at 945 cm⁻¹ in company with its shoulder at 960 cm⁻¹ are attributed to the C–H out of plane twisting bending mode.[44] A sharp strong peak at 707 cm⁻¹ is attributed to the asymmetric stretching mode of C–P bonds. Additionally, a weak peak observed at 654 cm⁻¹ is related to the symmetric stretching mode of C–P bonds. It is noteworthy that the band observed at 2810 cm⁻¹ is probably due to fermi resonance

between the overtone of the C–H bending mode at 1430 cm^{-1} and the symmetric stretching mode at 2895 cm^{-1}.

The solid sample was annealed to 120 K by 10 K intervals and the vibrational spectra were recorded each time. As presented in Figures 8.4b–8.4e, the features located at 960, 1270, 1420 cm^{-1} started to become taller and narrower by successive annealing to 120 K, the bands at 654, 707, 1270, and 1310 cm^{-1} were not changed by further annealing. Figure 8.4f shows that the intensity of all bands decreased after 5 minutes of annealing to 130 K. The FTIR spectrum in Figure 8.4g reveals a noticeable change in intensity of all peaks in the spectrum after warming the solid PMe$_3$ sample up to 140 K. Furthermore, all bands had disappeared after heating the deposited sample to 150 K, as demonstrated in Figure 8.4h indicating that the solid sample of PMe$_3$ had completely evaporated. The PMe$_3$ sample was also deposited at 9.3 K and the same intensity of peaks was detected as well.

Table 8.2: Vibrational frequencies (cm^{-1}) observed of neat PMe$_3$.

Experiment	Assignments[44]
654 cm^{-1}	C–P symmetric stretching mode
707 cm^{-1}	C–P asymmetric stretching mode
945 cm^{-1}	C–H out of plane twisting bending mode
960 cm^{-1}	C–H out of plane twisting bending mode
1270 cm^{-1}	C–H out of plane wagging bending mode
1290 cm^{-1}	C–H out of plane wagging bending mode
1310 cm^{-1}	C–H out of plane wagging bending mode
1420 cm^{-1}	C–H in plane scissoring bending mode
1430 cm^{-1}	C–H in plane scissoring bending mode
2810 cm^{-1}	C–H symmetric stretching mode
2895 cm^{-1}	C–H asymmetric stretching mode
2955 cm^{-1}	C–H asymmetric stretching mode
2965 cm^{-1}	C–H asymmetric stretching mode
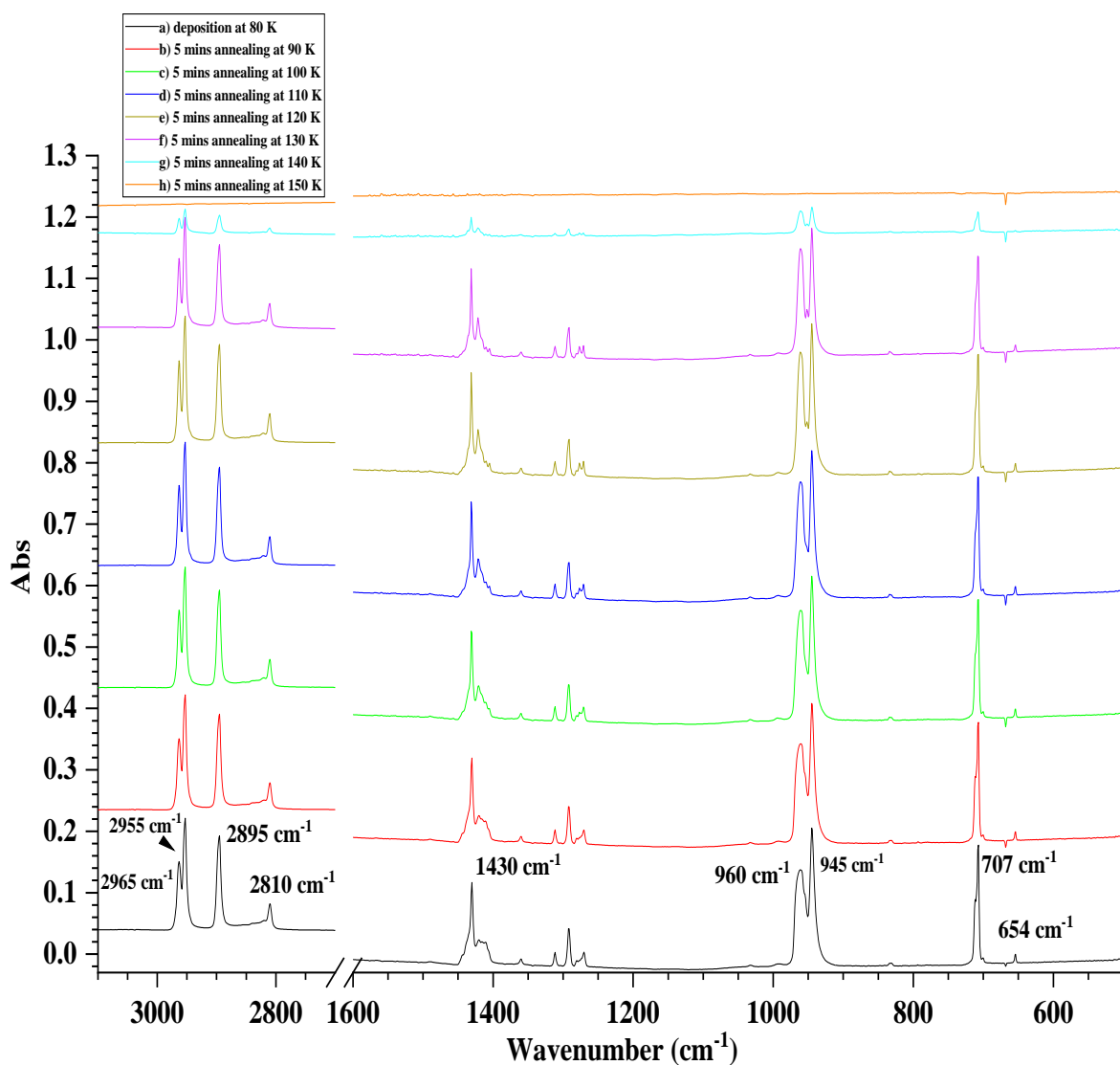
Figure 8.4: *FTIR spectra of neat PMe₃ (5 torr) (a) after deposition at 80 K, (b) after 5 mins annealing at 90 K, (c) after 5 mins annealing at 100 K, (d) after 5 mins annealing at 110 K, (e) after 5 mins annealing at 120 K, (f) after 5 mins annealing at 130 K, (g) after 5 mins annealing at 140 K, (h) after 5 mins annealing at 150 K.*

8.3.4 Far−IR spectroscopy of neat PMe₃

An aliquot of 9 shots of 12 torr (from a *ca*. 50 mL flask) of neat PMe₃ was put down on the deposition surface of the cryostat at 10 K. The vibrational spectra were collected in the far infrared range and no bands were observed as seen in Figure 8.5a. The sample was warmed by 10 K intervals up to 90 K and spectra were recorded at each time. The far−IR spectra in Figures 8.5b−8.5c reveal that no bands were obtained. It is obvious that neat PMe₃ has no bands in the far infrared region.
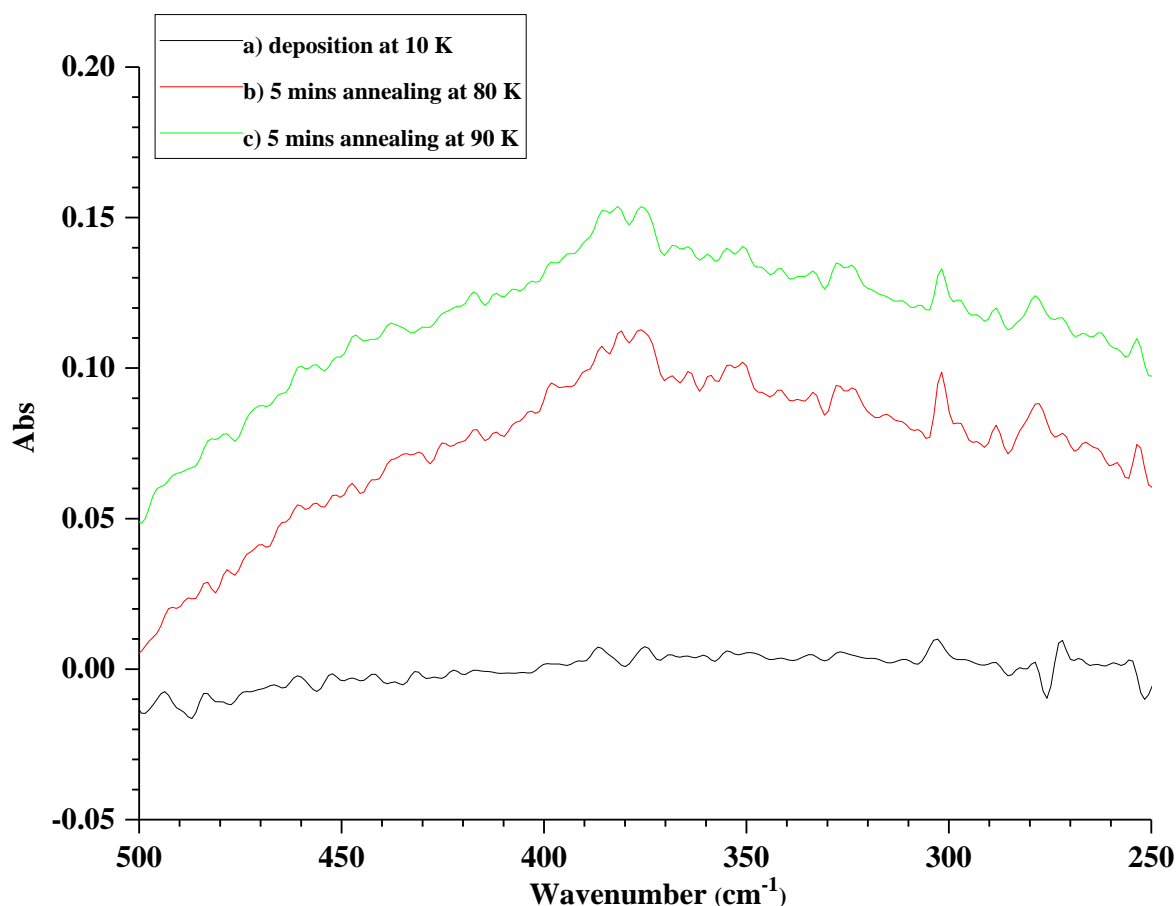
Figure 8.5: *Far–IR spectra of neat PMe₃ (12 torr) (a) after deposition at 10 K, (b) after 5 mins annealing at 80 K, (c) after 5 mins annealing at 90 K.*

8.3.5 FTIR spectroscopy of neat PEt₃

Three aliquots from a 5 torr sample of neat PEt$_3$ in a *ca*.50 mL flask were put down on the spectroscopic window at 80 K, and the vibrational spectrum was recorded each time. Figure 8.6a shows the spectrum recorded at 80 K after putting down three aliquots of neat PEt$_3$, all bands are presented in Table 8.3 as well. A strong band at 2955 cm^{-1} and a weak band at 2930 cm^{-1} were observed and these bands are assigned to asymmetric stretching mode of C–H.[44] The bands at 2870 and 2815 cm^{-1} are related to the vibrations of C–H symmetric stretching mode.[44] The weak bands 1455, 1420, 1375 cm^{-1} are assigned to C–H (in plane) scissoring bending vibrations, the weak peak at 1230 cm^{-1} and its shoulder at 1245 cm^{-1} are attributed to a mixture of wagging and twisting (out of plane) deformation vibrations. The weak peaks between at 1047 and 1025 cm^{-1} are assigned to a mixture of bending mode of C–H bonds (rocking and twisting),[44] while the band at 970 cm^{-1} is assigned to a mixture of bending mode of C–H bonds (rocking and wagging),[44] the group of peaks at 763, 747, and 720 cm^{-1} are from of C–H in plane rocking bending mode.[44] On the other hand, the bands due to the C–P asymmetric

172

stretching mode were obtained at 695 and 673 cm^{-1}, whilst the weak band at 660 cm^{-1} is due to the symmetric stretching mode of C–P bonds. The band observed at 2815 cm^{-1} is probably due to fermi resonance between the overtone of the C–H bending mode at 1455 cm^{-1} and the symmetric stretching mode at 2870 cm^{-1}.

The solid compound was warmed up increasingly by 10 K intervals. There was no change detected in intensity of bands with annealing the solid PEt$_3$ compound from 80 to 110 K. Figure 8.6b displays the FTIR spectrum after 5 minutes of annealing the solid sample to 120 K, the intensity of all bands increased obviously, whereas all bands became taller and narrower. Further annealing of the solid sample from 120 to 150 K resulted in no change in intensity of the peaks. Figure 8.6c displays the IR spectrum after 5 minutes of annealing the solid compound to 160 K. A new sharp strong peak is observed at 2952 cm^{-1}, the peaks at 763, 970, and 1461 cm^{-1} also became more intense. At 170 K, the intensity of all bands was reduced, as presented in Figure 8.6d. While, the infrared spectrum in Figure 8.6e recorded after heating the solid PEt$_3$ sample to 180 K, indicates that all peaks have disappeared and that the solid PEt$_3$ compound was thoroughly evaporated by 180 K. The deposition of PEt$_3$ sample was also conducted at 9.4 K and the same spectrum was obtained as deposition process at 80 K, there is no change in intensity of peaks. It is noteworthy that the changes on annealing of PEt$_3$ is more marked than those for PMe$_3$; it may be that the C$_2$H$_5$ chains relax to a more favourable position on annealing having been rapidly frozen from the gas phase. This would not be the case with PMe$_3$, where the changes would be more associated with rotation of the methyl groups to the most favourable position.

Table 8.3: Vibrational frequencies (cm^{-1}) observed of neat PEt$_3$.

Experiment	Assignments[44]
660 cm^{-1}	C–P symmetric stretching mode
673 cm^{-1}	C–P asymmetric stretching mode
695cm^{-1}	C–P asymmetric stretching mode
720 cm^{-1}	C–H in plane rocking bending mode
747 cm^{-1}	C–H in plane rocking bending mode
763 cm^{-1}	C–H in plane rocking bending mode
970 cm^{-1}	C–H out of plane rocking and wagging bending mode
1025 cm^{-1}	C–H out of plane rocking and twisting bending mode
1047 cm^{-1}	C–H out of plane rocking and twisting bending mode
1230 cm^{-1}	C–H out of plane wagging and twisting bending mode
1245 cm^{-1}	C–H out of plane wagging and twisting bending mode
1375 cm^{-1}	C–H in plane scissoring bending mode
1420 cm^{-1}	C–H in plane scissoring bending mode
1455 cm^{-1}	C–H in plane scissoring bending mode
2815 cm^{-1}	C–H symmetric stretching mode
2870 cm^{-1}	C–H symmetric stretching mode
2930 cm^{-1}	C–H asymmetric stretching mode
2955 cm^{-1}	C–H asymmetric stretching mode
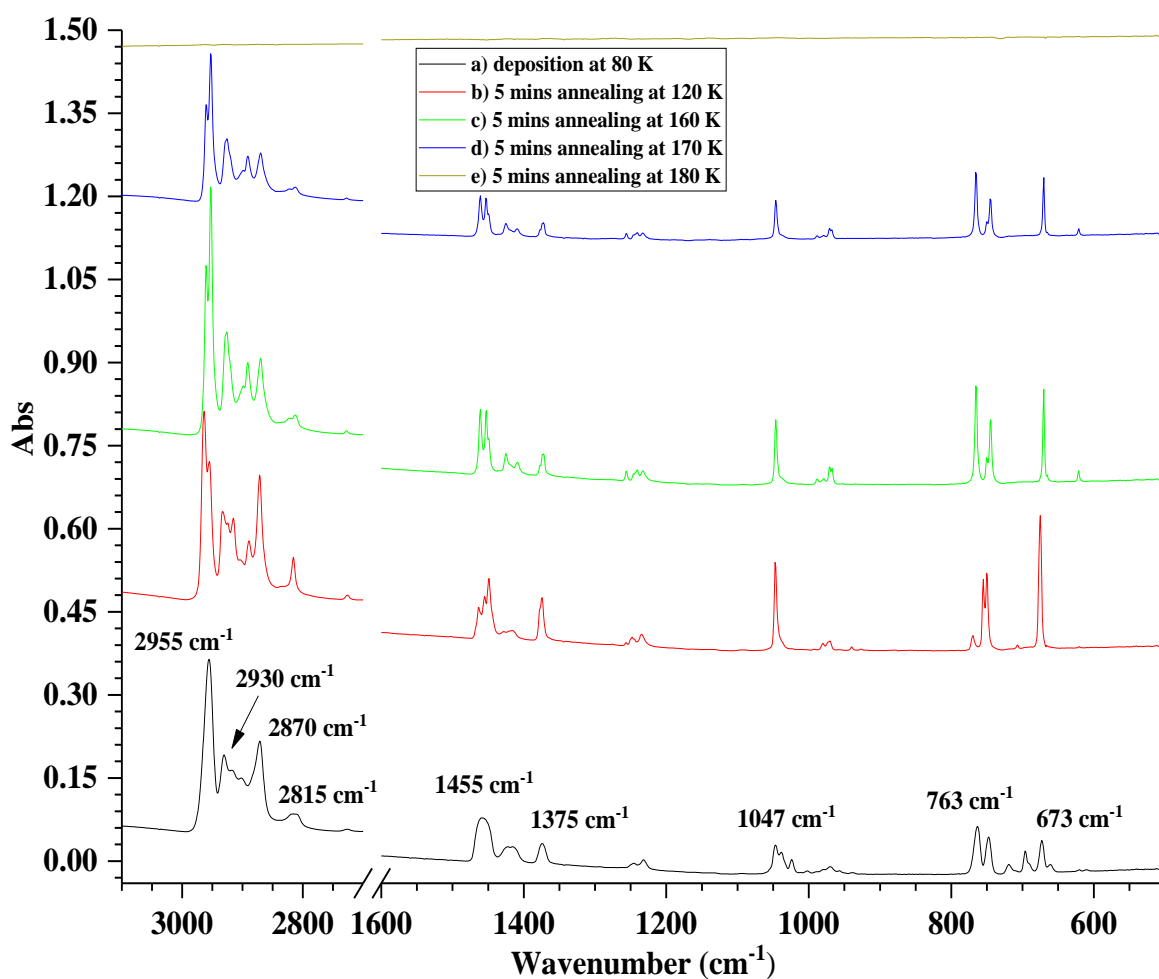
Figure 8.6: *FTIR spectra of neat PEt₃ (5 torr) (a) after deposition at 80 K, (b) after 5 mins annealing at 120 K, (c) after 5 mins annealing at 160 K, (d) after 5 mins annealing at 170 K, (e) after 5 mins annealing at 180 K.*

8.3.6 Far−IR spectroscopy of neat PEt₃

An aliquot of 50 shots of 9 torr (from a *ca*. 50 mL flask) of neat PEt₃ was laid down on the deposition window of the cryostat at 9.1 K, followed by an additional 5 shots to enhance the intensity of bands. Vibrational spectra were collected in the far infrared range as seen in Figure 8.7. At 9.1 K (Figure 8.7a) no bands were obtained. The sample was warmed by 10 K intervals up to 120 K and spectra were recorded at every turn. The far−IR spectra in Figures 8.7b−8.7d reveal no bands detected for neat PEt₃ in the far infrared region.
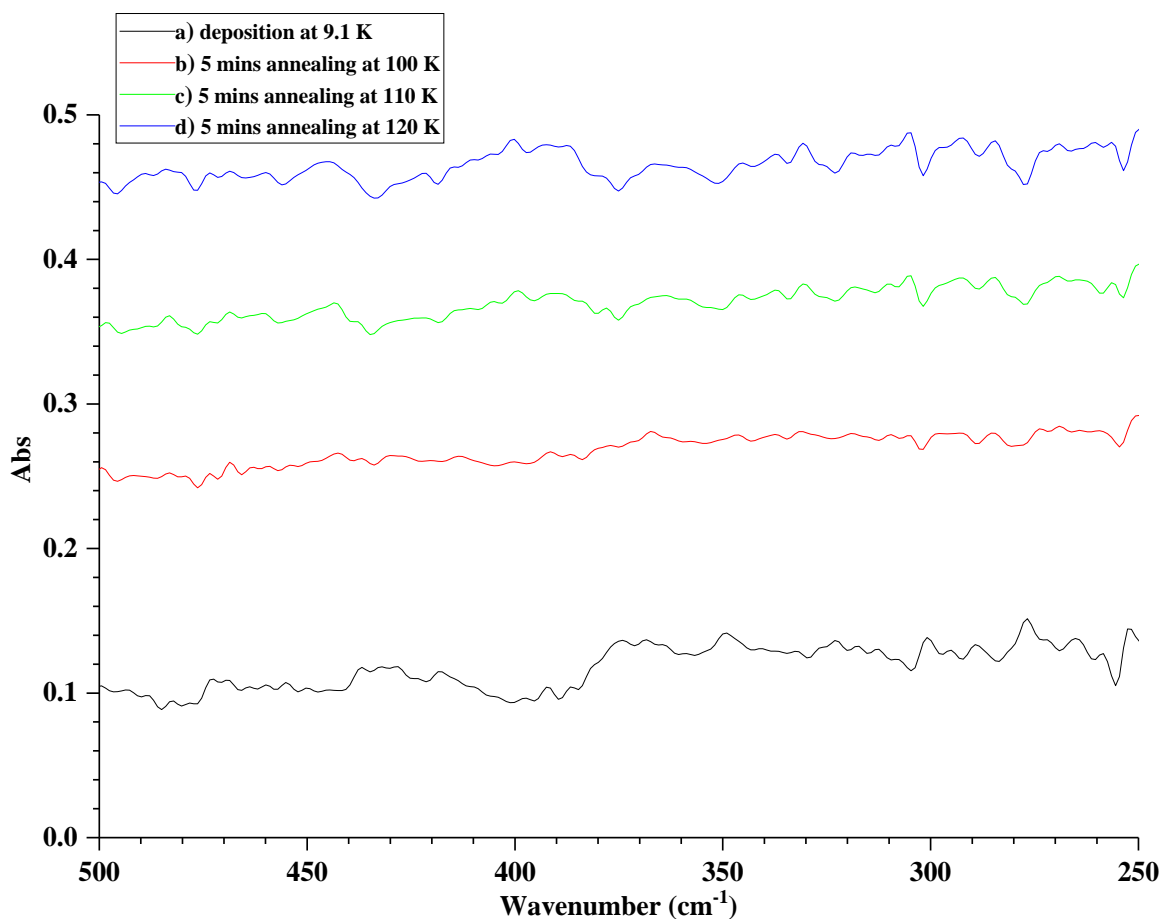
Figure 8.7: *Far–IR spectra of neat PEt₃ (9 torr) (a) after deposition at 9.1 K, (b) after 5 mins annealing at 100 K, (c) after 5 mins annealing at 110 K, (d) after 5 mins annealing at 120 K.*

8.3.7 FTIR spectroscopy of SiF₄−PMe₃ Mixture (1:1 ratio)

A prepared mixture of 1:1 ratio of SiF_4 and PMe_3 (5 torr each) was introduced onto the spectroscopic window of the cryostat at 80 K, the FTIR vibrational spectrum was collected each time after depositing five aliquots. Figure 8.8a shows bands due to SiF_4 changed considerably, while bands at 954, 894, 855, 789, 749, 725, 675, 426, shoulder peak at 420, and 388 cm^{-1}, these bands are not related to neither neat SiF_4 nor PMe_3 compounds, as illustrated in Figures 8.8b and 8.8c. In consequence, these peaks could be probably due to reaction between SiF_4 and PMe_3 and indicate the formation of a SiF_4−PMe_3 complex. The assignment of these bands are presented in computational section later. Furthermore, there is not much change in the 1200−3100 cm^{-1} region, where there is a little difference in bands positions of complex formation in C−H bending region (1200−1600 cm^{-1}) as well as there is shifting about 20 cm^{-1} wavenumbers for SiF_4−PMe_3 complex bands in C−H stretching region (2800−3100 cm^{-1}), and also the intensity of these bands in the SiF_4−PMe_3 complex is reduced.
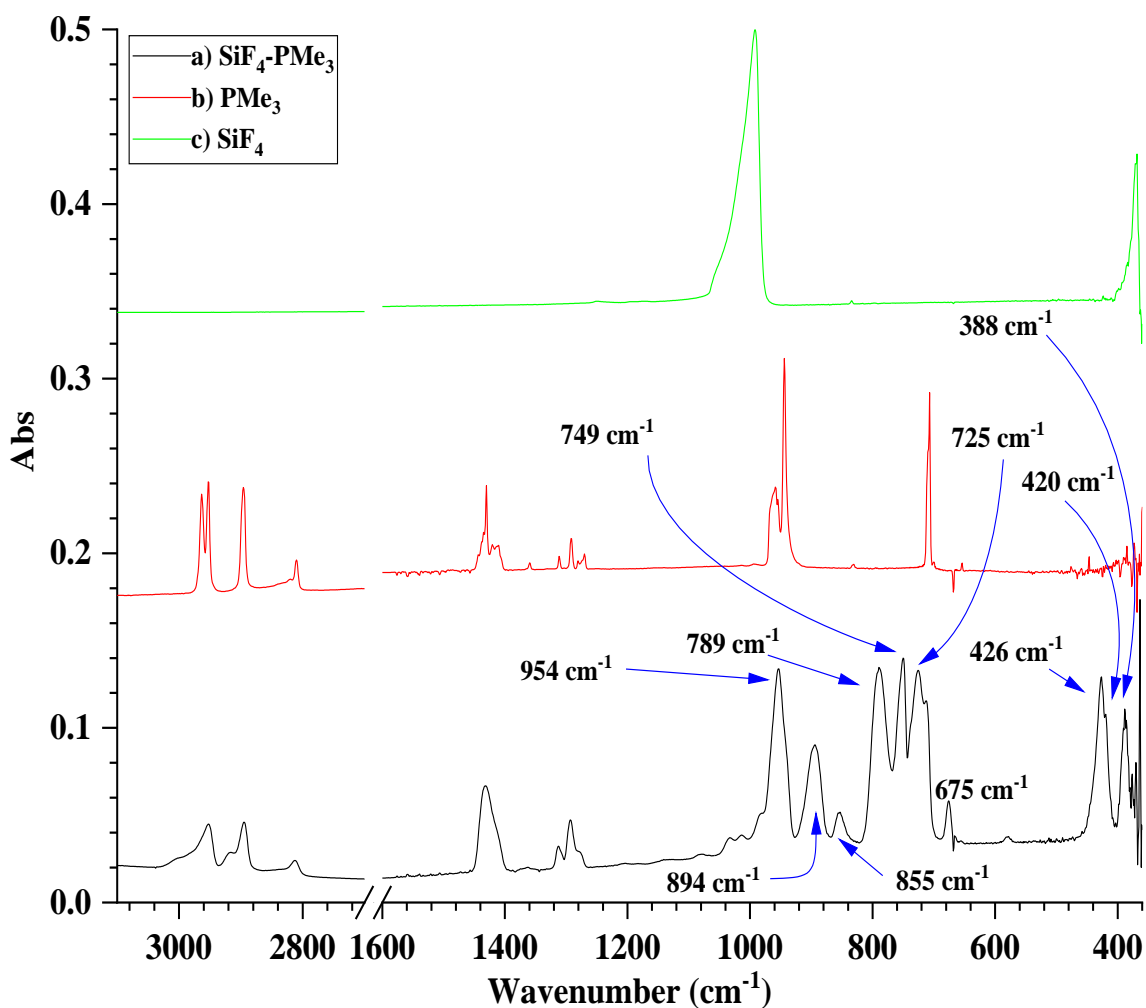
Figure 8.8: *FTIR spectra of (a) mixture of SiF₄ (5 torr)/PMe₃ (5 torr) after deposition at 80 K, (b) neat PMe₃ (5 torr) after deposition at 80 K, (c) neat SiF₄ (11 torr) after deposition at 9.1 K.*

The mixture was heated up by increments of 10 K up to 180 K. Figure 8.9b demonstrates that the features located at 855, 789, 749, 725, 675, 426, and 388 cm^{-1} became gradually more intense, whereas the peak at 894 cm^{-1} decreased with raising the temperature of the cryostat to 120 K. In contrast, the intensity of all bands shrinks by additional gradual annealing to 130 K, as presented in Figure 8.9c. The IR spectrum in Figure 8.9d indicates that the mixture was largely evaporated at 180 K. The behaviour of peaks at 426 cm^{-1} and especially 387.7 cm^{-1} are in the noisy part of the MIR region where the throughput is poor, and therefore this system was also investigated by FIR spectroscopy.
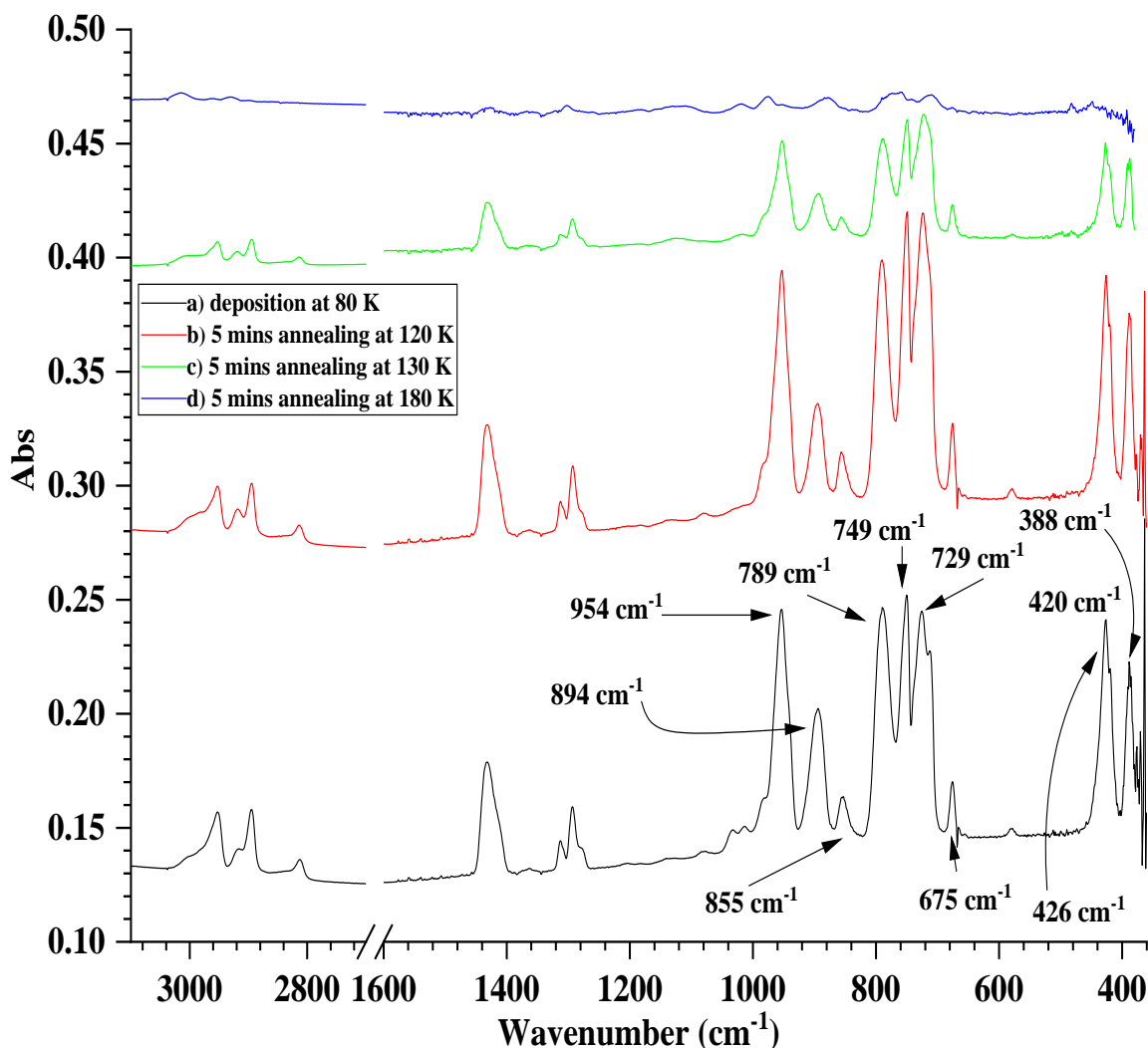
Figure 8.9: *FTIR spectra of mixture of SiF$_4$ (5 torr)/PMe$_3$ (5 torr) (a) after deposition at 80 K, (b) after 5 mins annealing at 120 K, (c) after 5 mins annealing at 130 K, (d) after 5 mins annealing at 180 K.*

Figure 8.10 demonstrates the spectrum in present work comparing with spectra recorded by M.Chem project student A. Niculau[41] using mixtures of different proportions of a 1:1 ratio of 7.5 torr SiF$_4$ and 7.5 torr PMe$_3$, a 1:2 mixture of 5 torr SiF$_4$ and 10 torr PMe$_3$, a 2:1 complex of 10 torr SiF$_4$ and 5 torr PMe$_3$. The two new bands at 942 and 709 cm^{-1} were only observed in a mixture of a 1:1 ratio of 7.5 torr SiF$_4$ and 7.5 torr PMe$_3$ (Figure 8.10b) indicates the presence of unreacted PMe$_3$ compound into the mixture. In addition, the obvious change in relative intensity of bands at 894 and 675 cm^{-1} assigned to a SiF$_4$−PMe$_3$ complex in all spectra comparing with the relative intensities of other bands related to the SiF$_4$−PMe$_3$ complex formed indicates the formation of two different species.

178
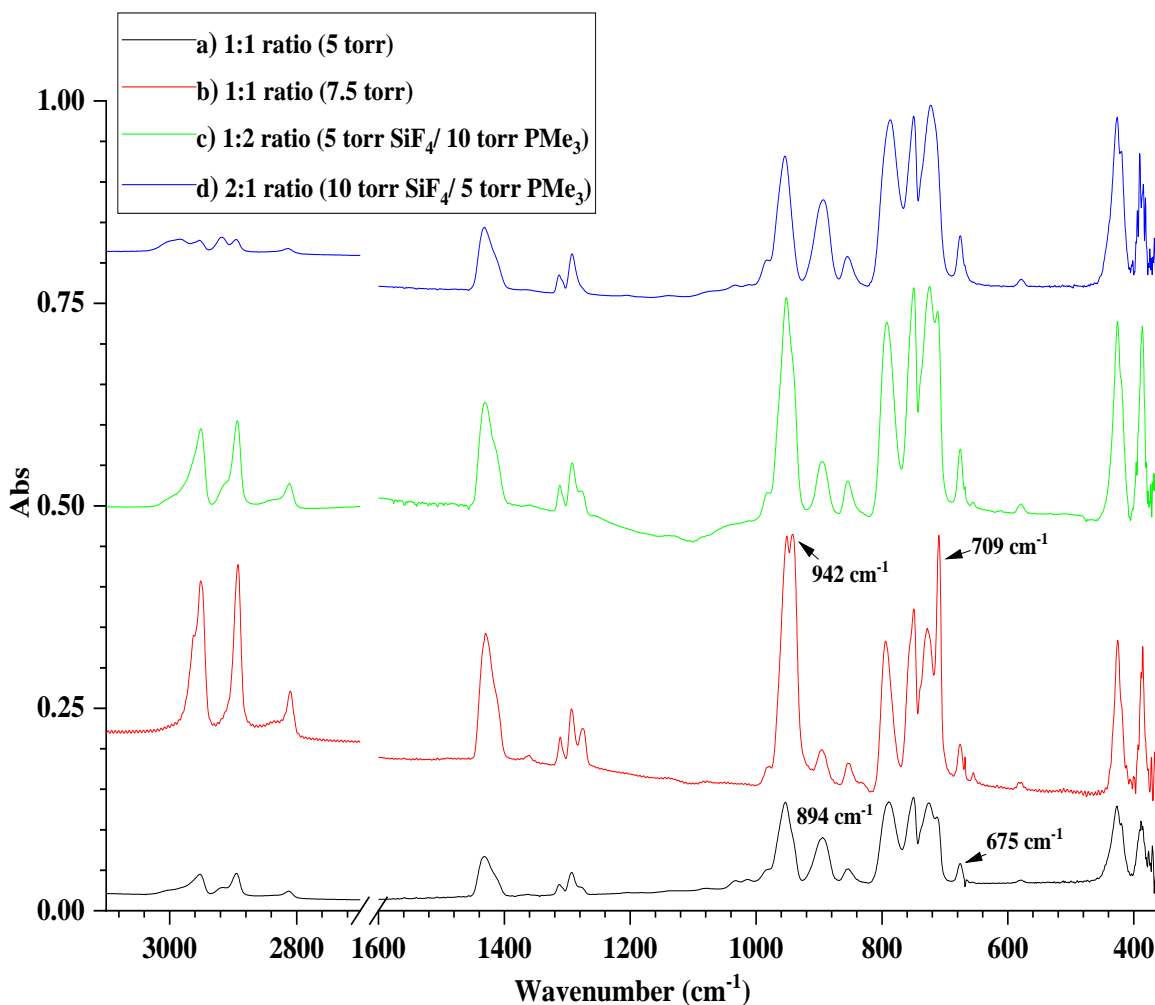
Figure 8.10: *FTIR spectra of mixture of SiF₄/PMe₃ after deposition at 80 K for (a) 1:1 ratio (5 torr), (b) 1:1 ratio (7.5 torr), (c) 1:2 ratio of SiF₄ (5 torr)/PMe₃ (10 torr), (d) 2:1 ratio ratio of SiF₄ (10 torr)/PMe₃ (5 torr).*

8.3.8 Far−IR spectroscopy of SiF₄−PMe₃ Mixture (1:1 ratio)

A prepared mixture of a 1:1 ratio was made up of 10 torr SiF_4 and 10 torr PMe_3 and used to attain more intense peaks; the mixture was introduced to the deposition window of the cryostat at 80 K. Figure 8.11a shows the IR spectrum collected in the far IR region after deposition, two peaks are observed; the peak located at 426 cm^{-1} with a shoulder peak at 420 cm^{-1} has a higher relative intensity than the peak at 388 cm^{-1}. The mixture was heated gradually by 10 K intervals. Figure 8.11b illustrates the spectrum after 5 minutes of annealing at 90 K, the intensity of peaks at 426, 420, and 388 cm^{-1} grew slightly. Further increase of peaks at 426, 420, and 388 cm^{-1} was obtained after annealing to 110 K, as seen in Figure 8.11c. The far−IR spectrum collected in Figure 8.11d after warming the compound to 120 K shows that the peaks at 426 and 388 cm^{-1} have now become less intense. The two absorptions at 426 and 388 cm^{-1} decreased by heating the mixture to 130 K, as presented in Figure 8.11e. The far infrared spectrum was

179

run after 5 minutes of annealing the deposited mixture to 140 K; Figure 8.11f displays that the peaks at 426, 420, and 388 cm^{-1} almost disappeared. As given in Figure 8.11g, no peaks were found after annealing the mixture to 150 K for 5 minutes. The behaviour of features at 426, 420, and 388 cm^{-1} looks similar in all the spectra.
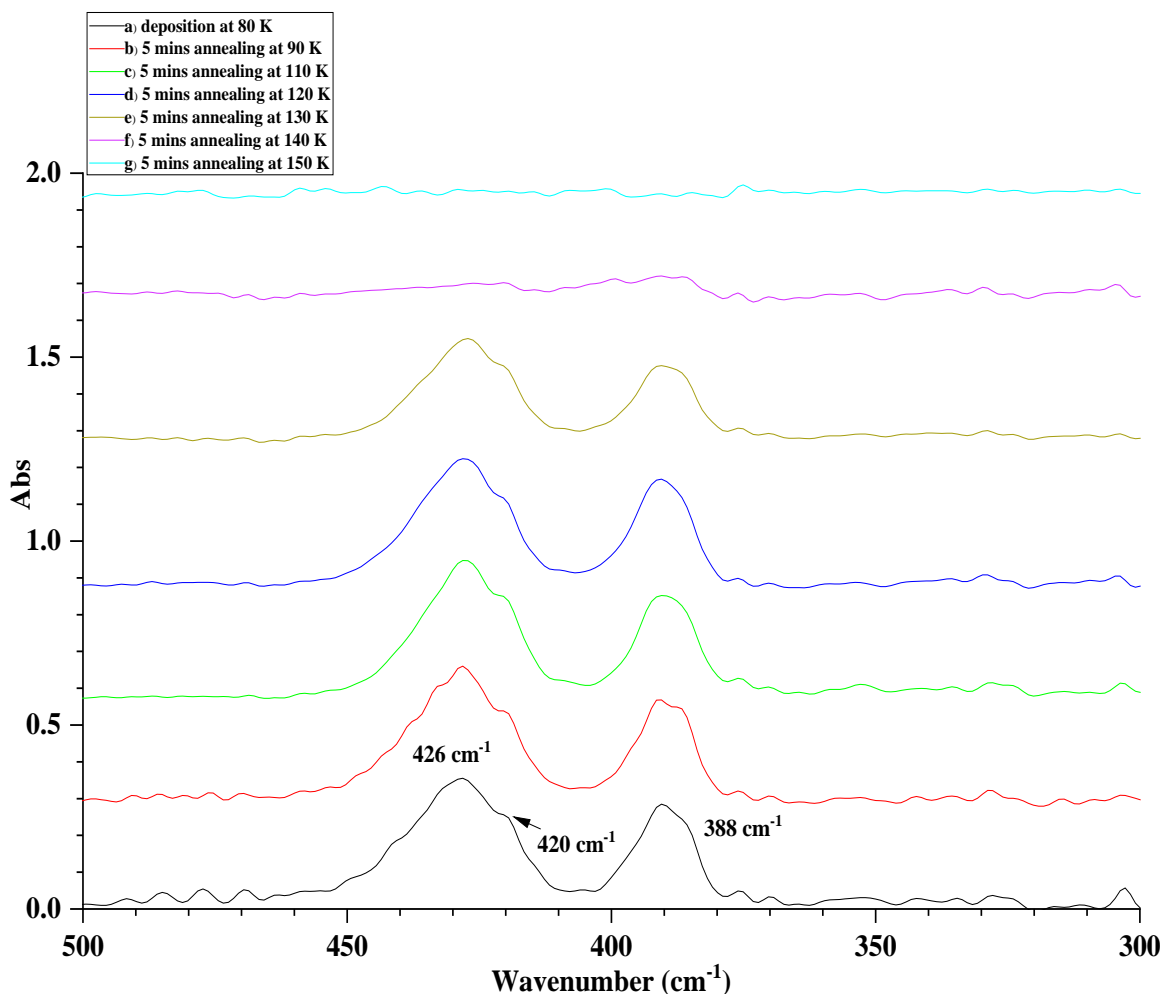
Figure 8.11: *Far–IR spectra of mixture of SiF₄ (10 torr)/PMe₃ (10 torr) (a) after deposition at 80 K, (b) after 5 mins annealing at 90 K, (c) after 5 mins annealing at 110 K, (d) after 5 mins annealing at 120 K, (e) after 5 mins annealing at 130 K, (f) after 5 mins annealing at 140 K, (g) after 5 mins annealing at 150 K.*

The experiment was conducted again using a different mixture of a 1:1 ratio of 7.5 torr SiF₄ and 7.5 torr PMe₃ and also a 1:2 mixture of 5 torr SiF₄ and 10 torr PMe₃, all complexes were placed down on the cold window at 80 K. the far−IR spectra were collected and are demonstrated in Figure 8.12. It is obvious that the two absorption at 426 with a shoulder at 420 and the band at 388 cm^{-1} have the same relative intensity in 1:1 and 1:2 complexes. Therefore, these two bands could belong to same species or two different species with the same proportion.
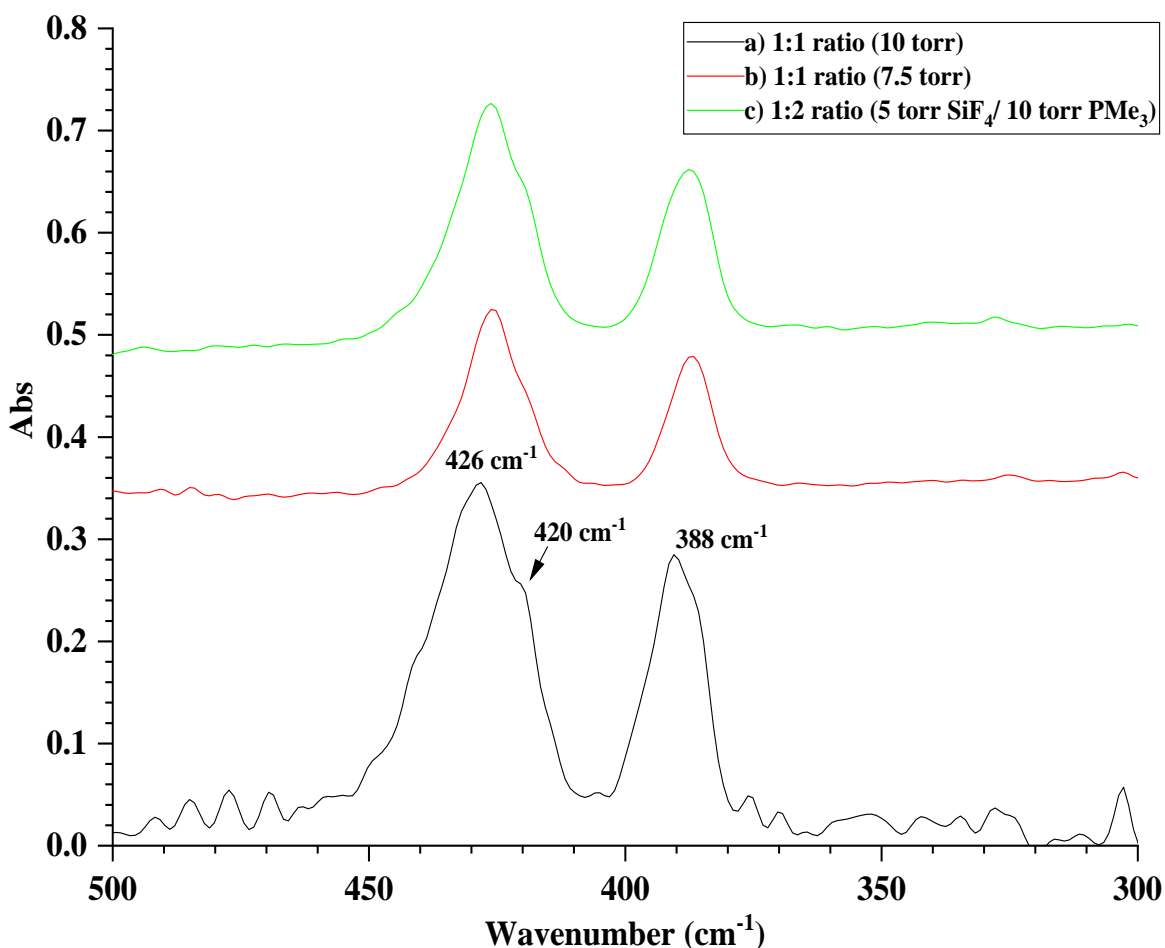
Figure 8.12: *Far–IR spectra of mixture of SiF$_4$/PMe$_3$ after deposition at 80 K for (a) 1:1 ratio (10 torr), (b) 1:1 ratio (7.5 torr), (c) 1:2 ratio of SiF$_4$ (5 torr)/PMe$_3$ (10 torr).*

8.3.9 FTIR spectroscopy of SiF$_4$−PEt$_3$ Mixture (1:1 ratio)

Sequential aliquots of a prepared mixture (1:1 ratio) of 5 torr SiF$_4$ and 5 torr PEt$_3$ were laid down onto the deposition window of the cryostat at 80 K, the infrared spectrum was collected at 80 K and is given in Figure 8.13a. It is obvious that the three bands located at 900, 796, and 415 cm^{-1} do not belong to either neat SiF$_4$ nor PEt$_3$, these bands are most likely related to a complex formed between SiF$_4$−PEt$_3$. Furthermore, the intensity of bands in C−H bending region (1200−1600 cm^{-1}) and C−H stretching region (2800−3100 cm^{-1}) of the SiF$_4$−PEt$_3$ complex is reduced.
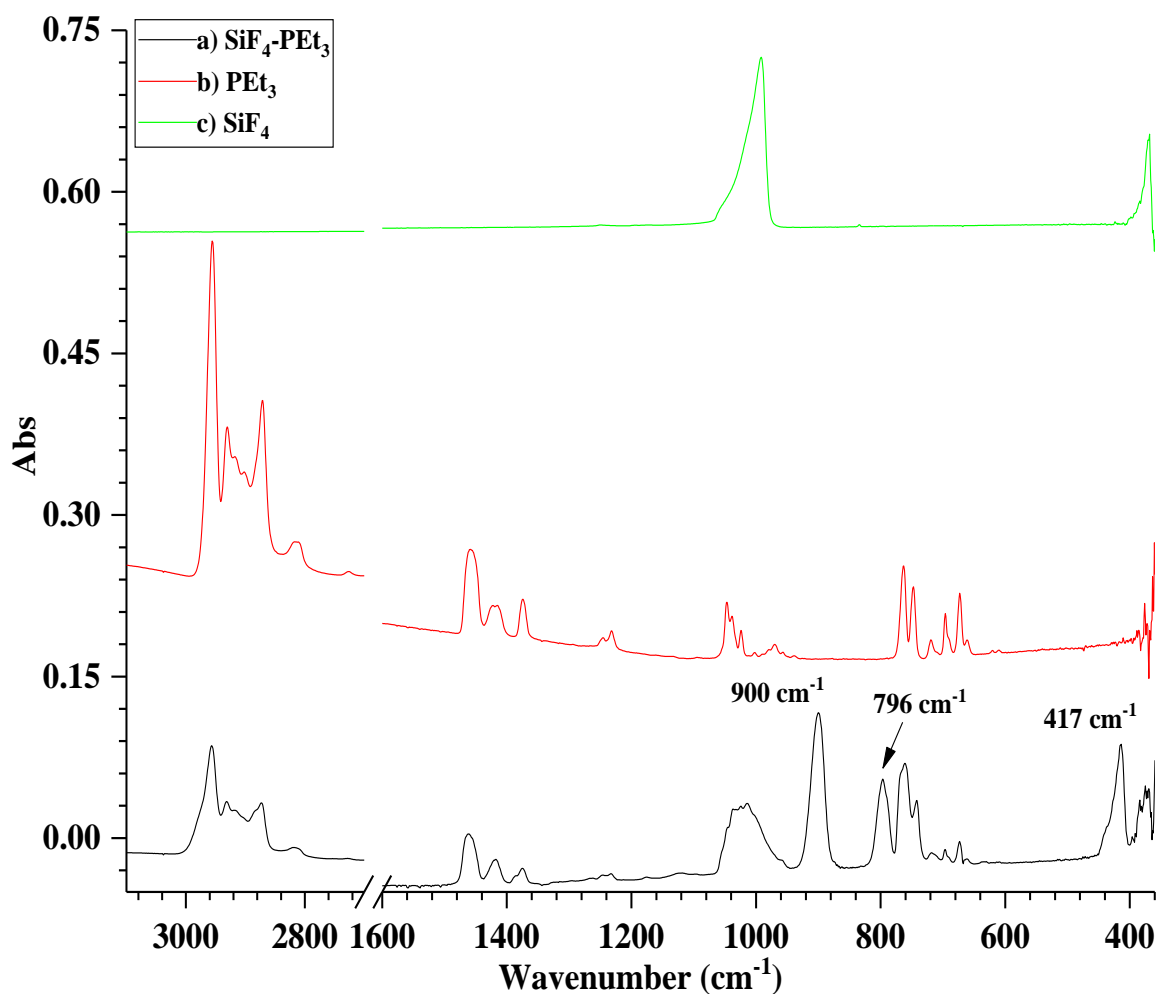
Figure 8.13: *FTIR spectra of (a) mixture of SiF₄ (5 torr)/PEt₃ (5 torr) after deposition at 80 K, (b) neat PEt₃ (5 torr) after deposition at 80 K, (c) neat SiF₄ (11 torr) after deposition at 9.1 K.*

The mixture was warmed up by increments of 10 K and the IR spectrum was recorded each time. Figure 8.14b reveals that the intensity of features at 900, 796, and 417 cm^{-1} increased by successive annealing the mixture from 80 to 120 K. Conversely, further annealing to 170 K led to consecutive reduction in intensity of these bands until they vanished at 180 K, as seen in Figures 8.14c and 8.14d.
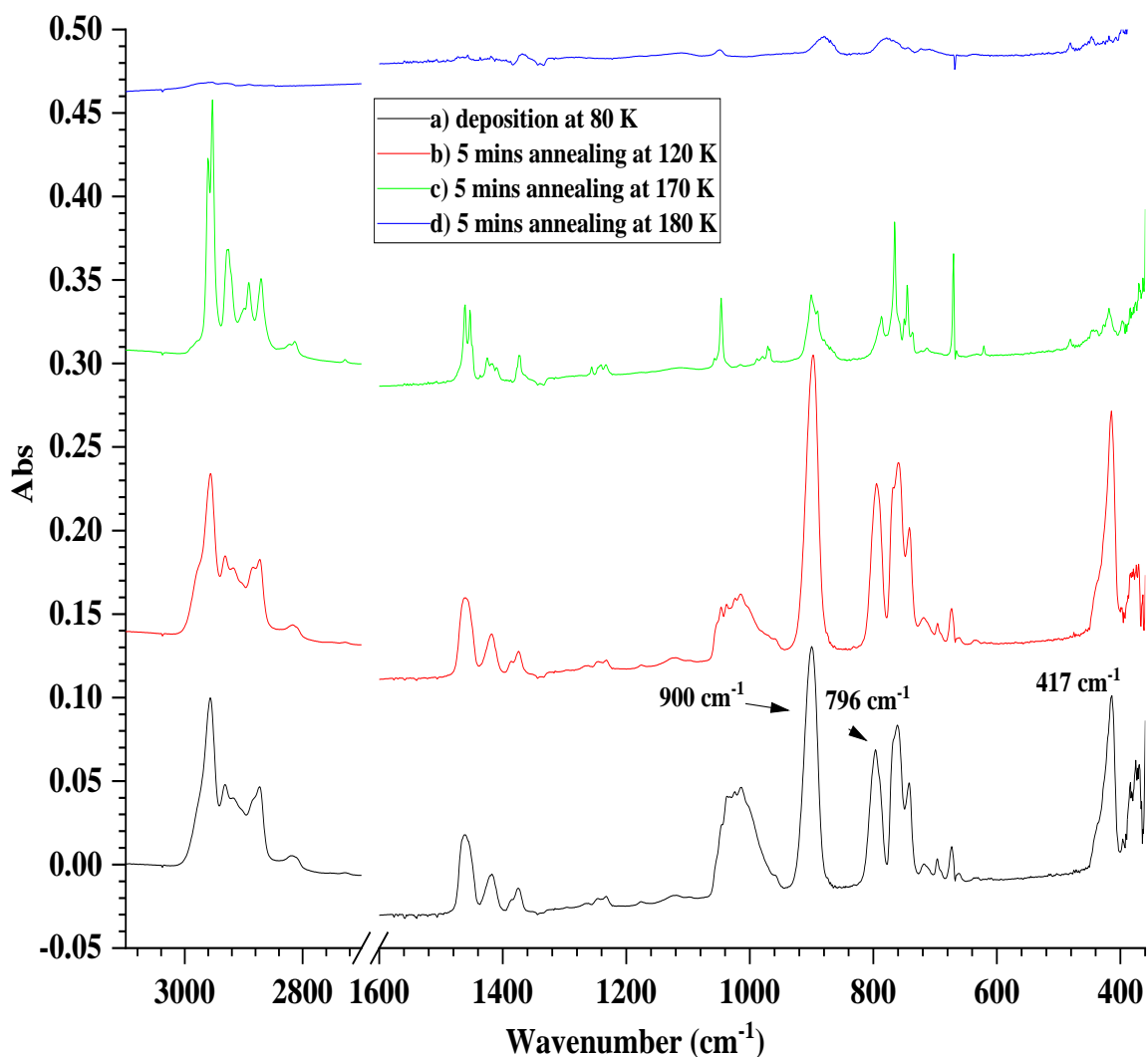
Figure 8.14: *FTIR spectra of mixture of SiF₄ (5 torr)/PEt₃ (5 torr) (a) after deposition at 80 K, (b) after 5 mins annealing at 120 K, (c) after 5 mins annealing at 170 K, (d) after 5 mins annealing at 180 K.*

8.3.10 Far−IR spectroscopy of SiF₄−PEt₃ Mixture (1:1 ratio)

A mixture made up of 8 torr of neat SiF_4 and 8 torr of neat PEt_3 was introduced to the deposition surface of the cryostat and the far−IR spectrum was collected at 80 K. Figure 8.14a demonstrates a weak broad peak at 386 cm⁻¹ and a strong band at 417 cm⁻¹. The mixture was annealed gradually by 10 K intervals. An increase in intensity of the peak at 417 cm⁻¹ was achieved by further annealing to 90 K, also the peak at 386 cm⁻¹ became broader and shifted slightly to 382 cm⁻¹, as given in Figures 8.15b. The far−IR spectra run after additional heating of the sample to 110 K, Figures 8.15c indicates a growth in intensity of the band at 417 cm⁻¹, whereas the peak at 386 cm⁻¹ was reduced. The vibrational spectrum in Figure 8.15d manifests a decline in intensity of both features at 417 and 386 cm⁻¹ after heating the mixture to 120 K. While, Figure 8.15e reveals that the intensity of the peak located at 417 cm⁻¹ decreased obviously, and the band at 386

cm^{-1} disappeared after warming the mixture up to 130 K. The far infrared spectrum recorded after 5 minutes of annealing at 150 K indicates that the peak at 417 cm^{-1} disappeared, as given in Figure 8.15f. Thus, these two bands are more likely belong to two different species.
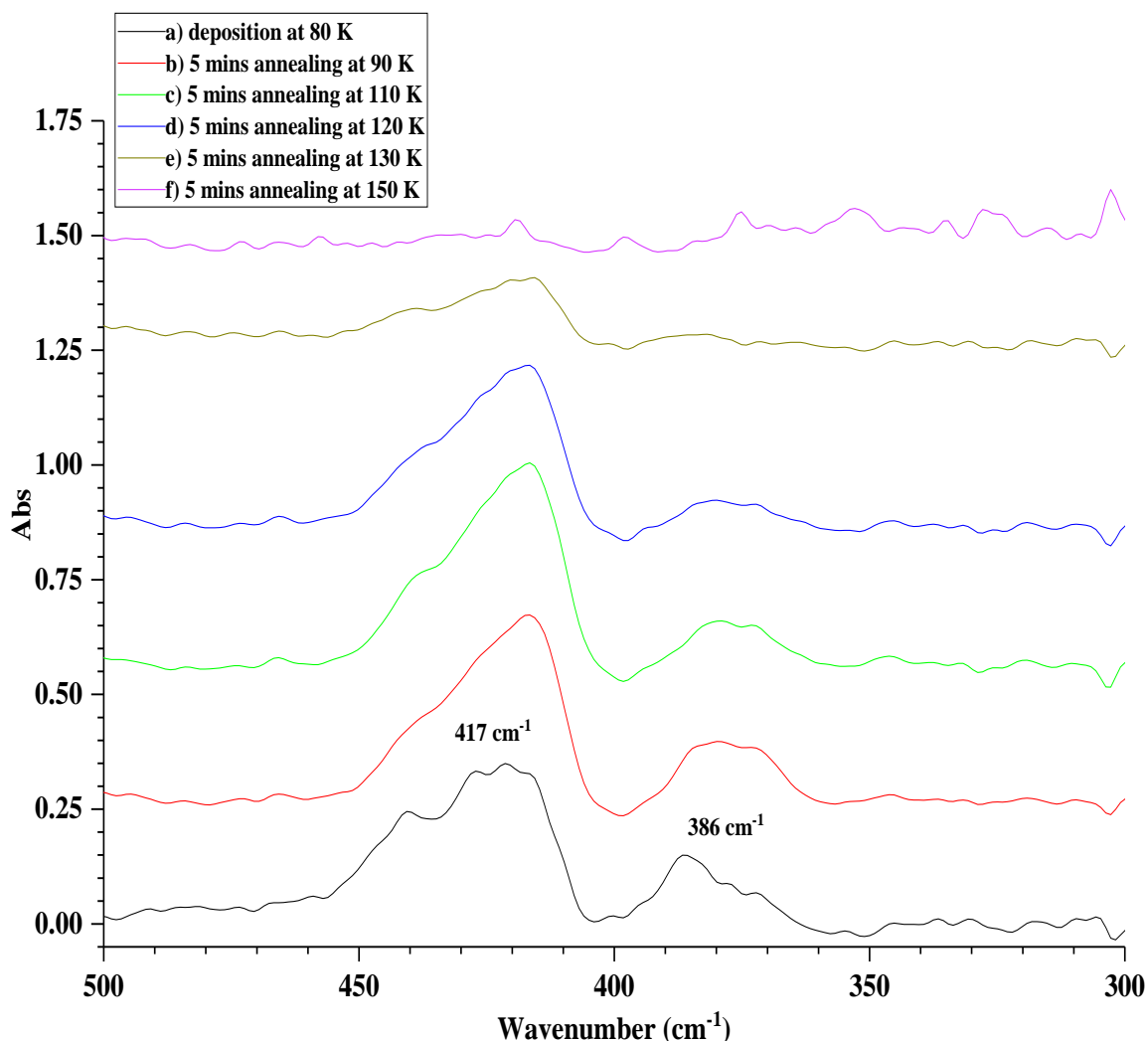
Figure 8.15: *Far–IR spectra of mixture of SiF$_4$ (8 torr)/PMe$_3$ (8 torr) (a) after deposition at 80 K, (b) after 5 mins annealing at 90 K, (c) after 5 mins annealing at 110 K, (d) after 5 mins annealing at 120 K, (e) after 5 mins annealing at 130 K, (f) after 5 mins annealing at 150 K.*

8.3.11 Computational calculations

8.3.11.1 Computational calculations of SiF$_4$

The computational calculation was conducted using B3LYP/def2tzvpp within G09W to help in the assignment of the peaks in the experimental IR spectrum and to investigate the structure of the SiF$_4$. The calculated IR spectrum of SiF$_4$ is presented in Figure 8.16, the spectrum has two bands, one in far–IR region and the second band in the

mid–IR region. The IR peaks, their intensities, and assignments are listed in Table 8.4. Moreover, the calculation revealed that the geometry of SiF_4 is tetrahedral (T_d) symmetry as illustrated in Figure 8.17.

Table 8.4: Vibrational frequencies (cm^{-1}) calculated of SiF_4.

Calculated B3LYP/def2tzvpp	IR intensity, $km.mol^{-1}$	Assignments
380.664 cm^{-1}	44.3950	Si–F Scissoring bending mod
783.20 cm^{-1}	0.0	Si–F symmetric stretching mode
1016.57 cm^{-1}	231.2217	Si–F asymmetric stretching mode
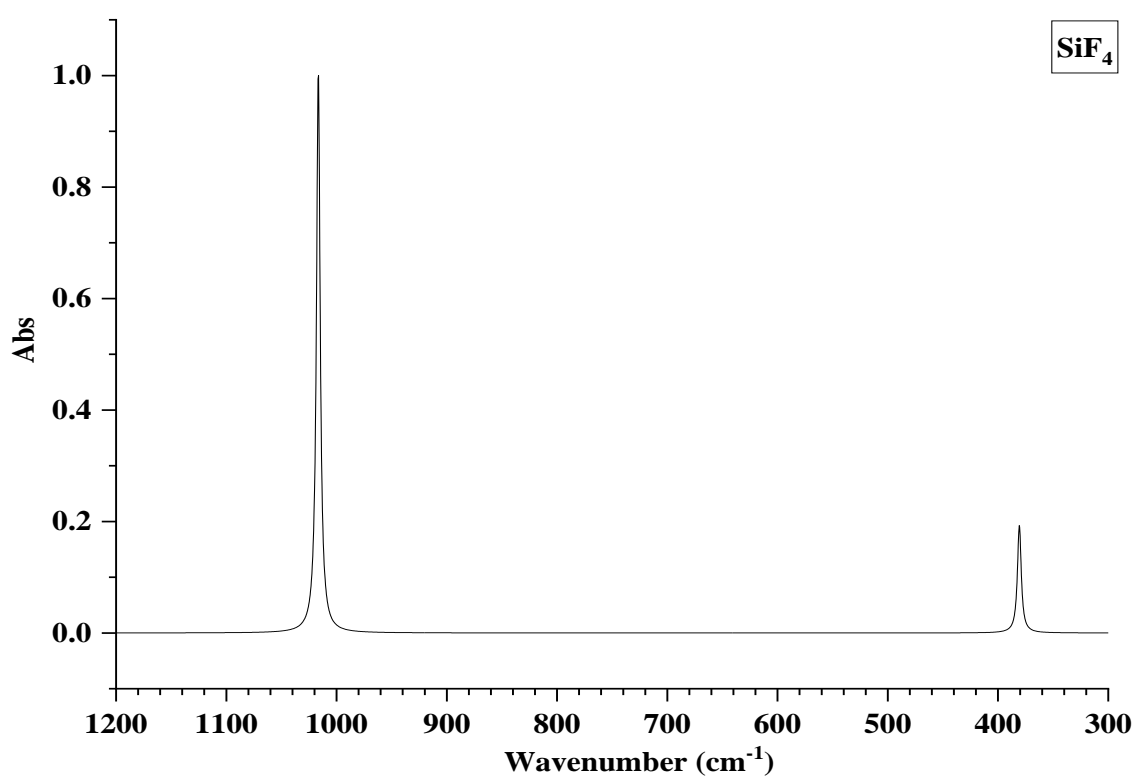
Figure 8.16: *Calculated (B3LYP/def2tzvpp) IR spectrum of SiF₄ at half−widths 4.0 cm⁻¹.*
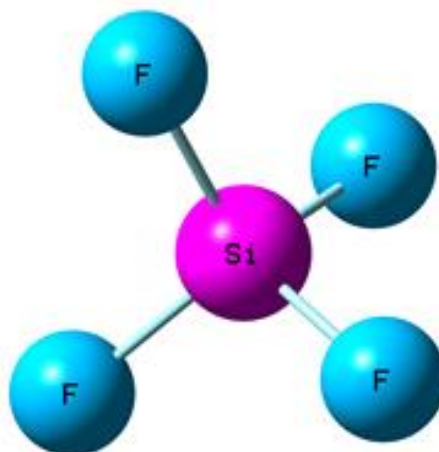
Figure 8.17: *Calculated (B3LYP/def2tzvpp) geometric structure of SiF$_4$.*

8.3.11.2 Computational calculations of PMe$_3$

The theoretical data for PMe$_3$ were attained using B3LYP/def2tzvpp within G09W in order to assign the peaks in the experimental IR spectrum. The calculated IR spectrum of PMe$_3$ is presented in Figure 8.18, the spectrum has no bands in the far–IR region. Also, the spectrum has no band around 2810 cm^{-1} as observed in experimental spectrum, indicating that it is due fermi resonance. Table 8.5 lists the IR peaks, their intensities, and assignments. Additionally, the calculated geometric structure of PMe$_3$ is given in Figure 8.19.

Table 8.5: Vibrational frequencies (cm^{-1}) calculated of PMe$_3$.

Calculated B3LYP/def2tzvpp	IR intensity, km.mol^{-1}	Assignments
205.66 cm^{-1}	0.0157	C–H rocking bending mode
243.38 cm^{-1}	0.1307	P–C scissoring bending mode
247.14 cm^{-1}	0.1501	
286.23 cm^{-1}	0.3470	
640.12 cm^{-1}	0.3966	P–C symmetric stretching mode
696.92 cm^{-1}	14.3499	P–C asymmetric stretching mode
698.19 cm^{-1}	14.2834	P–C asymmetric stretching mode
738.07 cm^{-1}	0.2291	C–H waging bending mode and vibrational motion of P–C bonds and
839.53 cm^{-1}	0.2664	
956.07 cm^{-1}	20.7041	C–H rocking bending mode and vibrational motion of P–C bonds
970.77 cm^{-1}	24.2976	
1314.27 cm^{-1}	3.5296	C–H scissoring bending mode and vibrational motion of P–C bonds and
1315.18 cm^{-1}	3.5492	
1336.22 cm^{-1}	4.7568	
1458.32 cm^{-1}	0.1790	
1458.32 cm^{-1}	4.8367	
1463.0 cm^{-1}	4.8367	C–H scissoring bending mode
1463.80 cm^{-1}	4.5681	
1472.09 cm^{-1}	7.9894	
1473.39 cm^{-1}	8.2883	
1481.71 cm^{-1}	9.4587	
3016.06 cm^{-1}	27.5661	C–H symmetric stretching mode
3016.72 cm^{-1}	20.2407	
3017.78 cm^{-1}	19.6224	
3092.77 cm^{-1}	37.9836	C–H asymmetric stretching mode
3106.93 cm^{-1}	15.4569	
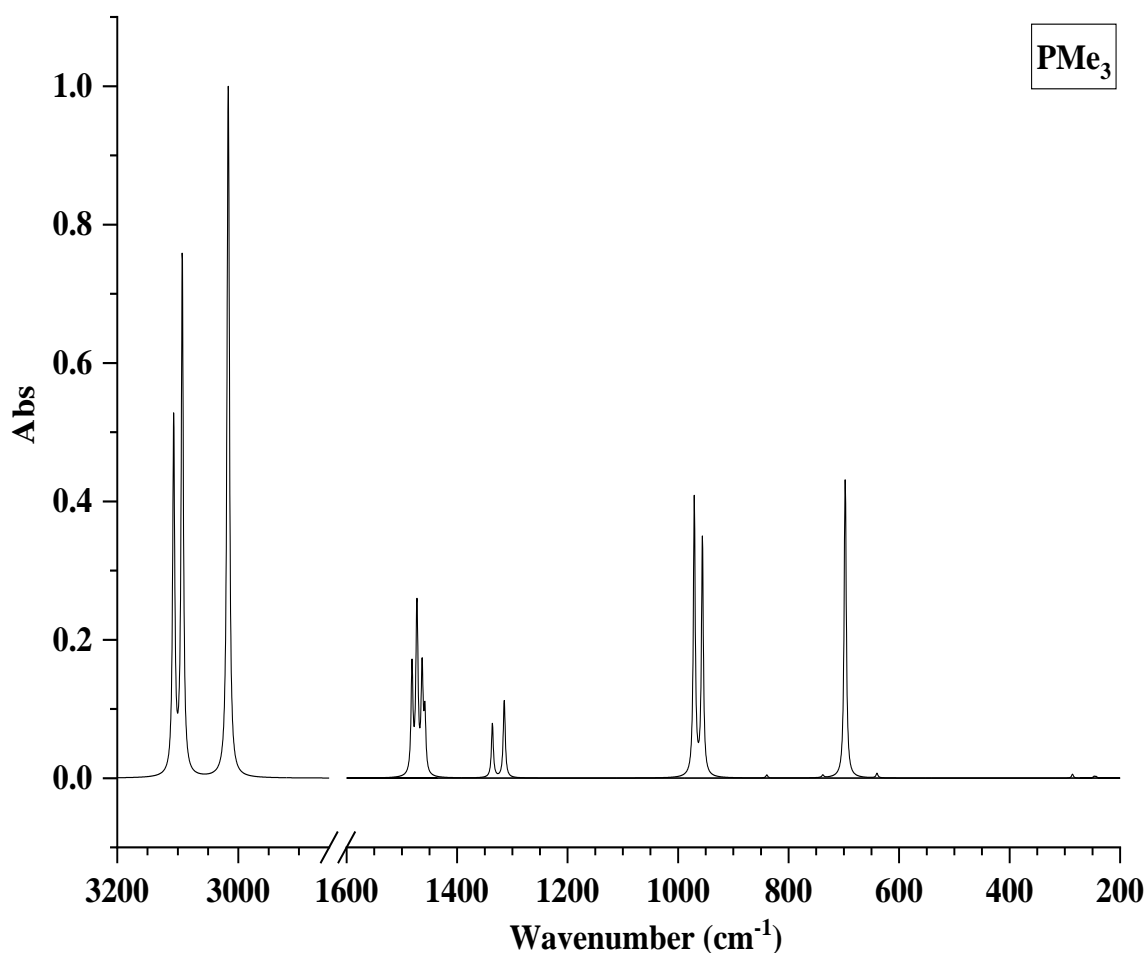
Figure 8.18: *Calculated (B3LYP/def2tzvpp) IR spectrum of PMe₃ at half−widths 4.0 cm⁻¹.*
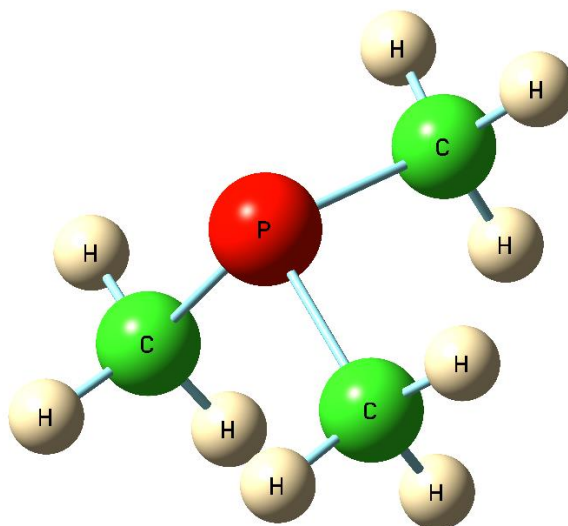
Figure 8.19: *Calculated (B3LYP/def2tzvpp) geometric structure of PMe₃.*

8.3.11.3 Computational calculations of PEt₃

The theoretical calculation for PEt₃ was carried out using B3LYP/def2tzvpp within G09W to help in assigning the bands in the experimental IR spectrum. Figure 8.20 shows the calculated IR spectrum of PEt₃, it is obvious that the spectrum has no intense

188

band in the far infrared region. Furthermore, there is no calculated band around 2815 cm^{-1} as in experimental spectrum, indicating that it is due fermi resonance. The IR peaks with their intensities and assignments are tabulated in Table 8.6. In addition, Figure 8.21 depicts the suggested geometric structure of PEt$_3$.
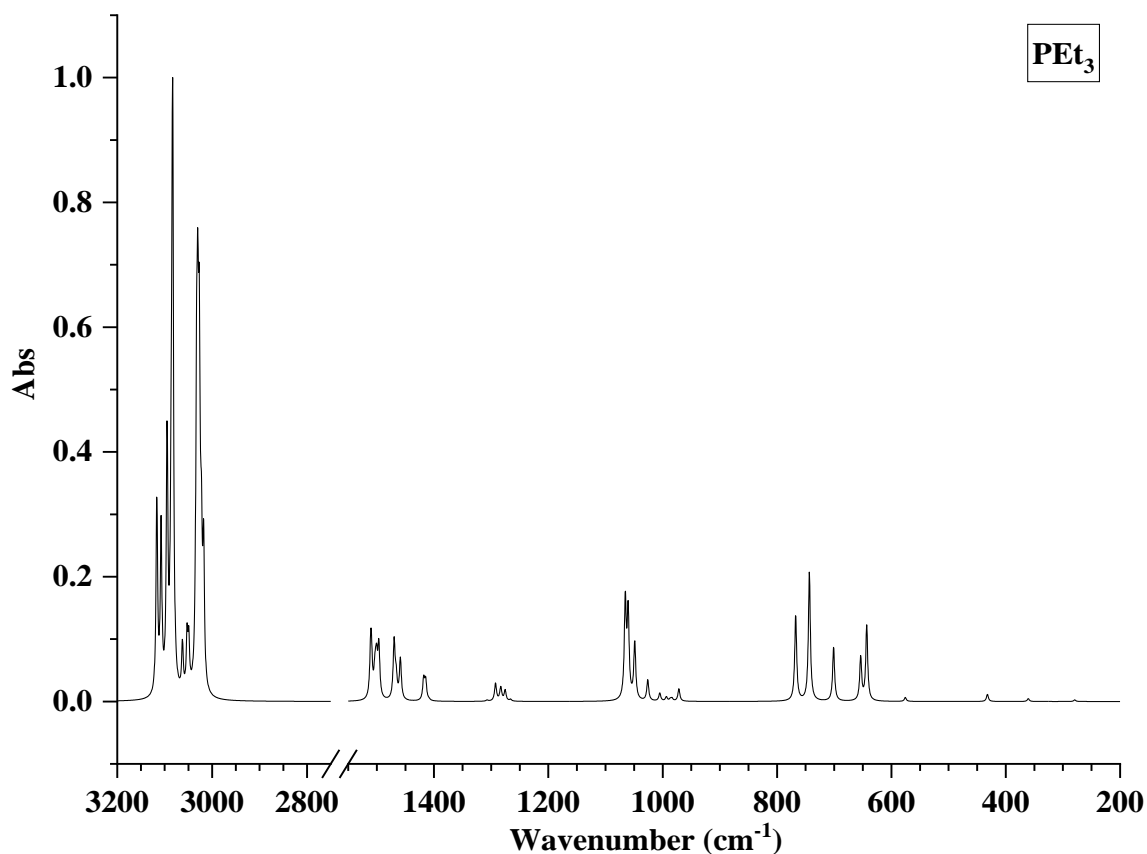
Figure 8.20: *Calculated (B3LYP/def2tzvpp) IR spectrum of PEt$_3$ at half−widths 4.0 cm^{-1}.*
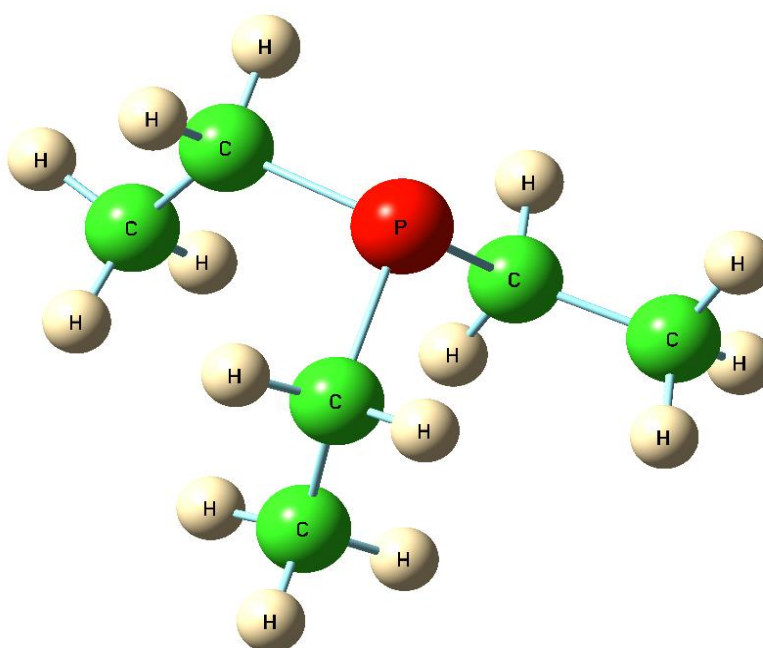
Figure 8.21: *Calculated (B3LYP/def2tzvpp) geometric structure of PEt$_3$.*

Table 8.6: Vibrational frequencies (cm^{-1}) calculated of PEt$_3$.

Calculated B3LYP/def2tzvpp	IR intensity, km.mol^{-1}	Assignments
279.49 cm^{-1}	0.2263	C–H rocking bending mode
432.12 cm^{-1}	0.9982	P–C scissoring bending mode and vibrational motion of C–C bonds
575.69 cm^{-1}	0.5508	P–C symmetric stretching mode and vibrational motion of C–C and C–H bonds
643.21 cm^{-1}	10.4594	P–C asymmetric stretching mode and vibrational motion of C–C and C–H bonds
653.78 cm^{-1}	6.0487	
701.10 cm^{-1}	7.4910	C–H bending mode and vibrational motion of P–C and C–C bonds and
743.50 cm^{-1}	17.9585	
767.43 cm^{-1}	11.9053	
971.71–993.59 cm^{-1}	1.7475–0.5803	Vibrational motion of P–C, C–C, and C–H bonds
1005.12–1065.45 cm^{-1}	1.1012–13.6448	C–H bending mode and vibrational motion of P–C and C–C bonds
1275.58–1292.40 cm^{-1}	1.5156–2.4658	
1408.52 cm^{-1}	0.1242	C–H symmetric stretching mode and vibrational motion of C–C bonds
1418.03 cm^{-1}	2.9701	
1458.80 cm^{-1}	5.6768	C–H Scissoring bending mode and vibrational motion of P–C and C–C bonds
1469.74 cm^{-1}	8.0557	
1496.47 cm^{-1}	7.1507	
1500.27–1510.72 cm^{-1}	4.2309–5.7848	C–H scissoring bending mode and vibrational motion of C–C bonds
3018.04–3032.91 cm^{-1}	18.7106–37.8191	C–H symmetric stretching mode
3049.29–3116.68 cm^{-1}	6.7002–35.0356	C–H asymmetric stretching mode and vibrational motion of C–C bonds

8.3.11.4 Adduct of SiF$_4$ and PMe$_3$

All the computational calculations were undertaken using B3LYP/def2tzvpp within G09W to help in the assignment of the peaks in the experimental IR spectra and to predict the geometry of the complexes formed. The most likely complexes to be formed

will be ether 1:1 or 1:2 SiF$_4$:PMe$_3$, and a number of initial starting geometries were used. For the SiF$_4$.PMe$_3$ (1:1) complex, four different configurations were assumed to start the calculations as presented in Table 8.7 below. However, three of the calculations ended with (C$_{2v}$) trigonal bipyramid symmetry with axial position of PMe$_3$ (Figure 8.22), whilst the minimised structure which started off as square pyramidal with an axial PMe$_3$ is a transition state with negative frequencies and cannot be optimised. The minimised geometries were found to disagree with the Muetterties rule,[22] as already noted for SiF$_4$.NH$_3$ complexes.[21] The difference in energy formation for complexes is very small confirming the instability of these complexes.

Table 8.7: The calculated geometries of (1:1) SiF$_4$.PMe$_3$ complex.

Initial molecular structure	Bond angles	Bond lengths (Å)	ΔH complex formation, kJ.mol^{-1}
Trigonal bipyramid structure with equatorial PMe$_3$	117.9º, 117.8º, 118.1º, 98.4º, 98.2º, 98.3 º, 81.8º, 81.6º, 81.7º, 179.9º	1.6028 (Si−F), 1.6006 (Si−F), (16002)×2 (Si−F), 2.6421 (Si−P)	−0.31
Trigonal bipyramid structure with axial PMe$_3$	(118.1º)×3, (98.1º)×2, 98.0º, 82.0º, 81.9º, 81.8º, 179.9º	1.6044 (Si−F), 1.6015 (Si−F), 1.6017 (Si−F), 1.6018 (Si−F), 2.62424 (Si−P)	−0.38
Square pyramidal structure with equatorial PMe$_3$	(118.1º)×2, (98.1º)×2, (82.1º)×2, 117.9º, 98.0º, 81.5 º, 179.5º	1.6042 (Si−F), 1.6020 (Si−F), 1.6012 (Si−F), 1.6016 (Si−F), 2.6246 (Si−P)	−0.49
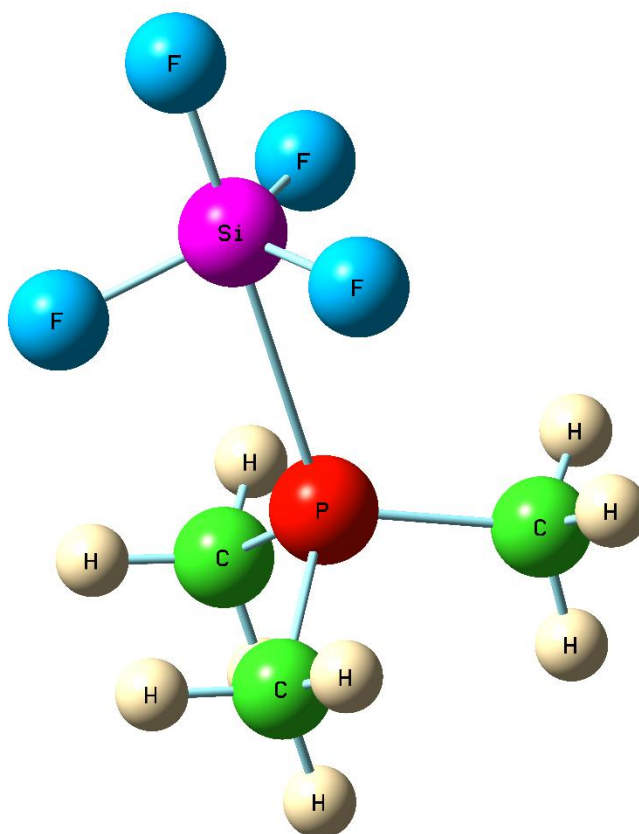
Figure 8.22: *Calculated (B3LYP/def2tzvpp) geometric structure of SiF₄.PMe₃ complex.*

The calculated IR spectra of the trigonal bipyramid symmetry with an axial PMe₃ are displayed in Figure 8.23. The spectra show one sharp peak in the far–IR region with a shoulder. In addition, there are four peaks with appreciable IR intensity in the mid–IR region; one weak peak, followed by three fundamental peaks and a shoulder. SiF_4 modes changed the most because the shape was changed considerably, while PMe₃ changed slightly. As observed in the experimental spectrum, there is also a little change in bands positions and intensities for bands C−H bending and stretching regions in the SiF_4−PMe₃ complex. The IR peaks and their intensities and assignments are tabulated in Tables 8.8– 8.10.

Table 8.8: Vibrational frequencies (cm^{-1}) calculated of the minimised structure which started off as trigonal bipyramid with an equatorial PMe$_3$.

Calculated B3LYP/def2tzvpp	IR intensity, km.mol^{-1}	Assignments
382.7 cm^{-1}	237.7240	Vibrational motion of Si–P bond and Si–F wagging bending mode
396.9 cm^{-1}	19.8699	Vibrational motion of Si–P bond Si–F and scissoring bending mode
728.85 cm^{-1}	11.2775	P–C asymmetric stretching mode and vibrational motion of Si–P bond
859.1 cm^{-1}	422.8624	Si–F asymmetric stretching mode, vibrational motion of Si–P bond, and C–H bending mode
942.6 cm^{-1}	136.7658	
943.9 cm^{-1}	133.5930	
968.5 cm^{-1}	70.9053	C–H bending mode
987.1 cm^{-1}	13.7909	
1300–1500 cm^{-1}		C–H bending mode
3000–3150 cm^{-1}		C–H stretching mode

Table 8.9: Vibrational frequencies (cm^{-1}) calculated of the minimised structure which started off as trigonal bipyramid with an axial PMe₃.

Calculated B3LYP/def2tzvpp	IR intensity, km.mol^{-1}	Assignments
385.5 cm^{-1}	237.5134	Vibrational motion of Si–P bond and Si–F wagging bending mode
397.3 cm^{-1}	19.9185	Vibrational motion of Si–P bond and Si–F scissoring bending mode
730.6 cm^{-1}	11.0981	P–C asymmetric stretching mode and vibrational motion of Si–P bond
855.1 cm^{-1}	326.3161	Si–F asymmetric stretching mode, vibrational motion of Si–P bond, and C–H bending mode
940.0 cm^{-1}	142.1736	
940.7 cm^{-1}	140.6645	
969.5 cm^{-1}	65.8016	C–H bending mode
988.0 cm^{-1}	14.3434	
1300–1500 cm^{-1}		C–H bending mode
3000–3150 cm^{-1}		C–H stretching mode

Table 8.10: Vibrational frequencies (cm^{-1}) calculated of the minimised structure which started off as square pyramidal with an equatorial PMe$_3$.

Calculated B3LYP/def2tzvpp	IR intensity, km.mol^{-1}	Assignments
385.5 cm^{-1}	237.0710	Vibrational motion of Si–P bond and Si–F wagging bending mode
397.8 cm^{-1}	19.9160	Vibrational motion of Si–P bond and Si–F scissoring bending mode
733.2 cm^{-1}	11.0720	P–C asymmetric stretching mode and vibrational motion of Si–P bond
855.6 cm^{-1}	77.9300	Si–F asymmetric stretching mode, vibrational motion of Si–P bond, and C–H bending mode
940.0 cm^{-1}	141.9582	
941.4 cm^{-1}	141.6286	
969.6 cm^{-1}	64.6380	C–H bending mode
988.2 cm^{-1}	14.3019	
1300–1500 cm^{-1}		C–H bending mode
3000–3150 cm^{-1}		C–H stretching mode
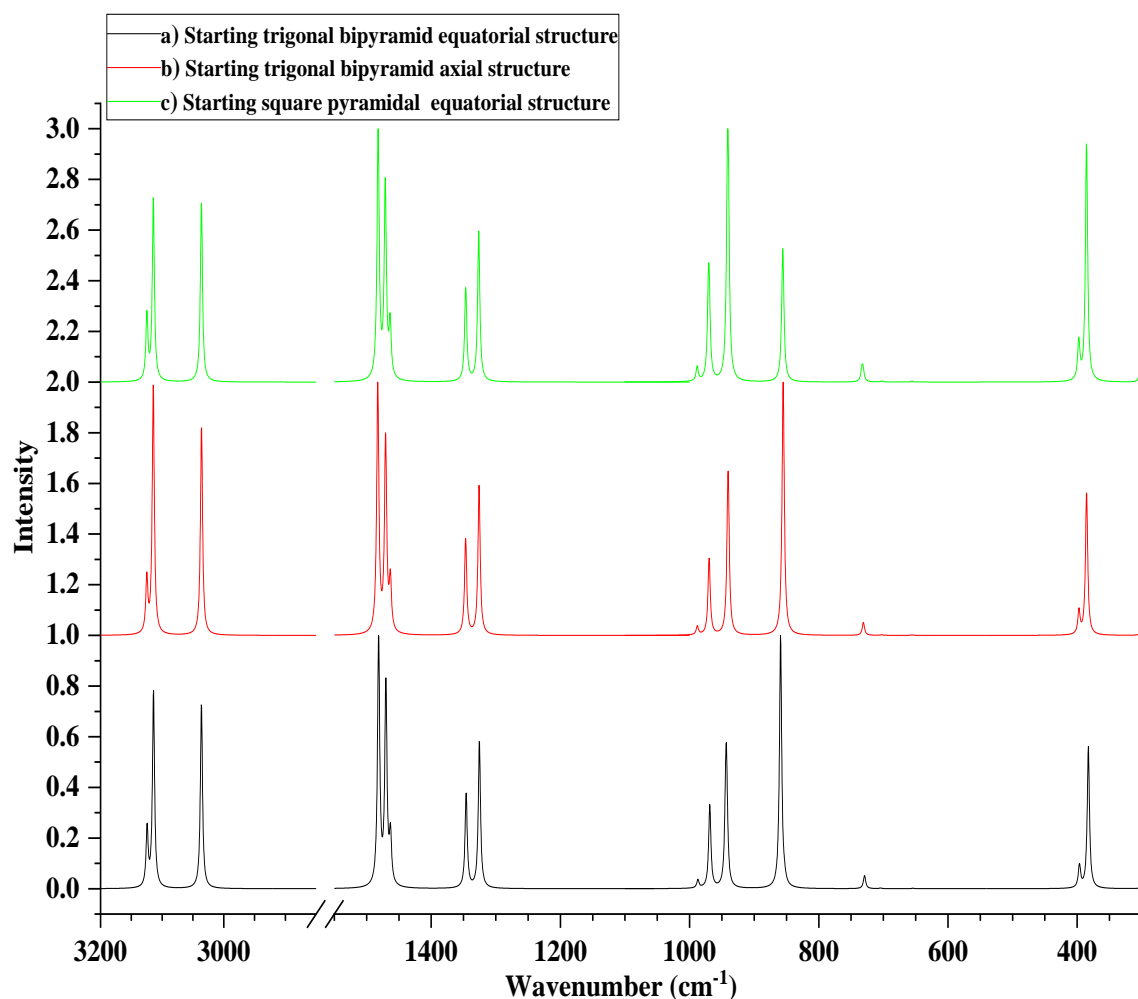
Figure 8.23: *Calculated (B3LYP/def2tzvpp) IR spectra of SiF$_4$.PMe$_3$ complex at half−widths 4.0 cm^{-1}.*

In terms of the 1:2 adduct of SiF$_4$ and PMe$_3$, the molecular structure of the complex could be either *cis*–[SiF$_4$.(PMe$_3$)$_2$] or *trans*–[SiF$_4$.(PMe$_3$)$_2$] as listed in Table 8.11. The minimised structure which started off as *cis*–[SiF$_4$.(PMe$_3$)$_2$] structure is a 1:1 complex of SiF$_4$.PMe$_3$ and an unbound PMe$_3$ molecule. The calculated distance between SiF$_4$ and an unbound phosphine molecule is 5.1744 Å (Table 8.11 and Figure 8.24). The enthalpy of formation of the complex is –8.78 kJ.mol^{-1}. The calculated spectrum shown in Figure 8.25a has only one intense peak at 395.3 cm^{-1}. Regarding the mid–IR region, the calculations manifested two less intense bands at 700.2 and 736.7 cm^{-1} accompanied by two more intense peaks at 841.8 and 920.7 cm^{-1}. Furthermore, medium intensity band at 970.2 cm^{-1} and weak peak at 991.0 cm^{-1} were observed as tabulated in Table 8.12.

Table 8.11: The calculated geometries of (1:2) $SiF_4.(PMe_3)_2$ complex.

Initial molecular structure	Minimised molecular structure	Bond angles	Bond lengths (Å)
Cis	1:1 complex with long distance PMe_3 interaction with SiF_4	118.77º, 118.61º, 118.39º, 97.02º, 96.90º, 96.71º, 82.65º, 83.18º, 83.55º, 179.55º	1.6068 (Si−F), 1.6077 (Si−F), 16096 (Si−F), 1.6097 (Si−F), 2.5535 (Si−P), 5.1744 (Si−P),
Trans	Trans	(90.05º)×2, (89.95º)×2, (90.94) ×4, (89.06º) ×4, 179.99º	(1.6804)×4 (Si−F), (2.3912)×2 (Si−P)
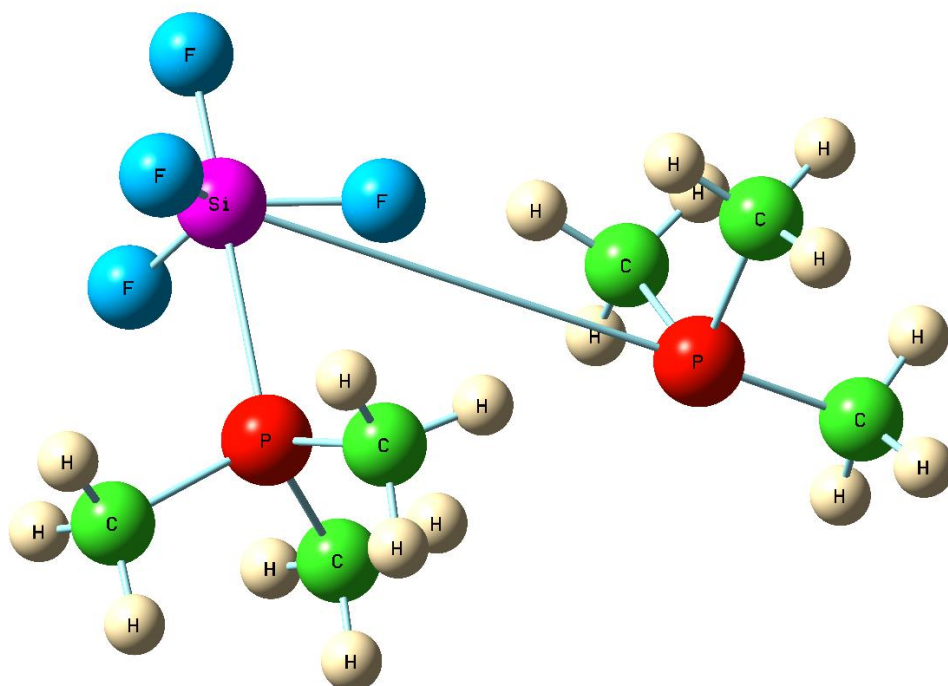
Figure 8.24: *Calculated (B3LYP/def2tzvpp) geometric structure of SiF₄.PMe₃ complex and an unbound PMe₃ molecule.*

Table 8.12: Vibrational frequencies (cm^{-1}) calculated of the minimised structure which started off as *cis*–[SiF$_4$.(PMe$_3$)$_2$].

Calculated B3LYP/def2tzvpp	IR intensity, km.mol^{-1}	Assignments
395.3 cm^{-1}	207.4079	Si–F wagging bending mode and vibrational motion of Si–P bond
700.2 cm^{-1}	14.0385	P–C asymmetric stretching mode and vibrational motion of Si–P bond
736.7 cm^{-1}	10.9178	P–C asymmetric stretching mode
841.8 cm^{-1}	231.3907	C–H bending mode and vibrational motion of Si–P bond
920.7 cm^{-1}	220.5809	Si–F asymmetric stretching mode, vibration motion of Si–P bond, and C–H bending mode
927.5 cm^{-1}	143.2639	
970.28 cm^{-1}	77.3127	C–H bending mode
991.0 cm^{-1}	13.4527	
1300–1500 cm^{-1}		C–H bending mode
3000–3150 cm^{-1}		C–H stretching mode
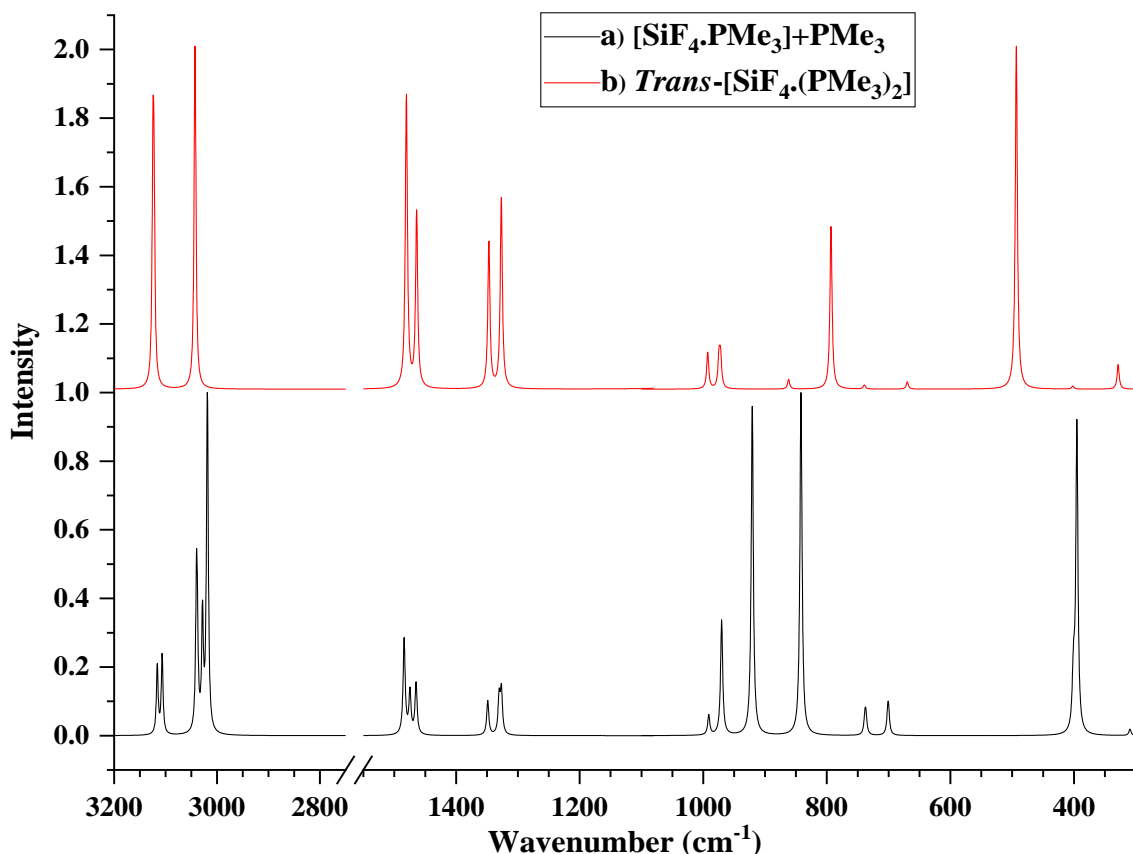
Figure 8.25: *Calculated (B3LYP/def2tzvpp) IR spectra of 1:1 adduct SiF₄.PMe₃ with an unbound PMe₃ molecule and trans–[SiF₄.(PMe₃)₂] complex at half−widths 4.0 cm⁻¹.*

The theoretical data of *trans*–[SiF$_4$.(PMe$_3$)$_2$] are displayed in Figure 8.25b and Table 8.13.Two bands in the far infrared region were calculated at 328.5 and 493.3 cm^{-1}, but of very different relative intensity. In the mid–IR region, there are two calculated weak features at 669.8 and 739.7 cm^{-1}, and one intense peak at 793.1 cm^{-1}, followed by a less intense peak at 862.1 cm^{-1} and two intense bands at 972.0 and 992.7 cm^{-1}. The enthalpy of the formation is 1.14 kJ.mol^{-1}, and the calculated geometry of *trans*–[SiF$_4$.(PMe$_3$)$_2$] complex is given in Figure 26, the geometric structure of SiF$_4$ is noticeably changed with slight change in PMe$_3$ structure.
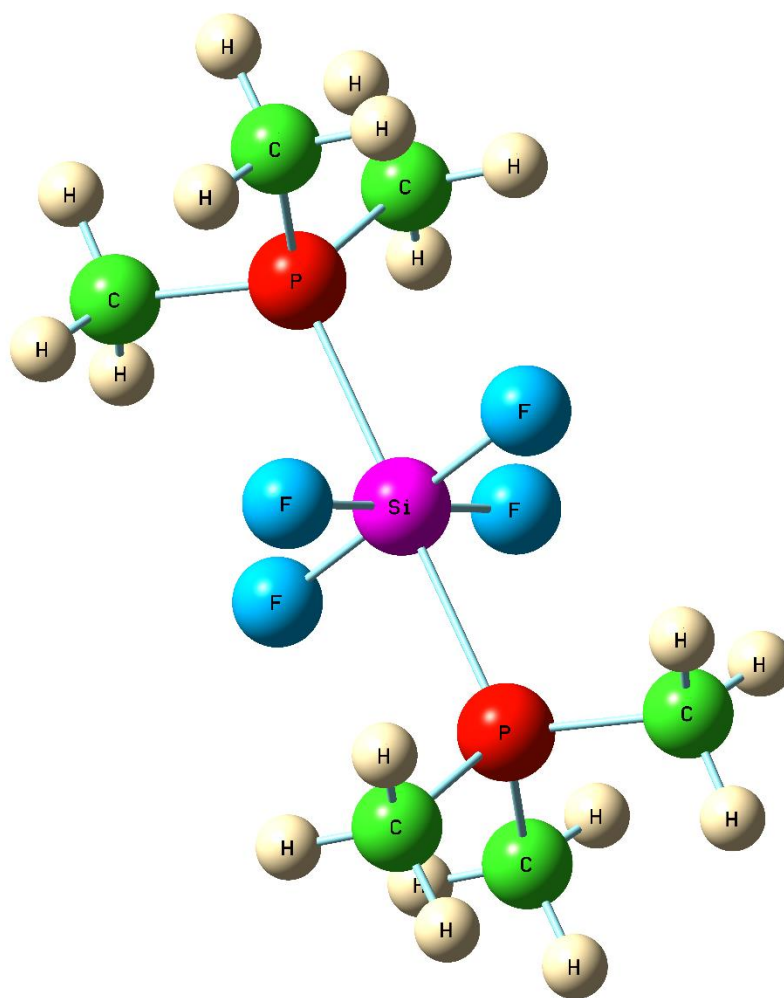
Figure 8.26: *Calculated (B3LYP/def2tzvpp) geometric structure of trans–[SiF₄.(PMe₃)₂] complex.*

Table 8.13: Vibrational frequencies (cm^{-1}) calculated of the *trans*–[SiF$_4$.(PMe$_3$)$_2$].

Calculated B3LYP/def2tzvpp	IR intensity, km.mol^{-1}	Assignments
328.5 cm^{-1}	55.9610	C–H bending mode and vibrational motion of Si–P bond
493.3 cm^{-1}	782.7758	Si–F wagging bending mode, C–H bending mode, and vibrational motion of Si–P bond
669.8 cm^{-1}	16.6623	P–C asymmetric stretching mode
739.7 cm^{-1}	5.0652	P–C asymmetric stretching mode and vibrational motion of Si–P bond
739.3 cm^{-1}	186.1949	Si–F asymmetric stretching mode, vibrational motion of Si–P bond, and C–H bending mode
862.1 cm^{-1}	11.4265	C–H bending mode
972.0 cm^{-1}	68.5764	C–H bending mode and vibrational motion of P–C bond
992.7 cm^{-1}	82.8736	C–H bending mode, vibrational motion of P–C bond, and vibrational motion of Si–P bond
1300–1500 cm^{-1}		C–H bending mode
3000–3150 cm^{-1}		C–H stretching mode

The calculated IR spectrum for the 1:1 adduct of SiF$_4$.PMe$_3$ does not match with the experimental spectrum (Figure 8.8a) which has two IR bands in the far infrared region at 388 and 426 cm^{-1} with a shoulder peak at 420 cm^{-1}. Thus, this structure is not favourable. Similarly, the calculated IR spectrum for a 1:1 complex of SiF$_4$.(PMe$_3$)$_2$ with long distance PMe$_3$ interacted with SiF$_4$ is not convenient with data of the experimental spectrum, as it has one IR peak in far infrared region as well. Furthermore, the intensity and position of bands of the *trans*–[SiF$_4$.(PMe$_3$)$_2$] in the mid–IR region are entirely dissimilar with vibrational data recorded.

The enthalpy of the complex formation energy of 1:1 adduct with long distance PMe$_3$ interacted with SiF$_4$ is the most favourable, followed by the enthalpy of the formation energy of 1:1 adduct of SiF$_4$.PMe$_3$. The 1:2 adduct *trans*–[SiF$_4$.(PMe$_3$)$_2$] was found the least favourable complex to be formed, where the energy of formation indicates it is endothermic. That is because the symmetry of SiF$_4$ is tetrahedral and Si–F bond is very strong comparing with Si–Cl bond.[39, 40] Therefore, it needs more energy for

rearrangement the Si–F bond angles to react with PMe$_3$ forming *trans*–[SiF$_4$.(PMe$_3$)$_2$] structure. It is more likely that the experimental spectrum might be due to a mixture of two complexes. It could be a 1:1 adduct of SiF$_4$.PMe$_3$ with long distance PMe$_3$ interacted with SiF$_4$ and 1:1 adduct of trigonal bipyramid structure with axial PMe$_3$. The calculated mixture has two absorption bands in far infrared region at 382.7 cm^{-1} and 395.3 cm^{-1}, these bands could be consistent with the two IR bands of the experimental spectrum at 388 and 426 cm^{-1}, although there is a change in position of these bands, as they are a little shifted. Also, the suggested mixture has the same numbers of peaks in mid infrared region, however the intensity and position of bands are entirely dissimilar with experimentally gathered IR peaks, as seen in Figure 8.27 It seems that the B3LYP/def2tzvpp calculation are not well suited to weak complexes, and future work will make use of other basis sets. It is clear that there are at least two different complexes formed. Although, this result with the study conducted by George *et al*. revealed the difficulty in reaction between SiF$_4$ and PMe$_3$, as they failed to make SiF$_4$ complexes with phosphines and suggested matrix isolation experiments might be worthwhile.[39] Nonetheless, this result is in agreement with previous study conducted by Baettie and Ozin,[20] indicating the formation of complexes between SiF$_4$ and PMe$_3$, their recorded Raman data had two bands at 532 and 596 cm^{-1} corresponding to 1:2 adduct,[20] whereas the band recorded at 672 cm^{-1} was related to 1:1 adduct suggesting the formation of *trans*–[SiF$_4$.(PMe$_3$)$_2$] complex as well as 1:1 complex of SiF$_4$.PMe$_3$.[15] Furthermore, this result is matching with the literature data of the reaction between SiF$_4$ and NH$_3$ where both 1:1 and 1:2 adducts were formed.[7]
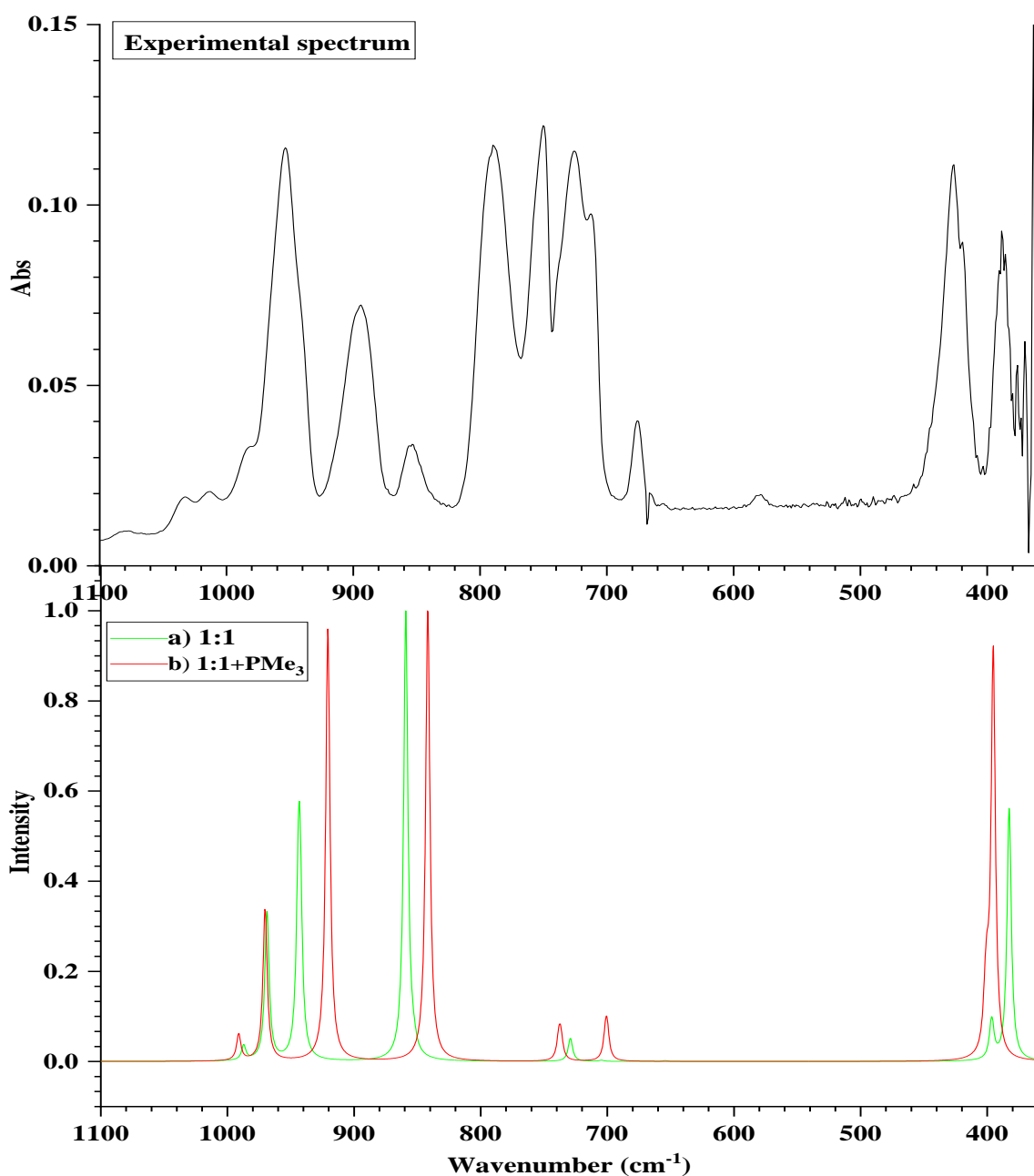
Figure 8.27: *Calculated (B3LYP/def2tzvpp) IR spectra of a mixture of 1:1 adduct SiF₄.PMe₃ and 1:1 adduct SiF₄.PMe₃ with an unbound PMe₃ molecule at half−width 4 cm⁻¹ and the experimental spectrum.*

8.3.11.5 Adduct of SiF₄ and PEt₃

The theoretical calculations were carried out using B3LYP/def2tzvpp within G09W to identify the molecular structure of the formed adduct and to assign the features obtained in the experimental IR spectrum as well. In terms of 1:1 suggested adduct of SiF_4 and PEt_3, the calculations started with four different molecular structures. Nonetheless, the final geometry was trigonal bipyramid symmetry (C_{2v}) with PEt_3 in axial position (Figure 8.28), with very similar enthalpies of complex formation, as presented in Table 8.14.

Table 8.14: The calculated geometry of (1:1) $SiF_4.PEt_3$ complex.

Initial molecular structure	Bond angles	Bond lengths (Å)	ΔH complex formation, kJ.mol^{-1}
Trigonal bipyramid equatorial structure	118.6°, 118.2°, 118.1°, 97.2°, 97.5°, 97.4°, 83.2, 83.1°, 81.4°, 178.7°	1.6074 (Si−F), 1.6036 (Si−P), 1.6055 (Si−P), 1.6039 (Si−P), 2.6075 (Si−P)	−12.38
Trigonal bipyramid axial structure	118.6°, 118.2°, 118.1°, 97.2°, 97.3°, 97.4°, 83.2, 83.1°, 81.4°, 178.7°	1.6074 (Si−F), 1.6036 (Si−F), 1.6039 (Si−F), 1.6055 (Si−F), 2.6076 (Si−P)	−12.37
Square pyramidal equatorial structure	117.9°, 118.2°, 118.7°, 97.6°, (97.4°)×2, 82.5°, 81.7°, 83.2°, 178.9°	1.6069 (Si−F), 1.6022 (Si−F), 1.6041 (Si−F), 1.6037 (Si−F), 2.6186 (Si−P)	−12.19
Square pyramidal axial structure	118.7°, 118.1°, 117.9°, 97.6°, (97.4°)×2, 81.6°, 82.5°, 83.2°, 178.9°	1.6069 (Si−P), 1.6022(Si−F), 1.6041 (Si−F), 1.6037 (Si−F), 2.6185 (Si−P)	−12.19
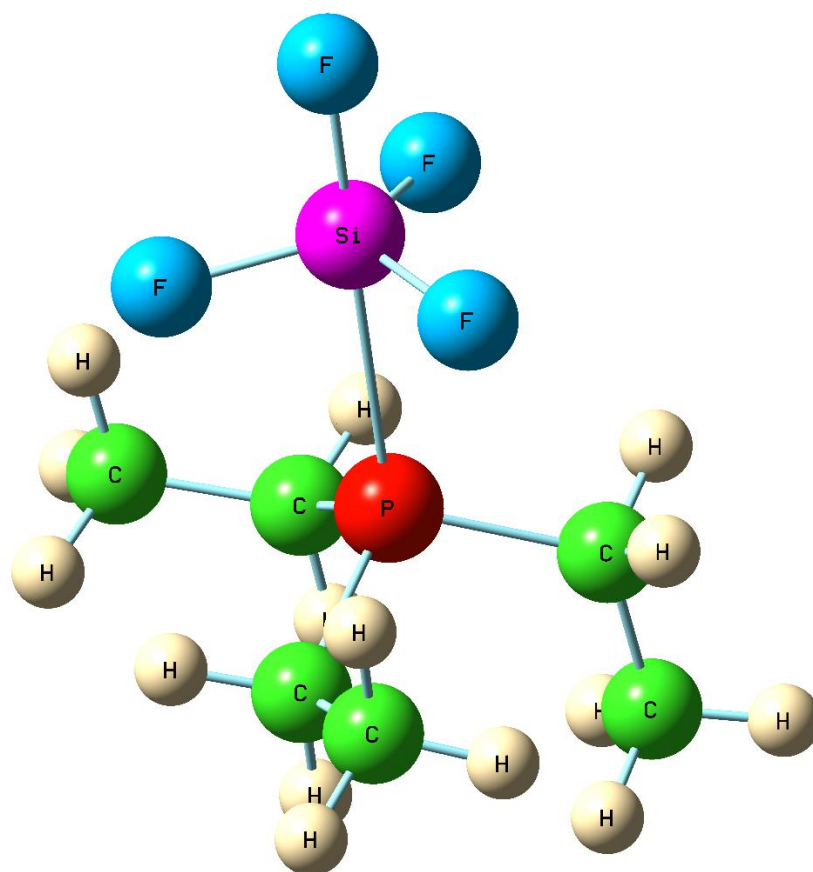
Figure 8.28: *Calculated (B3LYP/def2tzvpp) geometric structure of SiF₄.PEt₃ complex.*

Figure 8.29 shows the calculated IR spectrum for trigonal bipyramid symmetry with an axial PEt₃. In the far infrared region there is one sharp strong peak followed by shoulder. Meanwhile, in the mid infrared region there are a group of less intense peaks in the region of 500–800 cm^{-1}, and two intense bands between 800–900 cm^{-1}. The geometry of SiF₄ changed considerably comparing with less change in PEt₃, thus SiF₄ modes changed the most. Furthermore, is also slightly change in in bands positions and intensities for bands C−H bending as well as stretching region in the SiF₄−PEt₃ complex. The calculated wavenumbers, IR intensities and assignments are listed in Tables 8.15–8.18.

Table 8.15: Vibrational frequencies (cm^{-1}) calculated of the minimised structure which started off as trigonal bipyramid with an equatorial PEt$_3$.

Calculated B3LYP/def2tzvpp	IR intensity, $km.mol^{-1}$	Assignments
386.3 cm^{-1}	230.1074	Si–F wagging bending mode and vibrational motion of Si–P bond
399.5 cm^{-1}	17.9894	Si–F scissoring bending mode and vibrational motion of Si–P bond
671.0 cm^{-1}	3.6273	C–H bending mode, vibrational motion of P–C bond, and vibrational motion of Si–P bond
690.3 cm^{-1}	10.7488	C–H bending mode, vibrational motion of P–C bond, and vibrational motion of Si–P bond
740.3 cm^{-1}	25.4767	C–H bending mode
759.2 cm^{-1}	11.7640	
776.3 cm^{-1}	36.062	
849.6 cm^{-1}	385.7777	Si–F asymmetric stretching mode, vibrational motion of Si–P bond, and C–H bending mode
933.0 cm^{-1}	168.9671	
934.9 cm^{-1}	168.1839	
1050–1550 cm^{-1}		The animation available on G09W, these localised mode of PEt$_3$ C–H bending mode with no movement in the Si–F mode.
3000–3150 cm^{-1}		The animation available on G09W, these localised mode of PEt$_3$ C–H stretching mode with no movement in the Si–F mode.

Table 8.16: Vibrational frequencies (cm^{-1}) calculated of the minimised structure which started off as trigonal bipyramid with an axial PEt$_3$.

Calculated B3LYP/def2tzvpp	IR intensity, km.mol^{-1}	Assignments
386.2 cm^{-1}	230.1605	Si–F wagging bending mode and vibrational motion of Si–P bond
399.5 cm^{-1}	17.9732	Si–F scissoring bending mode and vibrational motion of Si–P bond
671.0 cm^{-1}	3.6328	C–H bending mode, vibrational motion of P–C bond, and vibrational motion of Si–P bond
690.3 cm^{-1}	10.7411	C–H bending mode, vibrational motion of P–C bond, and vibrational motion of Si–P bond
740.3 cm^{-1}	25.4723	C–H bending mode
759.1 cm^{-1}	11.7646	
776.2 cm^{-1}	36.0517	
849.6 cm^{-1}	385.7823	Si–F asymmetric stretching mode, vibrational motion of Si–P bond, and C–H bending mode
933.1 cm^{-1}	168.964	
934.92 cm^{-1}	168.1789	
1050–1550 cm^{-1}		The animation available on G09W, these localised mode of PEt$_3$ C–H bending mode with no movement in the Si–F mode.
3000–3150 cm^{-1}		The animation available on G09W, these localised mode of PEt$_3$ C–H stretching mode with no movement in the Si–F mode.

Table 8.17: Vibrational frequencies (cm^{-1}) calculated of the minimised structure which started off as square pyramidal with an equatorial PEt$_3$.

Calculated B3LYP/def2tzvpp	IR intensity, km.mol^{-1}	Assignments
383.9 cm^{-1}	226.2421	Si–F wagging bending mode and vibrational motion of Si–P bond
399.5 cm^{-1}	18.7962	Si–F scissoring bending mode and vibrational motion of Si–P bond
669.7 cm^{-1}	3.9651	C–H bending mode, vibrational motion of P–C bond, and vibrational motion of Si–P bond
687.9 cm^{-1}	9.6466	C–H bending mode, vibrational motion of P–C bond, and vibrational motion of Si–P bond
738.4 cm^{-1}	24.5627	C–H bending mode
757.7 cm^{-1}	12.5935	
774.2 cm^{-1}	34.055	
850.2 cm^{-1}	386.0648	Si–F asymmetric stretching mode, vibrational motion of Si–P bond, and C–H bending mode
935.35 cm^{-1}	166.8785	
936.9 cm^{-1}	169.1825	
1050–1550 cm^{-1}		The animation available on G09W, these localised mode of PEt$_3$ C–H bending mode with no movement in the Si–F mode.
3000–3150 cm^{-1}		The animation available on G09W, these localised mode of PEt$_3$ C–H stretching mode with no movement in the Si–F mode.

Table 8.18: Vibrational frequencies (cm^{-1}) calculated of the minimised structure which started off as square pyramidal with an axial PEt$_3$.

Calculated B3LYP/def2tzvpp	IR intensity, $km.mol^{-1}$	Assignments
383.9 cm^{-1}	226.2778	Si–F wagging bending mode and vibrational motion of Si–P bond
399.5 cm^{-1}	18.8837	Si–F scissoring bending mode and vibrational motion of Si–P bond
669.7 cm^{-1}	3.9645	C–H bending mode, vibrational motion of P–C bond, and vibrational motion of Si–P bond
687.9 cm^{-1}	9.6453	C–H bending mode, vibrational motion of P–C bond, and vibrational motion of Si–P bond
728.3 cm^{-1}	24.561	C–H bending mode
757.7 cm^{-1}	12.5954	
774.2 cm^{-1}	34.0653	
850.2 cm^{-1}	386.0544	Si–F asymmetric stretching mode, vibrational motion of Si–P bond, and C–H bending mode
935.3 cm^{-1}	166.9178	
936.95 cm^{-1}	169.1371	
1050–1550 cm^{-1}		The animation available on G09W, these localised mode of PEt$_3$ C–H bending mode with no movement in the Si–F mode.
3000–3150 cm^{-1}		The animation available on G09W, these localised mode of PEt$_3$ C–H stretching mode with no movement in the Si–F mode.
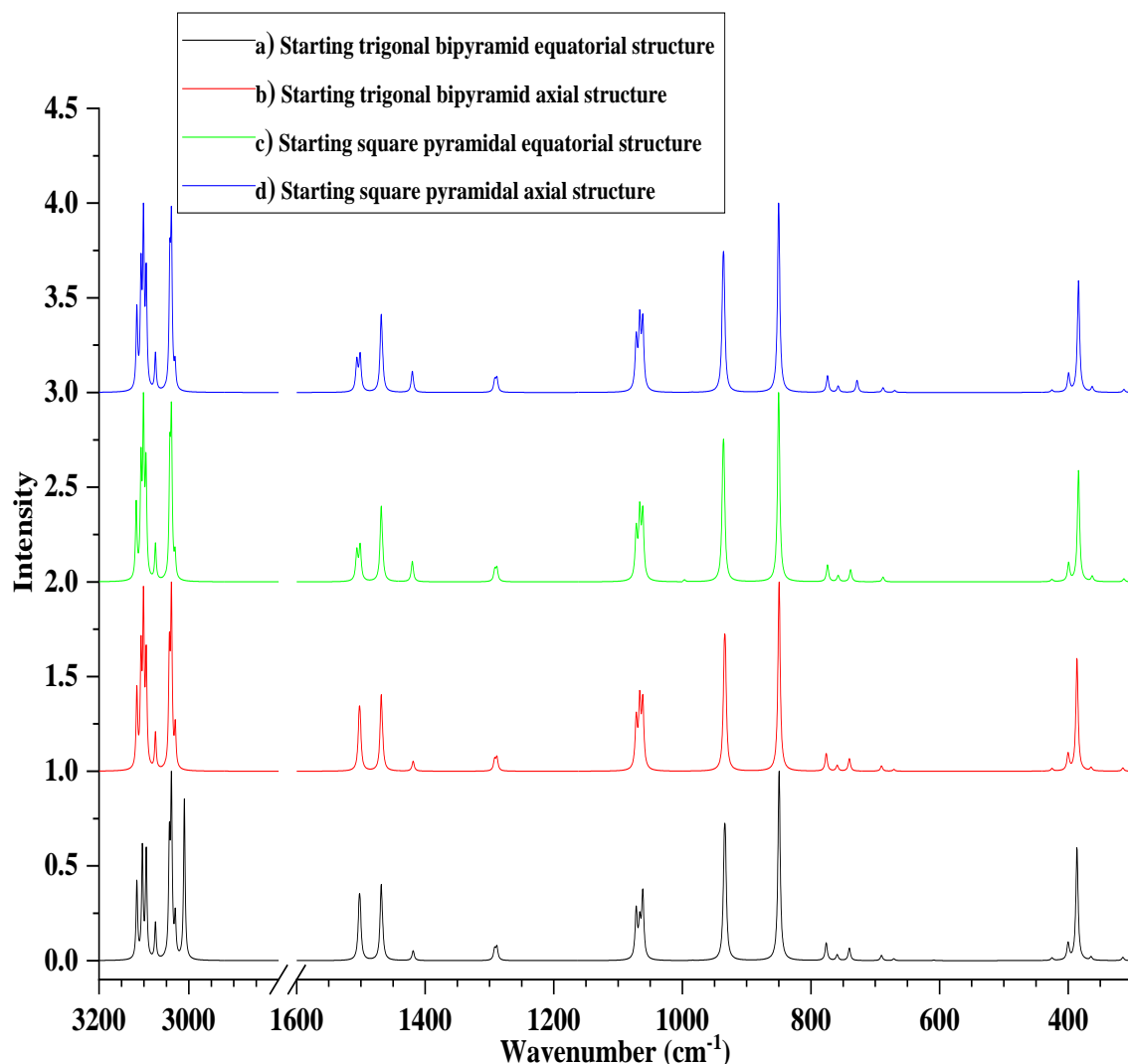
Figure 8.29: *Calculated (B3LYP/def2tzvpp) IR spectra of SiF₄.PEt₃ complex at half−widths 4.0 cm⁻¹.*

A theoretical study was also undertaken on the 1:2 adducts of SiF_4 and PEt_3; where two different geometrical structures are proposed as listed in Table 8.19, *cis*–[SiF_4.(PEt_3)$_2$] and *trans*–[SiF_4.(PEt_3)$_2$]. The distance suggesting the minimised structure which started off as *cis*–[SiF_4.(PEt_3)$_2$] structure is a 1:1 mono–phosphine adduct and an unbound phosphine molecule. The calculated distance between an unbound PEt_3 molecule and SiF_4 is 4.9079 Å (Figure 8.30). As presented in Figure 8.31a and Table 8.20, the calculated vibrational spectrum has one intense band at 398.9 cm⁻¹ and a weak shoulder at 371.4 cm⁻¹ in the far−IR region, and a group of weak intense peaks in the 500–800 cm⁻¹ region, and a significant intense band at 832.1 cm⁻¹ as well as another intense peak at 915 cm⁻¹. The reaction enthalpy of the complex is –22.65 kJ.mol⁻¹.
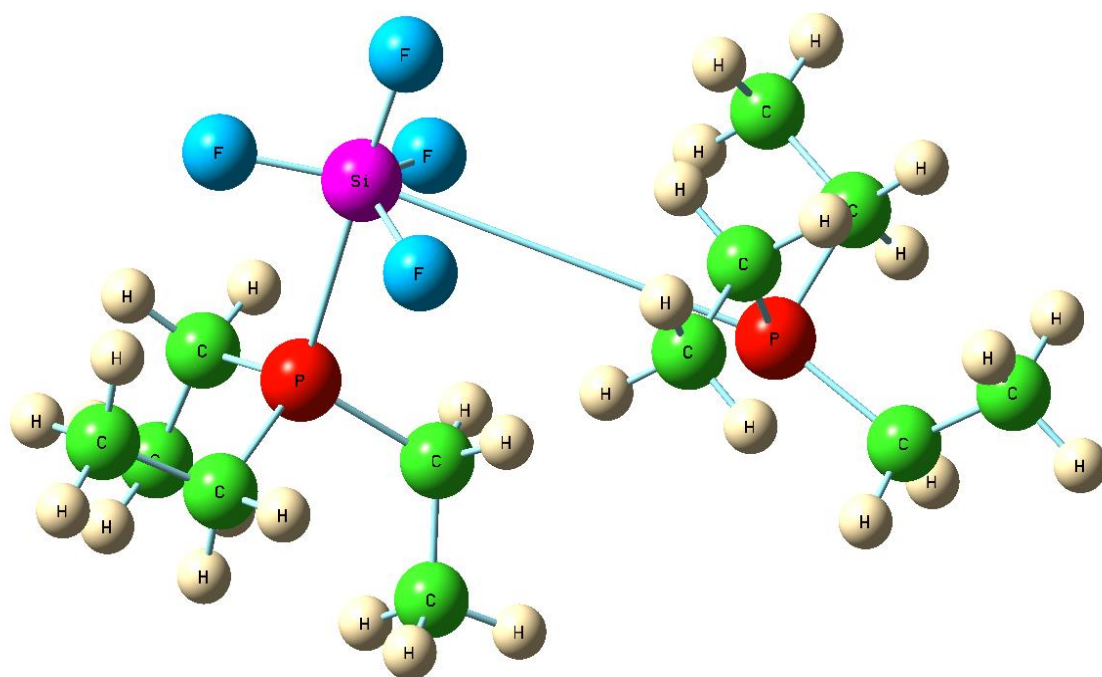
Figure 8.30: *Calculated (B3LYP/def2tzvpp) geometric structure of SiF₄.PEt₃ adduct and an unbound PEt₃ molecule.*

Table 8.19: The calculated geometries of (1:2) $SiF_4.(PEt_3)_2$ complex.

Initial molecular structure	Minimised molecular structure	Bond angles	Bond lengths (Å)
Cis	1:1 complex with long distance PEt₃ interaction with SiF₄	117.69º, 118.54º, 120.08º, 96.68º, 96.04º, 95.79º, 82.91º, 85.54º, 83.09º, 177.78º	1.6147 (Si−F), 1.6113 (Si−F), 1.6124 (Si−F), 1.6083 (Si−F), 2.5293 (Si−P), 4.9079 (Si−P),
Trans	Trans	(90.11º)×2, 90.07º, 89.73, (89.19)×2, (90.58)×2, (91.76)×2, (88.47)×2, 179.68º	(1.6807)×2 (Si−F), (1.6819)×2 (Si−F), (2.4115)×2 (Si−P)

Table 8.20: Vibrational frequencies (cm^{-1}) calculated of the minimised structure which started off as *cis*–[SiF$_4$.(PEt$_3$)$_2$].

Calculated B3LYP/def2tzvpp	IR intensity, km.mol^{-1}	Assignments
371.4 cm^{-1}	10.4788	C–H bending mode, and vibrational motion of Si–P bond
398.9 cm^{-1}	210.0859	Si–F wagging bending mode and vibrational motion of Si–P bond
651.5 cm^{-1}	5.6319	C–H bending mode, vibrational motion of P–C bond, and vibrational motion of Si–P bond
661.0 cm^{-1}	7.8800	C–H bending mode, vibrational motion of P–C bond, and vibrational motion of Si–P bond
681.9 cm^{-1}	3.2499	Si–F symmetric stretching mode and C–H bending mode
684.4 cm^{-1}	5.0979	
689.8 cm^{-1}	5.6368	
711.7 cm^{-1}	11.6067	C–H bending mode and vibrational motion of P–C bond
725.2 cm^{-1}	18.1222	
761.6 cm^{-1}	26.9188	C–H bending mode, vibrational motion of P–C bond, and vibrational motion of Si–P bond
773.8 cm^{-1}	25.9968	C–H bending mode and vibrational motion of P–C bond
832.1 cm^{-1}	342.0846	Si–F asymmetric stretching mode and vibrational motion of Si–P bond
919.2 cm^{-1}	222.9061	
1050–1550 cm^{-1}		The animation available on G09W, these localised mode of PEt$_3$ C–H bending mode with no movement in the Si–F mode.
3000–3150 cm^{-1}		The animation available on G09W, these localised mode of PEt$_3$ C–H stretching mode with no movement in the Si–F mode.
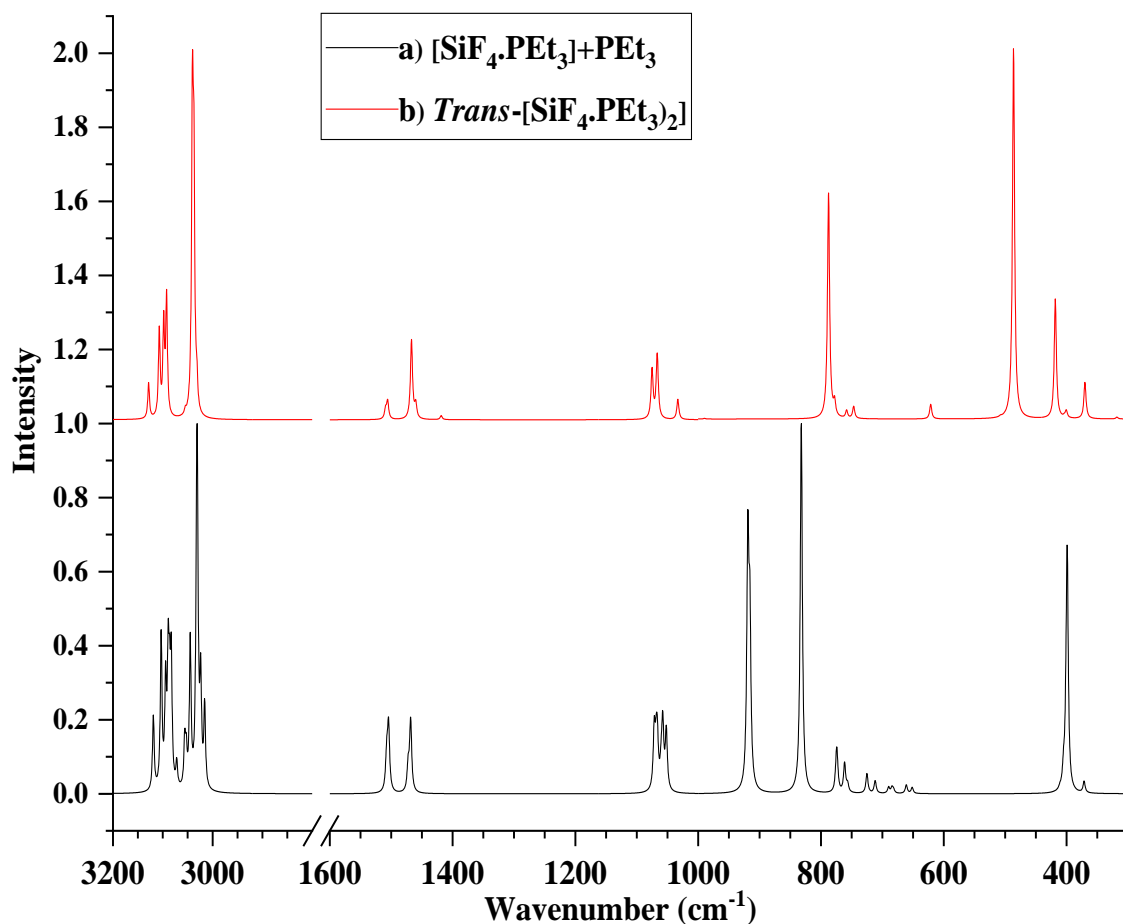
Figure 8.31: *Calculated (B3LYP/def2tzvpp) IR spectra of 1:1 adduct SiF₄.PEt₃ with an unbound PEt₃ molecule and trans–[SiF₄.(PEt₃)₂]complex at half−widths 4.0 cm⁻¹.*

The calculated data in Table 8.21 and Figure 6.31b represent the *trans–* $[SiF_4.(PEt_3)_2]$ complex, it has tiny peak at 370.1 cm^{-1} and two intense peaks at 370.1 and 486.4 cm^{-1} in the far–IR region. In terms of mid infrared region, the theoretical spectrum has one intense peak at 486.4 cm^{-1}, followed by weak intense bands in the 500–800 cm^{-1} region and one intense peak at 787.62 cm^{-1}. The enthalpy of the complex formation is – 25.17 kJ.mol^{-1}. The calculated geometric structure of *trans–*$[SiF_4.(PEt_3)_2]$ is shown in Figure 8.32, and the shape of SiF₄ changes from tetrahedral to square planar with a slight change in PEt₃ structure.

Table 8.21: Vibrational frequencies (cm^{-1}) calculated of the *trans*–[SiF$_4$.(PEt$_3$)$_2$].

Calculated B3LYP/def2tzvpp	IR intensity, km.mol^{-1}	Assignments
370.1 cm^{-1}	60.7607	C–H bending mode, and vibrational motion of Si–P bond
418.3 cm^{-1}	201.5854	Si–F wagging bending mode, C–H bending mode, and Si–P symmetric stretching bond
486.4 cm^{-1}	622.9125	Si–F wagging bending mode, C–H bending mode, and Si–P asymmetric stretching bond
621.3 cm^{-1}	24.8213	C–H bending mode, vibrational motion of P–C bond, and vibrational motion of Si–P bond
746.6 cm^{-1}	16.9070	C–H bending mode, vibrational motion of P–C bond, and vibrational motion of Si–P bond
758.3 cm^{-1}	8.5101	C–H bending mode and vibrational motion of P–C bond
787.6 cm^{-1}	204.6037	Si–F asymmetric stretching mode, C–H bending mode, and vibrational motion of Si–P bond
1050–1550 cm^{-1}		The animation available on G09W, these localised mode of PEt$_3$ C–H bending mode with no movement in the Si–F mode.
3000–3150 cm^{-1}		The animation available on G09W, these localised mode of PEt$_3$ C–H stretching mode with no movement in the Si–F mode.
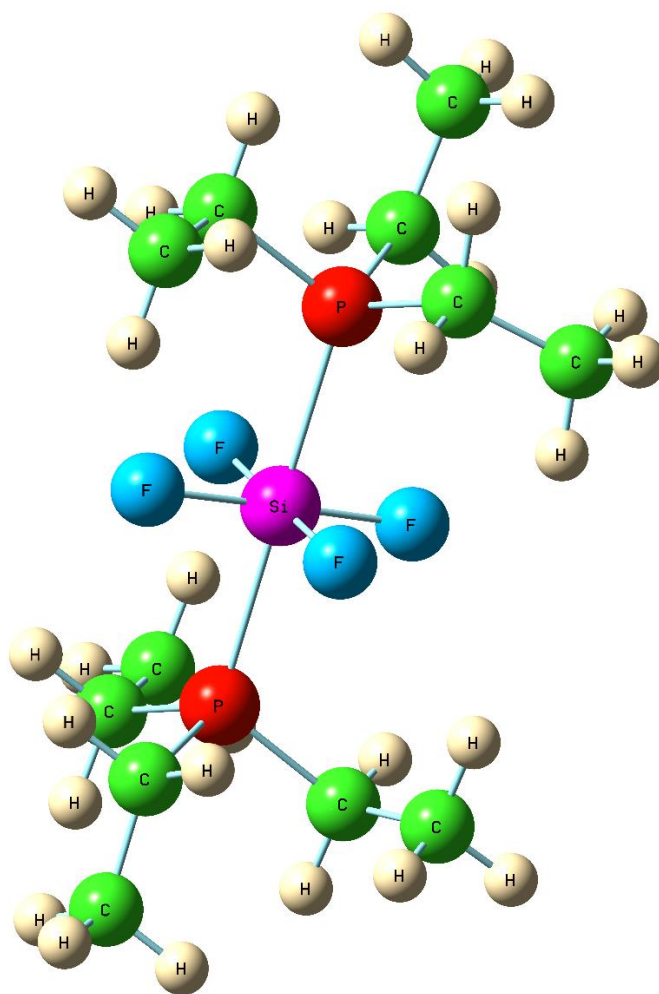
Figure 8.32: *Calculated (B3LYP/def2tzvpp) geometric structure of trans–[SiF₄.(PEt₃)₂] complex.*

The computer simulated IR spectrum for 1:1 $SiF_4.PEt_3$ complex in the far infrared region does not correlate with the experimental spectrum obtained, as it demonstrates one intense band with a shoulder rather than two intense bands. In spite of that, the calculated spectrum in the mid infrared region could be probably appropriate with the experimentally recorded spectrum considering the differences in intensity and position of bands. Accordingly, this molecular structure is unfavourable. Likewise, the theoretical spectrum for the 1:1 complex of $SiF_4.(PEt_3)_2$ with long distance PEt_3 interaction with SiF_4 has one IR band in the far–infrared region which does not correlate with the experimental vibrational spectrum. Moreover, the calculated spectrum of *trans*–[$SiF_4.(PEt_3)_2$] symmetry for 1:2 adduct of SiF_4 and PEt_3 is not in line with the two observed broad bands in far infrared region of experimental spectrum; the features in mid infrared part of both spectra are not correlated as well. As a consequence, the proposed *trans*–[$SiF_4.(PEt_3)_2$] symmetry for 1:2 adduct of SiF_4 and PEt_3 is not associated with experimental results obtained.

215

The far–infrared data for the experimental spectrum (Figure 8.13a) showed two broad peaks centred on 386 and 417 cm^{-1} and the relative intensity during annealing process indicated that these two bands are not related to the same species. The experimental spectrum could be a mixture of both 1:1 adduct of trigonal bipyramid structure with axial PEt$_3$ and 1:2 complex of *trans*–[SiF$_4$.(PEt$_3$)$_2$] structure, as the energy of formation for *trans*–[SiF$_4$.(PEt$_3$)$_2$] is the most thermodynamically preferable (–25.17 kJ.mol^{-1}) comparing with the formation energy for a 1:1 complex with long distance PEt$_3$ interacted with SiF$_4$. The calculated IR spectra (Figure 8.33) has a group of overlapped bands around 400 cm^{-1} and another intense peak at 486.4 cm^{-1} in FIR region, these bands correspond with the far infrared of experimental spectrum located at 386 and 417 cm^{-1} with a little shift in wavenumbers; whereas the features in the mid infrared part of calculated spectrum are relevant with the experimental vibrational frequencies. This result is in agreement with the literature data of the reaction between SiF$_4$ and PMe$_3$, and also the complexes formed of the reaction of SiCl$_4$ with PMe$_3$ as both 1:1 and 1:2 complexes were formed.[15, 20, 45]
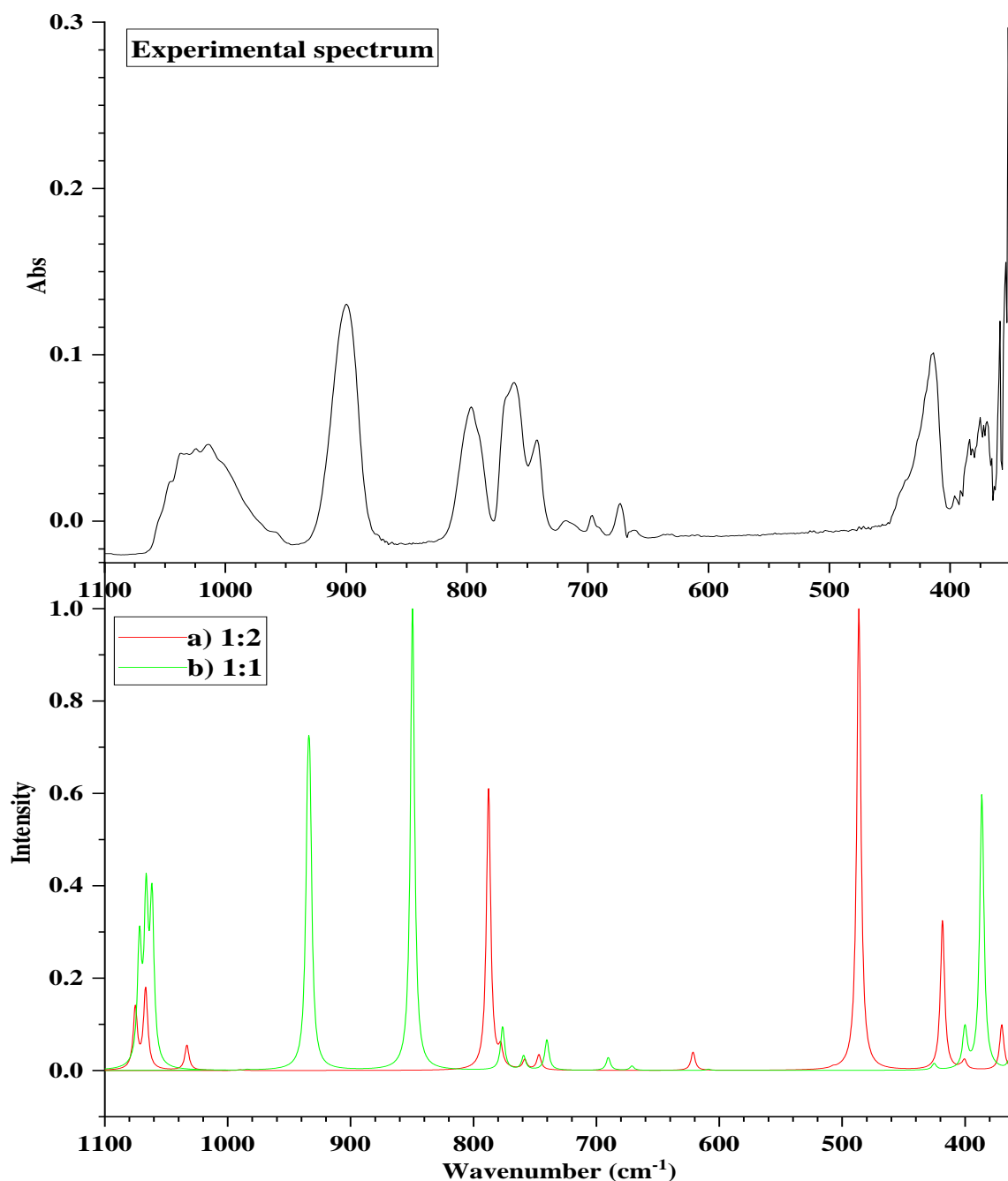
Figure 8.33: *Calculated (B3LYP/def2tzvpp) IR spectra of a mixture of 1:1 adduct SiF₄.PEt₃ and 1:2 adduct SiF₄.(PEt₃)₂ at half−width 4 cm⁻¹ and the experimental spectrum.*

8.4 Conclusion

The FTIR spectrum of SiF_4 in the mid IR region shows a strong asymmetric broad peak centred at 993 cm⁻¹ alongside two shoulders at 988 and 1055 cm⁻¹ assigned to Si–F asymmetric stretching mode,[32, 43, 44] and a very weak peak at 835 cm⁻¹ is attributed to the symmetric stretching mode of Si–F bonds; and only a sharp peak in the far infrared region at 369.6 cm⁻¹ which is related to the Si–F in plane scissoring bending mode.[44] The calculation confirmed that the geometry of SiF_4 is tetrahedral (T_d). Furthermore, the FIR

217

spectra for neat PMe$_3$ as well as neat PEt$_3$ showed no bands in the far infrared region. The interaction of SiF$_4$ with either PMe$_3$ or PEt$_3$ was conducted successfully using thin films at 80 K as performed previously by earlier undergraduate project students.[41, 42]

The FTIR spectrum collected after depositing five aliquots of 1:1 ratio of SiF$_4$ and PMe$_3$ shows bands at 954, 894, 855, 789, 749, 725, 675, 426, a shoulder peak at 420, and 388 cm^{-1}, these bands are due to reaction between SiF$_4$ and PMe$_3$ indicating the formation of a SiF$_4$−PMe$_3$ complex. Additionally, the FTIR spectra collected after using aliquots of different proportions of a SiF$_4$ and PMe$_3$ samples revealed noticeable changes in relative intensity of bands at 894 and 675 cm^{-1} in all spectra comparing with the relative intensities of other bands related to the indicating the formation of two different species. Although, there is strong evidence for the formation of complexes between SiF$_4$ and PMe$_3$.[15, 20] The B3LYP/def2tzvpp calculations have not really helped in identifying the geometries of them.

The FTIR spectrum recorded after introducing a 1:1 ratio of 5 torr SiF$_4$ and 5 torr PEt$_3$ at 80 K showed three bands located at 900, 796, and 415 cm^{-1} that do not belong to either neat SiF$_4$ nor PEt$_3$, alongside a weak feature at 386 cm^{-1} and a strong band at 417 cm^{-1} in the far infrared region suggesting the formation of SiF$_4$ complex with PEt$_3$. The two band in the far–IR region show different behaviour on annealing, these two bands are more likely belong to two different species. The computational data suggested the formation of a mixture of 1:1 adduct of trigonal bipyramid structure with axial PEt$_3$ and 1:2 complex of *trans*–[SiF$_4$.(PEt$_3$)$_2$] structure because of the presence of two bands in the FIR region. This result corresponds with literature data of the reaction of SiCl$_4$ with PMe$_3$ as both 1:1 and 1:2 complexes were formed.[15, 20, 45]

8.5 Summary

The bands at 954, 894, 855, 789, 749, 725, 675, 426, a shoulder peak at 420, and 388 cm^{-1} are due to products from reaction between SiF$_4$ and PMe$_3$ indicating the formation of a SiF$_4$−PMe$_3$ complexes. The noticeable changes in relative intensity of bands at 894 and 675 cm^{-1} recorded after using aliquots of different proportions of SiF$_4$ and PMe$_3$ samples indicate the formation of two different species. Calculated vibrational frequencies do not agree well with observed data suggesting the forcefields used are not entirely suitable for calculations of these complexes. The three bands located at 900, 796, and 415 cm^{-1}, alongside two features at 386 and 417 cm^{-1} in the far infrared region

suggest the formation of SiF$_4$−PEt$_3$ complex, which is first observation. The computational data suggested the formation of a mixture of 1:1 adduct of trigonal bipyramid structure with axial PEt$_3$ and 1:2 complex of *trans*–[SiF$_4$.(PEt$_3$)$_2$] structure.

8.6 References

1.   N. V. Sidgwick, *The Electronic Theory of Valency, Clarendon Press, Oxford*, 1927.
2.   M. Santelli and J.-M. Pons, *Lewis Acids and Selectivity in Organic Synthesis, CRC Press, Boca Raton*, 1996.
3.   W. B. Jensen, *The Lewis acid-base concepts: An overview, John Wiley & Sons, Inc., New York*, 1980.
4.   G. N. Lewis, *Valence and the structure of Atoms and Molecules, The Chemical Catalog Co., New York*, 1923, 141-142.
5.   T. Lowry, *Chem. lnd. (London)*, 1923, **42**, 43.
6.   J. Brønsted, *Recl. Trav. Chim. Pays-Bas.*, 1923, **42**, 718-728.
7.   W. Levason, G. Reid and W. Zhang, *Coord. Chem. Rev.*, 2011, **255**, 1319-1341.
8.   A. P. M. Robertson, J. N. Friedmann, H. A. Jenkins and N. Burford, *Chem. Commun.*, 2014, **50**, 7979-7981.
9.   J. Burt, W. Levason and G. Reid, *Coord. Chem. Rev.*, 2014, **260**, 65–115.
10. D. Gerlach, E. Brendler and J. Wagler, *Inorganics*, 2016, **4**, 18.
11. A. Kampfe, E. Brendler, E. Kroke and J. Wagler, *Chem.-Eur. J.*, 2014, **20**, 9409-9418.
12. J. C. Li, Y. Li, I. Purushothaman, S. De, B. Li, H. P. Zhu, P. Parameswaran, Q. S. Ye and W. P. Liu, *Organometallics*, 2015, **34**, 4209-4217.
13. N. Kuhn, T. Kratz, D. Blaeser and R. Boese, *Chem. Ber.*, 1995, **128**, 245−250.
14. N. A. Young, *Coord. Chem. Rev.*, 2013, **257**, 956–1010.
15. I. R. Beattie and G. A. Ozin, *J. Chem. Soc. A.*, 1969, 2267-2269.
16. P. Ramasami and T. A. Ford, *J. Mol. Struct.: THEOCHEM*, 2010, **940**, 50–55.
17. I. R. Beattie, *Quart. Rev. (London)*, 1963, **17**, 382.
18. G. Wilkinson, R. D. Gillard and J. A. McCleverty, *Comprehensive Coordination Chemistry I, vol. 3, Pergamon Press, NY*, 1987, p. 183.
19. J. A. McCleverty and T. J. Meyer, *Comprehensive Coordination Chemistry II, vol. 3, Elsevier, Oxford*, 2004, p. 545.
20. I. R. Beattie and G. A. Ozin, *J. Chem. Soc. A*, 1970, 370–377.
21. B. S. Ault, *Inorg. Chem.*, 1981, **20**, 2817–2822.
22. E. L. Muetterties, W. Mahler and R. Schmutzler, *Inorg. Chem. 2*, 1963, **2**, 613-618.
23. J. M. Chehayber, S. T. Nagy and C. S. Lin, *Can. J. Chem.-Rev. Can. Chim.*, 1984, **62**, 27-31.
24. T. J. Lorenz and B. S. Ault, *Inorg. Chem.*, 1982, **21**, 1758-1761.
25. B. S. Ault, *J. Mol. Struct.*, 1985, **129**, 287-298.
26. B. S. Ault, *J. Mol. Struct.*, 1985, **130**, 215-226.
27. R. S. Ruoff, T. Emilsson, A. I. Jaman, T. C. Germann and H. S. Gutowsky, *J. Chem. Phys.*, 1992, **96**, 3441-3446.
28. E. I. Davydova, A. Y. Timoshkin, T. N. Sevast'yanova, A. V. Suvorov and H. F. Schaefer, *Russ. J. Gen. Chem.*, 2003, **73**, 1742-1750.
29. V. O. Gel'mbol'dt, L. V. Koroeva and A. A. Ennan, *Russ. J. Coord. Chem.*, 2007, **33**, 160-167.
30. A. V. Sakharov, V. F. Sukhoverkhov, A. A. Ennan and V. O. Gel'mbol'dt, *Zh. Neorg. Khim.*, 1989, **34**, 1914-1918.
31. S. A. Baer and F. Kraus, *31- Preparation of SiF4(NH3)2 and Its Higher Ammoniate SiF4(NH3)2·2NH3, Efficient Methods for Preparing Silicon Compounds, Academic Press*, 2016, 395–397.
32. N. J. Hora, B. M. Wahl, C. Soares, S. A. Lara, J. R. Lanska and J. A. Phillips, *J. Mol. Struct.*, 2018, **1157**, 679-692.

33. J. L. Margrave, K. G. Sharp and P. W. Wilson, *J. Am. Chem. Soc.*, 1970, **92**, 1530-1532.
34. B. S. Ault, *J. Am. Chem. Soc.* , 1983, **105**, 5742-5746.
35. S. K. Ignatov, P. G. Sennikov, B. S. Ault, A. A. Bagatur'yants, I. V. Simdyanov, A. G. Razuvaev, E. J. Klimov and O. Gropen, *J. Phys. Chem. A* 1999, **103** 8328-8336.
36. P. Sennikov, M. Ikrin, S. Ignatov, A. A. Bagatur'yants and E. Klimov, *Russ. Chem. Bull.*, 1999, **48**, 93.
37. S. K. Ignatov, P. G. Sennikov, A. G. Razuvaev and L. A. Chuprov, *Russ. Chem. Bull.*, 2001, **50**, 2316-2324.
38. B. S. Ault, *J. Mol. Struct.* , 1985, **127**, 357-367.
39. K. George, A. L. Hector, W. Levason, G. Reid, G. Sanderson, M. Webster and W. Zhang, *Dalton Trans.*, 2011, **40**, 1584−1593.
40. D. J. D. Wilson, S. A. Couchman and J. L. Dutton, *Inorg. Chem.*, 2012, **51**, 7657–7668.
41. A. Niculau, *MChem final research project, University of Hull*, 2016.
42. R. Brighouse, *MChem final research project, University of Hull*, 2014.
43. H. M. Helminiak, R. R. Knauf, S. J. Danforth and J. A. Phillips, *J. Phys. Chem. A*, 2014, **118**, 4266-4277.
44. D. Lin-Vien, N. B. Colthup, W. G. Fateley and J. G. Grasselli, *The Handbook of Infrared and Raman Characteristic of Organic Molecules, Academic Press, San Diego, California, USA*, 1991.
45. W. Levason, D. Pugh and G. Reid, *Inorg. Chem.*, 2013, **52**, 5185-5193.

Appendix A

Table A.1: Calculation of NiF species using B3LYP/def2tzvpp.

Suggested molecular structure	Spin	Calculated molecular structure	Imaginary frequency	Total energy, kJ/mol	Relative energy, kJ/mol	Calculated Vibrational frequencies (cm^{-1})
NiF	Doublet	–	0	–4223276.0255	0	614.36 (74.08)
NiF	Quartet	–	0	–4223180.4700	95.555	631.99
NiF	Sexet	–	0	–4222465.9651	810.060	59.90

Table A.2: Calculation of NiF_2 species using B3LYP/def2tzvpp.

Suggested molecular structure	Spin	Calculated molecular structure	Imaginary frequency	Total energy, kJ/mol	Relative energy, kJ/mol	Calculated vibrational frequencies (cm^{-1})
NiF_2 Linear	Singlet	Linear	Yes	–4485550.6928	–	797.14
NiF_2 Bent 120°	Singlet	Bent	0	–4485585.5862	155.951	721.32, 675.82
NiF_2 Bent 90°	Singlet	Bent	0	–4485585.5862	155.951	721.14, 675.67
NiF_2 Linear	Triplet	linear	0	–4485741.5365	0	799.64 (170.53)
NiF_2 Bent 120°	Triplet	linear	0	–4485741.5365	0	799.65 (170.53)

Table A.3: Calculation of NiF$_3$ species using B3LYP/def2tzvpp.

Suggested molecular structure	Spin	Calculated molecular structure	Imaginary frequency	Total energy, kJ/mol	Relative energy, kJ/mol	Calculated vibrational frequencies (cm^{-1})
NiF$_3$ Trigonal planar	Doublet	Y–shaped	Yes	–4747858.3072	–	783.09, 688.94
NiF$_3$ T–shaped	Doublet	Distorted trigonal planar	Yes	–4747857.6584	–	682.67, 538.81, 448.45
NiF$_3$ Y–shaped 85°	Doublet	Distorted trigonal planar	0	–4747860.4023	67.536	783.91, 680.06
NiF$_3$ Y–shaped 80°	Doublet	Y–shaped	Yes	–4747858.3073	–	782.62, 688.87
NiF$_3$ Trigonal planar	Quartet	Distorted trigonal planar	Yes	–4747927.3428	–	692.17, 616.62
NiF$_3$ T–shaped	Quartet	Distorted trigonal planar	Yes	–4747927.3429	–	692.91, 606.19
NiF$_3$ Y–shaped 85°	Quartet	Y–shaped	0	–4747927.9378	0	737.29 (111.52), 650.33 (147.11)
NiF$_3$ Trigonal planar	Sextet	Trigonal planar	Yes	–4747203.4173	–	527.37
NiF$_3$ T–shaped	Sextet	Distorted trigonal planar	Yes	–4747243.6795	–	525.71, 421.33

Table A4: Calculation of NiF$_4$ species using B3LYP/def2tzvpp.

Suggested molecular structure	Spin	Calculated molecular structure	Imaginary frequency	Total energy, kJ/mol	Relative energy, kJ/mol	Calculated vibrational frequencies (cm^{-1})
NiF$_4$ Square planar	Singlet	Square planar	0	–5009833.6586	202.776	717.61
NiF$_4$ Seesaw	Singlet	Distorted seesaw	0	–5009971.4403	64.994	749.15, 709.58, 626.30
NiF$_4$ Tetrahedral	Singlet	Distorted seesaw	0	–5009971.4403	64.994	752.12, 706.86, 626.40
NiF$_4$ Square planar	Triplet	Square planar	Yes	–5009991.2590	–	761.61, 743.91
NiF$_4$ Seesaw	Triplet	Distorted seesaw	0	–5009991.8699	44.565	756.45, 744.86, 539.05
NiF$_4$ Tetrahedral	Triplet	Distorted seesaw	0	–5010035.0722	1.362	736.52, 612.20
NiF$_4$ Square planar	Quintet	Square planar	Yes	–5009914.6074	–	639.96
NiF$_4$ Seesaw	Quintet	Tetrahedral	Yes	–5010036.1635	–	681.45, 633.71
NiF$_4$ Tetrahedral	Quintet	Tetrahedral	0	–5010036.4347	0	696.37 (37.07), 649.86 (60.12)
NiF$_4$ Distorted square planar	Quintet	Tetrahedral	0	–5010036.4513	–0.0166	695.28, 656.58, 644.50

Table A.5: Calculation of NiF species using B3LYP/6–311G(+d).

Suggested molecular structure	Spin	Calculated molecular structure	Imaginary frequency	Total energy, kJ/mol	Relative energy, kJ/mol	Calculated Vibrational frequencies (cm^{-1})
NiF	Doublet	–	0	–4223041.961	0	606.61 (76.93)
NiF	Quartet	–	0	–4222940.814	101.147	618.52
NiF	Sextet	–	0	–4222189.1809	852.780	705.57

Table A.6: Calculation of NiF_2 species using B3LYP/6–311G(+d).

Suggested molecular structure	Spin	Calculated molecular structure	Imaginary frequency	Total energy, kJ/mol	Relative energy, kJ/mol	Calculated vibrational frequencies (cm^{-1})
NiF_2 Linear	Singlet	Bent	0	–4485296.13759	170.335	1115.27, 601.36
NiF_2 Bent 140°	Singlet	Bent	0	–4485313.14560	153.327	693.27, 654.03
NiF_2 Linear	Triplet	linear	0	–4485466.47206	0.00002626	790.75 (177.57)
NiF_2 Bent 140°	Triplet	linear	0	–4485466.47209	0	790.47 (177.55)

Table A.7: Calculation of NiF_3 species using B3LYP/6–311G(+d).

Suggested molecular structure	Spin	Calculated molecular structure	Imaginary frequency	Total energy, kJ/mol	Relative energy, kJ/mol	Calculated vibrational frequencies (cm^{-1})
NiF_3 Trigonal planar	Doublet	Distorted trigonal planar	0	–4747541.6989	75.021	976.43, 666.38, 403.01
NiF_3 T–shaped	Doublet	Distorted trigonal planar	0	–4747541.6985	74.284	976.56, 664.24, 403.05
NiF_3 Trigonal planar	Quartet	Y–shaped	0	–4747616.7201	0	720.33 (108.97), 636.60 (140.56)
NiF_3 T–shaped	Quartet	Distorted trigonal planar	0	–4747615.9821	0.738	679.67, 520.77
NiF_3 Trigonal planar	Sextet	Trigonal planar	0	–4746898.2678	718.452	489.31
NiF_3 T–shaped	Sextet	Distorted trigonal planar	0	–4746944.4783	672.242	449.09, 411.41

Table A.8: Calculation of NiF_4 species using B3LYP/6–311G(+d).

Suggested molecular structure	Spin	Calculated molecular structure	Imaginary frequency	Total energy, kJ/mol	Relative energy, kJ/mol	Calculated vibrational frequencies (cm^{-1})
NiF_4 Square planar	Singlet	Square planar	Yes	–5009480.7692	–	703.08
NiF_4 Seesaw	Singlet	Distorted seesaw	0	–5009625.5487	66.016	735.21, 690.84
NiF_4 Square planar	Triplet	Square planar	0	–5009639.8687	51.696	746.59, 732.59
NiF_4 Seesaw	Triplet	Square planar	0	–5009639.8691	51.695	747.22, 732.08
NiF_4 Tetrahedral	Triplet	Distorted seesaw	0	– 5009111.5972	579.967	744.30, 620.21
NiF_4 Square planar	Quintet	Square planar	Yes	–5009570.8966	–	621.49
NiF_4 Seesaw	Quintet	Tetrahedral	Yes	–5009691.5192	–	659.17, 617.96
NiF_4 Tetrahedral	Quintet	Tetrahedral	0	–5009691.5645	0	673.03 (33.05), 633.03 (55.33)

Appendix B

Table B.1: Calculation of CoF species using B3LYP/def2tzvpp.

Suggested molecular structure	Spin	Calculated molecular structure	Imaginary frequency	Total energy, kJ/mol	Relative energy, kJ/mol	Calculated Vibrational frequencies (cm^{-1})
CoF	Singlet	–	0	–3893363.2823	199.94	640.43
CoF	Triplet	–	0	–3893563.2248	0	618.64 (90.28)
CoF	Quintet	–	0	–3893482.0613	81.16	674.87

Table B.2: Calculation of CoF_2 species using B3LYP/def2tzvpp.

Suggested molecular structure	Spin	Calculated molecular structure	Imaginary frequency	Total energy, kJ/mol	Relative energy, kJ/mol	Calculated vibrational frequencies (cm^{-1})
CoF_2 Linear	Doublet	Linear	0	–4155891.0176	168.98	741.60
CoF_2 Bent 120°	Doublet	Bent	0	–4155909.6696	150.32	723.10, 649.92
CoF_2 Bent 90°	Doublet	Bent	0	–4155794.7748	265.22	697.02, 544.09
CoF_2 Linear	Quartet	Linear	0	–4156059.9939	0	770.82 (228.45)
CoF_2 Bent 120°	Quartet	Linear	0	–4156059.9930	0.0009191	770.42
CoF_2 Bent 90°	Quartet	Linear	0	–4156059.9936	0.0002626	770.82
CoF_2 Linear	Sextet	Linear	0	–4155621.6064	438.39	646.95
CoF_2 Bent 120°	Sextet	Bent	0	–4155711.6897	348.30	651.59, 639.57
CoF_2 Bent 90°	Sextet	Bent	0	–4155719.0494	340.94	663.17, 657.39

Table B.3: Calculation of CoF$_3$ species using B3LYP/def2tzvpp.

Suggested molecular structure	Spin	Calculated molecular structure	Imaginary frequency	Total energy, kJ/mol	Relative energy, kJ/mol	Calculated vibrational frequencies (cm^{-1})
CoF$_3$ Trigonal planar	Singlet	Trigonal planar	0	–4418103.1053	258.06	671.91
CoF$_3$ T–shaped	Singlet	Trigonal planar	0	–4418102.8114	258.35	706.60, 673.39, 659.51, 537.63
CoF$_3$ T–shaped	Triplet	Distorted trigonal planar	0	–4418273.5465	87.62	722.15, 692.33
CoF$_3$ Trigonal planar	Quintet	Trigonal planar	0	–4418361.1621	0.0029674	727.27
CoF$_3$ T–shaped	Quintet	Trigonal planar	0	–4418361.1651	0	727.83 (143.82), 723.23 (141.96)

Table B.4: Calculation of CoF$_4$ species using B3LYP/def2tzvpp.

Suggested molecular structure	Spin	Calculated molecular structure	Imaginary frequency	Total energy, kJ/mol	Relative energy, kJ/mol	Calculated vibrational frequencies (cm^{-1})
CoF$_4$ Square planar	Doublet	Square planar	Yes	–4680288.6534	–	556.89, 389.55
CoF$_4$ Distorted tetrahedral	Doublet	Distorted tetrahedral	0	–4680428.4814	106.29	756.84, 749.81, 727.77, 661.42
CoF$_4$ Square planar	Quartet	Square planar	Yes	–4680477.6453	–	779.66
CoF$_4$ Tetrahedral	Quartet	Distorted tetrahedral	0	–4680453.2947	81.48	724.64, 683.24
CoF$_4$ Square planar	Sextet	Square planar	Yes	–4680343.2810	–	652.01
CoF$_4$ Tetrahedral	Sextet	Tetrahedral	0	–4680534.7732	0	720.45 (92.36)

Table B.5: Calculation of CoF species using B3LYP/6–311G(+d).

Suggested molecular structure	Spin	Calculated molecular structure	Imaginary frequency	Total energy, kJ/mol	Relative energy, kJ/mol	Calculated Vibrational frequencies (cm^{-1})
CoF	Singlet	–	0	–3893167.5368	199.33	636.17
CoF	Triplet	–	0	–3893366.8661	0	609.86 (91.92)
CoF	Quintet	–	0	–3893275.9161	90.95	661.34

Table B.6: Calculation of CoF$_2$ species using B3LYP/6–311G(+d).

Suggested molecular structure	Spin	Calculated molecular structure	Imaginary frequency	Total energy, kJ/mol	Relative energy, kJ/mol	Calculated vibrational frequencies (cm^{-1})
CoF$_2$ Linear	Doublet	Linear	0	–4155655.7843	175.16	736.2
CoF$_2$ Bent 120°	Doublet	Bent	0	–4155677.0157	153.93	630.16, 701.66
CoF$_2$ Bent 90°	Doublet	Bent	Yes	–4155552.2775	–	764.84
CoF$_2$ Linear	Quartet	Linear	0	–4155820.4996	10.45	761.63
CoF$_2$ Bent 120°	Quartet	Linear	0	–4155830.9472	0	775.13 (182.78)
CoF$_2$ Linear	Sextet	Linear	Yes	–4155387.1315	–	632.80
CoF$_2$ Bent 120°	Sextet	Bent	0	–4155473.2359	357.71	620.12, 630.16
CoF$_2$ Bent 90°	Sextet	Bent	0	–4155479.9628	350.98	636.76

Table B.7: Calculation of CoF$_3$ species using B3LYP/6–311G(+d).

Suggested molecular structure	Spin	Calculated molecular structure	Imaginary frequency	Total energy, kJ/mol	Relative energy, kJ/mol	Calculated vibrational frequencies (cm^{-1})
CoF$_3$ Trigonal planar	Singlet	Trigonal planar	Yes	–4417815.3927	–	527.26, 487.87
CoF$_3$ T–shaped	Singlet	Y–shaped	0	–4417820.4423	266.97	833.08, 799.63, 657.18, 614.19
CoF$_3$ T–shaped	Triplet	Distorted trigonal planar	0	–4417996.5233	90.63	757.35, 678.84
CoF$_3$ Trigonal planar	Quintet	Trigonal planar	0	–4418087.1484	0.000055	705.91
CoF$_3$ T–shaped	Quintet	Trigonal planar	0	–4418087.1489	0	708.53 (144.94), 707.40 (145.91)

Table B.8: Calculation of CoF$_4$ species using B3LYP/6–311G(+d).

Suggested molecular structure	Spin	Calculated molecular structure	Imaginary frequency	Total energy, kJ/mol	Relative energy, kJ/mol	Calculated vibrational frequencies (cm^{-1})
CoF$_4$ Square planar	Doublet	Square planar	Yes	–4679949.4189	–	720.81
CoF$_4$ Seesaw	Doublet	Distorted seesaw	0	–4680059.3283	164.70	816.76, 761.24, 680.96, 631.45
CoF$_4$ Square planar	Quartet	Square planar	Yes	–4680162.2652	–	767.89
CoF$_4$ Seesaw	Quartet	Distorted square planar	0	–4680169.0045	55.02	755.54, 577.22
CoF$_4$ Tetrahedral	Quartet	Distorted square planar	0	–4680169.0045	55.02	755.25, 577.22
CoF$_4$ Square planar	Sextet	Square planar	Yes	–4680038.1055	–	636.41
CoF$_4$ Seesaw	Sextet	Tetrahedral	0	–4680223.8483	0.18	692.21
CoF$_4$ Tetrahedral	Sextet	Tetrahedral	0	–4680224.0276	0	697.82 (90.67)

Appendix C

Table C.1: Calculation of MoF species using B3LYP/def2tzvpp.

Suggested molecular structure	Spin	Calculated molecular structure	Imaginary frequency	Total energy, kJ/mol	Relative energy, kJ/mol	Calculated Vibrational frequencies (cm^{-1})
MoF	Doublet	–	0	–441172.2958	193.24	661.75 (118.41)
MoF	Quartet	–	0	–441243.9314	121.61	649.43 (116.92)
MoF	Sexet	–	0	–441365.5385	0	620.11 (148.09)

Table C.2: Calculation of MoF_2 species using B3LYP/def2tzvpp.

Suggested molecular structure	Spin	Calculated molecular structure	Imaginary frequency	Total energy, kJ/mol	Relative energy, kJ/mol	Calculated vibrational frequencies (cm^{-1})
MoF_2 Linear	Singlet	Linear	0	–703704.8248	173.87	739.94 (208.82)
MoF_2 Bent 120°	Singlet	Bent	0	–703713.0387	168.66	736.27 (204.05), 644.09 (17.63)
MoF_2 Bent 90°	Singlet	Bent	0	–703713.0387	168.66	736.13 (204.05), 633.94 (17.61)
MoF_2 Linear	Triplet	linear	0	–703794.3228	87.37	739.16 (206.84)
MoF_2 Bent 120°	Triplet	Bent	0	–703820.3071	61.39	711.83 (256.43), 667.0 (1.23)
MoF_2 Bent 90°	Triplet	Bent	0	–703707.5599	174.13	698.07 (130.78), 661.82 (73.19)
MoF_2 Linear	Quintet	Linear	0	–703864.3094	17.38	655.48 (265.76)
MoF_2 Bent 120°	Quintet	Bent	0	–703881.6944	0	655.49 (198.0), 634.01(59.5)
MoF_2 Bent 90°	Quintet	Bent	0	–703881.6943	0.00013	665.16 (197.9), 634.71 (59.55)

Table C.3: Calculation of MoF$_3$ species using B3LYP/def2tzvpp.

Suggested molecular structure	Spin	Calculated molecular structure	Imaginary frequency	Total energy, kJ/mol	Relative energy, kJ/mol	Calculated vibrational frequencies (cm^{-1})
MoF$_3$ Trigonal planar	Doublet	Distorted trigonal planar	0	−966333.9150	77.83	730.30 (216.83), 678.55 (0.03), 635.92 (177.68)
MoF$_3$ T–shaped	Doublet	Distorted trigonal planar	0	−966333.4635	78.28	698.66 (128.5), 687.33 (240.45), 682.67 (177.68)
MoF$_3$ Trigonal planar	Quartet	Trigonal planar	0	−966411.7455	0	692.26 (198.0)
MoF$_3$ T–shaped	Quartet	T–shaped	Yes	−966304.7690	–	–
MoF$_3$ Trigonal planar	Sextet	Distorted trigonal planar	0	−965987.1723	454.57	631.96 (165.38), 510.13 (30.14)
MoF$_3$ T–shaped	Sextet	Distorted trigonal planar	0	−965873.0664	538.68	523.51 (18.54), 409.79 (6.54)

Table C.4: Calculation of MoF$_4$ species using B3LYP/def2tzvpp.

Suggested molecular structure	Spin	Calculated molecular structure	Imaginary frequency	Total energy, kJ/mol	Relative energy, kJ/mol	Calculated vibrational frequencies (cm^{-1})
NiF$_4$ Square planar	Singlet	Square planar	0	−1228763.3086	91.74	734.89 (290.01)
NiF$_4$ Tetrahedral	Singlet	Distorted tetrahedral	0	−1228797.2479	57.80	734.20 (233.61), 34.11 (233.23), 641.66 (61.66)
NiF$_4$ Square planar	Triplet	Square planar	0	−1228770.1926	84.86	728.78 (313.3), 673.47 (324.23)
NiF$_4$ Tetrahedral	Triplet	Tetrahedral	0	−1228855.0477	0	678.78 (186.42)

Table C.5: Calculation of MoF$_5$ species using B3LYP/def2tzvpp.

Suggested molecular structure	Spin	Calculated molecular structure	Imaginary frequency	Total energy, kJ/mol	Relative energy, kJ/mol	Calculated vibrational frequencies (cm^{-1})
MoF$_5$ Square pyramidal	Doublet	Distorted trigonal bipyramid	Yes	–1419247.4869	–	746.99, 689.79, 677.08
MoF$_5$ Trigonal bipyramid	Doublet	Distorted trigonal bipyramid	Yes	–1491247.4749	–	761.01, 689.90, 648.39
MoF$_5$ Distorted trigonal bipyramid as T–shaped	Doublet	Distorted trigonal bipyramid	Yes	–1491247.7535	–	742.79, 725.33, 689.76, 626.96
MoF$_5$ Distorted trigonal bipyramid as Y–shaped	Doublet	Distorted trigonal bipyramid	Yes	–1491247.4748	–	761.16, 689.68, 648.19
MoF$_5$ Distorted trigonal bipyramid as bent axial	Doublet	Distorted trigonal bipyramid	Yes	–1491247.4710	–	760.58, 689.67, 647.43
MoF$_5$ Distorted trigonal bipyramid	Doublet	Distorted trigonal bipyramid	0	–1491247.7382	0	761.51 (244.31), 689.45 (355.32), 650.0 (277.82)
MoF$_5$ Square pyramidal	Quartet	Distorted Square pyramidal	Yes	–1490774.3336	–	691.77, 599.42
MoF$_5$ Trigonal bipyramid	Quartet	Distorted trigonal bipyramid	Yes	–1490845.8082	–	723.59, 668.41, 626.10, 440.77
MoF$_5$ Square pyramidal	Sextet	Distorted Square pyramidal	Yes	–1490349.3141	–	471.0, 441.56

Table C.6: Calculation of MoF_6 species using B3LYP/def2tzvpp.

Suggested molecular structure	Spin	Calculated molecular structure	Imaginary frequency	Total energy, kJ/mol	Relative energy, kJ/mol	Calculated Vibrational frequencies (cm^{-1})
NiF_6 Octahedral	Singlet	Octahedral	0	−1753614.8340	0	734.15 (338.56)
NiF_6 Octahedral	Triplet	Octahedral	0	−1753179.9772	434.86	698.67 (323.63), 470.06 (4.38)
NiF_6 Octahedral	Quintet	Octahedral	Yes	−175.2786.2725	–	–

Appendix D

Table D.1: Calculation of PdCl species using B3LYP/def2tzvpp.

Suggested molecular structure	Spin	Calculated molecular structure	Imaginary frequency	Total energy, kJ/mol	Relative energy, kJ/mol	Calculated Vibrational frequencies (cm^{-1})
PdCl	Doublet	–	0	–1544585.2072	0	311.94 (26.6.)
PdCl	Quartet	–	0	–1544346.7968	238.41	343.14 (19.33)

Table D.2: Calculation of PdCl$_2$ species using B3LYP/def2tzvpp.

Suggested molecular structure	Spin	Calculated molecular structure	Imaginary frequency	Total energy, kJ/mol	Relative energy, kJ/mol	Calculated vibrational frequencies (cm^{-1})
PdCl$_2$ Linear	Singlet	Linear	Yes	–2753112.2200	–	416.30, 110.96, –114.44
PdCl$_2$ Bent 120°	Singlet	Bent	0	–2753188.3465	15.20	383.48 (22.32), 101.94 (3.54)
PdCl$_2$ Bent 90°	Singlet	Bent	0	–2753188.3466	15.20	383.34 (22.33), 101.97 (3.54)
PdCl$_2$ Linear	Triplet	linear	0	–2753202.9680	0.57	419.85 (81.55), 21.64 (2.53)
PdCl$_2$ Bent 120°	Triplet	linear	0	–2753202.9680	0.57	419.68 (81.55), 21.89 (2.53)
PdCl$_2$ Bent 90°	Triplet	Linear	0	–2753203.5420	0	397.93 (73.63), 29.18 (5.9)
PdCl$_2$ Linear	Quintet	Linear	Yes	–2752717.4076	–	233.22, –88.37
PdCl$_2$ Bent 120°	Quintet	Bent	0	–2752787.0168	41653	303.75 (18.73), 216.43 (110.81), 91.33 (1.61)
PdCl$_2$ Bent 90°	Quintet	Bent	0	–2752787.0170	416.53	303.49 (18.73), 216.35 (110.81), 91.37 (10.61)

Table D.3: Calculation of PdCl₃ species using B3LYP/def2tzvpp.

Suggested molecular structure	Spin	Calculated molecular structure	Imaginary frequency	Total energy, kJ/mol	Relative energy, kJ/mol	Calculated vibrational frequencies (cm^{-1})
PdCl$_3$ Trigonal planar	Doublet	Y–shaped	Yes	–3961757.9478	–	396.48, 378.22, 346.13, –22.67, –88.48
PdCl$_3$ T–shaped	Doublet	Distorted trigonal planar	Yes	–3961764.4042	–	398.72, 379.50, 350.07, 89.11, –65.46
PdCl$_3$ distorted T–shaped	Doublet	Distorted trigonal planar	0	–3961766.0494	0	339.38 (64.16), 364.81 (19.87), 354.64 (6.78), 97.71 (2.69), 63.40 (7.24)
PdCl$_3$ Trigonal planar	Quartet	Y–shaped	Yes	–3961719.5121	–	370.19, 325.48, 294.80, 51.19, –94.12
PdCl$_3$ T–shaped	Quartet	Distorted trigonal planar	0	–3961720.5142	45.54	357.68 (106.10), 334.52 (31.11), 324.54 (0.99), 79.99 (0.07), 60.11 (7.55), 49.29 (3.28)
PdCl$_3$ Trigonal planar	Sextet	Trigonal planar	Yes	–3961143.9563	–	168.10, –44.25, –125.34
PdCl$_3$ T–shaped	Sextet	Distorted trigonal planar	0	–3961176.7056	589.34	325.34 (218.27), 261.22 (14.77), 168.27 (0.15), 103.29 (0.38), 92.89 (0.60)

Table D.4: Calculation of PdCl4 species using B3LYP/def2tzvpp.

Suggested molecular structure	Spin	Calculated molecular structure	Imaginary frequency	Total energy, kJ/mol	Relative energy, kJ/mol	Calculated vibrational frequencies (cm^{-1})
PdCl$_4$ Square planar	Singlet	Square planar	Yes	–5170145.00032	–	359.47, 109.19, –27.60
PdCl$_4$ Seesaw	Singlet	Distorted seesaw	0	–5170262.9354	10.73	396.41 (1.99) , 378.79 (78.21), 330.07 (0.79), 130.33 (0.79), 128.45 (1.22), 99.19 (0.08), 81.82 (0.01)
PdCl$_4$ Tetrahedral	Singlet	Distorted tetrahedral	Yes	–5170251.8929	–	394.35, 330.39, 175.56, 48.20, –55.08
PdCl$_4$ Square planar	Triplet	Square planar	Yes	–5170273.1152	–	337.78, 173.52, 86.59, –17.19
PdCl$_4$ Seesaw	Triplet	Square planar	Yes	–5170260.8182	–	362.84, 340.05, 254.99, 129.92, 123.67, 119.30, 31.19, –153.97
PdCl$_4$ Tetrahedral	Triplet	Distorted seesaw	0	–5170273.6685	0	368.14 (29.77), 305.47 (3.12), 122.35 (0.41), 103.94 (3.430
PdCl$_4$ Square planar	Quintet	Square planar	Yes	–5170087.9198	–	239.96, 46.54, –26616.42
PdCl$_4$ Seesaw	Quintet	Tetrahedral	0	–5170206.0196	67.65	324.92 14.59), 311.14 (29.77), 310.68 (0.21), 98.17 (0.04), 53.22 (1.19)
PdCl$_4$ Tetrahedral	Quintet	Tetrahedral	0	–5170206.0196	67.65	324.88 (14.60), 331.10 (29.98), 53.22 (1.19)